UNIVERSITY OF CALIFORNIA
RIVERSIDE

Ultrafast Spectroscopy of Force- or Light-Induced Chemical and Electronic Changes in Condensed Phase Materials

A Dissertation submitted in partial satisfaction
of the requirements for the degree of

Doctor of Philosophy

in

Chemistry

by

Chad Cruz

June 2019

Dissertation Committee:

Dr. Eric Chronister, Chairperson
Dr. Gregory Beran
Dr. Jingsong Zhang

The Dissertation of Chad Cruz is approved by:

_____

_____

_____

Committee Chairperson

University of California, Riverside

ACKNOWLEDGEMENTS

"There are no shortcuts to any place worth going." – Beverly Sills

It seems like it took a lifetime but now, when asked what it is that I do, I'll be able to say something other than, "I'm in school." It was a long and often a trying journey but well worth it in the end. As I look back, I can't help but think of those who were crucial in helping me achieve this goal.

First, I would like to thank my advisor, Dr. Eric Chronister, you have been an encouragement to me and have allowed me to develop as an independent physical chemist. You have forever impacted the way that I communicate science as I now constantly ask myself, "Are all those words necessary?" I am very grateful for your support and patience as I went through grad school at a snail's pace.

To Dr. Chris Bardeen, grad school would have been rather lonely were it not for your inclusion of me in all your groups' activities. More importantly, you have dedicated so much time and energy to helping further my research and career endeavors. Your, "They're-full-of-shit" skepticism has certainly rubbed off on me and has taught me how to critically assess the literature. I am very grateful for your willingness to work with me.

To Dr. Kerry Hanson, you have been both a friend and mentor to me. Your remarkable ability to be so positive all the time has helped me maintain a better attitude about my research when it wasn't going so well. You have provided me with so much practical advice from parenting to work-life balance, and I'm thankful that I got to know you over these past few years. Thank you as well for inviting my family into your home for celebrations and making them feel welcomed.

To my parents, thank you for your love and support throughout the years. Dad, your work ethic has been a shining example to me as I've tried to develop the grit to succeed. Mom, your words and text messages of love and encouragement have lifted my spirits during stressful times. You two have always believed in me, and your faith in me gave me hope when I doubted myself. I am so grateful that Colton has both of you in his life, and on that note, thank you for all the spoiling and all the love that you have shown him.

To my sisters, Hailee and Shayne, On-ee-Nah-nee-NEENEENINE-MmMmMm. You two weirdos have helped probably more than you realize. I can't count all the times you have joyously taken Colton off my hands so that I could focus on a project or just make it to class. Your silliness and endless supply of inside jokes brightens my day, and despite my usual grumpy demeanor, (this will be the sole admission of this) I enjoy the time we get to spend together. I am so proud of both of you as you pursue your own academic

goals, and I hope that in some way I can repay you for the way you have helped me succeed.

To my son, Colton, you don't know how much your loving distractions have kept me grounded throughout this journey. Among all the baseball, biking and video games that we've played you have been a constant source of joy and inspiration in my life. Thank you for your patience and understanding during all the times that we were unable to play together because I had something to work on. I also appreciate all the times that you weren't so patient and kept pushing for us to play together. Many times, that was exactly what I needed. You are an incredibly bright, funny and athletic young man, and I'm so very proud of you.

Finally, to my wife, Alysson, I don't have the words to truly capture how grateful I am to you. That you were able to put up with me and my nonsense this whole time with patience, love, encouragement and without smacking me with a baseball bat is astounding. You have carried our family on your back while I've been distracted with school for far too long. You have been right there with me on long sleepless nights helping me proofread papers and proposals, making graphics and putting together PowerPoint presentations. You have been my constant and it is no exaggeration that I would not have endured without you. It is a shame that the degree will only have my name on it, because your fingerprints are all over every success that I've had, and you deserve much more credit than you are getting.

Acknowledgement of Previously Published Material

(1) Section 3.1 was rewritten and is based on the following published work: Tong, F.; Cruz, C.; Jezowski, S.; Zhou, X.; Zhu, L.; Al-Kaysi, R. O.; Chronister, E. L.; Bardeen, C. J. Pressure Dependence of the Forward and Backward Rates of 9-tert-Butylanthracene Dewar Isomerization. *J. Phys. Chem. A* **2014,** *118* (27), 5122.

(2) Section 4.2 was rewritten and is based on the following published work: Cruz, C. D.; Christensen, P. R.; Chronister, E. L.; Casanova, D.; Wolf, M. O.; Bardeen, C. J. Sulfur-Bridged Terthiophene Dimers: How Sulfur Oxidation State Controls Interchromophore Electronic Coupling. *J. Am. Chem. Soc.* **2015,** *137* (39), 12552.

(3) Chapter 5 was rewritten and is based on the following published work: Cruz, C. D.; Choi, H. H.; Podzorov, V.; Chronister, E. L.; Bardeen, C. J. Photon Upconversion in Crystalline Rubrene: Resonant Enhancement by an Interband State. *J. Phys. Chem. C* **2018,** *122* (31), 17632.

ABSTRACT OF THE DISSERTATION

Ultrafast Spectroscopy of Force- or Light-Induced Chemical and Electronic Changes in Condensed Phase Materials

by

Chad Cruz

Doctor of Philosophy, Graduate Program in Chemistry
University of California, Riverside, June 2019
Professor Eric Chronister, Chairperson

A mechanophore is a molecule which displays sensitivity toward some applied force. Mechanophores show promise for applications in smart materials and nanomachines. Identifying structural motifs in photoactive molecules which enhance pressure sensitivity has been one focus of this research. It was demonstrated that 9-tert-butylanthracene dissolved in Zeonex polymer shows increased rates of back reaction upon applying mild pressures (< 1.5 GPa) in a diamond anvil cell. While strained rings can enhance pressure sensitivity, it is not the most effective handle for tuning mechanophoric properties. This work highlighted that large structural changes in the photoproduct are also required to bring about the desired pressure sensitivity.

Intermolecular interactions cause assemblies of conjugated chromophores to behave distinctly different from the monomer. Delocalized excited states which lead to novel photophysics are examined in systems of varying complexity from covalently linked chromophores to molecular crystals. In covalent dimers of simple organic molecules like terthiophene and anthracene, a sulfur atom is used to link the chromophores, and the

oxidation state of the sulfur is found to modulate the electronic coupling leading to photophysics and photochemistry which are controlled by the electronic structure of the linker. An added advantage of using the sulfur linker is that the geometry between molecules remains constant regardless of the oxidation state, allowing purely electronic effects to be isolated, demonstrating that chemical modification of a single atom can dramatically alter the excited state behavior of a molecular assembly. In molecular crystals, delocalized excited states can lead to technologically important multiexciton processes such as fission and fusion. In crystalline rubrene NIR-to-visible upconversion is observed without the use of extrinsic sensitizers, a process which may be facilitated by low energy intermolecular states. The mechanism of singlet fission in crystalline tetracene is also explored particularly regarding the correlated triplet pair state. Evidence of this spin superposition state is manifest by temporal oscillations in the photoluminescence decay of tetracene. Based on the temperature dependence, the triplets diffuse independently throughout the crystal while maintaining spin coherence. These results could have important implications for strategies which seek to use triplet states to enhance device efficiencies.

TABLE OF CONTENTS

LIST OF FIGURES

Chapter 1: Introduction

"Life is bottled sunshine…" – William Winwood Reade

1.1 Sunlight – the limitless energy source

Civilization has long sought to use nature to its advantage by harnessing sunlight, wind and water to do useful work through the use of mills[1] or solar water heaters.[2] The invention of the steam engine improved upon more rudimentary attempts at harvesting energy from nature by using a physical transformation to power transportation.[3] Today, myriad fuel sources exist to power machines capable of doing useful work, and the proliferation of machines has raised the global power demands to more than 18 terrawatts (TW) as of 2017.[4] However, a new obstacle presents itself as 15 TW of that demand was met by hydrocarbon fuels,[4] the burning of which leads to an increase in greenhouse gases which is causing an increase in global temperatures. The dire consequences of manmade climate change have given rise to an impassioned interest in developing renewable energy sources. Of all the renewable sources, solar energy has the most potential to meet the global energy demands since the sun produces upwards of 83,000 TW of power annually.[5] However,efficiently harnessing solar energy is a primary hurdle preventing this renewable source from supplanting the current dominance of hydrocarbons as the preeminent fuel source.

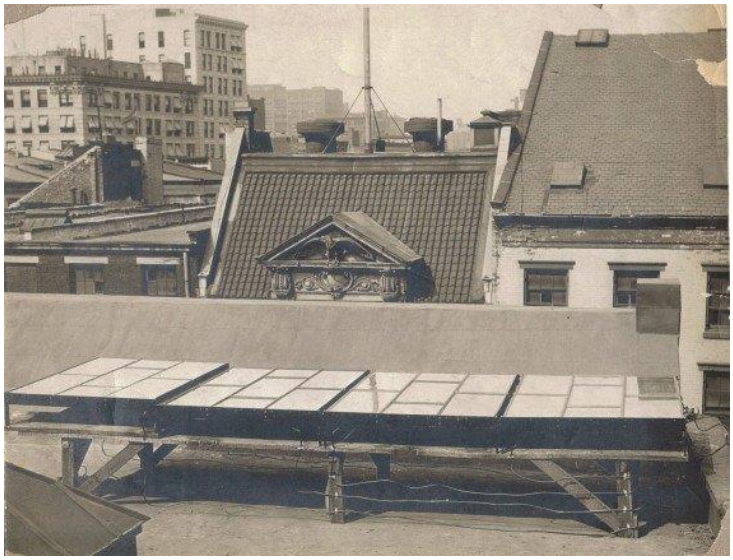

Figure 1.1.1 Image of the solar panel installed by Charles Fritts in 1883 on a New York City roof.[2]

Light has long been exploited as a source of energy in nature by plants which evolved the ability to convert photons into chemical energy through photosynthesis. Instead of storing solar energy in chemical bonds, recent work aims to convert solar energy into electricity through the photovoltaic effect. The ability of sunlight to generate electricity was first observed by a 19 year old Alexandre Edmond Becquerel in 1839, who shined light on a platinum sheet covered with silver chloride which was dipped into an electrolyte solution.[6] A current induced by sunlight was generated between the electrodes and he posited a chemical reaction to occur at the electrode (The correct one!).[7] A few decades later, while working on the transatlantic cable, Willoughby Smith reported that the selenium bars which were used in an electrical testing device, because of their high resistance, suddenly had a drastic reduction in resistance in the daylight.[8] Smith was able to rule out a heating effect and determined that light, in fact, was what

lead to the drastic change in the electrical properties of selenium. While this result generated intrigue from contemporaries, an explanation eluded the early scientists.[2] The first working solar cell was built by Charles Fritts in 1883 using selenium (Figure 1.1.1);[9] however with conversion efficiencies below 1%, the vision of solar powered cities would stall until the silicon revolution of the 1950's. At Bell Laboratories in 1954, Daryl Chapin along with Gerald Pearson and Calvin Fuller developed the first silicon solar cell which achieved efficiencies of 6%.[2] Today the power conversion efficiency of single junction crystalline silicon solar cells has improved to 26.1% which is near the single cell theoretical limit of 31% determined by Shockley and Queisser.[10,11]

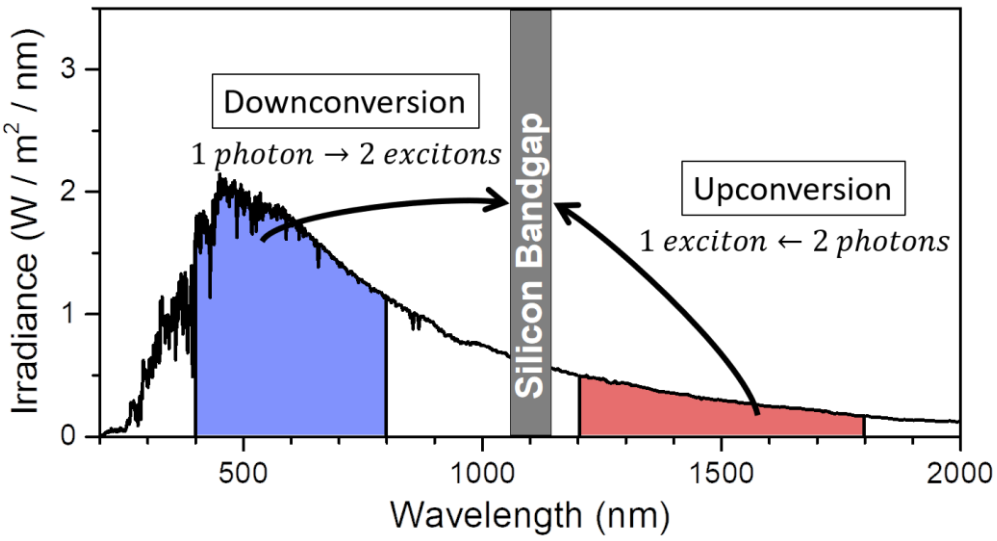

Figure 1.1.2. The AM-0 solar spectrum illustrating that the much of the spectrum is wasted when only silicon is used to generate photocurrent.

Third generation photovoltaics seek to surpass the Shockley-Queisser limit by utilizing more of the solar spectrum (Figure 1.1.2). Current silicon photovoltaics absorb photons with energies above the bandgap of 1.1 eV, but the excess energy is wasted as

heat as the electrons relax down to the bandgap. Photons below the bandgap are not absorbed and do not contribute to the photocurrent. A promising strategy capable of building on the existing silicon solar cell infrastructure is to add photon conversion materials on top of silicon cells enabling more of the solar spectrum to contribute to the photocurrent. These photon conversion strategies will be explored in chapters 5 and 6.

1.2 Tuning the photoresponse of symmetrically tethered dimers

Covalently tethered bichromophores provide an ideal proving ground to develop strategies for controlling excited state behavior in chromophore assemblies. In nature, light harvesting organisms make extensive use of energy and electron transfer between adjacent molecules. A great deal of work has been focused on synthesizing electron donor/acceptor pairs to mimic these efficient natural systems. The most common approach is to unite an electron-rich donor with an electron-deficient acceptor using a π-conjugated linkage or "bridge." Separation of the donor and acceptor by such a bridge can enable charge transfer (CT) over large distances, limiting charge recombination.[12] While remarkable photovoltaic performance has been achieved using this approach,[13] these asymmetric systems only partially mimic the naturally occurring photosynthetic reaction centers, where symmetric chromophore pairs have a central role in controlling excited-state dynamics.[14]

The rational design of symmetrically bridged chromophore dimers has attracted considerable theoretical[15,16] and practical[17,18] interest. For example, bichromophores have been used to study energy and charge transfer,[19-26] as well as singlet exciton fission[27-37] and triplet-triplet annihilation.[38,39] 9,9'- bianthryl, where two anthracene units are covalently bonded and adopt a nearly orthogonal orientation, has served as a model system for the study of excited-state electron transfer.[40] Thompson et al. have also synthesized a series of symmetric dipyrrin molecules that exhibit symmetry breaking CT using visible light.[24,25,41] These symmetric CT systems are of practical interest because the CT and neutral states are close in energy, which lowers the amount of energy lost in the charge separation event and has the potential to raise the open-circuit voltage of photovoltaic devices. Bichromophoric systems have also found applications in organic light emitting diodes (OLEDs).[42,43] Adachi et al. have also synthesized several types of organic molecules that harness both singlet and triplet excitons through a process known as thermally activated delayed fluorescence (TADF).[44,45] The singlet−triplet energy gap is most efficiently reduced when the HOMO and LUMO are spatially separated, which can be facilitated by intramolecular CT.[46] High-efficiency blue OLEDs were fabricated using SO2-bridged symmetric bichromophores.[47,48] While it was demonstrated that these SO2-bridged chromophores exhibit reduced singlet−triplet gaps facilitated by CT, the role of the symmetric nature of these emitters was not investigated.

It is anticipated that applications of dimeric molecules in photovoltaic and light emitting devices will require precise control of intradimer electronic interactions. One control strategy is to change the polarity of the environment and shift the relative energy levels of neutral and CT states; however, in solid-state devices, this is impractical. An alternate strategy is to control the electronic coupling between light absorbing units. Ideally, such a control element would be built into the dimer molecule itself, without inducing large conformational changes. Decreasing the distance and angle between chromophores can enhance electron transfer, but if molecules are too close together, aggregation-induced excited-state quenching often results.[49] The goal is then to control the interchromophore coupling in tethered assemblies while maintaining ideal dimer geometry. This structural motif allows the geometrical arrangement between the chromophores to be defined and the electronic interaction to be controlled. Such dimers or bichromophores form the smallest subunit of larger chromophore assemblies such as polymers and are useful for basic studies of phenomena relevant to organic electronic materials. Their unique properties may eventually lead to applications in technologies including light-emitting diodes and photovoltaics.

1.3 Photon upconversion with low energy intermolecular states

Photophysical phenomena in organic molecular materials can potentially form the basis of high-efficiency solar energy conversion technologies. Triplet−triplet annihilation (TTA) is an upconversion process in which a pair of low-energy triplet excitons fuses into one higher-energy singlet exciton that can emit a high-energy photon.[50,51] This physical process is one strategy to eventually surpass the Shockley−Queisser limit for single junction photovoltaic devices.[10,52-54]

In a crystal composed of rubrene (RUB), the triplet pair state is approximately isoenergetic with the singlet state and both singlet fission and triplet fusion can be quite efficient enabling rubrene to function as a photon conversion material.[55-63] These two processes are reflected in time-resolved photoluminescence (PL) experiments where both prompt and delayed components are observed (Figure 1.5.1).[62,64] In addition, these processes govern the unusual excitation intensity dependence of photoconductivity in RUB with fractional power exponents.[65] For organic triplet-triplet annihilation upconversion (TTA-UC), RUB is a commonly used emitter molecule due its long-lived triplet states and high PL quantum yield.[66-73] The low energy of RUB's triplet state (1.15 eV) allows it to be sensitized by near infrared (NIR) absorbing chromophores such as porphyrins[74,75] and inorganic nanocrystals.[67] After sensitization, triplet excited states on separate RUB molecules can fuse into a higher energy singlet state which then emits a

visible photon. Most reported upconversion schemes are performed in solutions, since facile diffusion permits the triplet sensitization and subsequent fusion events to occur in different spatial regions. This prevents energy transfer from the emitter back to the sensitizer.

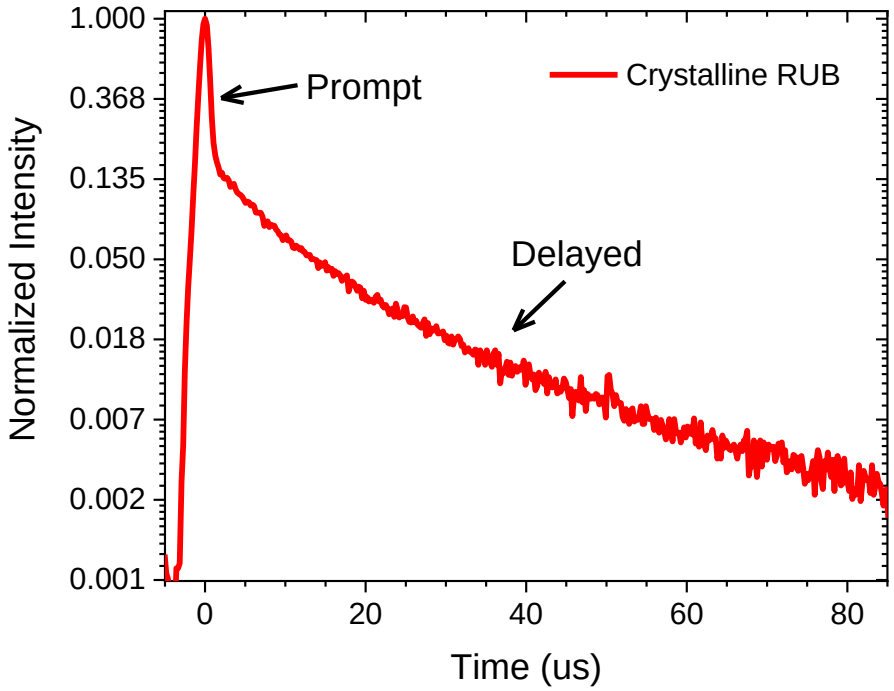

Figure 1.3.1. Photoluminescence trace illustrating the prompt singlet decay caused by singlet fission into pairs of triplets. At later times, triplet fusion regenerates the singlet state leading to delayed photoluminescence over a timescale longer than the singlet lifetime.

UC in solid-state systems is more challenging due to decreased diffusion and typically has a lower overall efficiency. Nevertheless, progress has been made on visible-to-UV solid-state systems.[76-78] Furthermore, two recent results suggest that RUB could form the basis of a solid-state material that upconverts NIR photons. First, the Baldo and Bulovic groups demonstrated that a layer of inorganic nanocrystals could sensitize triplets in a RUB film, enabling upconversion.[79] Even more surprising, an earlier paper by Liu et al.

reported visible PL excited by a continuous wave (CW) 980 nm laser in crystalline powders of RUB in the absence of any sensitization.[80] The authors of that work attributed the "upconversion" to nonresonant two-photon absorption (2PA). Although they did not attempt to extract a 2PA cross section, their data suggested it could be very high. Interestingly, there is significant disagreement over the magnitude of the two-photon cross section in crystalline RUB. Gurzadyan and coworkers performed an open aperture Z-scan to determine the cross section at 740 nm in crystalline RUB arriving at a value of 1000 GM (1 GM = 10^{-50} cm^4/s).[81] Biaggio and coworkers measured the nonlinear transmissivity of RUB between 750 and 920 nm and find a much lower two-photon cross section of 170 GM peaked at 850 nm,[82] that is in close agreement to the theoretical study by Zhao et al. which calculated a two-photon cross section of 185 GM.[83] Gurzadyan and coworkers use an 80 MHz laser to perform their Z-scan, while Biaggio and coworkers use a 1 kHz repetition rate. This difference in repetition rates was cited as a possible reason for the different magnitudes of the two-photon cross section. Given the important role of RUB in solid-state NIR upconversion schemes, the origin of the upconversion in pristine crystals is explored in chapter 5.

1.4 Singlet fission in crystalline tetracene

Multiple exciton generation is a photon downconversion strategy whereby a high energy photon is converted into lower energy excitons.[84] As first envisioned by Dexter, these low energy excitons can be fed into the bandgap of a semiconductor like silicon thereby increasing the photocurrent of the device.[85] Organic multiexciton generation is known as singlet fission. Singlet fission is a rapid, spin-allowed process in which a high energy singlet exciton is converted into two triplet excitons.[86] The advantage of using organics for photon downconversion lies in the low spin-orbit coupling meaning that the only pathway between singlet and triplets is through fission or fusion which leads to triplet states that are long-lived.

The process of singlet fission was first discovered by Singh et al while they studied the photoluminescence of crystalline anthracene resulting from excitation with a ruby laser.[51] They noticed that two processes of generating triplets were operative in anthracene depending on the excitation wavelength, and they were able to determine that upon exciting the higher lying singlet a pair of triplets was generated. One of the key parameters that must be met in order for singlet fission to occur is that the energy of the excited singlet should be greater than or equal to twice the energy of the triplet, $E(S_1) \geq 2E(T_1)$.[87] In anthracene the lowest singlet state is not greater than twice the triplet energy which is why fission was only observed when the higher lying singlet state was excited.[51]

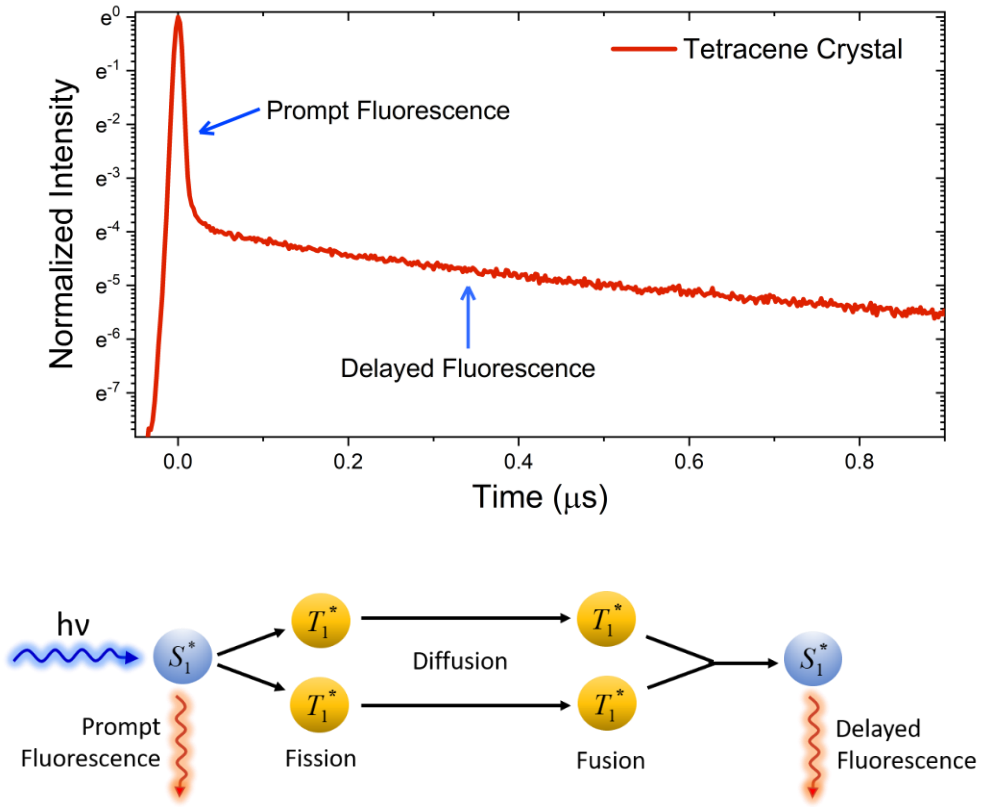

Figure 1.4.1. (Top) Fluorescence time trace of crystalline tetracene excited with a 400 nm femtosecond pulse. The prompt component represents the decay of the excited singlet due to singlet fission. At later times, the triplets generated via fission can recombine (fusion) to form the singlet and emit (delayed fluorescence). (Bottom) A cartoon illustrating fission and fusion and the contributions to the fluorescence time trace.

Other polyacenes such as tetracene[87-90] and pentacene[91,92] meet this energetic criterion making them the popular systems for gleaning information regarding the mechanism of singlet fission and for applications involving singlet fission. In pentacene, fission occurs on a femtosecond timescale since the process is highly exoergic; however, the lack of fluorescence limits the optical methods available to follow the photophysics. Tetracene is the prototypical fission material for photoluminescence studies of singlet fission because $E(S_1) \approx 2\ E(T_1)$ meaning that triplet fusion can also be efficient and the triplet dynamics

can be followed conveniently by monitoring the photoluminescence (Figure 1.4.1). The inherently low laser fluences used during time resolved fluorescence experiments is a distinct advantage for using emission to monitor the dynamics of singlet fission as other high energy bimolecular contributions to the kinetics can be avoided.

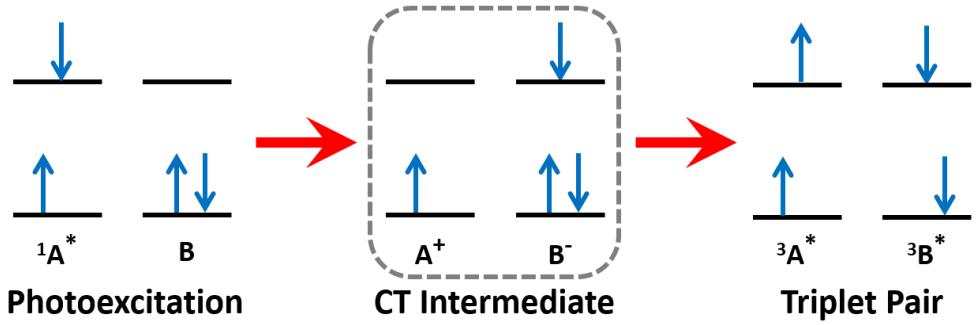

Figure 1.4.2. State diagram showing the steps involved to generate a triplet pair from an excited singlet state in a four-electron system. The steps are described in more detail in the text.

In a two-electron system generating a triplet from a singlet state only occurs through intersystem crossing which requires a spin flip and in organic molecules which typically have low spin-orbit coupling this spin-forbidden process is slow (nanoseconds and longer). Singlet fission requires at least two molecules with four electrons, say molecules A and B (Figure 1.4.2).[93] Photoexcitation generates an excited singlet state only on A while B remains in the ground state. Electron transfer from A to B yields a charge transfer intermediate state. Finally, back electron transfer from B to A produces the correlated triplet pair, which is a state that can maintain spin entanglement before decoherence leads to independent triplets. This correlated triplet pair has overall singlet spin character which explains why singlet fission can occur so rapidly (femtoseconds to

picoseconds). The properties of the triplet pair state have been of recent interest,[94-97] but they are hard to pin down due to its transient existence and low oscillator strength which precludes it from being readily observed using optical measurements. However, as mentioned above, the delayed fluorescence in tetracene provides an indirect observable to follow the triplet dynamics of fission. In tetracene, evidence of the correlated triplet pair state is provided through temporal oscillations in the fluorescence decay which are known as quantum beats (Figure 1.4.3).[90] In chapter 6, the mechanism of singlet fission as it pertains to the charge transfer intermediate and the correlated triplet pair will be examined in single crystals and blended films of tetracene.

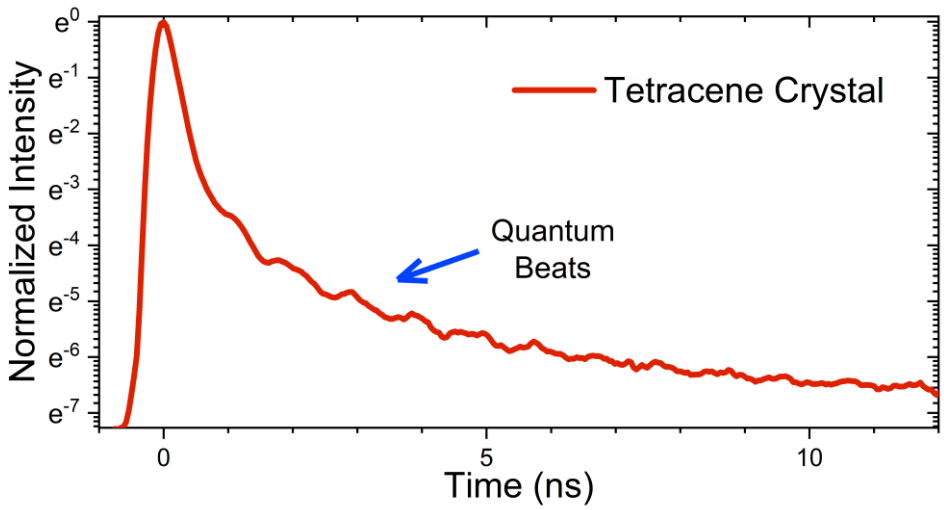

Figure 1.4.3. Fluorescence time trace of crystalline tetracene showing temporal oscillations that begin after the initial prompt decay caused by singlet fission.

1.5 Mechanochemistry

Complimentary to many of the familiar techniques for initiating chemistry such as photoexcitation, temperature changes and electrical stimulation, mechanical force can also be used to break or form covalent bonds – a field known as mechanochemistry.[98] Mechanical force is a unique experimental variable as it enables interatomic and intermolecular distances to be readily changed. For instance, easily obtained pressures can decrease the atomic spacing of a solid sample by 10%; whereas, temperature changes typically afford alterations in atomic spacing on the order of 1% provided there are no phase changes.[99] Such decreases in molecular or atomic spacing leads to overlap between neighboring electronic orbitals which tunes the electronic and vibrational transitions in the sample. In fact, at high enough pressures semiconductors can become conductors. There are many types of mechanical strain a sample can be subject to (Figure1.5.1), but hydrostatic pressure, or compression, is the focus of this research.

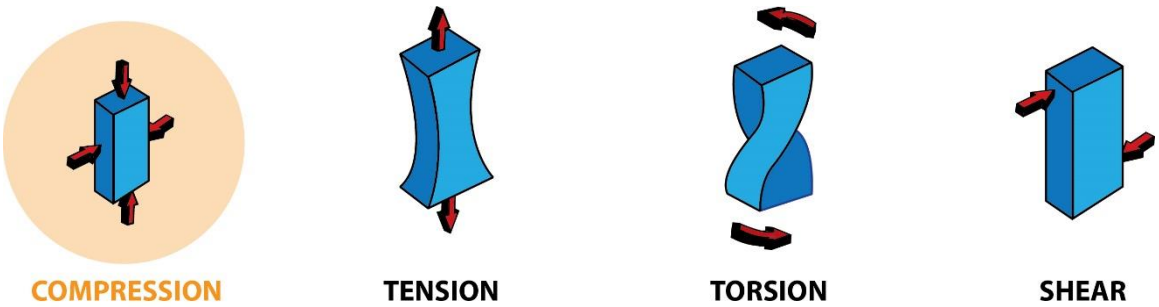

Figure 1.5.1. Cartoon illustrating mechanical strain types. In the diamond anvil cell compression is the goal.

Mechanochemistry has its roots in ancient times, where the first written record is of Aristotle's student, Theophrastus of Ephesus (371 – 286 BCE), using a mortar and pestle to transform cinnabar into metallic mercury.[100] The field of mechanochemistry is often attributed to Matthew Carey Lea, who published methodical studies of mechanical force on silver halides.[101] He is considered the first to demonstrate that heat and mechanical force could produce different responses on the same materials.[102] Emile Amagat was also actively involved in high pressure work at the end of the 19th century being able to routinely achieve pressures of 3 kbar and accurately measure that pressure.[99,103] While often overlooked, other scientists of the time were also utilizing higher pressures (typically under 1 kbar) to study the compressibility of liquids.[104] Notably, Jules Jamin measured the index of refraction of water under pressure in 1857 and is likely the first to study optical properties under pressure.[104-106]

Early work in mechanochemistry was restricted to pressures of only a few kbars or less until the development of the opposed anvil cell by Percy Williams Bridgman in the early 20th century.[104] Using an opposed anvil cell enabled pressures of 10 kbars to be achieved, but the pressure limitations were primarily the result of the material out of which the apparatus was made. High pressure chemistry was revolutionized in 1959 when scientists at the National Bureau of Standards (now NIST) invented the first diamond anvil cell (Figure 1.5.2).[107] Still accurately determining the pressure inside of the cell was problematic and prevented the diamond anvil cell from gaining wide-scale usage in research laboratories. This obstacle was finally surmounted in 1971 when National

Bureau of Standards scientists developed a reliable and convenient method to determine the pressure – ruby fluorescence (See 2.3.1).[108] Since then high pressure research has flourished and now with diamond anvil cells, pressures as high as 4 Mbar are attainable with standard flat diamond culets, nearly 7 Mbar can be achieved with specially synthesized diamond culets[109,110] and 10 Mbar is obtainable with double stage diamond anvil cells.[111]

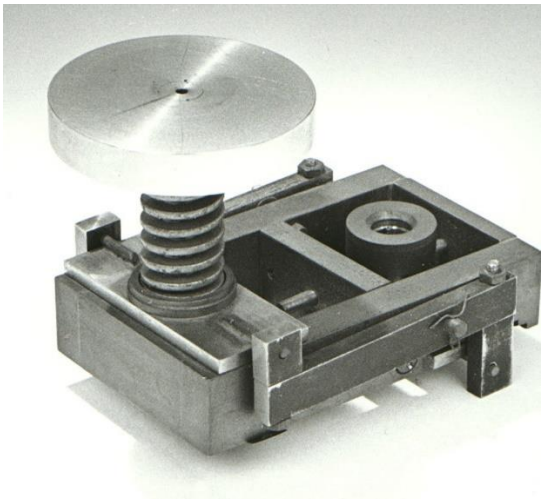

Figure 1.5.2. The first diamond anvil cell developed by the National Bureau of Standards.[107]

Finding molecules which are sensitive to mechanical forces is the first step toward the realization of smart materials such as self-healing polymers. Chemical groups designed to be activated by mechanical force include four-membered rings generated by both chemical and photochemical means,[112,113] as well as six-membered rings that are susceptible to Diels−Alder[114] and retro-Diels−Alder reactions.[115-117] To break chemical bonds, it is generally accepted that some sort of anisotropic shear force must be generated at the molecular level.[118] Examples of such shear forces include pulling on a

molecule using a scanning probe microscope tip,[119-121] stretching polymer films,[122] mechanical grinding,[98,123-126] and using cavitating bubbles in a sonicated sample.[98,127] Recently the ability of isotropic hydrostatic pressure, as opposed to shear, was investigated as a source to generate chemical changes in highly strained photoisomers with different three-dimensional structures.[128] By tethering two anthracene chromophores together using ethyl linkers, a cyclophane molecule, bi(anthracene-9,10-dimethylene) (BA), was made that could undergo intramolecular photodimerization to form a high energy isomer denoted PI, as shown in Figure 1.2.3A. The dissociation of PI in a polymer matrix was greatly accelerated by the application of relatively low pressures on the order of 1.0 GPa. Pressure-dependent rate measurements indicated that this reaction has a negative activation volume, and this was recently confirmed by ab initio calculations.[129] This pressure sensitivity was not observed in the untethered analogue An_2 (Figure 1.2.3B). The dramatic acceleration of the PI photodimer dissociation demonstrated that isotropic pressure, as opposed to anisotropic shear, could be used to break chemical bonds.

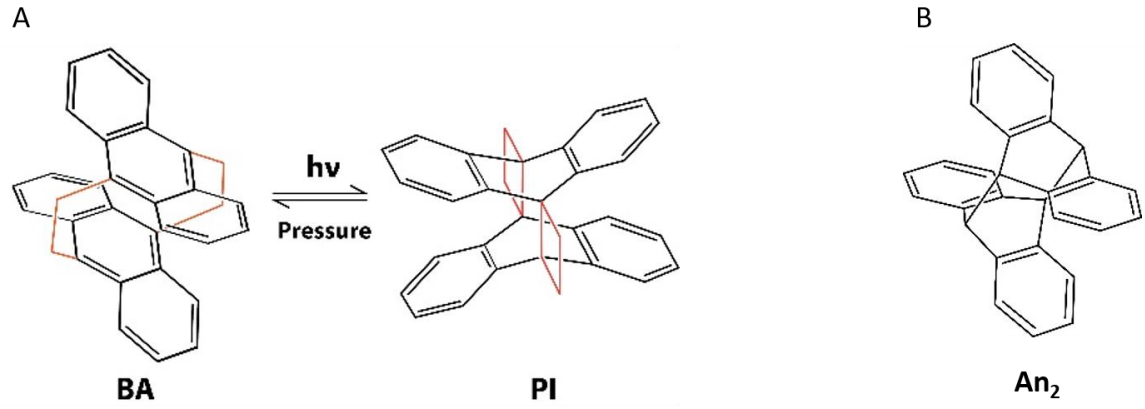

Figure 1.5.3. (A) The tethered anthracene bi(anthracene-9,10-dimethylene) (BA) converts to a photoisomer (PI) under UV irradiation. Pressure dissociates PI to reform BA. (B) The dianthracene (An_2) photoproduct formed under UV irradiation from anthracene monomers.

1.6 Research Projects Preview

In the subsequent chapters, projects involving both mechanophore behavior under high pressure and exciton dynamics in organic chromophores will be explored. In chapter 2, brief descriptions of the synthesis and preparation of samples is provided. The spectroscopic setups and ancillary equipment operation are also discussed. In chapter 3, the application of high pressure in a diamond anvil cell is used to monitor the back reaction of an anthracene photoisomer in search of pressure sensitive molecular motifs. Core-shell noble metal nanoparticles which can potential serve as an optically detected pressure sensor are also explored within the diamond anvil cell. In chapter 4, interchromophore electronic coupling is examined in covalently tethered terthiophene and anthracene dimers using sulfur atoms as the linker. Ultrafast spectroscopy and

theoretical calculations show how the oxidation state of the sulfur bridge imparts control over interchromophore electronic coupling and thus the photophysics of the terthiophene compounds and photochemistry of the anthracene compounds. In chapter 5, interband assisted NIR-to-visible upconversion in crystalline rubrene is investigated. A model is developed that captures the dependence of the upconverted photoluminescence on pulse spacing as well as quartic to quadratic to saturated intensity dependence. In chapter 6, singlet fission in solution grown single crystals of tetracene is probed with special attention given to the correlated triplet pair state that is evidenced in the temporal oscillations of photoluminescence time traces. Photoluminescence is recorded as a function of temperature from 20 – 500 K and the oscillation damping is found to be relatively independent of temperatures above 200 K. Finally, in chapter 7, the dissertation is summarized, put into context of the current state of the field and remaining questions are considered.

1.7 References

(1) Lucas, A. *Wind, Water, Work*; Brill, 2005.

(2) Perlin, J. Let it shine : the 6,000-year story of solar energy. **2013**.

(3) Rosen, W. *The Most Powerful Idea in the World: A Story of Steam, Industry and Invention*; Random House: New York, 2012.

(4) bp, 2019.

(5) Tsao, J. L., N.; Crabtree, G., 2006; Vol. 2019.

(6) Becquerel, A. E. Recherches sur les effets de la radiation chimique de la lumiere solaire au moyen des courants electriques. *Comptes Rendus de l' Academie des Sciences* **1839,** *9*, 145.

(7) Williams, R. Becquerel Photovoltaic Effect in Binary Compounds. *The Journal of Chemical Physics* **1960,** *32* (5), 1505.

(8) Engineering. The Photophone. *Scientific American Supplement* **1881,** *11* (270), 4302.

(9) von Siemens, W. On the electromotive action of illuminated selenium discovered by Mr. Fritts of New York. *Van Nostrand's Engineering Magazine* **1885,** *32*, 392n.

(10) Shockley, W.; Queisser, H. J. Detailed Balance Limit of Efficiency of p-n Junction Solar Cells. *Journal of Applied Physics* **1961,** *32* (3), 510.

(11) Haase, F.; Hollemann, C.; Schäfer, S.; Merkle, A.; Rienäcker, M.; Krügener, J.; Brendel, R.; Peibst, R. Laser contact openings for local poly-Si-metal contacts enabling 26.1%-efficient POLO-IBC solar cells. *Solar Energy Materials and Solar Cells* **2018,** *186*, 184.

(12) Ricks, A. B.; Brown, K. E.; Wenninger, M.; Karlen, S. D.; Berlin, Y. A.; Co, D. T.; Wasielewski, M. R. Exponential Distance Dependence of Photoinitiated Stepwise Electron Transfer in Donor–Bridge–Acceptor Molecules: Implications for Wirelike Behavior. *Journal of the American Chemical Society* **2012,** *134* (10), 4581.

(13) Mathew, S.; Yella, A.; Gao, P.; Humphry-Baker, R.; CurchodBasile, F. E.; Ashari-Astani, N.; Tavernelli, I.; Rothlisberger, U.; NazeeruddinMd, K.; Grätzel, M. Dye-sensitized solar cells with 13% efficiency achieved through the molecular engineering of porphyrin sensitizers. *Nat Chem* **2014,** *6* (3), 242.

(14) Collini, E.; Wong, C. Y.; Wilk, K. E.; Curmi, P. M. G.; Brumer, P.; Scholes, G. D. Coherently wired light-harvesting in photosynthetic marine algae at ambient temperature. *Nature* **2010,** *463* (7281), 644.

(15) Clayton, A. H. A.; Scholes, G. D.; Ghiggino, K. P.; Paddon-Row, M. N. Through-Bond and Through-Space Coupling in Photoinduced Electron and Energy Transfer: An ab Initio and Semiempirical Study. *The Journal of Physical Chemistry* **1996,** *100* (26), 10912.

(16) Curutchet, C.; Mennucci, B. Toward a Molecular Scale Interpretation of Excitation Energy Transfer in Solvated Bichromophoric Systems. *Journal of the American Chemical Society* **2005,** *127* (47), 16733.

(17) Zhong, Y.; Trinh, M. T.; Chen, R.; Wang, W.; Khlyabich, P. P.; Kumar, B.; Xu, Q.; Nam, C.-Y.; Sfeir, M. Y.; Black, C.et al. Efficient Organic Solar Cells with Helical Perylene Diimide Electron Acceptors. *Journal of the American Chemical Society* **2014,** *136* (43), 15215.

(18) Zhang, X.; Lu, Z.; Ye, L.; Zhan, C.; Hou, J.; Zhang, S.; Jiang, B.; Zhao, Y.; Huang, J.; Zhang, S.et al. A Potential Perylene Diimide Dimer-Based Acceptor Material for Highly Efficient Solution-Processed Non-Fullerene Organic Solar Cells with 4.03% Efficiency. *Advanced Materials* **2013,** *25* (40), 5791.

(19) McClure, D. S. Energy Transfer in Molecular Crystals and in Double Molecules. *Can. J. Chem.* **1958,** *36* (1), 59.

(20) Dantzig, N. A. v.; Levy, D. H.; Vigo, C.; Piotrowiak, P. Vibronic Coupling and Energy Transfer in Bichromophoric Molecules: The Effect of Symmetry. *The Journal of Chemical Physics* **1995,** *103* (12), 4894.

(21) Grabner, G.; Rechthaler, K.; Köhler, G. Two-State Model for the Photophysics of 9,9′-Bianthryl. Fluorescence, Transient-Absorption, and Semiempirical Studies†. *The Journal of Physical Chemistry A* **1998,** *102* (4), 689.

(22) Lu, L.; Lachicotte, R. J.; Penner, T. L.; Perlstein, J.; Whitten, D. G. Exciton and Charge-Transfer Interactions in Nonconjugated Merocyanine Dye Dimers: Novel Solvatochromic Behavior for Tethered Bichromophores and Excimers. *J Am Chem Soc* **1999,** *121* (36), 8146.

(23) Asami, N.; Takaya, T.; Yabumoto, S.; Shigeto, S.; Hamaguchi, H.-o.; Iwata, K. Two Different Charge Transfer States of Photoexcited 9,9′-Bianthryl in Polar and Nonpolar Solvents Characterized by Nanosecond Time-Resolved Near-IR Spectroscopy in the 4500−10 500 cm−1 Region. *The Journal of Physical Chemistry A* **2010,** *114* (22), 6351.

(24) Whited, M. T.; Patel, N. M.; Roberts, S. T.; Allen, K.; Djurovich, P. I.; Bradforth, S. E.; Thompson, M. E. Symmetry-breaking intramolecular charge transfer in the excited state of meso-linked BODIPY dyads. *Chemical Communications* **2012,** *48* (2), 284.

(25) Trinh, C.; Kirlikovali, K.; Das, S.; Ener, M. E.; Gray, H. B.; Djurovich, P.; Bradforth, S. E.; Thompson, M. E. Symmetry-Breaking Charge Transfer of Visible Light Absorbing Systems: Zinc Dipyrrins. *The Journal of Physical Chemistry C* **2014,** *118* (38), 21834.

(26) Cruz, C. D.; Christensen, P. R.; Chronister, E. L.; Casanova, D.; Wolf, M. O.; Bardeen, C. J. Sulfur-Bridged Terthiophene Dimers: How Sulfur Oxidation State Controls Interchromophore Electronic Coupling. *J Am Chem Soc* **2015,** *137* (39), 12552.

(27) Müller, A. M.; Avlasevich, Y. S.; Schoeller, W. W.; Müllen, K.; Bardeen, C. J. Exciton Fission and Fusion in Bis(tetracene) Molecules with Different Covalent Linker Structures. *J Am Chem Soc* **2007,** *129* (46), 14240.

(28) Johnson, J. C.; Nozik, A. J.; Michl, J. The Role of Chromophore Coupling in Singlet Fission. *Accounts Chem Res* **2013,** *46* (6), 1290.

(29) Aryanpour, K.; Shukla, A.; Mazumdar, S. Theory of Singlet Fission in Polyenes, Acene Crystals, and Covalently Linked Acene Dimers. *The Journal of Physical Chemistry C* **2015,** *119* (13), 6966.

(30) Sanders, S. N.; Kumarasamy, E.; Pun, A. B.; Trinh, M. T.; Choi, B.; Xia, J.; Taffet, E. J.; Low, J. Z.; Miller, J. R.; Roy, X.et al. Quantitative Intramolecular Singlet Fission in Bipentacenes. *J Am Chem Soc* **2015,** *137* (28), 8965.

(31) Feng, X.; Casanova, D.; Krylov, A. I. Intra- and Intermolecular Singlet Fission in Covalently Linked Dimers. *The Journal of Physical Chemistry C* **2016,** *120* (34), 19070.

(32) Korovina, N. V.; Das, S.; Nett, Z.; Feng, X.; Joy, J.; Haiges, R.; Krylov, A. I.; Bradforth, S. E.; Thompson, M. E. Singlet Fission in a Covalently Linked Cofacial Alkynyltetracene Dimer. *J Am Chem Soc* **2016,** *138* (2), 617.

(33) Margulies, E. A.; Miller, C. E.; Wu, Y.; Ma, L.; Schatz, G. C.; Young, R. M.; Wasielewski, M. R. Enabling singlet fission by controlling intramolecular charge transfer in π-stacked covalent terrylenediimide dimers. *Nature Chemistry* **2016,** *8*, 1120.

(34) Dean, J. C.; Zhang, R.; Hallani, R. K.; Pensack, R. D.; Sanders, S. N.; Oblinsky, D. G.; Parkin, S. R.; Campos, L. M.; Anthony, J. E.; Scholes, G. D. Photophysical characterization and time-resolved spectroscopy of a anthradithiophene dimer: exploring the role of conformation in singlet fission. *Physical Chemistry Chemical Physics* **2017,** *19* (34), 23162.

(35) Kumarasamy, E.; Sanders, S. N.; Tayebjee, M. J. Y.; Asadpoordarvish, A.; Hele, T. J. H.; Fuemmeler, E. G.; Pun, A. B.; Yablon, L. M.; Low, J. Z.; Paley, D. W.et al. Tuning Singlet Fission in π-Bridge-π Chromophores. *J Am Chem Soc* **2017,** *139* (36), 12488.

(36) Chen, M.; Bae, Y. J.; Mauck, C. M.; Mandal, A.; Young, R. M.; Wasielewski, M. R. Singlet Fission in Covalent Terrylenediimide Dimers: Probing the Nature of the Multiexciton State Using Femtosecond Mid-Infrared Spectroscopy. *J Am Chem Soc* **2018,** *140* (29), 9184.

(37) Korovina, N. V.; Joy, J.; Feng, X.; Feltenberger, C.; Krylov, A. I.; Bradforth, S. E.; Thompson, M. E. Linker-Dependent Singlet Fission in Tetracene Dimers. *J Am Chem Soc* **2018,** *140* (32), 10179.

(38) Kozlov, D. V.; Castellano, F. N. Anti-Stokes Delayed Fluorescence from Metal–Organic Bichromophores. *Chemical Communications* **2004,** (24), 2860.

(39) Guo, X.; Liu, Y.; Chen, Q.; Zhao, D.; Ma, Y. New Bichromophoric Triplet Photosensitizer Designs and Their Application in Triplet–Triplet Annihilation Upconversion. *Advanced Optical Materials* **2018,** *6* (4), 1700981.

(40) Kang, T. J.; Kahlow, M. A.; Giser, D.; Swallen, S.; Nagarajan, V.; Jarzeba, W.; Barbara, P. F. Dynamic Solvent Effects in the Electron-Transfer Kinetics of S_1 Bianthryls. *J. Phys. Chem.* **1988,** *92*, 6800.

(41) Bartynski, A. N.; Gruber, M.; Das, S.; Rangan, S.; Mollinger, S.; Trinh, C.; Bradforth, S. E.; Vandewal, K.; Salleo, A.; Bartynski, R. A.et al. Symmetry-Breaking Charge Transfer in a Zinc Chlorodipyrrin Acceptor for High Open Circuit Voltage Organic Photovoltaics. *J Am Chem Soc* **2015**.

(42) Wohlgenannt, M.; Tandon, K.; Mazumdar, S.; Ramasesha, S.; Vardeny, Z. V. Formation cross-sections of singlet and triplet excitons in [pi]-conjugated polymers. *Nature* **2001,** *409* (6819), 494.

(43) Segal, M.; Singh, M.; Rivoire, K.; Difley, S.; Van Voorhis, T.; Baldo, M. A. Extrafluorescent electroluminescence in organic light-emitting devices. *Nat Mater* **2007,** *6* (5), 374.

(44) Endo, A.; Sato, K.; Yoshimura, K.; Kai, T.; Kawada, A.; Miyazaki, H.; Adachi, C. Efficient up-conversion of triplet excitons into a singlet state and its application for organic light emitting diodes. *Applied Physics Letters* **2011,** *98* (8), 083302.

(45) Uoyama, H.; Goushi, K.; Shizu, K.; Nomura, H.; Adachi, C. Highly efficient organic light-emitting diodes from delayed fluorescence. *Nature* **2012,** *492* (7428), 234.

(46) Sato, K.; Shizu, K.; Yoshimura, K.; Kawada, A.; Miyazaki, H.; Adachi, C. Organic Luminescent Molecule with Energetically Equivalent Singlet and Triplet Excited States for Organic Light-Emitting Diodes. *Physical Review Letters* **2013,** *110* (24).

(47) Zhang, Q.; Li, J.; Shizu, K.; Huang, S.; Hirata, S.; Miyazaki, H.; Adachi, C. Design of Efficient Thermally Activated Delayed Fluorescence Materials for Pure Blue Organic Light Emitting Diodes. *J Am Chem Soc* **2012,** *134* (36), 14706.

(48) Zhang, Q.; Li, B.; Huang, S.; Nomura, H.; Tanaka, H.; Adachi, C. Efficient Blue Organic Light-Emitting Diodes Employing Thermally Activated Delayed Fluorescence. *Nature Photonics* **2014**.

(49) Xu, B.; Holdcroft, S. Molecular control of luminescence from poly(3-hexylthiophenes). *Macromolecules* **1993,** *26* (17), 4457.

(50) Kepler, R. G.; Caris, J. C.; Avakian, P.; Abramson, E. Triplet excitons and Delayed Fluorescence in Anthracene Crystals. *Physical Review Letters* **1963,** *10* (9), 400.

(51) Singh, S.; Jones, W. J.; Siebrand, W.; Stoicheff, B. P.; Schneider, W. G. Laser Generation of Excitons and Fluorescence in Anthracene Crystals. *The Journal of Chemical Physics* **1965,** *42* (1), 330.

(52) Shpaisman, H.; Niitsoo, O.; Lubomirsky, I.; Cahen, D. Can up- and down-conversion and multi-exciton generation improve photovoltaics? *Solar Energy Materials and Solar Cells* **2008,** *92* (12), 1541.

(53) Congreve, D. N.; Lee, J.; Thompson, N. J.; Hontz, E.; Yost, S. R.; Reusswig, P. D.; Bahlke, M. E.; Reineke, S.; Van Voorhis, T.; Baldo, M. A. External Quantum Efficiency Above 100% in a Singlet-Exciton-Fission–Based Organic Photovoltaic Cell. *Science* **2013,** *340* (6130), 334.

(54) Schulze, T. F.; Schmidt, T. W. Photochemical upconversion: present status and prospects for its application to solar energy conversion. *Energy & Environmental Science* **2015,** *8* (1), 103.

(55) Biaggio, I.; Irkhin, P. Extremely efficient exciton fission and fusion and its dominant contribution to the photoluminescence yield in rubrene single crystals. *Applied Physics Letters* **2013,** *103* (26), 263301.

(56) Jankus, V.; Snedden, E. W.; Bright, D. W.; Arac, E.; Dai, D.; Monkman, A. P. Competition between polaron pair formation and singlet fission observed in amorphous rubrene films. *Physical Review B* **2013,** *87* (22), 224202.

(57) Bera, K.; Douglas, C. J.; Frontiera, R. R. Femtosecond Raman Microscopy Reveals Structural Dynamics Leading to Triplet Separation in Rubrene Singlet Fission. *The Journal of Physical Chemistry Letters* **2017,** *8* (23), 5929.

(58) Sutton, C.; Tummala, N. R.; Beljonne, D.; Brédas, J.-L. Singlet Fission in Rubrene Derivatives: Impact of Molecular Packing. *Chem. Mater.* **2017,** *29* (7), 2777.

(59) Breen, I.; Tempelaar, R.; Bizimana, L. A.; Kloss, B.; Reichman, D. R.; Turner, D. B. Triplet Separation Drives Singlet Fission after Femtosecond Correlated Triplet Pair Production in Rubrene. *J Am Chem Soc* **2017,** *139* (34), 11745.

(60) Ishibashi, Y.; Inoue, Y.; Asahi, T. The excitation intensity dependence of singlet fission dynamics of a rubrene microcrystal studied by femtosecond transient microspectroscopy. *Photochemical & Photobiological Sciences* **2016,** *15* (10), 1304.

(61) Ma, L.; Zhang, K.; Kloc, C.; Sun, H.; Michel-Beyerle, M. E.; Gurzadyan, G. G. Singlet fission in rubrene single crystal: direct observation by femtosecond pump-probe spectroscopy. *Physical Chemistry Chemical Physics* **2012,** *14* (23), 8307.

(62) Piland, G. B.; Burdett, J. J.; Kurunthu, D.; Bardeen, C. J. Magnetic Field Effects on Singlet Fission and Fluorescence Decay Dynamics in Amorphous Rubrene. *J. Phys. Chem. C* **2013,** *117* (3), 1224.

(63) Miyata, K.; Kurashige, Y.; Watanabe, K.; Sugimoto, T.; Takahashi, S.; Tanaka, S.; Takeya, J.; Yanai, T.; Matsumoto, Y. Coherent singlet fission activated by symmetry breaking. *Nature Chemistry* **2017,** *9*, 983.

(64) Ryasnyanskiy, A.; Biaggio, I. Triplet exciton dynamics in rubrene single crystals. *Physical Review B* **2011,** *84* (19), 193203.

(65) Irkhin, P.; Najafov, H.; Podzorov, V. Steady-state photoconductivity and multi-particle interactions in high-mobility organic semiconductors. *Scientific Reports* **2015,** *5*, 15323.

(66) Singh-Rachford, T. N.; Castellano, F. N. Photon upconversion based on sensitized triplet–triplet annihilation. *Coord. Chem. Rev.* **2010,** *254* (21–22), 2560.

(67) Huang, Z.; Li, X.; Mahboub, M.; Hanson, K. M.; Nichols, V. M.; Le, H.; Tang, M. L.; Bardeen, C. J. Hybrid Molecule–Nanocrystal Photon Upconversion Across the Visible and Near-Infrared. *Nano Letters* **2015,** *15* (8), 5552.

(68) Nienhaus, L.; Wu, M.; Geva, N.; Shepherd, J. J.; Wilson, M. W. B.; Bulović, V.; Van Voorhis, T.; Baldo, M. A.; Bawendi, M. G. Speed Limit for Triplet-Exciton Transfer in Solid-State PbS Nanocrystal-Sensitized Photon Upconversion. *ACS Nano* **2017,** *11* (8), 7848.

(69) Mahboub, M.; Huang, Z.; Tang, M. L. Efficient Infrared-to-Visible Upconversion with Subsolar Irradiance. *Nano Letters* **2016,** *16* (11), 7169.

(70) Amemori, S.; Sasaki, Y.; Yanai, N.; Kimizuka, N. Near-Infrared-to-Visible Photon Upconversion Sensitized by a Metal Complex with Spin-Forbidden yet Strong S0–T1 Absorption. *J Am Chem Soc* **2016,** *138* (28), 8702.

(71) Duan, P.; Yanai, N.; Nagatomi, H.; Kimizuka, N. Photon Upconversion in Supramolecular Gel Matrixes: Spontaneous Accumulation of Light-Harvesting Donor–Acceptor Arrays in Nanofibers and Acquired Air Stability. *J Am Chem Soc* **2015,** *137* (5), 1887.

(72) Mahboub, M.; Maghsoudiganjeh, H.; Pham, A. M.; Huang, Z.; Tang, M. L. Triplet Energy Transfer from PbS(Se) Nanocrystals to Rubrene: the Relationship between the Upconversion Quantum Yield and Size. *Adv. Funct. Mater.* **2016,** *26* (33), 6091.

(73) Deng, F.; Sun, W.; Castellano, F. N. Texaphyrin sensitized near-IR-to-visible photon upconversion. *Photochemical & Photobiological Sciences* **2014,** *13* (5), 813.

(74) Deng, F.; Sommer, J. R.; Myahkostupov, M.; Schanze, K. S.; Castellano, F. N. Near-IR phosphorescent metalloporphyrin as a photochemical upconversion sensitizer. *Chemical Communications* **2013,** *49* (67), 7406.

(75) Cheng, Y. Y.; Khoury, T.; Clady, R. G. C. R.; Tayebjee, M. J. Y.; Ekins-Daukes, N. J.; Crossley, M. J.; Schmidt, T. W. On the efficiency limit of triplet-triplet annihilation for photochemical upconversion. *Physical Chemistry Chemical Physics* **2010,** *12* (1), 66.

(76) Wu, T. C.; Congreve, D. N.; Baldo, M. A. Solid state photon upconversion utilizing thermally activated delayed fluorescence molecules as triplet sensitizer. *Applied Physics Letters* **2015,** *107* (3), 031103.

(77) Sripathy, K.; MacQueen, R. W.; Peterson, J. R.; Cheng, Y. Y.; Dvorak, M.; McCamey, D. R.; Treat, N. D.; Stingelin, N.; Schmidt, T. W. Highly efficient photochemical upconversion in a quasi-solid organogel. *Journal of Materials Chemistry C* **2015,** *3* (3), 616.

(78) Singh-Rachford, T. N.; Lott, J.; Weder, C.; Castellano, F. N. Influence of Temperature on Low-Power Upconversion in Rubbery Polymer Blends. *J Am Chem Soc* **2009,** *131* (33), 12007.

(79) Wu, M.; Congreve, D. N.; Wilson, M. W. B.; Jean, J.; Geva, N.; Welborn, M.; Van Voorhis, T.; Bulović, V.; Bawendi, M. G.; Baldo, M. A. Solid-state infrared-to-visible upconversion sensitized by colloidal nanocrystals. *Nat Photon* **2016,** *10* (1), 31.

(80) Liu, H.; Yan, F.; Li, W.; Lee, C.-S.; Chu, B.; Chen, Y.; Li, X.; Han, L.; Su, Z.; Zhu, J.et al. Up-conversion luminescence of crystalline rubrene without any sensitizers. *Org. Electron.* **2010,** *11* (5), 946.

(81) Ma, L.; Galstyan, G.; Zhang, K.; Kloc, C.; Sun, H.; Soci, C.; Michel-Beyerle, M. E.; Gurzadyan, G. G. Two-photon-induced singlet fission in rubrene single crystal. *J. Chem. Phys.* **2013,** *138* (18), 184508/1.

(82) Irkhin, P.; Biaggio, I. Two-photon absorption spectroscopy of rubrene single crystals. *Physical Review B* **2014,** *89* (20), 201202.

(83) Zhao, L.; Yang, G.; Su, Z.; Qin, C.; Yang, S. Theoretical studies on one- and two-photon absorption properties of rubrene and its derivatives. *Synthetic Metals* **2006,** *156* (18–20), 1218.

(84) Schaller, R. D.; Klimov, V. I. High Efficiency Carrier Multiplication in PbSe Nanocrystals: Implications for Solar Energy Conversion. *Physical Review Letters* **2004,** *92* (18), 186601.

(85) Dexter, D. L. Two ideas on energy transfer phenomena: Ion-pair effects involving the OH stretching mode, and sensitization of photovoltaic cells. *Journal of Luminescence* **1979,** *18-19*, 779.

(86) Smith, M. B.; Michl, J. Singlet Fission. *Chemical Reviews* **2010,** *110* (11), 6891.

(87) Burdett, J. J.; Bardeen, C. J. The Dynamics of Singlet Fission in Crystalline Tetracene and Covalent Analogs. *Accounts of Chemical Research* **2013,** *46* (6), 1312.

(88) Swenberg, C. E.; Stacy, W. T. Bimolecular radiationless transitions in crystalline tetracene. *Chemical Physics Letters* **1968,** *2* (5), 327.

(89) Smith, A. W.; Weiss, C. Fluorescence decay time measurements in tetracene crystals. *Chemical Physics Letters* **1972,** *14* (4), 507.

(90) Burdett, J. J.; Bardeen, C. J. Quantum Beats in Crystalline Tetracene Delayed Fluorescence Due to Triplet Pair Coherences Produced by Direct Singlet Fission. *Journal of the American Chemical Society* **2012,** *134* (20), 8597.

(91) Chan, W.-L.; Ligges, M.; Jailaubekov, A.; Kaake, L.; Miaja-Avila, L.; Zhu, X.-Y. Observing the Multiexciton State in Singlet Fission and Ensuing Ultrafast Multielectron Transfer. *Science* **2011,** *334* (6062), 1541.

(92) Wilson, M. W. B.; Rao, A.; Clark, J.; Kumar, R. S. S.; Brida, D.; Cerullo, G.; Friend, R. H. Ultrafast Dynamics of Exciton Fission in Polycrystalline Pentacene. *J. Am. Chem. Soc.* **2011,** *133* (31), 11830.

(93) Bardeen, C. J. Excitonic Processes in Molecular Crystalline Materials. *MRS Bulletin* **2013,** *38* (01), 65.

(94) Yong, C. K.; Musser, A. J.; Bayliss, S. L.; Lukman, S.; Tamura, H.; Bubnova, O.; Hallani, R. K.; Meneau, A.; Resel, R.; Maruyama, M.et al. The entangled triplet pair state in acene and heteroacene materials. *Nature Communications* **2017,** *8*, 15953.

(95) Scholes, G. D. Correlated Pair States Formed by Singlet Fission and Exciton–Exciton Annihilation. *The Journal of Physical Chemistry A* **2015,** *119* (51), 12699.

(96) Stern, H. L.; Cheminal, A.; Yost, S. R.; Broch, K.; Bayliss, S. L.; Chen, K.; Tabachnyk, M.; Thorley, K.; Greenham, N.; Hodgkiss, J. M.et al. Vibronically coherent ultrafast triplet-pair formation and subsequent thermally activated dissociation control efficient endothermic singlet fission. *Nature Chemistry* **2017,** *9*, 1205.

(97) Lukman, S.; Richter, J. M.; Yang, L.; Hu, P.; Wu, J.; Greenham, N. C.; Musser, A. J. Efficient Singlet Fission and Triplet-Pair Emission in a Family of Zethrene Diradicaloids. *Journal of the American Chemical Society* **2017,** *139* (50), 18376.

(98) Beyer, M. K.; Clausen-Schaumann, H. Mechanochemistry: The Mechanical Activation of Covalent Bonds. *Chemical Reviews* **2005,** *105* (8), 2921.

(99) Stewart, J. W. *The World of High Pressure*; D. Van Nostrand Company, INC.: Princeton, New Jersey, 1967.

(100) Boldyrev, V. V.; Tkáčová, K. Mechanochemistry of Solids: Past, Present, and Prospects. *Journal of Materials Synthesis and Processing* **2000,** *8* (3), 121.

(101) Lea, M. C. Disruption of the silver haloid molecule by mechanical force. *American Journal of Science* **1892,** *43* (3), 527.

(102) Takacs, L. M. Carey Lea, the first mechanochemist. *Journal of Materials Science* **2004,** *39* (16), 4987.

(103) Anonymous. Minutes of the Forty-fifth Meeting. *Physical Review (Series I)* **1909,** *28* (2), 140.

(104) Bridgman, P. W. *The Physics of High Pressure*; G. Bell and Sons, LTD: London, 1958.

(105) Jamin, J. Memoire sur la mesure des indices de refraction des gaz. *Ann. Chim. Phys* **1857,** *49*, 282.

(106) Jamin, J. Memoire sur les variations de l'indice de refraction de l'eau a diverses pressions. *Ann. Chim. Phys* **1858,** *52*, 163.

(107) Weir, C. E. L., E. R.; Van Valkenburg, A; Bunting, E. N. Infrared studies in the 1- to 15-micron region to 30,000 atmospheres. *J. Res. Natl. Bur. Stand.* **1959,** *63A* (1), 55.

(108) Forman, R. A.; Piermarini, G. J.; Barnett, J. D.; Block, S. Pressure Measurement Made by the Utilization of Ruby Sharp-Line Luminescence. *Science* **1972,** *176* (4032), 284.

(109) Dubrovinsky, L.; Dubrovinskaia, N.; Prakapenka, V. B.; Abakumov, A. M. Implementation of micro-ball nanodiamond anvils for high-pressure studies above 6 Mbar. *Nature communications* **2012,** *3*, 1163.

(110) Dewaele, A.; Loubeyre, P.; Occelli, F.; Marie, O.; Mezouar, M. Toroidal diamond anvil cell for detailed measurements under extreme static pressures. *Nature Communications* **2018,** *9* (1), 2913.

(111) Dubrovinskaia, N.; Dubrovinsky, L.; Solopova, N. A.; Abakumov, A.; Turner, S.; Hanfland, M.; Bykova, E.; Bykov, M.; Prescher, C.; Prakapenka, V. B.et al. Terapascal static pressure generation with ultrahigh yield strength nanodiamond. *Science Advances* **2016,** *2* (7), e1600341.

(112) Kean, Z. S.; Niu, Z.; Hewage, G. B.; Rheingold, A. L.; Craig, S. L. Stress-Responsive Polymers Containing Cyclobutane Core Mechanophores: Reactivity and Mechanistic Insights. *J. Am. Chem. Soc.* **2013,** *135* (36), 13598.

(113) Kean, Z. S.; Black Ramirez, A. L.; Yan, Y.; Craig, S. L. Bicyclo[3.2.0]heptane Mechanophores for the Non-scissile and Photochemically Reversible Generation of Reactive Bis-enones. *J. Am. Chem. Soc.* **2012,** *134* (31), 12939.

(114) Bian, S.; Scott, A. M.; Cao, Y.; Liang, Y.; Osuna, S.; Houk, K. N.; Braunschweig, A. B. Covalently Patterned Graphene Surfaces by a Force-Accelerated Diels–Alder Reaction. *Journal of the American Chemical Society* **2013,** *135* (25), 9240.

(115) Wiggins, K. M.; Syrett, J. A.; Haddleton, D. M.; Bielawski, C. W. Mechanically Facilitated Retro [4 + 2] Cycloadditions. *Journal of the American Chemical Society* **2011,** *133* (18), 7180.

(116) Larsen, M. B.; Boydston, A. J. "Flex-Activated" Mechanophores: Using Polymer Mechanochemistry To Direct Bond Bending Activation. *Journal of the American Chemical Society* **2013,** *135* (22), 8189.

(117) Larsen, M. B.; Boydston, A. J. Successive Mechanochemical Activation and Small Molecule Release in an Elastomeric Material. *Journal of the American Chemical Society* **2014,** *136* (4), 1276.

(118) Gilman, J. J. Mechanochemistry. *Science* **1996,** *274* (5284), 65.

(119) Davis, D. A.; Hamilton, A.; Yang, J.; Cremar, L. D.; Van Gough, D.; Potisek, S. L.; Ong, M. T.; Braun, P. V.; Martinez, T. J.; White, S. R.et al. Force-induced activation of covalent bonds in mechanoresponsive polymeric materials. *Nature* **2009,** *459* (7243), 68.

(120) Lenhardt, J. M.; Ong, M. T.; Choe, R.; Evenhuis, C. R.; Martinez, T. J.; Craig, S. L. Trapping a Diradical Transition State by Mechanochemical Polymer Extension. *Science* **2010,** *329* (5995), 1057.

(121) Wu, D.; Lenhardt, J. M.; Black, A. L.; Akhremitchev, B. B.; Craig, S. L. Molecular Stress Relief through a Force-Induced Irreversible Extension in Polymer Contour Length. *Journal of the American Chemical Society* **2010,** *132* (45), 15936.

(122) Caruso, M. M.; Davis, D. A.; Shen, Q.; Odom, S. A.; Sottos, N. R.; White, S. R.; Moore, J. S. Mechanically-Induced Chemical Changes in Polymeric Materials. *Chemical Reviews* **2009,** *109* (11), 5755.

(123) Todres, Z. V. Recent advances in the study of mechanochromic transitions of organic compounds. *Journal of Chemical Research* **2004,** *2004* (2), 89.

(124) Sheth, A. R.; Lubach, J. W.; Munson, E. J.; Muller, F. X.; Grant, D. J. W. Mechanochromism of Piroxicam Accompanied by Intermolecular Proton Transfer Probed by Spectroscopic Methods and Solid-Phase Changes. *Journal of the American Chemical Society* **2005,** *127* (18), 6641.

(125) Ito, H.; Saito, T.; Oshima, N.; Kitamura, N.; Ishizaka, S.; Hinatsu, Y.; Wakeshima, M.; Kato, M.; Tsuge, K.; Sawamura, M. Reversible Mechanochromic Luminescence of [(C6F5Au)2(μ-1,4-Diisocyanobenzene)]. *Journal of the American Chemical Society* **2008,** *130* (31), 10044.

(126) Zhang, G.; Lu, J.; Sabat, M.; Fraser, C. L. Polymorphism and Reversible Mechanochromic Luminescence for Solid-State Difluoroboron Avobenzone. *Journal of the American Chemical Society* **2010,** *132* (7), 2160.

(127) Klukovich, H. M.; Kean, Z. S.; Iacono, S. T.; Craig, S. L. Mechanically induced scission and subsequent thermal remending of perfluorocyclobutane polymers. *J Am Chem Soc* **2011,** *133* (44), 17882.

(128) Jezowski, S. R.; Zhu, L. Y.; Wang, Y. B.; Rice, A. P.; Scott, G. W.; Bardeen, C. J.; Chronister, E. L. Pressure Catalyzed Bond Dissociation in an Anthracene Cyclophane Photodimer. *Journal of the American Chemical Society* **2012,** *134* (17), 7459.

(129) Slepetz, B.; Kertesz, M. Volume Change during Thermal [4 + 4] Cycloaddition of [2.2](9,10)Anthracenophane. *J. Am. Chem. Soc.* **2013,** *135* (37), 13720.

Chapter 2: Experimental

2.1 Sample Synthesis and Preparation

2.1.1: 9-tert-butylanthracene

9-tert-butlyanthracene (9tBA) was synthesized in the dark following a previously published scheme.[1] Briefly, the tert-butyl group can be added to anthrone with a Grignard reaction followed by dehydration with phosphorous pentoxide. The 9tBA was subsequently purified via recrystallization from methanol. Characterization of 9tBA was performed in cyclohexane solution at millimolar concentrations. Zeonex was chosen as the polymer host for the 9tBA thin films since it is transparent in the ultraviolet region (λ >237 nm) where the anthracene chromophore absorbs intensely. Zeonex pellets were dissolved in millimolar 9tBA cyclohexane solutions. The resulting mixture was sonicated in the dark for 1 h. After sonication, the solution was drop cast onto a glass slide and allowed to evaporate leaving behind a transparent film of 9tBA-doped Zeonex. Residual oxygen was removed from the thin films by storing them in a vacuum cryostat (10^{-4} torr) for at least 48 h.

2.1.2: Sulfur bridged terthiophene dimers and methyl terminated monomers

Synthesis was performed by a collaborator.[2] Briefly, terthiophene is synthesized using a Kumada coupling between 2-bromothiophene and 2,5-bromothiophene. A solution of terthiophene in tetrahydrofuran had n-butyllithium added to it under a nitrogen atmosphere. Dropwise addition of bis(phenylsulfonyl)sulfide produces **T3ST3** which is extracted with diethylether and purified with column chromatography. Adding 0.36 millimoles of meta-chloroperoxybenzoic acid to **T3ST3** yields the sulfoxide bridged dimer, T3SOT3. Using 1.11 millimoles of meta-chloroperoxybenzoic acid added to **T3ST3** produces the sulfone bridged dimer, **T3SO$_2$T3**. The methyl terminated monomers were synthesized in a similar fashion but by substituting dimethyl disulfide for bis(phenylsulfonyl)sulfide. For optical characterization, solutions in cyclohexane, acetonitrile, and dichloromethane were prepared in micromolar concentrations.

2.1.3: Sulfur-bridged anthracene dimers and phenyl terminated monomers

Sulfur bridged anthracene compounds were synthesized from commercially purchased bromoanthracene by a collaborator.[3] Briefly, a palladium cross-catalyzed coupling of bromoanthracene and potassium thioacetate yielded **AnSAn**. Two equivalents of meta-chloroperoxybenzoic acid were added to **AnSAn** to produce **AnSO$_2$An**. The phenyl terminated AnSph was synthesized by substituting potassium thioacetate with

diphenyl disulfide. Three equivalents of meta-chloroperoxybenzoic acid were added to **AnSPh** to produce **AnSO$_2$Ph**. For optical characterization, micromolar solutions of each compound in cyclohexane, acetonitrile and dichloromethane were prepared.

2.1.4: Rubrene

Two commercially available bottles of rubrene (Sigma-Aldrich, sublimed grade 99.99%; Acros Organics, 99%) were used for solution and microcrystalline powder measurements. Single crystals of rubrene were grown via physical vapor transport by a collaborator and the procedure is briefly summarized here. Into quartz growth tubes is placed a ~300 mg of rubrene powder on one end. The end of the tube containing the rubrene powder is placed into a furnace at 583 K and the remainder of the tube has cold water flowing through a copper tube surrounding it. Purified hydrogen gas flows over the rubrene powder toward the cooler end of the growth tube. After ~48 h, rubrene crystals with extended *ab* facets (on average 1 mm^2) appear on the cooler end of the growth tube.

2.1.5: Tetracene single crystals

Tetracene was purchased from Sigma-Aldrich (sublimed grade 99.99%) and used as received. To make single crystals, ~ 7 mg of tetracene were weighed out, dissolved in 50 mL of toluene and sonicated for ~20 min in the dark. Under only red ambient lighting,

the solution was filtered through a Whatman qualitative #1 filter into a separate precleaned flask which was covered in aluminum foil and sealed. Glass slides were cleaned by bathing in concentrated hydrochloric acid for at least 4 h. The glass slides were rinsed with deionized water and methanol and then allowed to dry. The filtered tetracene solution was then drop cast onto the cleaned glass or silanized glass slides and allowed to evaporate in a dark drawer for a minimum of 1 h. Using an optical microscope, crystals which resembled a stretched hexagon were selected for further measurements. For low temperature studies, the crystals were left uncovered and mounted on the heat exchanger of a vacuum cryostat (10^{-5} torr). Indium scrap metal was placed between the glass slide and cold finger to obtain good thermal contact. For high temperature measurements, the crystals required protection to prevent sublimation at T > 350 K. In a glove bag filled with nitrogen, a drop of fomblin oil (PFPE) was placed over the crystal and subsequently covered with a glass coverslip. To seal the sample, copper room temperature vulcanizing (RTV) sealant (Permatex 81878 Ultra Copper Maximum Temperature Silicone Sealant, rated to 644 K) was placed at the edges of the coverslip to adhere it to the glass slide. After a 24 h curing period, the samples were impervious to sublimation at elevated temperature.

2.2: Optical Characterization

2.2.1: Steady-state measurements

Electronic absorption spectroscopy was performed with a Varian Cary 500 UV-Vis / Near IR spectrophotometer. The wavelength interval was varied between 0.5 – 1.0 nm/step and integration time was varied between 0.1 – 1.0 s/step. For pressure-dependent absorption measurements, samples were placed into a diamond anvil cell (DAC). Type II diamonds with 1.0 mm diameter culets were used in the DAC. Inconel gaskets with a typical aperture diameter of ~ 500 µm were used between the diamonds (Figure 2.2.1a). To take the absorption spectra, a 38 mm focal length fused silica lens is used to focus the white light through the DAC aperture and another 38 mm fused silica lens is used to collect the light and couple it to the spectrophotometer. To monitor the pressure, ruby dust was placed in the aperture along with the sample. The shift of R1 emission line of ruby microcrystals with pressure enables the pressure to be calculated by using $p = \frac{v_1 - v_0}{-0.753 cm^{-1}/kbar}$, where p is pressure in kilobars, v_0 is the energy of the ruby R1 line in wavenumbers (cm^{-1}) at ambient pressure, v_1 is the energy of the ruby R1 line under pressure (Figure 2.2.1B).[4] The pressure is measured by exciting the ruby microcrystals with a 532 nm continuous wave laser and detecting the emission in a front face configuration.

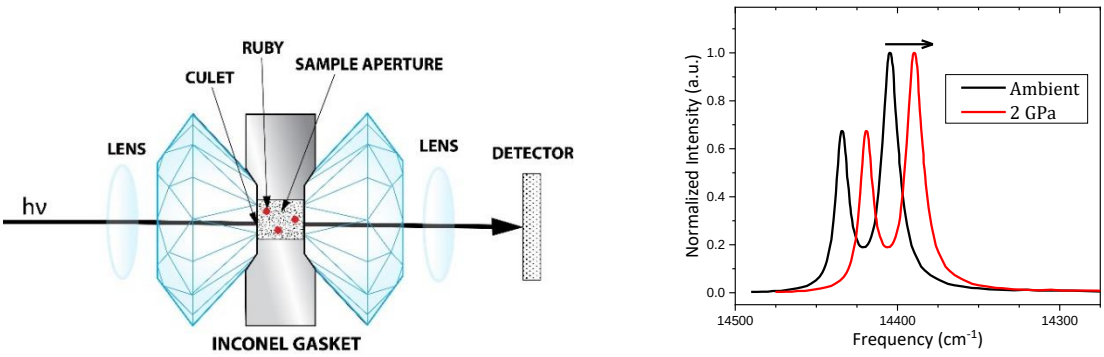

Figure 2.2.1. (A) Diagram of diamond anvil cell (DAC) setup showing two 38 mm lenses used to guide the light through the DAC and then to the detector. The flat face of the diamond is the culet and is 1.0 mm in diameter. The sample is placed into the aperture of the Inconel gasket along with ruby microcrystals. (B) The measured emission of the ruby microcrystal under 532 nm excitation showing both the R1 (14,400 cm^{-1}) and R2 (14,430 cm^{-1}) emission lines. Upon the application of pressure both lines shift to lower frequencies. The shift in the R1 frequency is used to calculate the hydrostatic pressure in the DAC.

Steady-state photoluminescence (PL) spectra were recorded in a right-angle configuration with a PTI QuantaMaster-400 fluorimeter which utilizes a xenon arc lamp as the excitation source and is capable of detecting emission from the UV to NIR wavelengths. Intensity dependent measurements on rubrene were performed by varying the incident laser power with a neutral density (ND) filter and recording the intensity of the PL with a photomultiplier tube (PMT) which was coupled to a lock-in amplifier. When a dichroic was available front-face detection was used; otherwise, an angled detection set up was employed. The front-face configuration was used for 800 nm and 808 nm excitation. For 800 nm excitation, the Coherent Vitesse which can be run in pulsed (80 MHz, 100 fs) or CW mode was used as the excitation source (Figure 2.2.2). The beam was incident upon the *ab* facet of the crystal and the polarization was aligned parallel to the *b* axis. The sample was kept in a vacuum cryostat fitted with optical windows. A 750 nm

short wave pass (SWP) filter was used to minimize the contribution of the laser scatter to the signal which was collected with a PMT.

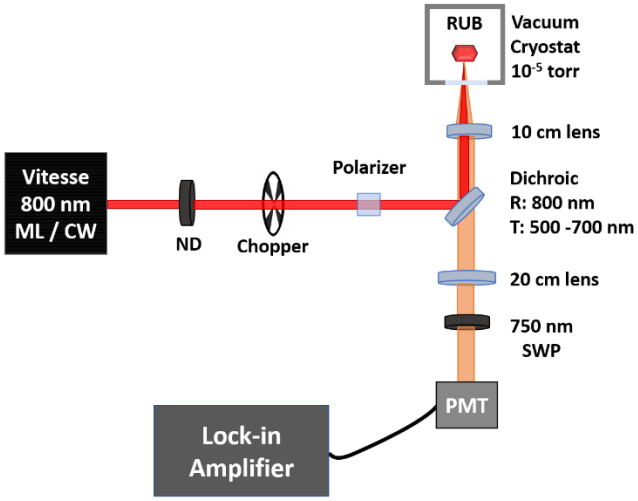

Figure 2.2.2. Diagram of the experimental set up used to measure the intensity dependence of the upconverted PL in crystalline rubrene using both a modelocked and continuous wave source at 800 nm.

The angled experimental setup used to record the power dependence of crystalline RUB utilized a 980 nm laser diode as the excitation source (Figure 2.2.3). A 950 nm long wave pass filter (LWP) was used to clean up the laser line and an ND filter was used to vary the laser power. The beam was horizontally polarized and incident on the *ab* facet of the RUB crystal. The crystal was rotated so that horizontally polarized beam was aligned parallel to the *b* axis. The PL was collected with a PMT through a 750 nm short wave pass (SWP) filter. This configuration was also used to collect the PL spectra of RUB by switching laser diodes (532 nm, 808 nm and 980 nm) into the setup and replacing the PMT with a fiber optic coupled to the Ocean Optics USB 4000 spectrophotometer. The chopper was removed for this measurement. The 950 nm LWP was used for the 980 nm

laser, the 810 nm IF was used for the 808 nm laser and no laser line filter was used for the 532 nm laser. The 750 nm LWP was used in the detection for 808 nm and 980 nm while an OG 550 nm LWP was used for the 532 nm excitation. Each laser was incident upon the *ab* facet and the polarization aligned parallel to the *b* axis. This configuration was also used to measure the polarization dependence by replacing the vacuum cryostat was with a rotatable mount.

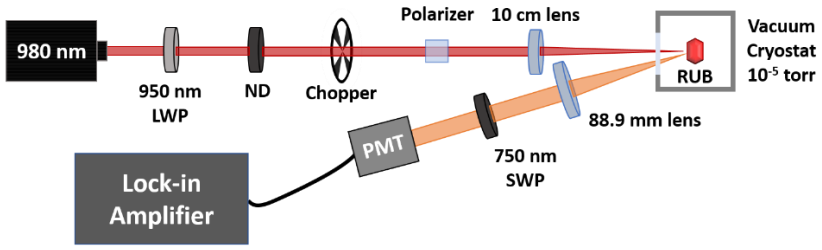

Figure 2.2.3. Diagram of the angled-detection setup used to record the upconverted PL in crystalline rubrene under vacuum. For intensity dependent measurements a PMT was used for detection. The PL spectra were recorded by replacing the PMT with a fiber optic which was coupled to an Ocean Optics 4000 USB spectrometer. To record the spectra under different excitation wavelengths, the 980 nm laser diode was replaced with a 532 nm or 800 nm laser diode.

To measure the lifetime of the intermediate state in rubrene, a Pockels cell was used as a pulse picker to vary the repetition rate of the laser (Figure 2.2.4). The Coherent Vitesse (80 MHz, 100 fs) was operated in pulsed mode for the variable repetition rate experiment. The pulse picker enables the repetition rate to be varied from 0.8 to 80 MHz. A glass slide is used as a beam splitter (BS) to direct ~1% of the beam onto a photodiode (PD) whose signal is displayed on an oscilloscope to monitor the repetition rate. The laser was incident upon the *ab* facet of the RUB crystal and the polarization aligned parallel to the *b* axis. The PL is detected with PMT through a 750 nm short wave pass filter (SWP).

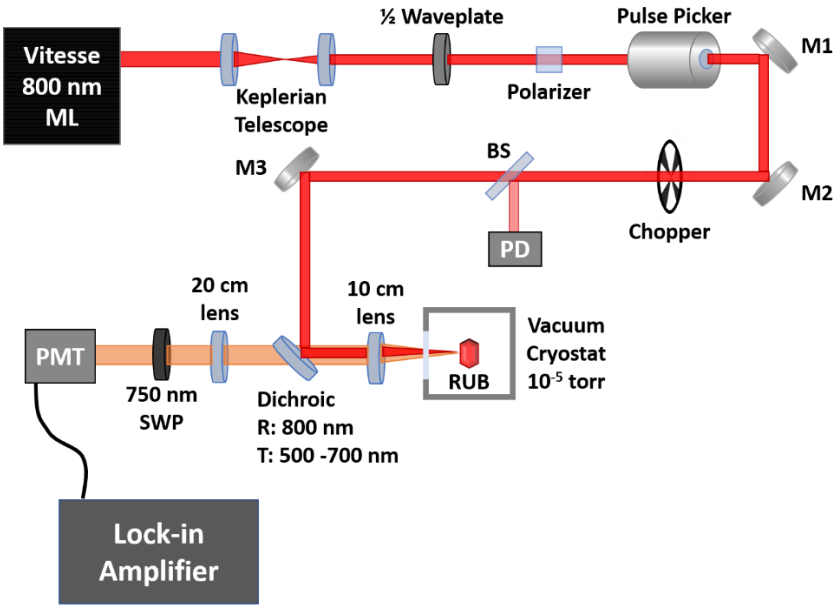

Figure 2.2.4. Simplified diagram showing how the output of the 80 MHz Vitesse laser was fed into a pulse picker in order to vary the repetition rate by an order of magnitude. Front face detection was used to measure the upconverted PL in crystalline rubrene as a function of pulse spacing.

2.2.2: Laser systems for time-resolved spectroscopy

The Coherent Vitesse laser is used as the seed laser for the Libra system described below; however, by placing a flip mirror in the cavity of the Libra, the Vitesse could be used independently of the Libra system. The Vitesse outputs 100-fs modelocked pulses at 800 nm with a repetition rate of 80 megahertz. It typically operates at powers between 800-900 milliwatts. The output of the Vitesse was coupled to a ConOptics pulse picker in order to control the repetition rate. The 800 nm fundamental beam was used for two-photon experiments. For one photon experiments, the fundamental was frequency doubled using a 3.5 mm beta-barium borate (BBO) crystal. The Pockels cell used in the

pulse picker introduces a significant temporal chirp to the fundamental beam making frequency doubling inefficient. To achieve efficient frequency doubling after the Pockels cell of the pulse picker, it was necessary to compress the beam using prism pairs before the doubling crystal. A 400 nm dichroic was used as a mirror after the doubling crystal to filter out any residual 800 nm.

The 1 kilohertz Coherent Libra is used for both time-resolved photoluminescence and transient absorption measurements. The Vitesse laser (described above) is used as the seed laser for the Libra assembly. While a second harmonic Q-switched laser, the Coherent Evolution, serves as the pump in the regenerative amplifier. The Libra utilizes chirped pulsed amplification to achieve high intensity femtosecond pulses. Briefly, the femtosecond 800 nm oscillator is temporally stretched with a grating known as the stretcher. A Ti:Sapphire crystal which is pumped by the 527 nm output of the Evolution is used as the amplifier. The seed pulse is confined to the regenerative amplifier cavity using the polarization of a Pockels cell allowing the pulse to make many passes through the Ti:Sapphire crystal which results in amplifications of $\sim 10^6$. The polarization of the Pockels cell then rotates allowing the amplified pulse to be dumped out of the cavity. At this point, the amplified pulse is temporally compressed with another grating before exiting the Libra optical cavity.

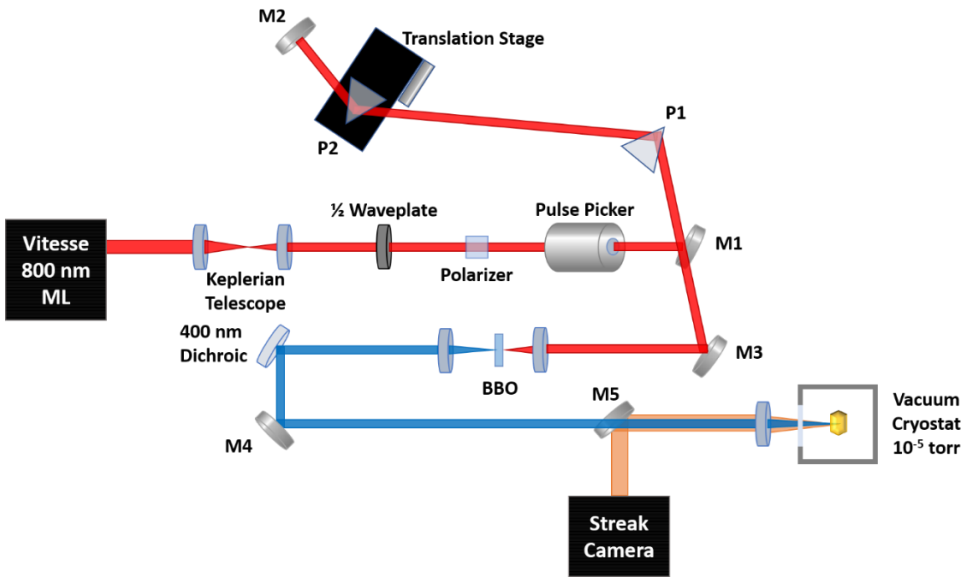

Figure 2.2.5. Simplified diagram showing how the prism pair was used to compress the 800 nm pulse after passing through the pulse picker to efficiently generate the frequency-doubled 400 nm beam used for excitation. The first mirror (M1) steers the beam into the bottom of the prism (P1). The beam passes through the second prism (P2) onto the second mirror (M2) which raises the height of the beam to pass back through both P2 and P1 at the top of the prisms in order to have the beam pass above M1 and be incident on the third mirror (M3). There is a distance of 80 cm between both prisms, and P2 is mounted on a translation stage to allow fine tuning of the beam compression. After compression, a 5 cm lens focuses the 800 nm pulse onto a beta-Barium borate (BBO) crystal to generate 400 nm which is recollimated with a 4 cm lens. A 400 nm dichroic is used as a mirror to filter out any residual 800 nm before the beam is focused onto the sample with a 15 cm fused silica lens. The sample is housed in a vacuum cryostat fitted with optical windows. Photoluminescence is collected with a 10 cm fused silica lens and detected with the Hamamatsu streak camera. The excitation and emission beams are shown colinearly for simplicity.

2.2.3: Ultrafast Transient Absorption Spectroscopy

The Coherent Libra laser system and Ultrafast Systems Helios transient absorption spectrometer are used for ultrafast pump-probe measurements. The majority (90%) of the 800 nm fundamental beam is frequency doubled with a BBO crystal to serve as the 400 nm pump beam. The remaining 10% of the fundamental is focused onto a 3 millimeter sapphire plate to generate the white light continuum probe beam. The pump and probe

beams are focused onto the same spot of a 1 millimeter path length quartz flow cell. Approximately 30 milliliters of the sample solution are flowed through the cell with a peristaltic pump. The scattered probe beam is collected with a 4 centimeter focal length lens and focused onto a fiber optic which is coupled to the spectrometer. The time delay between the arrival of the pump and probe beam is obtained by using a delay stage in the pump beam line which is controllable with the Helios software.

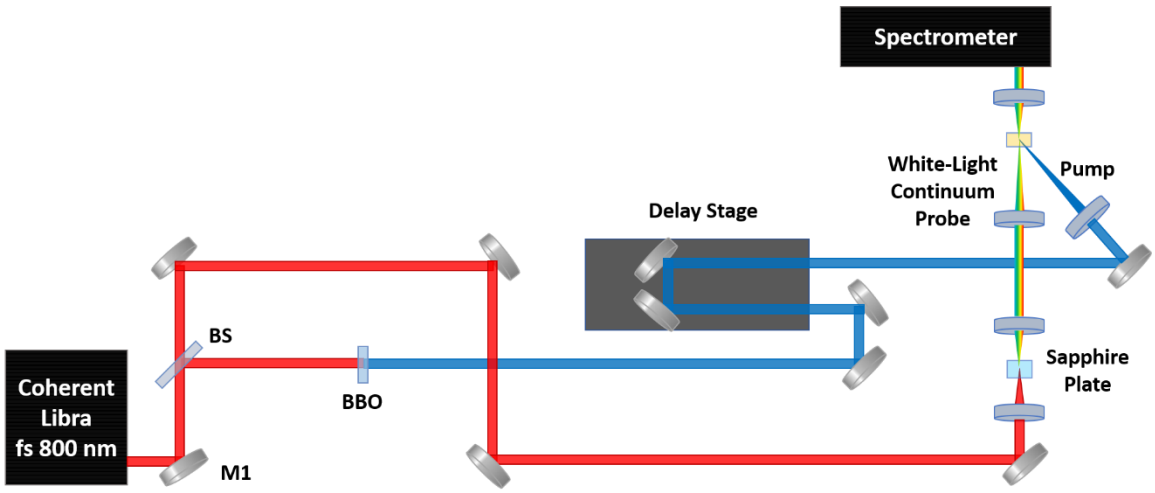

Figure 2.2.6. Simplified diagram showing the transient absorption setup using the femtosecond Coherent Libra laser system. The fundamental 800 nm beam is split (BS) into the pump and probe beams. The 400 nm pump beam is generated with unfocused incidence on a BBO crystal. The white-light continuum probe beam is generated by focusing a small portion of the fundamental onto a sapphire or calcium fluoride plate. The pump and probe beams overlap on a 1 millimeter pathlength, quartz flow cell and the scattered probe is collected with a 4 centimeter lens which is then detected with the Helios spectrometer. Time resolution is obtained by altering the distance traversed of the pump beam with a delay stage.

2.2.4: Time-resolved Photoluminescence Spectroscopy

Both the Coherent Libra and Vitesse can be used to obtain time-resolved photoluminescence spectra with a Hamamatsu C4334 Streakscope. The streak camera provides both spectral and dynamical data from the sample with 2.5 nm and 15 ps

spectral and temporal resolution, respectively. Briefly, sample emission enters the detector and a monochromator splits the emission into separate wavelengths. Photons then encounter a photocathode which converts the photons into electrons which are ejected into a cathode tube. A time varying electric field across the cathode tube provides the time resolution since electrons generated at different times experience different electric fields. A micro-channel plate after the cathode tube amplifies the electron signal after which a phosphor screen is impacted, whose emission is record with a charge coupled device (CCD).

2.3 Theoretical Calculations

Theoretical calculations were performed by a collaborator and are described briefly here.

2.3.1 Terthiophene calculations

Electronic structure calculations of terthiophene (**T3**), **T3SO$_n$Me** and **T3SO$_n$T3** molecules were performed using density functional theory (DFT)[5,6] with the long-range corrected version of B3LYP energy functional (CAM-B3LYP).[7] Electronic transitions were obtained with the time-dependent version of DFT (TDDFT)[8,9] and with the Tamm-Dancoff approximation.[10,11] The 6-31G(d) and 6-31+G(d) basis sets were employed for molecular

geometry optimizations and the computation of excitation energies to low-lying states, respectively. The B3LYP energy functional has shown good performance in the computation of electronic excitations of sulfur-organic compounds.[12] Although it is often advisable to use tight d-functions to account for core polarization effects when dealing with second row elements such as sulfur. One of the main limitations of TDDFT is its difficulty with CT-type of excitations. For this reason, the long-range corrected version of B3LYP energy functional, i.e. CAM-B3LYP, has been used which has shown to be capable of reliably computing CT transitions in organic molecules.[13-15]

The effect of the solvent was taken into consideration in all calculations with the polarizable continuum model (PCM).[16] Diabatic states have been constructed with the Edmiston-Ruedenberg localization scheme[17] as linear combinations from the four lowest excited singlet eigenstates. Coupling energies between locally excited (LE) and CT diabats correspond to off diagonal terms of the four by four diabatic Hamiltonian. All calculations were done using the Q-Chem program.[18] Natural bond orbital (NBO) analysis was performed at the CAM-B3LYP/6-31+G(d) level in dichloromethane with the NBO 5.0 package.[19]

2.3.2 Anthracene calculations

Electronic structure calculations for the ground and excited states were performed within the framework of density functional theory (DFT)[20,21] and its time-dependent version (TDDFT)[9,22] respectively. To account for weak interactions and

important electronic redistribution between the anthracene moieties and the SO_n bridges upon photoexcitation, the ωB97X-D functional[23] is used together with the 6-31+G(d) basis set. CH_2Cl_2 solvent effects are accounted for with the polarizable continuum model using the C-PCM variant.[24] Critical points on the ground state potential energy surface (PES) are optimized with no restrictions. Computation of the diabatic states is performed by means of the Edmiston–Ruedenberg localization scheme.[17] Energy crossing points are optimized within the spin-flip DFT (SF-DFT) approximation[25] with the BHHLYP functional.[26,27] All calculations are performed with the Q-Chem program.[18]

2.4 Other experimental methods

2.4.1 Performing measurements under vacuum

A Drivac BH2-60HD oil-free turbo pump is used to pull vacuum (10^{-5} torr) for solid state samples mounted in the Janis Research ST-300 or ST-500 cryostat which are fitted with optical windows. The pressure in the cryostat and vacuum line is monitored with a Televac 4A convection vacuum gauge controlled by a Televac MC300 vacuum controller.

2.4.2 Variable temperature experiments

A heat exchanger (cold finger) in the cryostat enables temperatures between 4 K and 500 K to be achieved at the sample. Indium scrap metal is used between the cold

finger and the sample to enable good thermal contact. To ensure thermal equilibrium was attained the samples were allowed to remain at a given temperature for at least 30 min before measurements were performed. For temperatures above 293 K, a Lake Shore Cryogenics 335 temperature controller is used to control a heater which heats the sample. For temperatures below 293 K, the Lake Shore Cryogenics temperature controller is used in conjunction with a cryogenic fluid. A Linde 25 L dewar is used to house N_2(l) for temperatures down to 77 K. A Janis Research transfer line (ST-LINE) connects the dewar to the heat exchanger of the cryostat. When N_2(l) is used the dewar must be pressurized by feeding in air from the hood. For temperatures below 77 K, He(l) is used and must be transferred directly from the tank to the cryostat with the transfer line (Figure 2.4.1). It is important to evacuate the insulating jacket around the transfer line before using He(l). Connect the vacuum pump to the evacuation valve on the transfer line and pump on the line for at least 48 h. To connect the transfer line to the He(l) tank, a ½" MNPT connector was used along with a #11 rubber o-ring. The flow of He(l) into the cryostat is driven by the overpressure in the He(l) tank which is generated from the boiling He(l) when the transfer line is inserted. To connect the tank and cryostat, first connect the transfer line to the cryostat, then ensure that the vent and pressure control valve on the tank are both closed. Remove the dust cover from the liquid valve and insert the transfer line. Open the liquid valve and slowly insert the transfer line until the bottom of the tank is reached and then lift the transfer line ¼". Secure the transfer line with ½" connector. During insertion, the pressure in the tank will rise. Eventually (5-10 min) the He(l) will begin to vent out of

the cryostat and the temperature will rapidly drop. Monitor the pressure throughout the experiment. The vent can temporarily be opened to lower the pressure if it exceeds ~6 psi. To achieve temperatures lower than 20 K, the heat shield must be placed around the cold finger. To stop the flow of He(l), open the vent valve until the tank pressure returns to atmospheric pressure. To measure the fill level of the He(l) tank, use the transfer line as a dipstick. With the vent open, insert the transfer line until the bottom of the tank is reached then pull it out. The transfer line will freeze once pulled out and this is an indication of the He(l) level. Measure the level and convert to volume using the chart which is welded to each tank. An important note when using He(l) and the Lake Shore Cryogenics 335 temperature controller is that the diode type must be changed from silicon to GaAlAs in order to measure temperatures below ~20 K.

Care must be taken when heating any sample back up from cryogenic temperatures for two reasons. First, when using the heater the cold finger at the sample can often be at a higher temperature than the temperature controller indicates until thermal equilibrium is achieved, which takes many hours after going to cryogenic temperatures. This can lead to accidental annealing of samples. Second, opening the cryostat before it has fully warmed to room temperature (~8 h) will lead to ice being deposited on the heat exchanger which makes achieving vacuum again very time consuming.

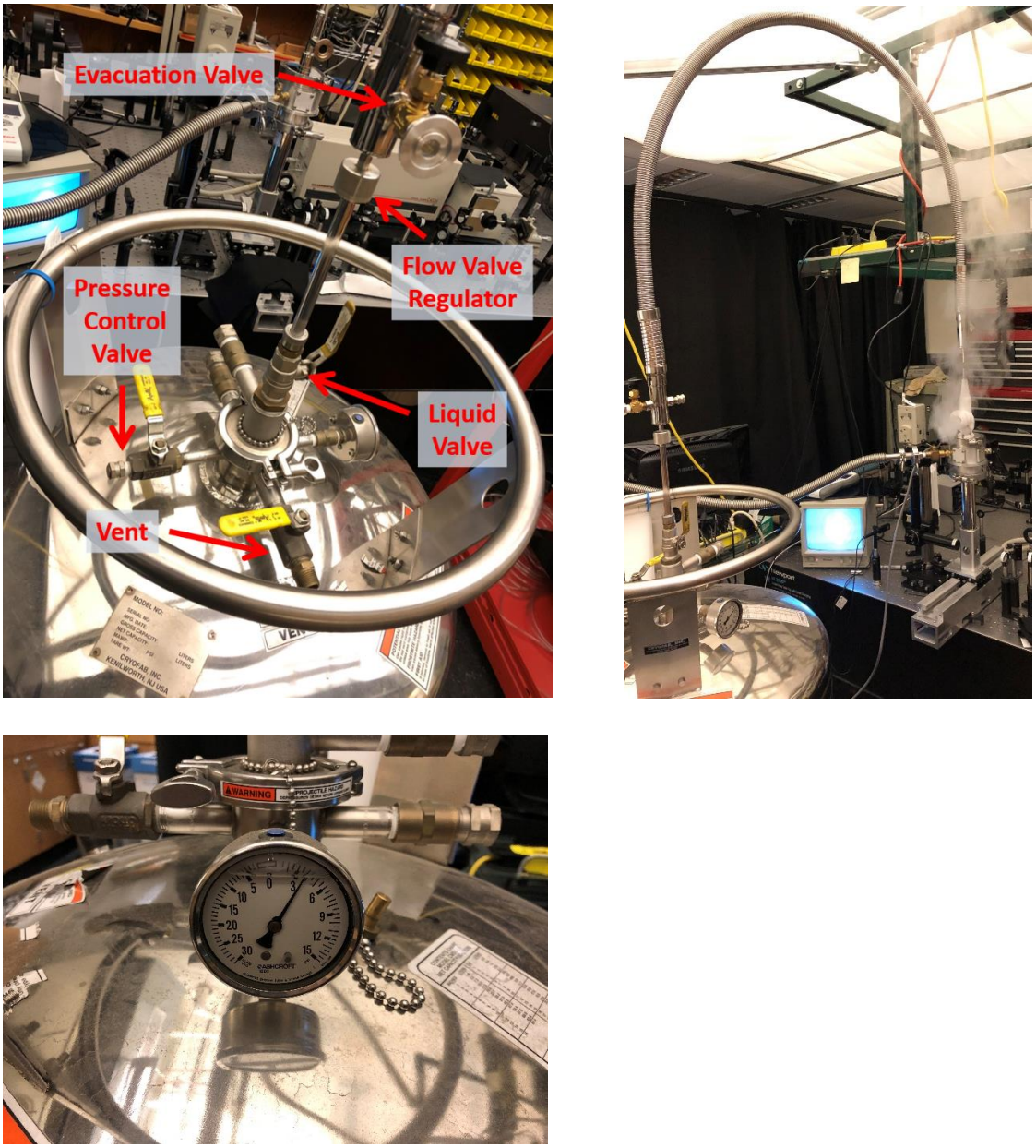

Figure 2.4.1. Images showing the connections between the Janis Research ST-300 cryostat and a liquid helium tank.

2.4.3 Measuring PL as a function of magnetic field strength

Measuring the PL of a sample in a magnetic field is imperative for determinations of singlet fission. Two cylindrical 2 inch tall and 2 inch diameter neodymium magnets were purchased from K&J Magnetics (DY0Y – N50). They were each placed in custom machined holders (Figure 2.4.2) to allow them to be mounted on a custom machined stage (Figures 2.4.3). The field generated between the magnets was measured with an AlphaLab DC Gaussmeter (GM-1-ST). The field ranged from 500 Gauss with the magnets fully apart to 3300 Gauss with the magnets as close as they can get to the cryostat.

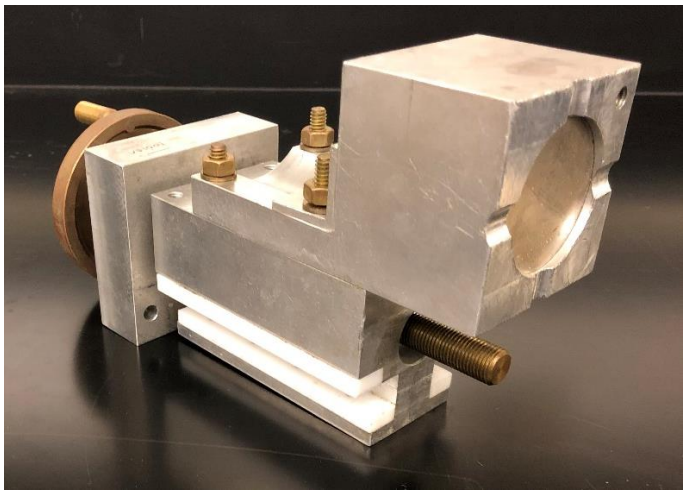

Figure 2.4.2. Magnet holder and mount for the stage. The brass wheel enabled the magnetic field to be tuned by varying the distance between the two magnets.

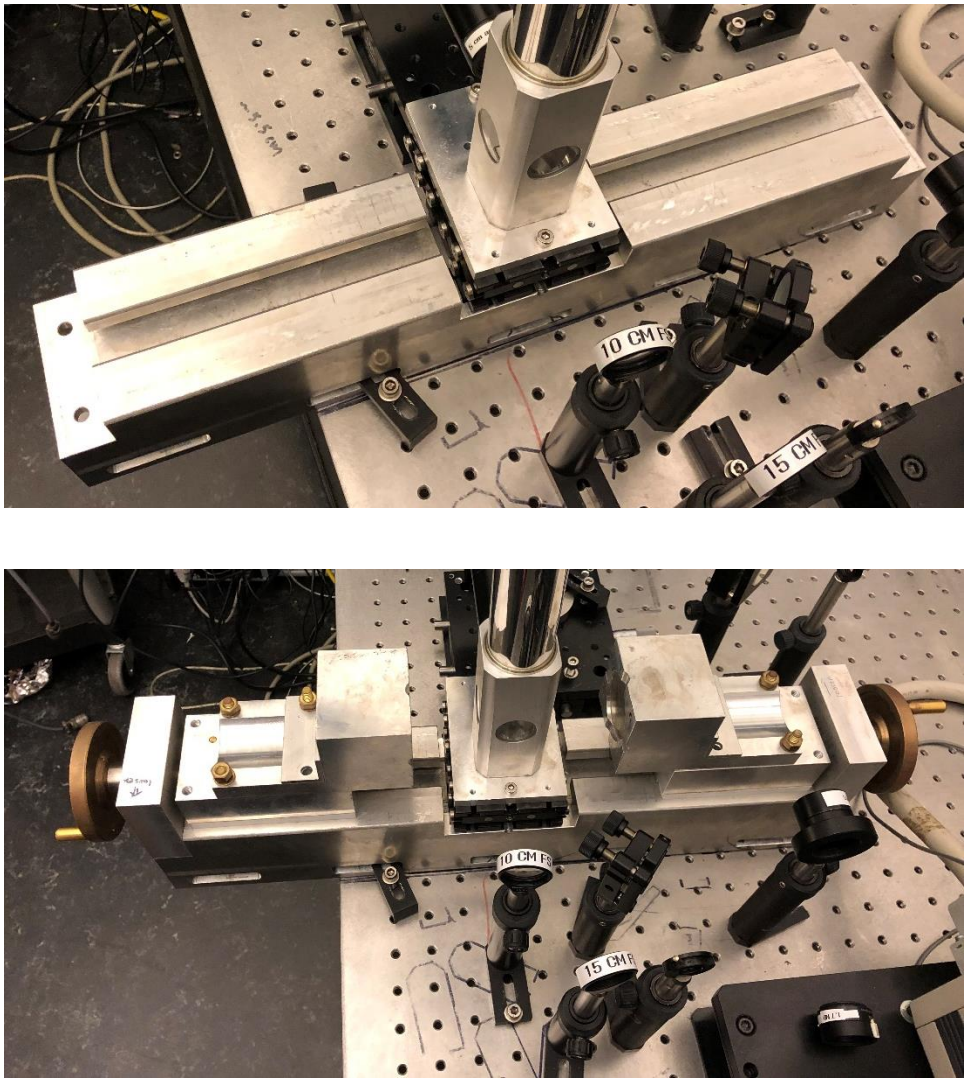

Figure 2.4.3. The mounting stage for the magnet holders was bolted to the laser table and the Janis Research ST-300 cryostat was placed on a 3D stage at the center (top). The two magnets mounted onto the stage at the maximum separation point (bottom).

2.5 References

(1) Parish, R. C.; Stock, L. M. 9-t-Butylanthracene1. *The Journal of Organic Chemistry* **1966,** *31* (12), 4265.

(2) Cruz, C. D.; Christensen, P. R.; Chronister, E. L.; Casanova, D.; Wolf, M. O.; Bardeen, C. J. Sulfur-Bridged Terthiophene Dimers: How Sulfur Oxidation State Controls Interchromophore Electronic Coupling. *Journal of the American Chemical Society* **2015,** *137* (39), 12552.

(3) Christensen, P. R.; Patrick, B. O.; Caron, E.; Wolf, M. O. Oxidation-State-Dependent Photochemistry of Sulfur-Bridged Anthracenes. *Angew Chem Int Ed Engl* **2013,** *52* (49), 12946.

(4) Jayaraman, A. Diamond Anvil Cell and High-Pressure Physical Investigations. *Rev Mod Phys* **1983,** *55* (1), 65.

(5) Parr, R. G.; Yang, W. *Density-Functional Theory of Atoms and Molecules*; Oxford University Press, USA, 1994.

(6) Ziegler, T. Approximate density functional theory as a practical tool in molecular energetics and dynamics. *Chem. Rev.* **1991,** *91* (5), 651.

(7) Yanai, T.; Tew, D. P.; Handy, N. C. A new hybrid exchange–correlation functional using the Coulomb-attenuating method (CAM-B3LYP). *Chem. Phys. Lett.* **2004,** *393* (1–3), 51.

(8) Mark E, C. In *Recent Advances in Density Functional Methods*; WORLD SCIENTIFIC, 1995; Vol. Volume 1.

(9) Runge, E.; Gross, E. K. U. Density-Functional Theory for Time-Dependent Systems. *Phys. Rev. Lett.* **1984,** *52* (12), 997.

(10) Fetter, A. L.; Walecka, J. D. *Quantum Theory of Many-particle Systems*; Dover Publications, 2003.

(11) Hirata, S.; Head-Gordon, M. Time-dependent density functional theory within the Tamm–Dancoff approximation. *Chem. Phys. Lett.* **1999,** *314* (3–4), 291.

(12) Fabian, J. Electronic excitation of sulfur-organic compounds – performance of time-dependent density functional theory. *Theor Chem Acc* **2001,** *106* (3), 199.

(13) Preat, J. Photoinduced Energy-Transfer and Electron-Transfer Processes in Dye-Sensitized Solar Cells: TDDFT Insights for Triphenylamine Dyes. *J. Phys. Chem. C* **2010,** *114* (39), 16716.

(14) Camino, B.; De La Pierre, M.; Ferrari, A. M. Photoelectrochemical properties of the CT1 dye: A DFT study. *J. Mol. Struct.* **2013,** *1046*, 116.

(15) Jungsuttiwong, S.; Tarsang, R.; Sudyoadsuk, T.; Promarak, V.; Khongpracha, P.; Namuangruk, S. Theoretical study on novel double donor-based dyes used in high efficient dye-sensitized solar cells: The application of TDDFT study to the electron injection process. *Org. Electron.* **2013,** *14* (3), 711.

(16) Truong, T. N.; Stefanovich, E. V. A new method for incorporating solvent effect into the classical, ab initio molecular orbital and density functional theory frameworks for arbitrary shape cavity. *Chem. Phys. Lett.* **1995,** *240* (4), 253.

(17) Subotnik, J. E.; Cave, R. J.; Steele, R. P.; Shenvi, N. The initial and final states of electron and energy transfer processes: Diabatization as motivated by system-solvent interactions. *J. Chem. Phys.* **2009,** *130* (23), 234102.

(18) Shao, Y.; Gan, Z.; Epifanovsky, E.; Gilbert, A. T. B.; Wormit, M.; Kussmann, J.; Lange, A. W.; Behn, A.; Deng, J.; Feng, X.et al. Advances in molecular quantum chemistry contained in the Q-Chem 4 program package. *Molecular Physics* **2014,** *113* (2), 184.

(19) Glendening, E. D. B., J.K.; Reed, A.E.; Carpenter, J.E.;Bohmann, J.A.;Morales, C.M.;Weinhold, F.; Theoretical Chemistry Institute: University of Wisconsin, Madison, WI, 2001.

(20) Kohn, W.; Sham, L. J. Self-Consistent Equations Including Exchange and Correlation Effects. *Phys. Rev.* **1965,** *140* (4A), A1133.

(21) Becke, A. D. Density-Functional Thermochemistry. III. The Role of Exact Exchange. *J. Chem. Phys.* **1993,** *98* (7), 5648.

(22) Casida, M. E. In *Recent Advances in Density Functional Methods*; WORLD SCIENTIFIC, 1995; Vol. Volume 1.

(23) Chai, J.-D.; Head-Gordon, M. Long-Range Corrected Hybrid Density Functionals with Damped Atom–Atom Dispersion Corrections. *Phys. Chem. Chem. Phys.* **2008,** *10* (44), 6615.

(24) Liu, J.; Liang, W. Analytical Second Derivatives of Excited-State Energy within the Time-Dependent Density Functional Theory Coupled with a Conductor-Like Polarizable Continuum Model. *J. Chem. Phys.* **2013,** *138* (2), 024101.

(25) Shao, Y.; Head-Gordon, M.; Krylov, A. I. The Spin–Flip Approach within Time-Dependent Density Functional Theory: Theory and Applications to Diradicals. *J. Chem. Phys.* **2003,** *118* (11), 4807.

(26) Becke, A. D. Density-Functional Exchange-Energy Approximation with Correct Asymptotic Behavior. *Phys. Rev. A* **1988,** *38* (6), 3098.

(27) Lee, C.; Yang, W.; Parr, R. G. Development of the Colle-Salvetti Correlation-Energy Formula into a Functional of the Electron Density. *Phys. Rev. B* **1988,** *37* (2), 785.

Chapter 3: Structural motifs which lead to enhanced pressure sensitivity – strained four-membered rings in Dewar 9TBA and core-shell nanoparticles

3.1 Pressure enhanced back reaction rate of the 9-tert-butylanthracene photoisomer

The ability of isotropic hydrostatic pressure, as opposed to shear, had been previously investigated as a source to generate chemical changes in highly strained photoisomers with different three-dimensional structures. By tethering two anthracene chromophores together using ethyl linkers, a cyclophane molecule, bi(anthracene-9,10-dimethylene) (BA), was made that could undergo intramolecular photodimerization to form a high energy isomer denoted PI.[1] The dissociation of PI in a polymer matrix was greatly accelerated by the application of relatively low pressures on the order of 1.0 GPa. Pressure-dependent rate measurements indicated that this reaction has a negative activation volume, and this was recently confirmed by ab initio calculations.[2] This pressure sensitivity was not observed in an untethered analogue An_2. The dramatic acceleration of the PI photodimer dissociation demonstrated that isotropic pressure, as opposed to anisotropic shear, could be used to break chemical bonds.

Motivated by the results on BA, pressure-sensitive structural motifs present in photoproducts were sought. Since the dissociation of the untethered anthracene dimer An_2 was not sensitive to pressure, it seemed clear that the presence of internal six-

membered 1,4-cyclohexadiene rings of the [4 + 4] photoisomer was insufficient to induce pressure sensitivity. Here, the presence of a pair of internal four-membered rings were explored as a means to enhance the pressure sensitivity.[3] The Dewar photoisomerization of aromatic molecules is an example of a reaction that produces a pair of strained four-membered rings.[4] Therefore, 9-tert-butylanthracene (9TBA), a molecule that photoisomerizes to its 9,10 Dewar form (D-9TBA) in liquid solution[5,6] (Figure 3.1.1) was used to test this hypothesis. The Dewar form is somewhat stable in room temperature solution, with a lifetime of several hours in hexane. By dissolving 9TBA in a polymer matrix and placing it in a diamond anvil cell (DAC), the effect of pressure on the rate of the D-9TBA → 9TBA reaction can be tested, which is analogous to the PI → BA conversion.

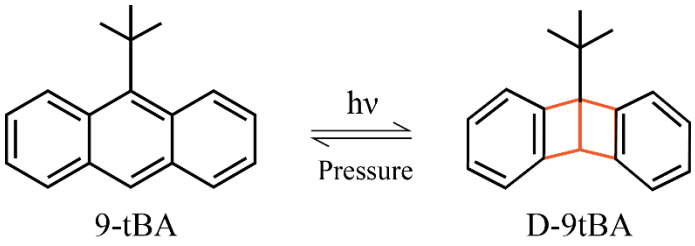

Figure 3.1.1. UV irradiation of 9-tert-butylanthracene (9tBA) produces the Dewar photoisomer (D-9tBA). Isotropic pressure enhances the back reaction.

The 9TBA → D-9TBA transformation can be monitored using absorption spectroscopy. As shown in Figure 3.1.2, the anthracene chromophore in 9TBA has two distinct absorption features that diminish when D-9TBA is formed: the characteristic anthracene $S_0 \rightarrow S_1$ absorption in the 350−450 nm range and the $S_0 \rightarrow S_3$ feature peaked at 263 nm.[7] Since the $S_0 \rightarrow S_3$ absorption coefficient is approximately 10× larger than that

of the visible $S_0 \rightarrow S_1$ transition, the area under this peak was integrated to assess the concentration of 9TBA present in the sample. One complication is that the presence of O_2 can lead to peroxidation of the anthracene ring,[8] providing a competing reaction channel. Side reactions with O_2 are a much bigger concern for 9TBA than for BA due to its lower isomerization quantum yield (~1% versus >50% for BA). The O_2 photoproduct does not revert to 9TBA at room temperature, unlike D-9TBA, and this lack of reversibility provides a measure of the relative importance of this reaction channel. Exposing the polymer sample to a vacuum of 10^{-4} Torr for approximately 48 h was required to sufficiently remove O_2, consistent with previous results on 9TBA in polystyrene.[9] If a thoroughly degassed 9TBA/Zeonex sample is photolyzed and then left in the dark for >24 h, complete recovery of the absorption spectrum is observed.

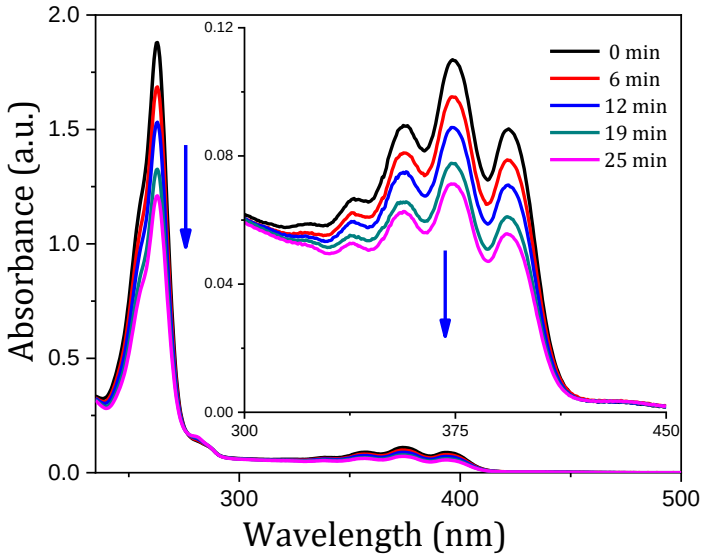

Figure 3.1.2. Absorption spectrum of 9tBA in Zeonex illustrating the decrease in absorbance as a function of irradiation time. Integrating the high energy peak provides a way to monitor the conversion of 9tBA to D-9tBA.

In cyclohexane solution at room temperature, both the forward and reverse Dewar reaction dynamics were measured. The forward reaction (9TBA → D-9TBA) quantum yield was found to be 6% for 365 nm irradiation, while the reverse reaction rate was measured to be 4.0×10^{-5} s^{-1}, both in good agreement with values previously reported in the literature for similar solvents.[5,6] The forward rate for the 9TBA → D-9TBA reaction is found to be 1.5×10^{-4} s^{-1} under 2.7 mW/cm^2 365 nm irradiation in a Zeonex matrix under vacuum. From this data, the photochemical reaction yield of 0.6 ± 0.3% can be determined using the absorption cross section for 9tBA of 5.8×10^{-18} cm^2 at 365 nm. This quantum yield value is similar to what has been observed in polystyrene[9] but about an order of magnitude smaller than what is seen in solution. The reverse reaction rate was measured to be 4.5×10^{-5} s^{-1} in Zeonex, consistent with the values obtained both in liquid solution and in polystyrene.[9] The different forward rates in solid polymers versus liquid solutions are understandable considering the large geometry changes required for the Dewar isomerization, which is presumably inhibited by the solid polymer matrix. Since the reverse reaction occurs in a cavity that is already expanded to accommodate the Dewar form, steric constraints are anticipated to play less of a role, as previously observed for Dewar benzene.[10] The rate of 9TBA reaction for a Zeonex sample that had not been placed under vacuum was also measured, and the forward reaction rate was measured to be 3.1×10^{-4} s^{-1} under the same illumination conditions. Assuming that this rate is the sum of the Dewar isomerization and peroxidation rates, then the two rates must be almost equal at ambient pressure and temperature.

The rate of the 9TBA → D-9TBA photoreaction is very pressure-dependent. Since O_2 cannot be completely excluded from the DAC during the pressure-loading process, the pressure dependence of the Dewar isomerization and peroxidation rates cannot be separated. As shown in Figure 3.1.3A, the total rate at ambient pressure (3.1×10^{-4} s^{-1}) slowed down considerably at 1.55 GPa (1.5×10^{-7} s^{-1}). Both the isomerization and the photoperoxidation rates must be pressure-dependent, since if only one of these rates decreased with pressure, the total rate would never drop below the ambient value of $\sim 1.5 \times 10^{-4}$ s^{-1} for either reaction. The Dewar isomerization is expected to be pressure-dependent because it requires a large geometry change that will become more difficult in a denser medium. It has also been shown that the photoperoxidation reaction is sensitive to the free volume in the polymer host,[11] presumably because it requires O_2 diffusion. Increased pressure reduces the available volume for O_2 diffusion, which should slow the peroxidation reaction as well.

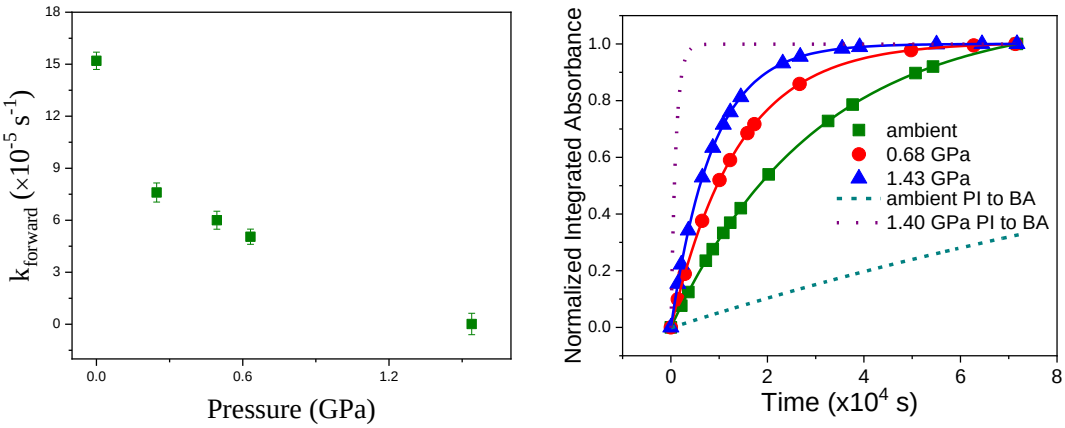

Figure 3.1.3. (A) The rate of the forward reaction as a function of pressure. (B) The recovery of the absorbance of 9tBA with respect to time at a given pressure (symbols) compared to previous results on the back reaction of PI → BA (dashed lines) at under ambient conditions and under pressure. The solid lines represent the fits using equation 1.

Pressure (GPa)	0	0.1	0.42	0.68	1.10	1.43
k_{back} ($\times 10^{-5}$ s^{-1})	4.5 ± 0.3	6.4 ± 0.5	7.7 ± 0.9	7.4 ± 0.4	9.5 ± 0.3	11.5 ± 1.3

Table 3.1.1. Measured rate constants of the back reaction at room temperature as a function of pressure.

The presence of O_2 should not affect the back-reaction of D-9TBA to 9TBA, which is of primary interest here. To measure the pressure dependence of the D-9TBA → 9TBA back reaction, the 9TBA / Zeonex sample is first photolyzed under vacuum and then loaded into the DAC within 5 min to minimize O_2 exposure. The absorption of the sample within the DAC was then monitored over the course of hours as the D-9TBA → 9TBA back-reaction proceeded. Typical recovery curves are shown in Figure 3.1.3B for ambient, 0.68 and 1.43 GPa pressures. The recovery becomes more rapid at higher pressures, roughly by a factor of three. Also shown for comparison are the pressure-dependent components of the PI → BA recovery at ambient and high pressures. This component of the PI → BA reaction is clearly much slower at ambient pressure but much faster at high pressures – bracketing the D-9TBA → 9TBA data. To model the recovery, the D-9TBA → 9TBA back-reaction is assumed to be a simple first-order process and the concentration of 9TBA, N_{9TBA}, is given by

$$N_{9TBA} = N^0_{9TBA}(1 - f_{conv}e^{-k_{back}t}) \qquad (3.1)$$

where $N^0_{9TBA}$is the original 9TBA concentration before the photoreaction, f_{conv} is the fraction reacted by 365 nm excitation (f_{conv} < 0.4 in all experiments), and k_{back} is the back-reaction rate. Fits to the data using equation 3.1 are overlaid with the data in Figure 3.1.3B. The k_{back} values obtained from the fits are given in Table 3.1.1. The activation

volume, $\Delta V^{\ddagger}$, of the back reaction can be determined by plotting the natural log of k_{back} versus pressure P, using the relation

$$\mathrm{Ln}(k_{back}) = \frac{-\Delta V^{\ddagger}}{RT} P + constant \qquad (3.2)$$

where R is the ideal gas constant and T is the temperature.[12] A linear fit to the data yields $\Delta V^{\ddagger} = -2.3 \pm 0.2$ Å^3. The activation volume can be associated with the volume change of the transition state, which in this case must be smaller than that of the reactant D-9TBA. A smaller transition state is favored at high pressure and thus accelerates the reaction. While this $\Delta V^{\ddagger}$ value is significant, it is almost an order of magnitude smaller than the $\Delta V^{\ddagger} = -16$ Å^3 previously obtained for the PI → BA reaction.

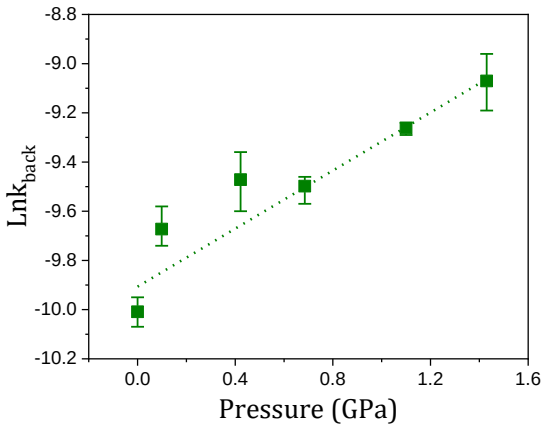

Figure 3.1.4. Dependence of the natural log of the back reaction rate on pressure. A linear least-squares fit to the data yields an estimate of the activation volume $\Delta V^{\ddagger} = -2.3 \pm 0.2$ Å^3.

The recovery rate of 9TBA increases by almost a factor of three as the pressure is increased, while the PI → BA recovery rate increased nearly three orders of magnitude over the same pressure range. One can then ask why are the pressure-dependent

reaction dynamics of D-9TBA and PI so different? Both are metastable, high energy photoisomers. DFT calculations place D-9TBA 184 kJ/mol above 9TBA, close to the experimental ΔH_0 = 172 kJ/mol (Figure 3.1.5).[13,14] PI is calculated to be only 87 kJ/mol above BA, again comparable to experimental values.[1] The higher energy of D-9TBA is likely due to the formation of two adjacent cylcobutene rings with higher strain than the two separate cyclobutane rings in PI. Despite their enthalpic differences, the PI → BA and D-9TBA → 9TBA reactions have very similar activation energies of 93−96 kJ/mol at room temperature and pressure.[1,5,13] Thus, from an energetic standpoint, there is no reason to suspect that PI would become so reactive at high pressure relative to D-9TBA. A second point of comparison involves the product and reactant molecular volumes obtained from the crystal structures. Although estimating molecular size from crystal structures is inexact due to packing considerations, these numbers provide a well-defined reference point for comparing similar molecules. In many organic isomerization reactions, the activation volume is close to the reaction volume,[15] i.e., the difference between equilibrium product and reactant molecular volumes. Thus, destabilization of a higher volume reactant at higher pressures is typically expected to lead to more rapid reaction kinetics. 9TBA has a volume of 325 Å^3, while D-9TBA occupies a larger volume of 334 Å^3.[16] The negative reaction volume (−9 Å^3) calculated from the crystal structures predicts a negative activation volume for the D-9TBA → 9TBA reaction, as observed. PI, on the other hand, occupies a slightly smaller volume than BA, as estimated from their crystal structures, and thus a positive activation volume would be predicted for the PI → BA

reaction, with a concomitant slowing of the reaction at higher pressures. This is the opposite of what is observed experimentally. If energy differences and volume changes are solely considered, the high-energy, high-volume D-9TBA would be expected to be more sensitive to pressure than PI, contrary to what is observed.

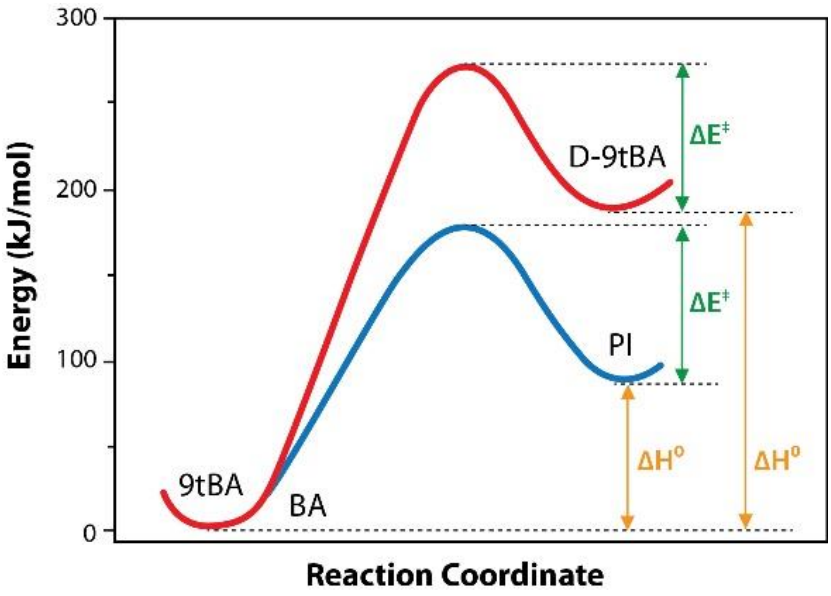

Figure 3.1.5. Comparison of the potential energies of PI and D-9tBA reactions, where the activation energy ($\Delta E^{\ddagger}$) is approximately 94 kJ/mol for both reactions.

A theoretical report sheds some light on this discrepancy suggesting that the tethering of the two anthracenes in PI leads to an asymmetric diradicaloid transition state whose volume is significantly smaller than that of the reactant or product.[2] The idea is that this asynchronous transition state avoids transient crowding by nonbonded carbons. If this is true, then a large negative $\Delta V^{\ddagger}$ is expected only for the cyclophane PI, as observed. Neither An_2 nor D-9tBA has the same degree of crowding, and neither shows

the same pressure sensitivity as PI.[3] From these results, some ideas begin to form about what is important for making a pressure-sensitive mechanophore. For example, in PI, it was hypothesized that the symmetric three-dimensional structure could exclude most of the pressurized medium (i.e., the polymer) from its interior and permit the generation of local shear forces on the top and bottom anthracene rings. If correct, this idea suggests that boxlike molecular structures should exhibit greater pressure sensitivity than planar structures. However, the absence of a pressure effect in An_2 shows that such a boxlike structure by itself is ineffective. Now the results on D-9TBA, a two-dimensional molecule, show that the presence of strained four-membered rings is also not sufficient to generate enhanced pressure sensitivity although it is more pressure-sensitive than An_2. Taken together, the results on these three anthracene molecules are consistent with the idea that a crowded three-dimensional carbon environment provides constraints on the transition state that lead to a highly negative $\Delta V^{\ddagger}$. Although much work needs to be done, both experiment and theory imply that there may exist general principles for designing molecules whose reactivity can be modulated by pressure.

The pressure dependence of the back-reaction rate of the Dewar isomer of 9TBA increases by a factor of ∼3 at high pressure (1.43 GPa). Despite being a highly strained isomer, this reaction rate is at least 100× less sensitive to pressure than the PI → BA back-reaction studied previously. These results suggest that the pressure sensitivity of the PI → BA reaction arises from the unique molecular geometry of PI, as opposed to the presence of a single structural motif. Further experiments will be necessary to understand

the precise molecular origins of PI's pressure sensitivity and guide the development of other strained molecules that are sensitive to pressure. Eventually, these insights will enable the design of molecules that can act as pressure sensors or as components of self-healing materials.

3.2 Pressure-induced plasmonic response of noble metal nanoparticles

Nanoscale materials have attracted much interest in recent years as quantum confinement leads to optical properties that are quite different from that found in the bulk material. In addition, these properties are size and shape tunable and the small size makes them sensitive to the surrounding environment. The ease of synthesis and inherent tunability makes nanoparticles well suited for use as functional materials.[17] In noble metal nanoparticles incident photons induce a plasmonic response which leads to a broad absorption band in spherical shapes and two distinct plasmon peaks in rod shaped particles that can be correlated with the long (longitudinal band) and short (transverse band) axis of the rod.[18,19] Since pressure can change the polarizability of the environment surrounding a nanoparticle and such changes will alter the plasmonic response, noble metal nanoparticles can be used as pressure sensors by monitoring the optical response. Both rod shaped Au nanoparticles and Au core-Ag shell nanoparticles (Au@Ag) were explored for optically detectable pressure sensing. Au is a popular choice for

nanoparticles due to its chemical stability and ease of surface modification,[20] but the high plasmonic response of Ag in the visible region of the electromagnetic spectrum makes it an ideal material for optical applications,[21] and the enhanced environmental sensitivity of Ag is desirable for pressure sensing applications.[22] However, synthesizing Ag nanospheres with a diversity of sizes has proven to be difficult.[23] Since the plasmonic response of core-shell particles is governed by the properties of the shell,[24] an alternate way of making size-disperse Ag nanoparticles is to use the easily controllable Au nanospheres as a template for Ag.[23] By varying the mixing ratios of Au and Ag, the optical properties of these core-shell nanoparticles can be tuned. Using a diamond anvil cell (DAC), the optical absorption is measured as a function of hydrostatic pressure for both Au nanorods and Au@Ag core-shell nanospheres embedded in polymer matrices.

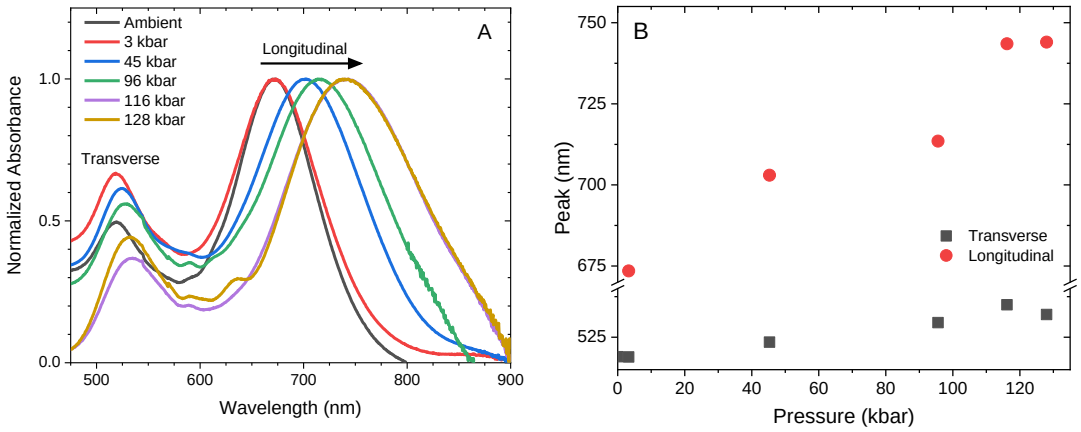

Figure 3.2.1: (A) The absorption spectra of Au nanorods in PVA showing the evolution of the transverse and longitudinal plasmon resonances with increasing hydrostatic pressure. (B) The longitudinal peak is more sensitive to the application of pressure.

Figure 3.2.1A shows the normalized spectra of Au nanorods as the pressure is increased from 3 kbar to 128 kbar. The decrease in the intensity of absorption is caused by a shortened pathlength within the aperture of the DAC since the pressure is increased by bringing the diamond culets together. Up to 96 kbar, the peaks shift reversibly upon releasing the pressure; however, pressures above 96 kbar lead to irreversible changes in the ambient absorption spectrum of the gold nanorods. Furthermore, the spectra above 96 kbar seem relatively insensitive to the additional pressure increases as is most evident in the flattening of the peak shift curves in figure 3.2.1B. The likely culprit for the irreversibility and diminished pressure sensitivity at the highest pressures is a permanent shape change in the nanorod. The longitudinal plasmon response exhibits a more sensitive response to the applied pressure as compared to the transverse peak. This is not surprising as the environmental insensitivity of the transverse plasmon band has been previously reported where both the aspect ratio of nanorods and the surrounding media yield only subtle changes in the peak shape and location.[19]

Au@Ag core-shell structures were also examined at a variety of different mixing ratios for their pressure sensitivity. Similar to the Au nanorods, a redshift of the Ag plasmonic response is observed as the pressure is increased in 1:5 Au@Ag particles (Figure 3.2.2A). The peak shift is more sensitive to pressure changes when compared to the Au nanorods; however, after only 30 kbar the ambient spectrum cannot be reproduced. The lack of reversibility at moderate hydrostatic pressure probably results from breaking or deforming the Ag shell. Among the different mixing ratios, the plasmonic

response for the 1:5 Au@Ag is the sharpest which leads to more easily identifiable peak shifts. The 1:2 Au@Ag nanoparticles exhibit a broadened plasmon response that redshifts with increasing pressure (Figure 3.2.3A). Irreversibility is once again obtained around 30 kbar. In this case increased pressure appears to also cause the plasmon response to sharpen as the bluer feature becomes less prominent at higher pressures. This behavior is similar to that observed in the 1:1 Au@Ag particles (Figure 3.2.3B) where increased pressure only leads to a small redshift and a distinct sharpening of the plasmon response. The decreased pressure sensitivity could be the result of increased Au character in the optical response as the Ag concentration is lowered.

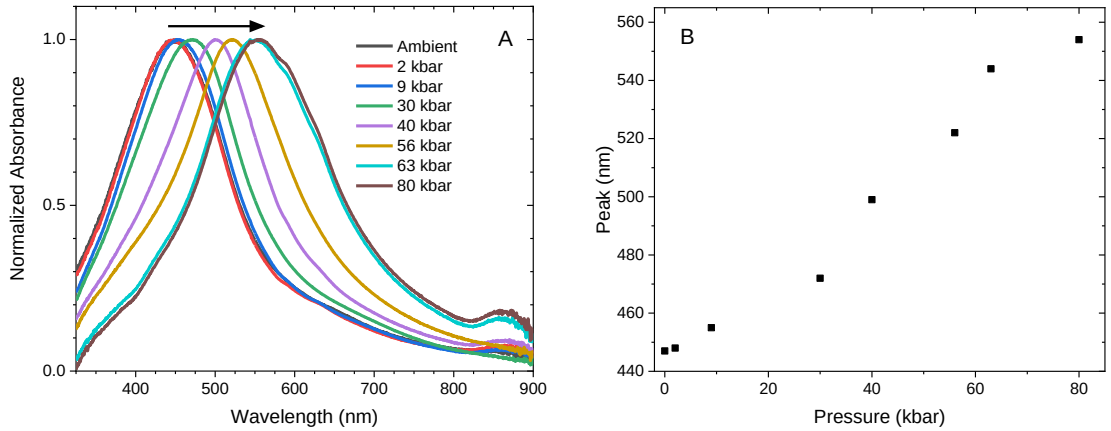

Figure 3.2.2: (A) The absorption spectra of 1:5 Au@Ag in PVA as a function of pressure. (B) The absorption peak red shifts with increased hydrostatic pressure.

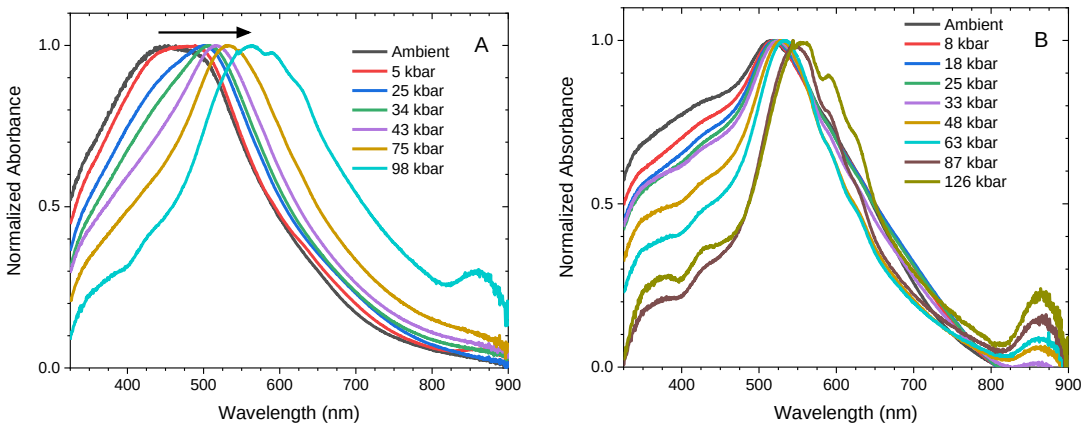

Figure 3.2.3: The normalized absorption spectra of 1:2 Au@Ag (A) and 1:1 Au@Ag (B) embedded in a PVA matrix.

Noble metal particles display optical properties which respond to changes in hydrostatic pressure. The longitudinal plasmonic peak in the Au nanorods is more sensitive to changes in hydrostatic pressure compared to the transverse peak, and the peak shift is reversible up to the relatively high pressure of 126 kbar at which point the rod likely deforms. The Au@Ag particles benefit from higher concentrations of Ag which leads to a sharp plasmon response enabling a clearer identification of the pressure-induced peak shift. The reversibility is not as robust as the nanorods since 30 kbar presumably breaks the shell of the nanoparticle leading to a permanent spectral change. Future work needs to correlate the high pressure measurements with scanning electron microscopy to confirm the inferred changes to the nanoparticle structures which inhibit reversibility. Optical detection at lower pressures is still desirable, but these particles require relatively high pressures to see a plasmonic shift. Different core-shell shapes may provide enhanced sensitivity at lower pressures. Alloyed Au/Ag particles may be a fruitful

avenue of exploration for the Ag plasmonic response and the possibility of obtaining reversibility at higher pressures much like the Au nanorods. Noble metal nanoparticles show much promise for their in novel functional materials.

3.3 References

(1) Jezowski, S. R.; Zhu, L. Y.; Wang, Y. B.; Rice, A. P.; Scott, G. W.; Bardeen, C. J.; Chronister, E. L. Pressure Catalyzed Bond Dissociation in an Anthracene Cyclophane Photodimer. *J. Am. Chem. Soc.* **2012,** *134* (17), 7459.

(2) Slepetz, B.; Kertesz, M. Volume Change during Thermal [4 + 4] Cycloaddition of [2.2](9,10)Anthracenophane. *J. Am. Chem. Soc.* **2013,** *135* (37), 13720.

(3) Tong, F.; Cruz, C.; Jezowski, S.; Zhou, X.; Zhu, L.; Al-Kaysi, R. O.; Chronister, E. L.; Bardeen, C. J. Pressure Dependence of the Forward and Backward Rates of 9-tert-Butylanthracene Dewar Isomerization. *J. Phys. Chem. A* **2014,** *118* (27), 5122.

(4) Van Tamelen, E. E. Valence bond isomers of aromatic systems. *Acc. Chem. Res.* **1972,** *5* (5), 186.

(5) Kraljic, I.; Mintas, M.; Klasinc, L.; Ranogajec, F.; Guesten, H. Thermo- and photochemical aspects of the valence isomerization of 9-tert-butylanthracene. *Nouv. J. Chim.* **1983,** *7* (4), 239.

(6) Guesten, H.; Mintas, M.; Klasinc, L. Deactivation of the fluorescent state of 9-tert-butylanthracene. 9-tert-Butyl-9,10(Dewar anthracene). *J. Am. Chem. Soc.* **1980,** *102* (27), 7936.

(7) Birks, J. B. *Photophysics of Aromatic Molecules*; Wiley - Interscience: New York, 1970.

(8) Stevens, B.; Perez, S. R.; Ors, J. A. Photoperoxidation of unsaturated organic molecules. XIV. O21.DELTA.g acceptor properties and reactivity. *J. Am. Chem. Soc.* **1974,** *96* (22), 6846.

(9) Minaylov, V. V.; Gurman, V. S.; Vorobiev, A. K. Photoisomerization of 9-tert-butylanthracene in polystyrene films under photoselection conditions. Consideration of molecular thermal rotation. *J. Photochem. Photobiol., A* **1995,** *87* (1), 67.

(10) Ferrar, L.; Mis, M.; Robello, D. R. Thermal isomerization of dewarbenzene derivatives. *Tetrahedron Lett.* **2008,** *49* (26), 4130.

(11) Sheats, J. R. Media effects on the kinetics of anthracene photo-oxidation in polymers. *Journal of Photochemistry and Photobiology A: Chemistry* **1994,** *80* (1), 377.

(12) Jenner, G. High-pressure mechanistic delineation based on activation volumes. *J. Phys. Org. Chem.* **2002,** *15* (1), 1.

(13) Jahn, B.; Dreeskamp, H., 1983; p 159.

(14) Grimme, S.; Peyerimhoff, S. D. Theoretical Study of the Valence Isomerization of Anthracene and 9-tert-Butylanthracene to Their Dewar Forms in the Ground and Excited States. *J. Phys. Chem.* **1994,** *98* (49), 12927.

(15) Tohru, T.; Yoshimi, S.; Shunzo, Y.; Norio, N. PRESSURE DEPENDENCE OF THE PHOTOSTATIONARY trans/cis CONCENTRATION RATIO OF 4-DIMETHYLAMINO-4'-NITROAZOBENZENE. A NEW METHOD OF EVALUATING THE REACTION VOLUME. *Chem. Lett.* **1985,** *14* (8), 1203.

(16) Angermund, K.; Claus, K. H.; Goddard, R.; Krüger, C. High-Resolution X-ray Crystallography—An Experimental Method for the Description of Chemical Bonds. *Angewandte Chemie International Edition in English* **1985,** *24* (4), 237.

(17) Jain, P. K.; Huang, X.; El-Sayed, I. H.; El-Sayed, M. A. Noble Metals on the Nanoscale: Optical and Photothermal Properties and Some Applications in Imaging, Sensing, Biology, and Medicine. *Accounts of Chemical Research* **2008,** *41* (12), 1578.

(18) Cao, J.; Sun, T.; Grattan, K. T. V. Gold nanorod-based localized surface plasmon resonance biosensors: A review. *Sensors and Actuators B: Chemical* **2014,** *195*, 332.

(19) Huang, X.; Neretina, S.; El-Sayed, M. A. Gold Nanorods: From Synthesis and Properties to Biological and Biomedical Applications. *Advanced Materials* **2009,** *21* (48), 4880.

(20) Dreaden, E. C.; Alkilany, A. M.; Huang, X.; Murphy, C. J.; El-Sayed, M. A. The golden age: gold nanoparticles for biomedicine. *Chemical Society Reviews* **2012,** *41* (7), 2740.

(21) Liz-Marzán, L. M. Tailoring Surface Plasmons through the Morphology and Assembly of Metal Nanoparticles. *Langmuir* **2006,** *22* (1), 32.

(22) Lee, Y. H.; Chen, H.; Xu, Q.-H.; Wang, J. Refractive Index Sensitivities of Noble Metal Nanocrystals: The Effects of Multipolar Plasmon Resonances and the Metal Type. *The Journal of Physical Chemistry C* **2011,** *115* (16), 7997.

(23) Samal, A. K.; Polavarapu, L.; Rodal-Cedeira, S.; Liz-Marzán, L. M.; Pérez-Juste, J.; Pastoriza-Santos, I. Size Tunable Au@Ag Core–Shell Nanoparticles: Synthesis and Surface-Enhanced Raman Scattering Properties. *Langmuir* **2013,** *29* (48), 15076.

(24) Fernanda Cardinal, M.; Rodríguez-González, B.; Alvarez-Puebla, R. A.; Pérez-Juste, J.; Liz-Marzán, L. M. Modulation of Localized Surface Plasmons and SERS Response in Gold Dumbbells through Silver Coating. *The Journal of Physical Chemistry C* **2010,** *114* (23), 10417.

Chapter 4: Tuning electronic coupling in sulfur-bridged chromophores – oxidation state dependent photophysics and photochemistry of terthiophene and anthracene dimers

4.1 Tuning electronic interactions in covalent molecular assemblies

The rational design of symmetrically bridged chromophore dimers, also called bichromophores, has attracted considerable interest, because bichromophores provide an ideal proving ground to develop strategies for controlling excited state behavior in chromophore assemblies. Of particular interest in these symmetric systems is the ability to control the charge transfer (CT) character of the excited state, because the CT and neutral states are close in energy, the amount of energy lost in the charge separation event is reduced; thus, the open-circuit voltage of photovoltaic devices can potentially be reduced.

It is anticipated that practical applications of dimeric molecules in photovoltaic and light emitting devices will require precise control of electronic interactions between chromophores. Ideally, such a control element would be built into the dimer molecule itself, without inducing large conformational changes. Covalently tethering the chromophores together allows the geometrical arrangement to be defined and the electronic interaction to be controlled. Such dimers or bichromophores form the smallest

subunit of larger chromophore assemblies such as polymers and are useful for basic studies of phenomena relevant to organic electronic materials.

Bridging two conjugated chromophores symmetrically about a sulfur atom was shown to result in systematic enhancement of the photoluminescence (PL) by oxidizing the bridging sulfur.[1] Increasing the oxidation state of the sulfur bridge also resulted in pronounced red-shifts of the PL spectra in polar solvents, an indication of increasing CT character. Changing the oxidation state of the sulfur from S to SO to SO_2 allows modification of the electronic properties of the bridge while maintaining almost identical molecular conformations, as determined from the crystal structures. The observation that simply linking two chromophores together could lead to new CT excited states and increase the PL yield by an order of magnitude raised several questions regarding the origin of the changes in spectroscopic behavior. The first question concerns the role of the sulfur linker: Does it actively participate in the electronic states, and why does its oxidation state have such a large effect? Related to this question, one may ask whether the second chromophore plays an important role. If the CT state involves only one of the chromophores and the bridging sulfur, then perhaps the second chromophore is not even necessary. The question of electronic structure is intimately related to the excited-state dynamics: How is the CT state formed and why is its relaxation different from that of a single chromophore? These classes of sulfur-bridged dimers, with potential applications in organic electronics, provides an ideal model system in which to study fundamental questions about the excited-state behavior in symmetric bichromophore systems.

Combining optical spectroscopy and electronic structure theory enables a complete picture of the photophysics to be developed of the terthiophene (**T3**) and anthracene (**An**) derivatives shown in Figure 4.1.1 and Figure 4.3.1, respectively. In the terthiophene compounds the bridge itself does not significantly affect the excited-state structure, but the oxidation state of the sulfur bridge mediates the amount of electronic coupling between the two terthiophene chromophores. Using femtosecond transient absorption (TA) experiments, the initial excited state is shown to be a delocalized excitonic state with an overall neutral character that relaxes within 10 ps to a second state

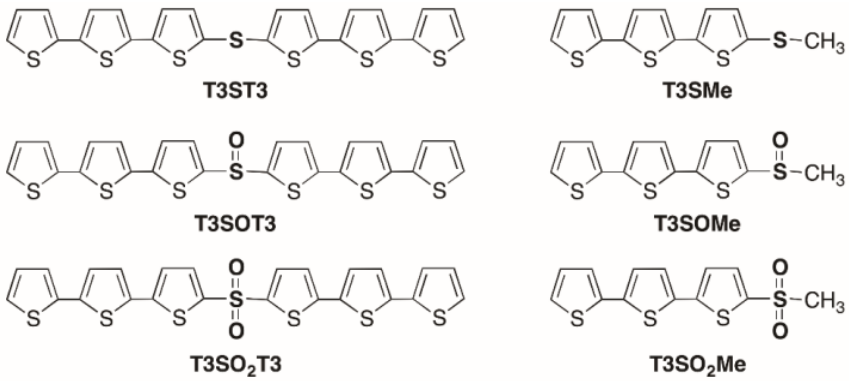

Figure 4.1.1. Terthiophene derivatives explored in this work.

where the CT character depends on the bridge oxidation state. This CT state has different radiative and intersystem crossing (ISC) rates when compared to monomeric terthiophene. Based on computational results, a mechanism in which electrostatic screening by lone pairs on the sulfur linker controls the CT character of the excited-state wave function is proposed. However, in the **An** compounds, this separation does not hold for the S-bridge, whose orbitals do participate in the optically accessible excited states and contribute to rapid ISC in both the symmetric and asymmetric bichromophores. The

SO_2 bridged **An** dimers exhibit more complex dynamics, with rapid internal conversion and the generation of a long-lived emissive state that is likely the precursor to the intramolecular [4+4] photocycloaddition. The most surprising result is that the bridge oxidation state provides a way to control the photochemistry of **An** dimers. Intramolecular reactivity in covalent anthracene assemblies is usually assumed to be completely controlled by steric effects and geometry, for example through the topochemical principle.[2-6] These results suggest that it is possible to use electron density on the bridge to mediate intramolecular interactions and tune the electronic coupling between identical chromophores without altering the dimer geometry or solvent polarity, providing a new quantum mechanical strategy for controlling the photochemical behavior of covalent molecular assemblies that may find applications in fields ranging from artificial photosynthesis to organic electronics.

4.2 Tuning the charge transfer state of terthiophene compounds

4.2.1. Steady state and time resolved spectroscopy

The experimental absorption spectra of **T3**, **T3SO$_2$Me**, and **T3SO$_2$T3** in dichloromethane are shown in Figure 4.2.1. When a methyl-terminated SO_2 linker is added to **T3**, the absorption peak shifts from 350 to 370 nm, but the overall peak shape remains the same, and there is no discernible broadening. The same is true for the S and SO linkers. When the methyl group is replaced by a second **T3** (**T3SO$_2$T3**), the absorption

not only redshifts farther but also broadens considerably, with two distinguishable peaks at 400 and 375 nm. This change in the absorption line shape is the first clue that the **T3**–**T3** electronic interaction plays an important role. Similar changes in absorption lineshapes are observed for the **T3ST3** and **T3SOT3** dimers. Since the lowest-energy transition for all **T3SO$_n$T3** species (~400 nm) is higher in energy than that of sexithiophene (~435 nm),[7,8] the electronic interactions in these dimers are not as strong as in a fully conjugated system. Although the absorption spectra are sensitive to the presence of the second **T3**, they are not very sensitive to solvent polarity.[1]

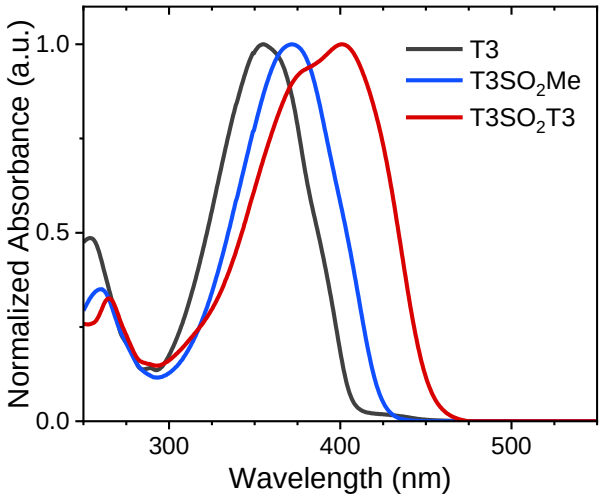

Figure 4.2.1. UV-Vis spectra for unsubstituted terthiophene (**T3**), the monomer (**T3SO$_2$Me**), and dimer (**T3SO$_2$T3**) all in dichloromethane.

The splitting of the dimer absorption spectra likely originates from through-space Coulombic interactions between the two **T3** chromophores. The two bands observed in the absorbance spectra of **T3SO$_n$T3** are attributed to interacting transition dipoles of the two monomers resulting in exciton splitting.[9,10] The low-energy bands in the absorption spectra of the **T3SO$_n$T3** dimers can be fit using a pair of Gaussians, allowing the excitonic

splitting energy, Δε, to be estimated. The splitting Δε increases with sulfur oxidation state (Δε = 1870 cm^{-1} for **T3ST3**, Δε = 2050 cm^{-1} for **T3SOT3**, and Δε = 2150 cm^{-1} for **T3SO$_2$T3**). This interaction is slightly smaller than the H-type aggregate coupling typically seen in oligothiophene crystals, in which the chromophores have an approximately parallel orientation.[11] The exciton splitting observed in the absorption spectra can be estimated by using equation 4.2.1 to describe the interaction of two point dipoles A and B:

$$\Delta\boldsymbol{\varepsilon} = \frac{\mathbf{2}|\boldsymbol{\mu}|^{\mathbf{2}}}{\boldsymbol{r}_{\boldsymbol{AB}}^{\mathbf{3}}}(\boldsymbol{cos\,\alpha} + \mathbf{3}\boldsymbol{cos}^{\mathbf{2}}\boldsymbol{\theta}) \qquad (4.2.1)$$

where μ is the transition dipole moment, r_{AB} is the center-to center vector between dipoles, α is the angle between the dipoles, and θ is the angle between the transition dipole moment and r_{AB} (Table 4.2.1 and Figure 4.2.2). Using equation 4.2.1, with values of r_{AB}, α, and θ (from computational results and X-ray crystallographic data)[1,12] and μ for unsubstituted terthiophene,[13] the exciton splitting is found to be 2000 cm^{-1} for **T3ST3**, 2100 cm^{-1} for **T3SOT3** and 1900 cm^{-1} for **T3SO$_2$T3**. All the values are close to 2000 cm^{-1}, consistent with the experimental results. This is somewhat surprising, considering that the point dipole approximation of equation 4.2.1 tends to overestimate Δε for chromophores in close proximity.[14-17] The calculations predict no systematic increase in Δε from **T3ST3** to **T3SO$_2$T3** because the molecular geometries are quite similar. However equation 4.2.1 only considers through-space dipole−dipole interactions, and it is known that electron-transfer terms can also contribute to excitonic splittings.[16,18-21] Comparing the calculated exciton splitting energy with those determined experimentally, it appears

that such electron-transfer contributions to Δε may play a larger role as the sulfur oxidation state is increased.

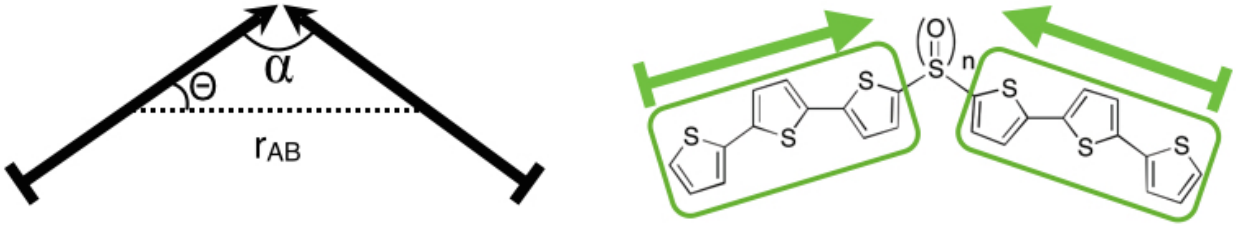

Figure 4.2.2. Cartoon illustrating obliquely oriented transition dipoles for S-bridged terthiophenes.

Parameter	T3ST3	T3SOT3	$T3SO_2T3$
T3 to Bridging S (pm)	175.8	180.3	176.3
L (pm)	1205.8	1210.3	1206.3
α°	105	101.4	108
θ°	37.5	39.3	36
r_{AB} (pm)	956.63	936.58	975.92
Δε (cm^{-1})	**1988.0**	**2078.7**	**1901.3**

Table 4.2.1. Exciton splitting (Δε) for each dimer as calculated through use of equation 4.2.1 with the length of **T3** determined from X-ray crystallographic data[12] to be 1030 pm (assuming a linear **T3** moiety). The transition dipole moment for **T3** is 10.3 Debye.[13] The angle α and the **T3**-to-Bridge distances have been determined previously.[1] The parameters r_{AB} and θ are calculated through the relationships $r_{AB} = L * \cos\theta$ and $\theta = 180^{\circ} - (0.5\alpha + 90^{\circ})$.

The steady-state PL spectra of **$T3SO_2Me$** and **$T3SO_2T3$** are compared in nonpolar cyclohexane, moderately polar dichloromethane, and highly polar acetonitrile (Figure 4.2.3). Increasing the solvent polarity for the monomer (**$T3SO_2Me$**) solutions results in only a small red-shift, with no change observed between moderately polar dichloromethane and polar acetonitrile (Figure 4.2.3A). Similar behavior is observed for the S and SO linkers. When the dimer (**$T3SO_2T3$**) is examined, however, an ~100 nm red

shift in the PL maximum is observed when the solvent polarity is increased from nonpolar cyclohexane to highly polar acetonitrile (Figure 4.2.3B). The different solvatochromic behaviors are accompanied by different fluorescence lineshapes. In acetonitrile, the fluorescence spectra of the **T3SO$_n$Me** monomer series hardly change from those in dichloromethane. In the same solvent, the dimers (**T3SO$_n$T3**) display relatively broad and unstructured profiles. These results reinforce the previous conclusion that the absorption spectra of **T3SO$_n$T3** are relatively insensitive to solvent, while the fluorescence spectra of the dimers exhibit strong solvatochromism.[1] The new results with the **T3SO$_n$Me** monomers demonstrate that the CT character of the emitting state arises from the presence of the second **T3** chromophore and not from the linker itself. Finally, the degree of dimer solvatochromism depends on the linker oxidation state, with the SO_2 linker showing the largest shift and the S linker showing much smaller shifts.

Unsubstituted **T3** has a relatively short PL lifetime (τ_{PL} = 190 ps), due to rapid ISC to its triplet state.[22,23] When the SO_nMe group is added, the PL lifetimes change very little. The monomers in dichloromethane have a τ_{PL} which varies only slightly depending upon the oxidation state of the sulfur, with a slight increase observed with increasing oxidation (171 ps for **T3SMe**, 195 ps for **T3SOMe**, and 219 ps for **T3SO$_2$Me**). The lifetimes are not appreciably different from that of unsubstituted **T3** nor do they exhibit a strong solvent dependence.

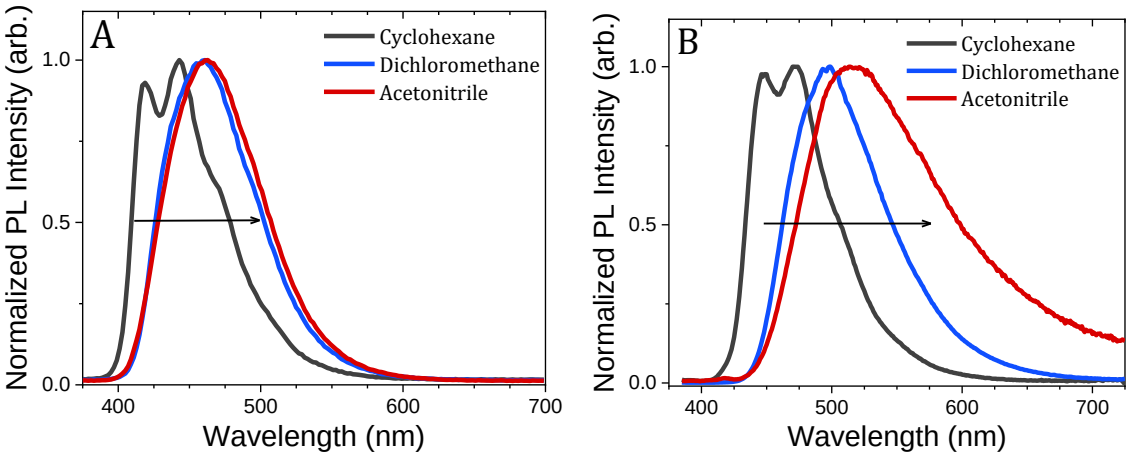

Figure 4.2.3. PL spectra for **T3SO₂Me** (A), and **T3SO₂T3** (B) in increasingly polar solvents from left to right (→) cyclohexane, dichloromethane, and acetonitrile.

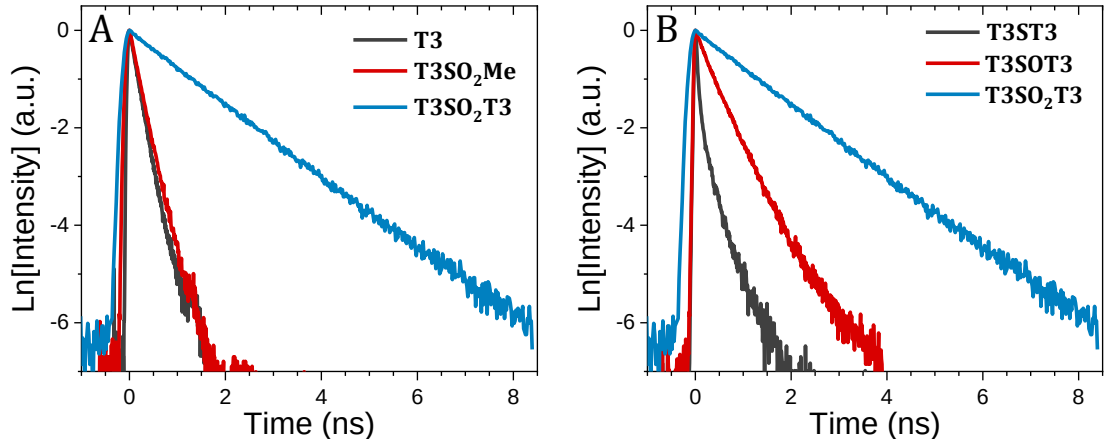

Figure 4.2.4. Fluorescence decays illustrating the effect of adding a second chromophore to the bridge (A) and comparing the oxidation states of the bridging sulfur for the bichromophoric compounds (B) all in dilute solutions of dichloromethane.

When the terminal methyl substituent is changed to **T3**, however, there is a significant increase in the fluorescence lifetime, as shown in Figure 4.2.4A. The different bridge oxidation states also give rise to different lifetimes in the dimers, as shown in Figure 4.2.4B. In all solvents, the lifetimes of the unoxidized sulfur-bridged dimer **T3ST3** are consistently shorter than those of the sulfoxide **T3SOT3**, which in turn are shorter than those of the sulfone **T3SO₂T3**. Of the compounds studied, only **T3ST3** deviated from monoexponential decay behavior, requiring a minor (~15%) second component when fit

to a biexponential function. A stretched exponential function could also be used, but since there is some evidence that two different conformers may be present (see Section 4.2.2), a biexponential is more justified physically. Despite this complication, the average fluorescence lifetime of **T3ST3** fits well with the trend observed in Figure 4.2.4.

The radiative lifetime τ_{rad} of **T3SO$_2$T3** increases with solvent polarity, consistent with a loss of oscillator strength in more polar solvents. This decrease in oscillator strength is concordant with an increasing degree of charge separation and is another hallmark of a CT state.[24,25] The effect of the oxidation state of the bridging sulfur group on the emission lifetime is similar for both the monomers and dimers, in that increasing the oxidation state from S to SO_2 results in an increase in the observed τ_{PL}. However, the trend is much more pronounced in the bridged dimers. The PL lifetimes (τ_{PL}) and relevant spectroscopic parameters of the terthiophene compounds are summarized in Table 4.2.2. In general, a higher oxidation state for the bridge leads to a more pronounced solvatochromic character of the emitting state as well as longer lifetimes and higher quantum yields.

	Parameter	T3ST3	T3SOT3	$T3SO_2T3$
Acetonitrile	Φ_{PL}	0.007	0.026	0.137
	τ_{PL} (ps)	120.8[a]	270.0	646.5
	τ_{rad} (ps)	1948	10385	4719
Dichloromethane	Φ_{PL}	0.012	0.173	0.565
	τ_{PL} (ps)	87.1[b]	405.3	1382.1
	τ_{rad} (ps)	7256	2343	2446
Cyclohexane	Φ_{PL}	—	—	0.138
	τ_{PL} (ps)	—	—	264.7
	τ_{rad} (ps)	—	—	1918

Table 4.2.2. PL quantum yields (Φ_{PL}), PL lifetimes (τ_{PL}) and radiative rates (τ_{rad}) for **T3SO$_n$T3** in various solvents.

The preceding results indicate that the excited state character of the dimers changes between the absorption and emission events. The absorbing state has an overall neutral character, as inferred from its lack of solvatochromism. The emitting state, on the other hand, has pronounced CT character that is strongly influenced by both solvent polarity and the oxidation state of the bridge. In order to understand how these two excited states are connected, TA measurements were performed.

The femtosecond TA of unsubstituted **T3** in solution has been measured previously.[26] In **T3**, an initial singlet $S_1 \rightarrow S_n$ excited-state absorption in the visible region decays to a signature $T_1 \rightarrow T_n$ triplet absorption on the same time scale as the PL decay. The photophysical behavior is consistent with that of a simple three-state system: absorption from S_0 to S_1, followed by ISC from S_1 to T_1 on a 190 ps time scale. The T_1 state then survives for nanoseconds before decaying back to S_0 nonradiatively. The TA spectra

of the **T3SO$_n$Me** monomers show similar behavior. At early times (t < 100 ps), the **T3SO$_2$Me** monomer shows a negative feature at 490 nm (Figure 4.2.5A), corresponding to stimulated emission, as well as a positive feature at ~595 nm assigned to the singlet induced absorption ($S_1 \rightarrow S_n$). At longer times (t > 100 ps), the triplet induced absorption ($T_1 \rightarrow T_n$) grows in at ~500 nm, while the $S_1 \rightarrow S_n$ feature and the stimulated emission both decay. The positive feature at 500 nm is assigned to the triplet since in **T3** the $T_1 \rightarrow T_n$ absorption is located at ~470 nm.[26,27] The redshift of the $T_1 \rightarrow T_n$ feature is expected because the T_n states tend to be less localized than T_1 and undergo a greater bathochromic shift upon substitution with electron-donating and -withdrawing groups.[28] The spectra in Figure 4.2.5A show an approximate isosbestic point, located at 545 nm, that suggests that the dominant relaxation process occurs between two well-defined electronic states. Using a principal component analysis, combined with a global fitting algorithm, the data in Figure 4.2.5A can be described using three components linked by two relaxation times τ_1 = 30 ps and τ_2 = 219 ps. The latter time is just the measured fluorescence decay time and reflects the ISC time in this molecule. The 30 ps time describes a small shift in the $S_1 \rightarrow S_n$ absorption peak and probably reflects conformational relaxation or solvent reorganization. The amplitude of the pre-exponential factor that corresponds to this time is <20% of the initial component. In Figure 4.2.5B, the global amplitudes of the three components that contribute to the signal are shown along with their decay times. The agreement with the data is very good at different probe wavelengths.

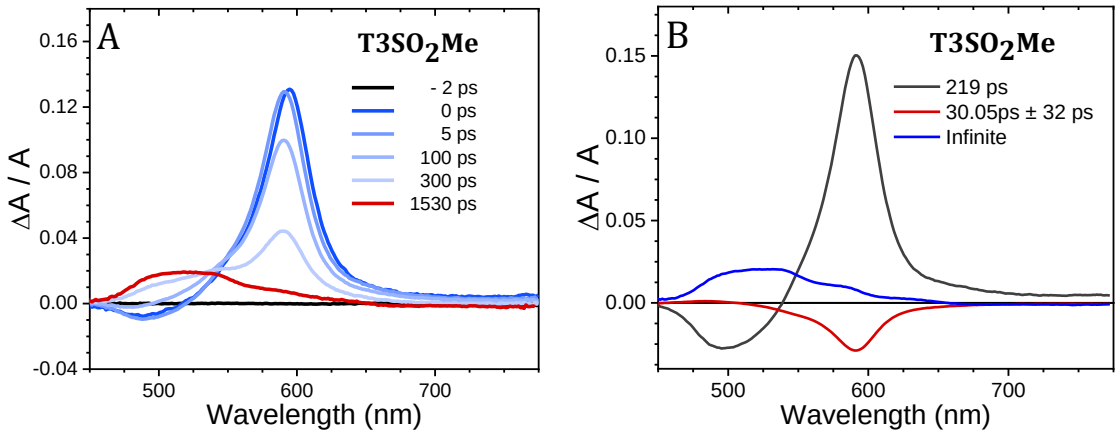

Figure 4.2.5. TA spectra (A) of **T3SO₂Me** in dichloromethane with the corresponding pre-exponential amplitudes obtained from the global fitting analysis (B).

In the **T3SOₙT3** dimers, the behavior is more complicated. All three compounds in dichloromethane show a much broader $S_1 \rightarrow S_n$ absorption that extends from the visible through the near-infrared, with a peak at ~600 nm and a second feature near 750 nm (Figure 4.2.6). As in the methyl-terminated compounds, the $S_1 \rightarrow S_0$ stimulated emission around 490 nm is eventually replaced by an induced absorption that is assigned to the triplet $T_1 \rightarrow T_n$ transition. For all three compounds, however, there is no clear isosbestic point because the induced absorption at 600 nm undergoes a rapid blueshift which is much more pronounced than in the monomer. For all three dimers, global analysis required a minimum of three components with two time constants. There is a fast (5−10 ps) component, followed by a slower component where the relaxation time mirrors the PL decay time. The third component is strongly peaked around 500 nm, suggesting that it is associated with the triplet state T_1. In all three dimers, the fast component is comparable in magnitude to the other components, unlike in the monomer, where it leads only to a small spectral shift. The TA kinetic parameters for the dimers **T3SOₙT3** and

the sulfone-bridged monomer **T3SO$_2$Me** in dichloromethane are summarized in Table 4.2.3. The important conclusion is that excited-state relaxation in the dimers appears to occur in two steps: fast relaxation from the absorbing state S_1 to an intermediate state S_1*, followed by slower relaxation from S_1* to the T_1 and S_0 states. The fluorescence behavior of the dimers is dominated by the relatively long-lived S_1* state.

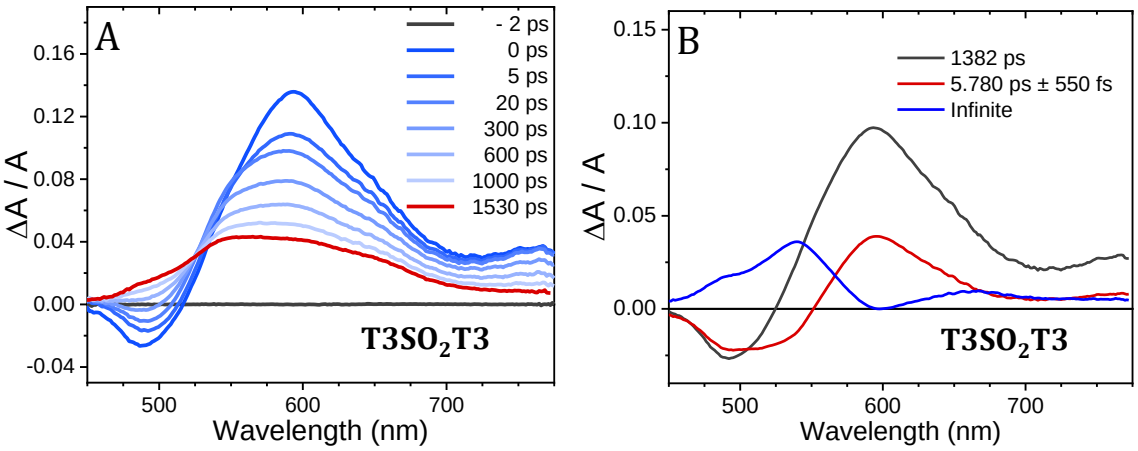

Figure 4.2.6. TA spectral slices of **T3SO$_2$T3** (A) in dichloromethane with the corresponding pre-exponential amplitudes obtained from a global analysis fit (B).

	T3ST3	**T3SOT3**	**T3SO$_2$T3**	**T3SO$_2$Me**
τ_1 (ps)	5.42	8.65	5.78	30.05
τ_2 (ps)	49	405	1382	219

Table 4.2.3. TA lifetimes determined from the global fitting analysis of the principal components for **T3SO$_n$T3** and **T3SO$_2$Me** in dichloromethane

The solvent polarity was varied in order to probe the CT character of the S_1* intermediate state. There is little dependence upon solvent polarity observed in the TA spectra of the monomers. The spectral evolution of **T3SO$_2$T3** in nonpolar cyclohexane (Figure 4.2.7) is strongly reminiscent of that seen in **T3SO$_2$Me** (Figure 4.2.5), albeit with a

broader $S_1 \rightarrow S_n$ absorption feature that extends into the near-infrared region. There is a recognizable isosbestic point located at 530 nm as the $T_1 \rightarrow T_n$ absorption grows in. A global fitting analysis yields only two components linked by a relaxation time of 265 ps, the experimentally measured PL lifetime. The single wavelength traces in Figure 4.2.7B show only a decay and concomitant rise in the $T_1 \rightarrow T_n$ absorption. Thus, in nonpolar cyclohexane, **T3SO$_2$T3** behaves like monomeric **T3** and the methyl-terminated bridge compounds with a one-step population transfer between S_1 and the triplet manifold.

The dynamics are qualitatively different for **T3SO$_2$T3** in acetonitrile (Figure 4.2.8). In this polar solvent, a clear isosbestic point is also observed, now shifted to 570 nm. A global analysis of the two principal spectral components yields three fit parameters. The amplitude of the pre-exponential coefficient that corresponds to the isosbestic point at 570 nm is peaked at 525 nm and forms within 2.8 ± 1.1 ps. This feature then decays with the measured fluorescence lifetime of 646 ps. The rapid growth of the intermediate state can also be seen in the single wavelength traces in Figure 4.2.8, where a clear increase in the signal is resolved at 530 nm, which then decays on a much slower time scale, close to the fluorescence decay time.

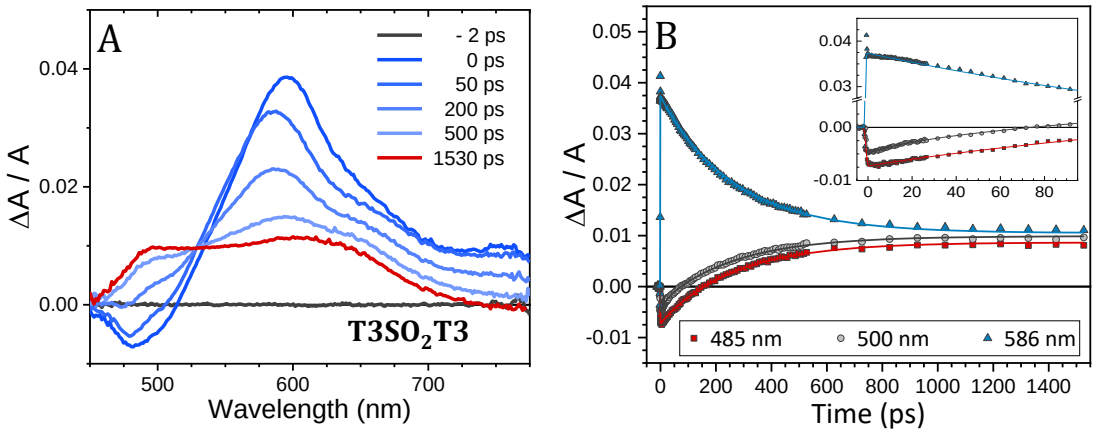

Figure 4.2.7. TA spectral slices of **T3SO$_2$T3** in cyclohexane (A) and the corresponding single wavelength traces (symbols) with fits overlaid (lines). The inset shows the early time (100 ps) dynamics (B).

Comparing the cyclohexane and acetonitrile data, it seems that the energetic separation of S_1* from S_1 depends on solvent polarity and that, in the most polar solvent used (acetonitrile), relaxation to the S_1* state leads to the appearance of a distinct electronic absorption feature. S_1* must correspond to a state with a high degree of charge separation that is stabilized by the surrounding medium. This S_1* state is most pronounced for **T3SO$_2$T3**. Similar relaxation dynamics are observed for **T3ST3** and **T3SOT3** in acetonitrile: the intermediate S_1* states are formed on comparable time scales (3.4 and 4.7 ps, respectively) but are not as pronounced spectrally.

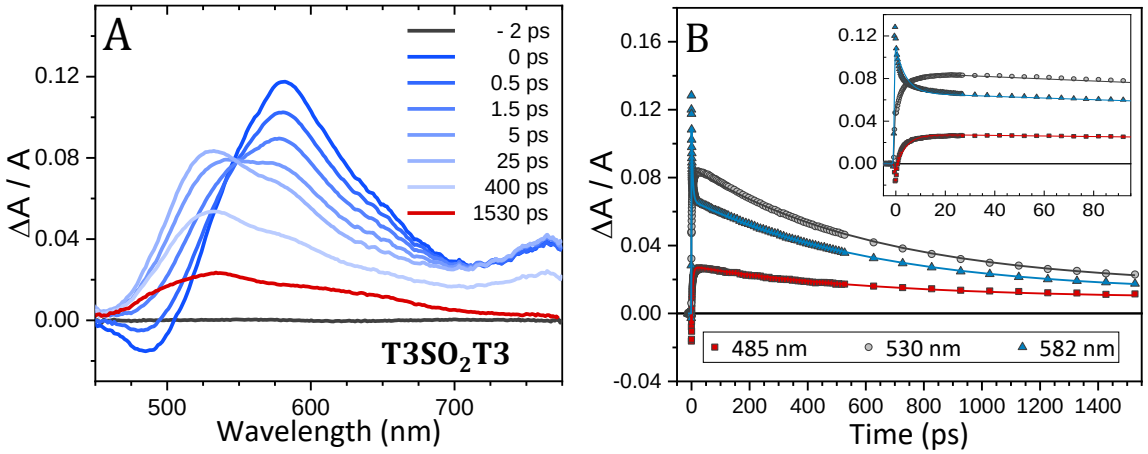

Figure 4.2.8. TA spectral slices in acetonitrile (A) and the corresponding single wavelength traces (symbols) with fits overlaid (lines). The inset shows the early time (100 ps) dynamics (B).

4.2.2 Time-dependent density functional theory calculations

In order to gain insight into the nature of the dimer excited states, time dependent density functional theory (TDDFT) calculations were performed. One concern is that the molecules used in this study are relatively large and incorporate flexible linkers, which could lead to conformational disorder and distributed kinetic behavior. To address this concern, the ground-state potential energy surfaces for bending and torsion of the dimers were computed. In all cases the barriers are substantially higher than the thermal energy, kT. Even though the barriers to rotation are high, the energy difference between rotational conformers (*cis* and *trans*) can be small, which is why both are considered when calculating excitonic energy splittings. The fact that almost all the PL decays and TA data in the preceding section could be fit with a single exponential function provides experimental evidence that the spectroscopic behavior of these conformers must be quite similar. The only exception is the **T3ST3** dimer, which had a minor (~15%) long-lived

component in its fluorescence decays, suggesting that *cis* and *trans* isomers may have different relaxation dynamics in this molecule. Overall, both experiment and theory suggest that conformational disorder does not play a decisive role in the observed dynamics.

The nature of the S_1 and S_1* states are of particular interest and energetics of these states are considered first. Electronic structure calculations indicate that in all cases, the optical excitations correspond to a $\pi \rightarrow \pi^*$, HOMO-to-LUMO transition. Starting with the optimized ground-state geometries, the computed vertical transition energies of **T3** and **T3SO$_n$T3** are in reasonable agreement with the experimental absorption maxima in dichloromethane and properly reflect the relative shift observed when increasing the oxidation state of the linker (Table 4.2.4). The absorption redshift of **T3SO$_n$Me** with respect to **T3** can be rationalized, to a first approximation, as a result of LUMO stabilization due to the bonding interaction of the **T3** fragment with the SO_n bridge. This effect increases with the oxidation state of the sulfur atom in the linker group. Oxidation of the sulfur atom also results in stabilization of the HOMO, but this effect is smaller than the energy lowering of the LUMO. The excited states for all monomer molecules are qualitatively the same, involving a neutral state similar to that of **T3**.

λ_{max} (nm)	T3	T3SO$_2$Me	T3ST3	T3SOT3	T3SO$_2$T3
Experimental	350	370	374	371	410
Calculated	348	362	366	371	380

Table 4.2.4. Experimental absorption maxima and computed vertical excitation energies to the lowest excited singlet state of indicated molecule in dichloromethane solutions. All values are in nm.

When the excited states are calculated for the optimized ground-state geometries of the **T3SO$_n$T3** series, the lowest excited singlet state (S_1) can be described, to a first approximation, as the coupling of local excitons on each of the **T3** fragments. In symmetric dimers, the strength of this electronic interaction can be quantified by the orbital energy gap between the HOMO and HOMO−1 (ΔHOMO), the LUMO and LUMO+1 (ΔLUMO) and the exciton splitting energy Δε (Figure 4.2.9). Table 4.2.5 reports orbital energy differences and computed exciton splitting energies for the *cis* and *trans* conformers of the **T3SO$_n$T3** dimers (Figure 4.2.9).

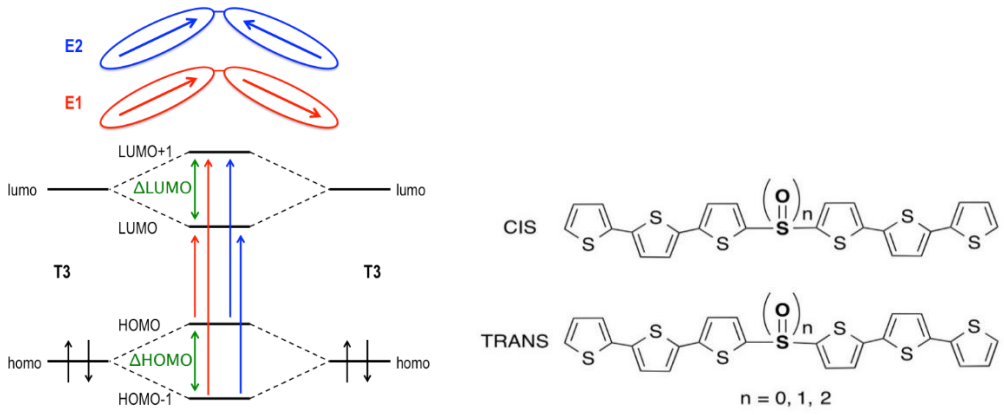

Figure 4.2.9. Molecular orbital diagram of **T3SO$_n$T3** dimers as a result of the interaction between HOMO and LUMO frontier orbitals of two interacting T3 moieties (left). Red and blue arrows correspond to the major electronic excitations in the E1 and E2 excitons, respectively. Structure of the *cis* and *trans* conformers of the **T3SO$_n$T3** dimers (right).

	Parameter	T3ST3	T3SOT3	T3SO$_2$T3
trans	**ΔHOMO** (cm^{-1})	1114	929	1400
	ΔLUMO (cm^{-1})	909	1374	3053
	Δε (cm^{-1})	1057	951	1430
cis	**ΔHOMO** (cm^{-1})	615	835	1784
	ΔLUMO (cm^{-1})	1148	1722	3518
	Δε (cm^{-1})	238	1098	1731

Table 4.2.5. Computed orbital energy gaps ΔHOMO and ΔLUMO, and exciton splitting Δε for the **T3SO$_n$T3** series in dichloromethane. Ground state energy differences between *cis* and *trans* conformers of **T3SO$_n$T3** are in the order of 1 kcal/mol, with the *trans* form being the most stable structure in the three dimers.

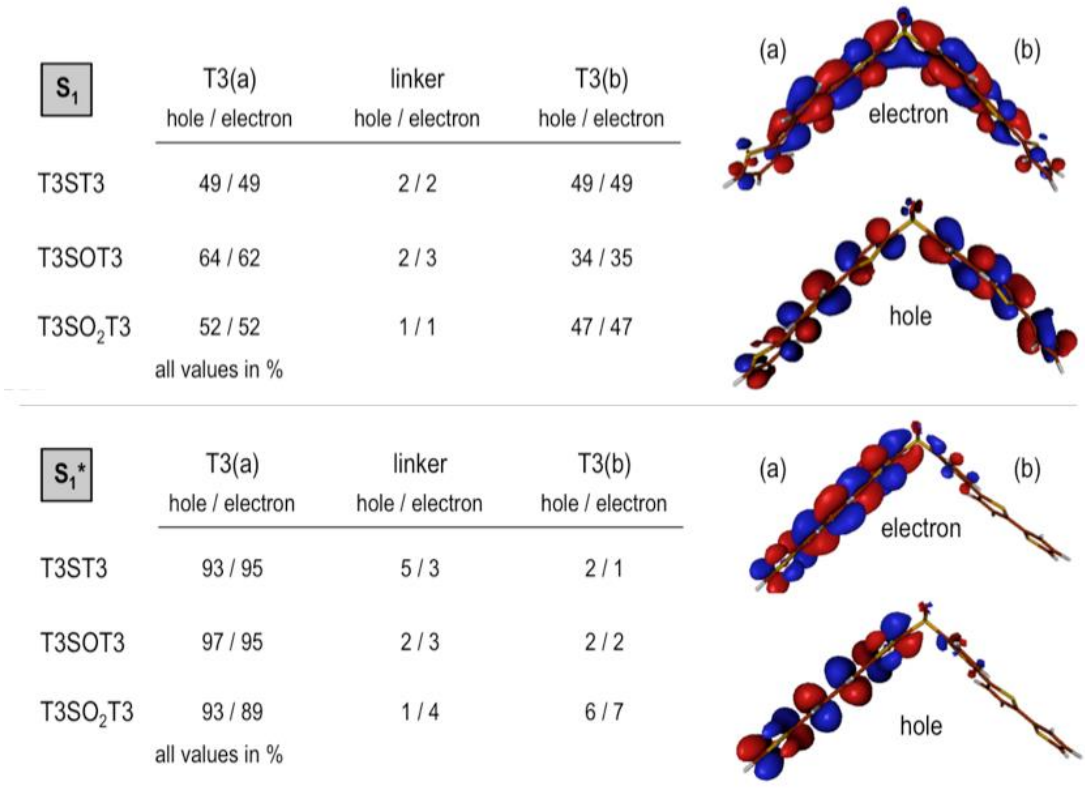

Figure 4.2.10. Fragment localization of the lowest singlet exciton of the **T3SO$_n$T3** dimers in dichloromethane and electron and hole NTOs accounting for 70% of the electronic transition in **T3SO$_2$T3** (top). Fragment localization of the lowest singlet exciton of the **T3SO$_n$T3** dimers for the S_1* optimized geometries in dichloromethane and electron and hole NTOs (bottom). The percentage of hole and electron exciton on each fragment (exciton localization) is obtained through NTO analysis.

For the *cis* conformers, the calculated values follow similar trends as the measured Δε values with respect to sulfur oxidation state, with the strongest exciton coupling obtained for the SO_2 linker. For the *trans* conformers, the **T3SOT3** dimer is the only case where the two **T3** moieties are not equivalent due to the absence of a C_2 axis and there is a deviation from the trend of symmetric dimers. The computed differences in energy for the ground-state *cis* and *trans* conformers are small (less than kT), and it is likely that there is a statistical mixture of these conformers in solution.

When the S_1 excited states of the dimers are examined in detail, several noteworthy features emerge. In all three **T3SO$_n$T3** dimers, the electron−hole pair of the S_1 state fully delocalizes over the two **T3** fragments with minor contributions from the SO_n bridge, as characterized by means of a natural transition orbital (NTO) analysis (Figure 4.2.10, top).[29] Although the S_1 state is delocalized in all three dimers, exciton decomposition in terms of two LE and two CT diabatic states highlights the distinctive nature of the S_1 state in **T3SO$_2$T3** with respect to **T3ST3** and **T3SOT3**. The lowest exciton for the S and SO bridged dimers exhibits strong neutral character with ≤5% of CT participation, but in **T3SO$_2$T3** CT contributions account for 35% of the wave function (Table 4.2.6). The energy gap between the lowest neutral and CT states in **T3ST3** and **T3SOT3** is ∼1.0 eV, while it reduces to ∼0.5 eV for **T3SO$_2$T3**. This leads to neutral-CT couplings that are much larger for **T3SO$_2$T3**. It is important that due to the symmetry of the dimers, opposite CT contributions in these species are degenerate (charge resonance,

CR), resulting in no net electron transfer between **T3** moieties. This could explain the weak dependence of the absorbance peak with solvent polarity.

	Parameter	T3ST3	T3SOT3	$T3SO_2T3$
Optimized Geometry	**% CT**	5	1	35
	ΔE (eV)	1.00	0.95	0.53
	Neutral-CT Coupling (meV)	149	41	429
$T3SO_2T3$ Geometry	**% CT**	7	8	35
	ΔE (eV)	0.98	0.79	0.53
	Neutral-CT Coupling (meV)	238	269	429

Table 4.2.6. Computed CT contributions, energy gap between the lowest neutral and CT diabatic states and their absolute electronic coupling for the S_1 state in the **$T3SO_nT3$** series at their optimized and **$T3SO_2T3$** like geometries.

Experimentally, absorption to S_1 does not involve a large change in the net dipole moment, but geometrical relaxation to S_1* clearly does, as evidenced by the strong solvatochromism of this state. In order to gain insight into the formation of the S_1* state, the electronic structure of each dimer was calculated after allowing them to fully relax in their first excited state (Table 4.2.7). The molecular relaxation on the S_1 potential energy surface localizes the exciton onto one of the **T3** fragments for all **$T3SO_nT3$** molecules. Comparing the S_1 state (Figure 4.2.10, top) to the S_1* state (Figure 4.2.10, bottom) shows that relaxation induces a symmetry breaking where one of the **T3** chromophores planarizes, localizing the charge and collapsing the CR state.[30-32] The bottom panel of Figure 4.2.10 shows that there is now a net partial electron transfer to the other **T3**. The

S_1* state thus has a net dipole and can be thought of as a true CT state. Surprisingly, the overall CT contribution at the S_1* optimized geometry of **T3SO$_2$T3** in dichloromethane is on the order of 25%, slightly lower in comparison to the 35% computed at the ground-state geometry (Table 4.2.8). However, the most important difference is that in the ground-state geometry, the CT character is symmetrically shared between the two **T3** fragments, while in the S_1* structure 22% is localized on one **T3** fragment and 3% on the other.

		T3ST3	**T3SOT3**	**T3SO$_2$T3**	**T3SH$_4$T3**	**T3SF$_4$T3**
Charge	bridging S	0.351	1.383	2.269	0.655	2.322
	X	-	-1.023	-0.985	-0.003/0.021	-0.518/-0.510
Electron Occupancy	3p	3.99	3.06	2.50	3.85	2.37
	$3p_x$ / $3p_z$	1.82 / 1.27	1.14 / 1.03	0.72 / 0.85	1.37 / 1.23	0.66 / 0.82
	$3p_y$	0.89	0.89	0.93	1.25	0.90

X = O, H, F

Table 4.2.7. Atomic charges and electron occupancies of $3p_x$, $3p_y$ and $3p_z$ bridging sulfur atom (S) orbitals at the SO_n, SH_4 and SF_4 bridges obtained from NBO analysis at the CAM-B3LYP/6-31+G(d) level in dichloromethane. X = O, H, F.

The CR/CT character of the S_1* state provides a qualitative explanation for the longer fluorescence lifetimes of the dimers. In **T3**, the lowest excited singlet decays rapidly to a high-lying triplet state which has been variously assigned as T_2 or T_4.[28,33,34] This state then internally converts to the lowest triplet state T_1 on a subpicosecond time

scale. ISC limits the fluorescence quantum yield of **T3** to 5% or less in solution. In the dimers, the calculations indicate that the triplet levels on separate **T3** chromophores combine to form new excitonic states. These new excitonic states are denoted T_1 and T_1' (from mixing the original T_1 states on different **T3** moieties), while T_2 and T_2' arise from mixing the original T_2 states on different **T3** moieties. The excitonic T_1, T_1', T_2, and T_2' triplet states are all close in energy to the S_1/S_1* states, and calculations indicate that all these states have predominantly neutral character. Due to the one electron nature of the spin−orbit operator, CT contributions to S_1/S_1* cannot couple to the neutral terms in the triplet-state wave functions. If the S_1 state in the dimer has a pure neutral character, the ISC rate should be similar to that of **T3**. Increasing the CR/CT character of S_1/S_1* should lead to less effective singlet−triplet coupling and less efficient ISC. This reasoning has also been used to rationalize the decreased ISC rates in oligothiophenes[23,28] and helps explain the increased fluorescence as the sulfur linker is oxidized from S to SO to SO_2. The ISC rate in the dimeric species also decreases with increasing solvent polarity from cyclohexane to dichloromethane. This behavior can again be rationalized in terms of increased CT mixing in the lowest exciton. This trend of increasing CT state mixing does not explain the shorter PL lifetime in acetonitrile, however. It is likely that other factors affect the lifetime of the S_1* state in highly polar solvents, for example, the smaller S_0-S_1* and S_1*$-T_1$ energy gaps that could facilitate more rapid internal conversion or ISC.

	Parameter	Cyclohexane	Dichloromethane	Acetonitrile
S_0 Geometry	**% CT**	31	35	36
	Δ E (eV)	0.570	0.534	0.531
	Coupling (meV)	383	429	439
S_1 Geometry	**% CT**	21	24	25
	Δ E (eV)	0.783	0.769	0.760
	Coupling (meV)	398	507	531

Table 4.2.8. Computed CT contributions, energy gap between the lowest LE and CT diabatic states (ΔE) and their absolute electronic coupling for the ground and lowest excited state of the **T3SO$_2$T3** dimer in acetonitrile, dichloromethane and cyclohexane solvents.

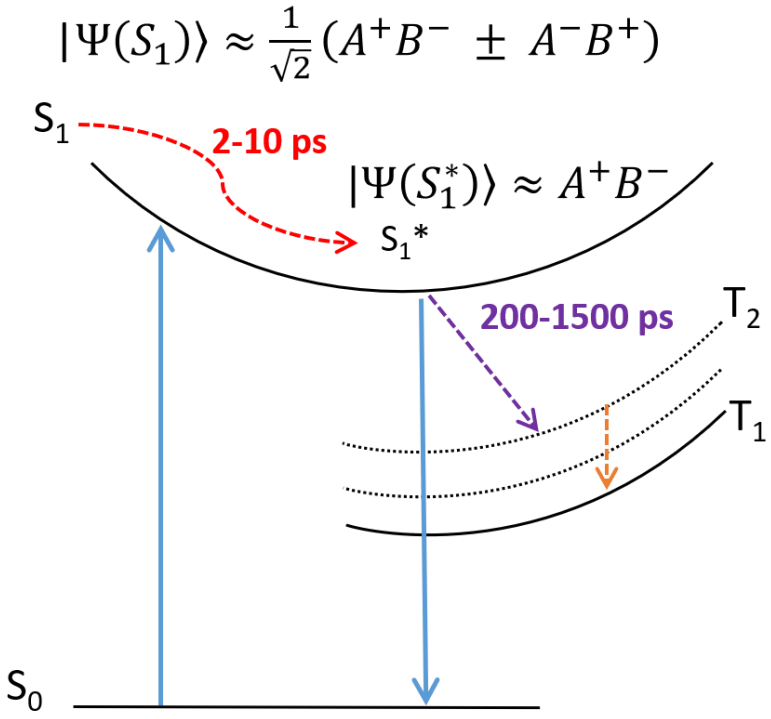

Figure 4.2.11. Schematic illustration of excited state relaxation in the dimers. Note that the S_1 and S_1* states are in general superposition states with contributions from both charge transfer and neutral states. We show the dominant charge transfer terms to emphasize the symmetry breaking between the two states.

The overall picture of the excited-state dynamics that emerges is summarized schematically in Figure 4.2.11. Photoexcitation leads to an excitonic S_1 state with symmetric CR character that relaxes rapidly (<10 ps) to an asymmetric S_1* state with strong CT character. Although the excited-state structure of the dimers is mapped out in this work, the question remains as to how the oxidation state of sulfur controls the amount of CT character. Below, two possible mechanisms are considered.

One mechanism by which the sulfur oxidation state could affect the electronic coupling is through inducing changes in the dimer geometry. To investigate the impact of the molecular geometry on the S_1 state, the **T3ST3** and **T3SOT3** dimers were constrained to adopt the **T3SO$_2$T3** optimized geometry (Table 4.2.6), and their lowest electronic transitions were analyzed. The results obtained for these models, both regarding the CT character of the electronic transition and the neutral-CT energy difference, are similar to the values obtained for **T3ST3** and **T3SOT3** with their own optimized geometries. That is to say, changes in the **T3SO$_2$T3** geometry cannot explain the enhanced CT character of the S_1 state. Moreover, the data in Table 4.2.6 show that when the relative arrangement of the two **T3** units is fixed, a clear correlation between the exciton splitting $\Delta\varepsilon$ and the oxidation state of the sulfur atom in the linker emerges (one that follows the experimental data closely).

A second possible mechanism for the changes in electronic coupling involves different Coulombic interactions. A major electronic structure difference between the SO_2 bridge and the S and SO linkers is the absence of sulfur lone pairs in the former. To

investigate this difference in more detail, the electronic structure at the SO_n linkers in the $T3SO_nT3$ dimers are evaluated by means of a natural bond orbital (NBO) analysis.[35] Table 4.2.7 summarizes the most relevant results obtained. The charge of the bridging sulfur atom increases with oxidation state, while the oxygen charge remains almost constant. This behavior is a consequence of the strong polarity of the SO bonds toward the oxygen atom, as indicated by the decrease in the electronic occupation of p orbitals involved in the SO bonds ($3p_x$ and $3p_z$) and constant occupation of the p orbital oriented in the perpendicular direction ($3p_y$). In other words, the oxygen atoms pull electron density away from the sulfur atom in the bridge. These results are in line with a study of the nature of bonding in SO and SO_2 systems by Chesnut and Quin.[36]

To further explore the impact of the electronic configuration of the sulfur atom in the bridge, the neutral-CT mixing and electronic couplings were computed for two additional **T3** dimers, **T3SH$_4$T3** and **T3SF$_4$T3**. As in the SO_2 case, the SH_4 and SF_4 linkers lack electron lone pairs on the sulfur atom, but they represent very different situations with respect to the polarization of the SX bonds. NBO analysis shows that the electron occupation of the 3p level of the sulfur atom in SH_4 (3.85 electrons) is of the same magnitude as that in **T3ST3**, while in **T3SF$_4$T3** the electron density is polarized toward the fluorine atoms (2.37 electrons in the 3p level). As a result, **T3SH$_4$T3** exhibits strong electronic screening, similar to that in the **T3ST3** dimer, while the neutral-CT mixing and coupling obtained for the SF_4 linker is similar to that of the SO_2 bridge (4.2.12). Decreased CT coupling was also observed when the linker was changed to an O atom, which has lone

pairs, while a CH_2 linker (with no lone pairs) resulted in a CT coupling comparable to the SO_2 linker. These results suggest that the electronic configuration of the sulfur atom in the SO_n bridge is the key factor that can suppress or enhance the neutral-CT mixing. In particular, the presence of electron lone pairs in the bridge can screen Coulombic interactions between **T3** moieties and suppress intradimer electronic coupling that stabilizes delocalized CR states. The polarization of the SO bonds also has a major role in this mechanism and that in SX_4 linkers, with formally no available electron lone pairs on the sulfur atom, polarization of the SX bonds dictates the screening strength of the electronic interactions between the **T3** moieties.

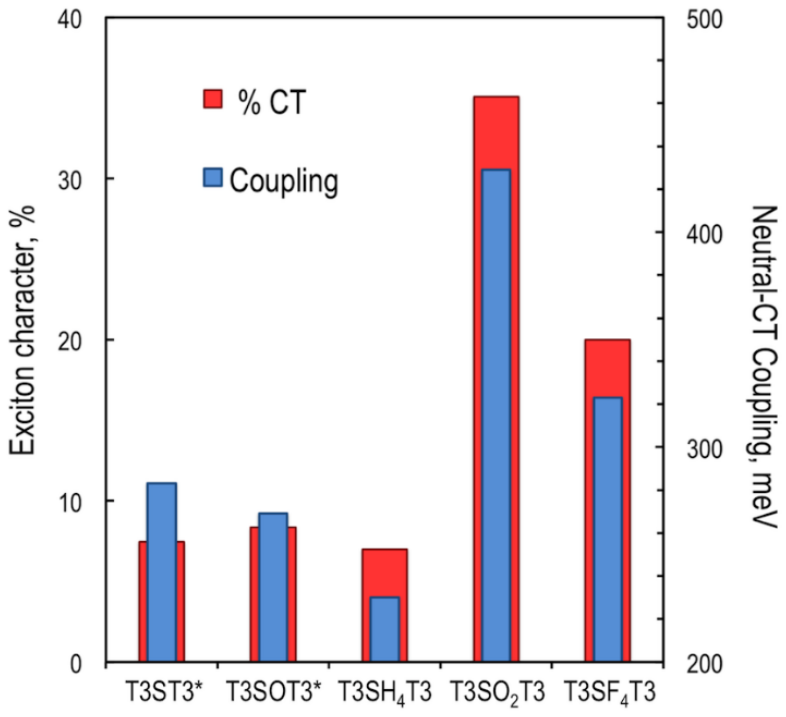

Figure 4.2.12. Exciton character as contributions (in %) of CT diabatic states to S_1 transition (red wide bars) and neutral-CT couplings (blue thin bars) for the **T3SO$_2$T3**, **T3SH$_4$T3** and **T3SF$_4$T3** dimers, and the **T3ST3*** and **T3SOT3*** molecular models obtained at the CAM-B3LYP/6-31+G(d) computational level in dichloromethane.

4.2.3 Electron density on the bridge dictates the photophysics of the terthiophene dimers

The first important point of this work is that the sulfur bridge itself has only a minor effect on the behavior of the molecule. For example, in the **T3SO$_n$Me** monomers, the presence of the additional sulfur functionality leads to a slight (~20 nm) redshift of the absorption spectrum in the monomer series (**T3SO$_n$Me**) relative to unsubstituted **T3**, while the overall shape of the spectrum remains largely unchanged. The PL lifetime (τ_{PL}) of the **T3SO$_2$Me** monomer is nearly identical to that of unsubstituted **T3** (~200 ps). The **T3SO$_n$Me** monomer series exhibits very similar features in the TA data to that of **T3**. As in **T3**, the excited state of the monomers evolves from an S_1 state with predominantly neutral character to T_1 through ISC. The addition of a second **T3** chromophore generates qualitative changes in the electronic structure and photophysics of the dimers. The appearance of a splitting in the dimer absorption is a clear indication that interaction between the two absorbing units has an important role in the excited-state dynamics. The solvatochromism in the steady-state fluorescence behavior of the dimers, which is absent in the monomers, indicates stabilization of a polarized CT excited-state, denoted S_1*, that is present only in the S-bridged dimers. This CT state leads to a fluorescence lifetime and quantum yield for the dimer (**T3SO$_2$T3**) that are significantly greater than those of **T3SO$_2$Me** or unsubstituted **T3**.

The second major finding is the dynamic nature of the S_1* state, which is formed within 10 ps, consistent with relaxation via symmetry breaking. The ability of an initially delocalized system to relax into an asymmetric charge distribution is an interesting

fundamental process[37] and has been characterized in several types of multichromophoric systems,[30,32,38-41] including bianthryl.[31] Common features in the photophysics of this class of molecules include the shift of the CT emission with solvent polarity, with no shift in absorption, and the rapid relaxation from the neutral absorption state to the CT emitting state. However, there are also some notable differences between these sulfur-bridged dimers and the prototypical bichromophore, bianthryl. In bianthryl, the absorption spectrum closely resembles that of monomeric **An**. The initial excited state of bianthryl is assumed to be localized on one of the **An** chromophores and is referred to as the "locally excited" (LE) state. In the **T3** dimers, the two chromophores have significant interactions even in the ground-state configuration, as evaluated from the changes in the absorption spectra. This is likely the result of the following: the larger transition dipole moment of the **T3** chromophore, the sulfur bridge orienting the transition dipole moments of the chromophores at an oblique angle, and more facile electron-transfer interactions through the bridge. Strong interchromophore interactions are in a sense built into these sulfur-bridged dimers. A second major difference is that **T3**, unlike **An**, has a very low fluorescence quantum yield to begin with due to rapid ISC. Typically, the quantum yield of dimeric **An** decreases relative to the monomer due to the lower radiative rate of the dimer CT state.[42,43] In the **T3** dimers, the lower ISC rate in the CT state more than compensates for the decrease in radiative rate, and the fluorescence quantum yield increases by an order of magnitude for **T3SO$_2$T3** in dichloromethane.

The most obvious difference between the sulfur-bridged dimers and bianthryl is the ability to tune the amount of electronic coupling by changing the oxidation state of the bridging sulfur. The computational results indicate that the electron lone pairs present in the S and SO bridges screen the interaction between the π electrons from the two **T3** chromophores. Oxidation of the sulfur atom to form the sulfone (SO_2) linker leads to polarized bonds that decrease this screening, stabilizing the CT contributions that mix with the neutral states. It might naively be expected that greater electron density on the sulfur would facilitate electronic communication between the **T3** chromophores, but the results show that the opposite occurs. The role of solvent in screening electrostatic interactions between different regions of molecules that undergo electron transfer has been the subject of theoretical attention,[44,45] but the possibility that the polarization of the bridge valence electrons can modulate interchromophore electronic interactions has not been a significant focus.[46] Both the experimental and computational results provide evidence that the electron distribution on the bridging atom can suppress the electrostatic interactions that stabilize a luminescent CT state, suggesting that this may be an effective strategy to explore in molecular design.

The ability of the SO_2 linker to facilitate the formation of CT states may explain its utility in chromophores that exhibit thermally activated delayed fluorescence (TADF), where CT interactions lead to small exchange energies and near degeneracy of the singlet and triplet states.[47,48] Oxidizing the sulfur in polythiophenes has also been shown to be an effective way to modulate the polymer bandgap,[49] most likely due to the creation of

extended CT states. These results provide an explanation for previous observations and, furthermore, show that formation of CT states can suppress ISC and lead to higher fluorescence quantum yields.

While enhancement of CT interactions led to a high PL yield in the **T3** dimers, it is possible that this approach can be used in other systems to suppress CT formation. For example, if the chromophore neutral states are highly emissive (i.e., not subject to rapid ISC), then one would want to avoid CT mixing that lowers the radiative rate. To make a superradiant assembly of such chromophores,[50] one would want to use the unoxidized S linker in order to prevent CT state formation. Another application for tuning the amount of CT interaction would be to optimize singlet fission. There is general agreement that efficient singlet fission requires some CT interaction,[51-54] but too much CT character can lead to excimer formation that competes with the fission channel. Although these examples are somewhat speculative, they serve to illustrate how controlling interchromophore interactions in covalent assemblies could be useful for the design of functional supermolecules.

4.2.4. Enhanced excited state CT character in the terthiophene bichromophores leads to behavior that is greater than the sum of its parts

Through the combination of spectroscopy and computation a comprehensive picture of the photodynamics of sulfur-bridged terthiophene dimers has been obtained. Their novel excited-state behaviors (high PL quantum yields, solvatochromism, two-step excited-state relaxation) stem from the formation of a delocalized CR state (S_1) that

relaxes quickly (<10 ps) to a CT state (S_1*). The amount of CT in S_1 and S_1* can be modified by changing the oxidation state of the bridging sulfur group. Computational work indicates that electrostatic screening by the sulfur valence electrons is the key parameter that controls the amount of CT participation. The results presented in this paper provide a new strategy for tuning interchromophore interactions in covalent dimers.

4.3 Sulfur-bridged symmetric and phenyl-terminated anthracene assemblies

4.3.1. Steady-state and time-resolved spectroscopy

The steady state absorption spectra of **An-S-An**, **An-S-Ph**, **An-SO_2-An** and **An-SO_2-Ph** (molecular structures shown in Figure 4.3.1) in cyclohexane are shown in Figure 4.3.2. The absorption spectra of all sulfur-bridged anthracenes display vibronic structure which is reminiscent of unsubstituted **An**. The enhanced relative intensity of the 0-0 vibronic peaks in both the **An**-terminated dimers indicates the presence of excitonic interaction between chromophores.[11] This enhancement of the 0-0 peak is more pronounced for **An-S-An** than for **An-SO_2-An**, which also undergoes a 20 nm redshift that is not observed for the oxidized species. The absorption redshift and 0-0 peak enhancement is indicative of J-type excitonic coupling in **An-S-An**. For all compounds, the absorption spectra are relatively insensitive to solvent polarity, with acetonitrile and CH_2Cl_2 causing only a slight broadening of the spectra.

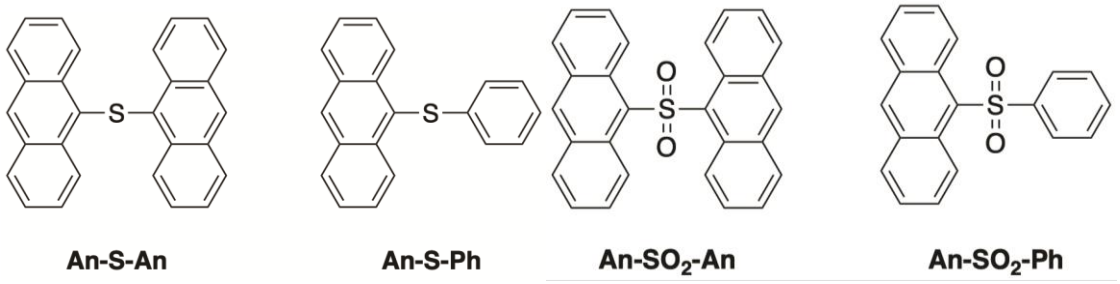

Figure 4.3.1. Molecular structures of the compounds used in this study.

The steady-state photoluminescence (PL) of the phenyl-terminated (**Ph)** compounds is measured in cyclohexane, CH_2Cl_2 and acetonitrile after 400 nm excitation. The PL spectra for the **An-SO$_x$-An** compounds are extracted from the time-resolved measurements in order to avoid a long-lived impurity emission that contaminated the steady-state spectra reported in earlier reports.[55] The PL spectrum of **An-S-Ph** peaks at 420 nm in cyclohexane with a small shoulder present at 440 nm (Figure 4.3.2A). In solutions of CH_2Cl_2 and acetonitrile, the spectra are featureless and red-shift slightly ~20 nm (Figure 4.3.3A). When the **Ph** group is replaced by **An**, the PL of **An-S-An** in cyclohexane has a strong, featureless PL centered at 475 nm (Figure 4.3.2A). This feature red-shifts to ~540 nm and ~560 nm in CH_2Cl_2 and acetonitrile respectively (Figure 4.3.3C), suggesting that the emissive state possesses significant CT character. The PL spectrum of **An-SO$_2$-Ph** in cyclohexane is similar to that of **An-S-Ph** (Figure 4.3.2B), again broadening in polar solvents and shifting to lower energies (Figure 4.3.3D). However, when the **Ph** group is replaced by **An**, the high sensitivity to the second chromophore and solvent polarity is not observed. Unlike the S-bridge, the PL spectra of **An-SO$_2$-An** barely shifts with solvent polarity, although a slight broadening of the spectra is observed in CH_2Cl_2

and acetonitrile (Figure 4.3.3B). The spectra retains much of the structure observed in the cyclohexane spectrum and the broadened red portions seen in the polar solvents are likely due to a species with some CT character in the excited state as they resemble excimer PL observed in methyl bridged anthracene dimers.[56]

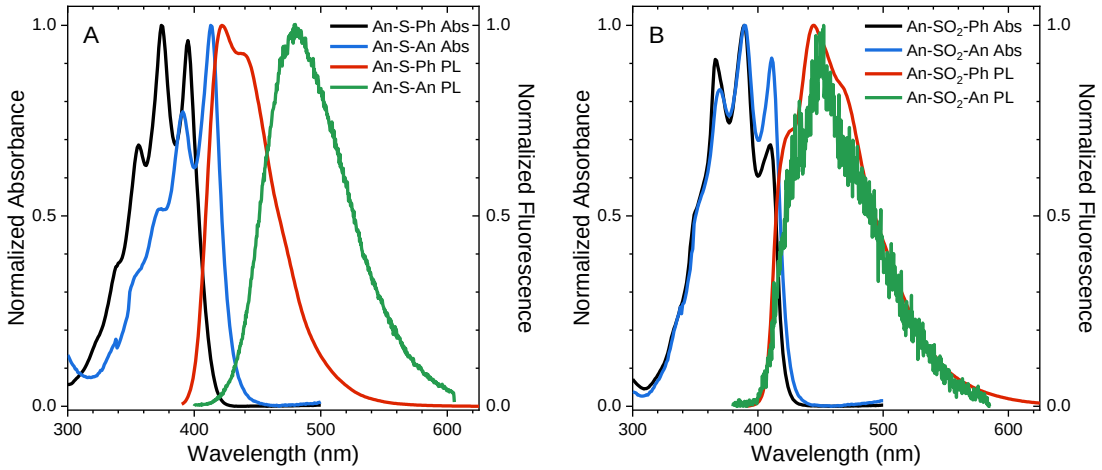

Figure 4.3.2. The steady state absorption and PL spectra of the S-bridged (A) and SO_2-bridged (B) monomers in dilute solutions of cyclohexane. The PL spectra shown for the **An-SO_x-An** dimers are from the time-resolved measurements. All PL spectra were recorded after 400 nm excitation.

The different behaviors observed in the steady-state spectra suggest that there are significant differences between the S- and SO_2-bridged compounds. These differences become even more pronounced when the time-resolved data is analyzed. For this reason, in the following sections the dynamic behavior of the S- and SO_2-bridged compounds are analyzed separately before comparing them theoretically.

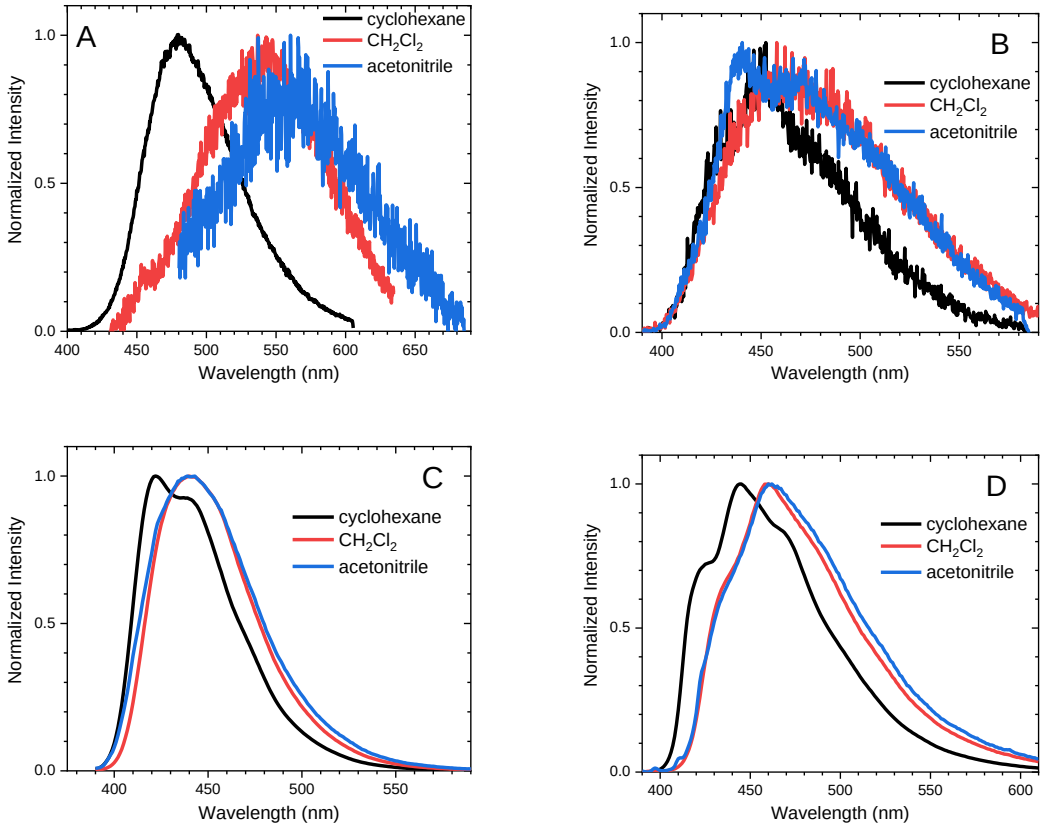

Figure 4.3.3. The normalized PL spectra of **An-S-An** (A) and **An-SO_2-An** (B) in dilute solutions of cyclohexane (black), CH_2Cl_2 (red), and acetonitrile (blue). The steady-state PL spectra of **An-S-Ph** (C) and **An-SO_2-Ph** (D).

*4.3.2 Excited state dynamics of **An-S-Ph** and **An-S-An**.*

Excited state relaxation in unsubstituted **An** is caused by a combination of intersystem crossing (ISC), internal conversion, and radiative relaxation.[57] ISC in anthracene is efficient (~70% triplet quantum yield) and contributes to a relatively short PL lifetime of ~4 ns.[57] The addition of the **S-Ph** moiety leads to shorter PL lifetimes of 1.4 ns in cyclohexane, 300 ps in CH_2Cl_2 and 130 ps in acetonitrile (Figure 4.3.4A). Replacing the **Ph** by **An** quenches the PL more effectively with PL lifetimes of 400 ps in cyclohexane, 120 ps in CH_2Cl_2 and 90 ps in acetonitrile (Figure 4.3.4B). The decays are mono-

exponential at earlier times, with a slight deviation at later times caused by residual fluorescent impurities (Figure 4.3.5). For both S-bridged dimers, the solvent-dependent PL lifetimes suggest that an excited state with some CT character undergoes much more rapid nonradiative relaxation than monomeric **An**.

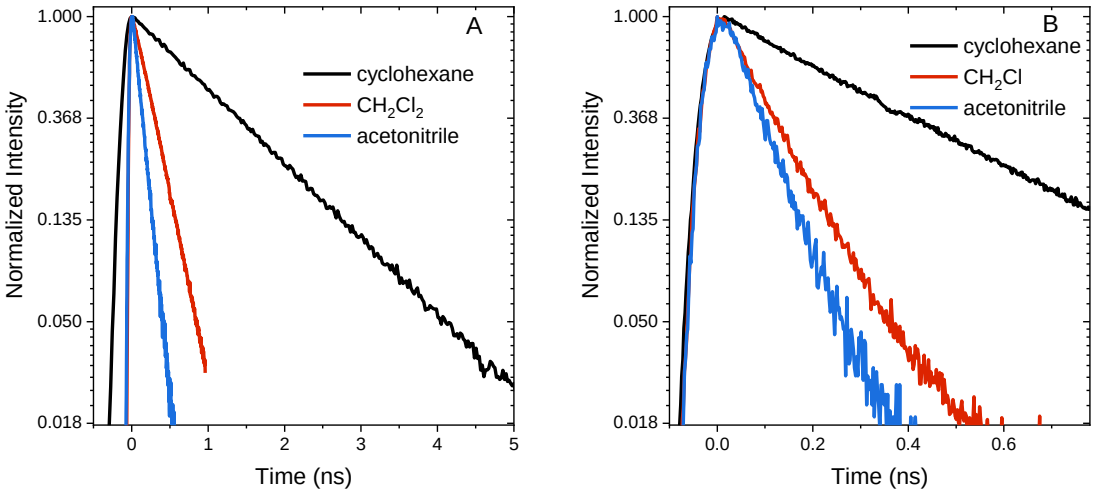

Figure 4.3.4. Normalized PL time traces on a natural log scale for **An-S-Ph** (A) and **An-S-An** (B) in cyclohexane, CH_2Cl_2, and acetonitrile. These figures show that the PL lifetime decreases with increasing solvent polarity for both **An-S-Ph** and **An-S-An**, and the second anthracene chromophore induces a more rapid decay than the phenyl terminated molecules in any solvent.

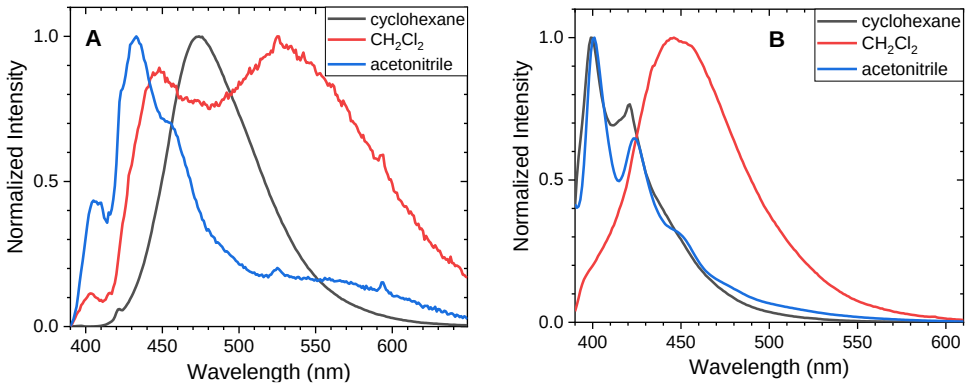

Figure 4.3.5. Steady-state emission spectra of An-S-An (A) and An-SO_2-An (B) excited at 375 nm. Due to the inherent sensitivity of emission spectroscopy residual impurities can be identified in the emission spectra which are absent in the absorption spectra. The features between 390 – 420 nm overlap the absorption spectra of the dimers (Figure 1) indicating that the origin of these features is an impurity. The most likely culprit is an anthracene derivative used during the synthesis of the dimers. Using time-resolved emission spectroscopy, the impurity emission can be windowed out of the analysis.

Femtosecond transient absorption (fs-TA) can help elucidate the mechanism which leads to rapid PL quenching in the S-bridged molecules. The behavior of all S-bridged compounds is similar. A representative example of the TA data is shown in Figure 4.3.6A for **An-S-An** in acetonitrile. At early times, a broad positive feature centered at ~600 nm is assigned to the singlet $S_1 \rightarrow S_N$ induced absorption. By 30 ps a new positive feature emerges at ~430 nm, similar to the triplet $T_1 \rightarrow T_N$ feature observed in **An** and its derivatives.[58-60] By 100 ps the $T_1 \rightarrow T_N$ feature dominates the spectrum while the singlet absorption has decayed. In cyclohexane and CH_2Cl_2 the same features emerge in the TA spectra, but the triplet transition appears more slowly, mirroring the trend found in the PL decays (Figure 4.3.7). In all solvents, a clear isosbestic point between the singlet and triplet induced absorptions is seen, indicating that a population transfer is occurring between these two well-defined electronic states. A global analysis of the TA data for both **An-S-An** and **An-S-Ph** yields a fit that best describes the data with two species associated spectra. One spectrum corresponds to the singlet feature which decays with a lifetime closely matching the PL lifetime. The second spectral component has an extremely long lifetime and represents the triplet feature which does not decay during the experiment. An example of this fitting of the fs-TA decays is shown in Figure 4.3.6B. For all the S-bridged compounds, ISC appears to be the dominant mechanism that removes the S_1 population.

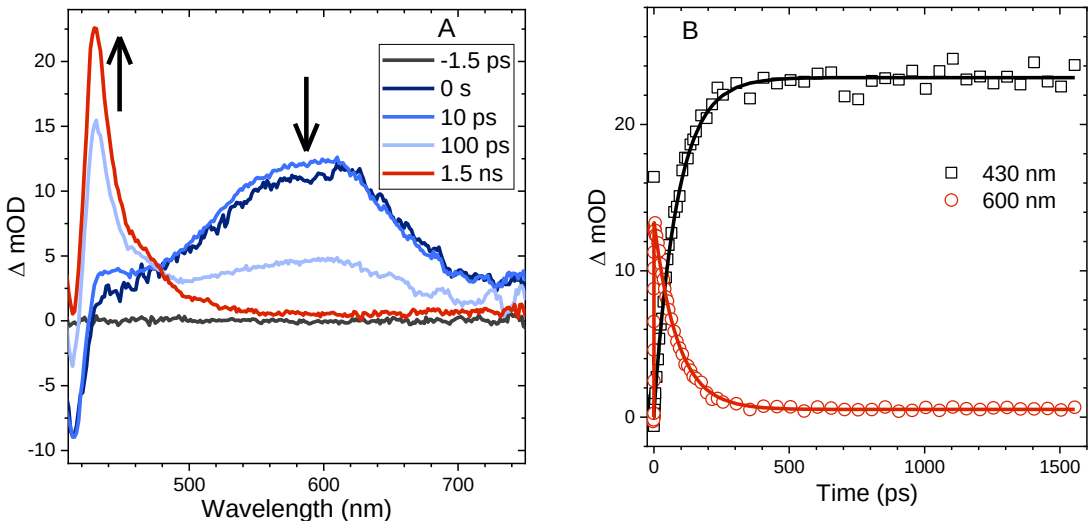

Figure 4.3.6. (A) TA spectra of **An-S-An** in acetonitrile showing singlet induced absorption at early times (600 nm) and a ground state bleach (420 nm). At later times, the triplet induced absorption is the dominant feature (430 nm). An isosbestic point is observed between the singlet and triplet features. (B) Kinetic traces corresponding to the singlet induced absorption (600 nm, red circles) and the triplet induced absorption (430 nm, black squares). Both traces are fit with an exponential function (solid lines) having a time constant of 87 ps consistent with the PL lifetime.

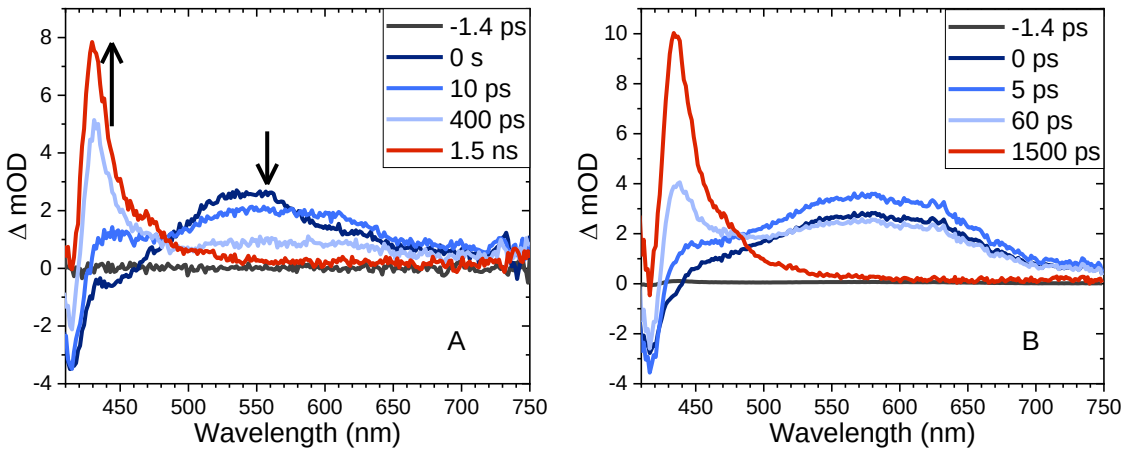

Figure 4.3.7. The transient absorption spectra of **An-S-An** in cyclohexane (A) and CH_2Cl_2 (B). Similar features which are described in Figure 4.3.6 are observed albeit on different timescales.

The relaxation constants measured for **An-S-Ph** and **An-S-An** in the different solvents are summarized in Table 4.3.1. For all compounds, the time constants obtained from independently fitting the PL decays and the fs-TA evolution are the same to within 10%. This good correspondence indicates that we are not missing an important relaxation channel in our analysis. In all the S-bridged compounds, singlet state relaxation is dominated by ISC and we assume that the singlet decay rate reflects the ISC rate k_{ISC}. The increase in k_{ISC} with increasing solvent polarity for **An-S-An** and **An-S-Ph** is shown in Figure 4.3.8. Qualitatively, this behavior is consistent with the involvement of a singlet state that is stabilized in polar solvents and by the presence of a larger, more polarizable chromophore. These trends, combined with the fluorescence spectra in Figure 4.3.2A, suggest that the singlet state has appreciable CT character. As the energy of this state decreases, it moves closer to the low-lying triplet of **An** and presumably facilitates ISC. Note that if the bridging S atom was merely an innocent bystander that only contributed to electronic screening of the **An-An** interaction (i.e. analogous to the **T3** system) we would expect **An-S-Ph** and **An-S-An** to exhibit behavior like monomeric **An**. The large deviations already indicate that the **An** dimer system behaves differently from the **T3** system.

		cyclohexane	CH_2Cl_2	acetonitrile
An-S-Ph	PL (ps)	1390 ± 5	303 ± 5	132 ± 3
	TA (ps)	1743	280 ± 110	136 ± 97
An-S-An	PL (ps)	407 ± 5	118 ± 2	87 ± 2
	TA (ps)	416 ± 153	128 ± 24	84 ± 16
An-SO_2-Ph	PL (ps)	3560 ± 6	229 ± 2	130 ± 2
	TA (ps)	> 1500	226 ± 6	144 ± 13
An-SO_2-An	PL (ns)	11.2 ± 0.12	16.8 ± 0.5	10.9 ± 0.03
	TA (ps)	NA	23.8 ± 0.7	19.6 ± 0.3

Table 4.3.1. Excited singlet state lifetimes of each molecule determined from a single exponential fit of the photoluminescence (PL) and transient absorption (TA) time traces. The S-bridged molecules show good agreement between the different methods. The lifetimes for **An-SO_2-Ph** and **An-S-Ph** in cyclohexane are too long to be accurately determined from the TA data. The PL lifetimes for **An-SO_2-An** correspond to the long-lived emission, while the TA lifetimes correspond to the bleach recovery at 400 nm. A reliable bleach recovery lifetime for **An-SO_2-An** in cyclohexane could not be determined.

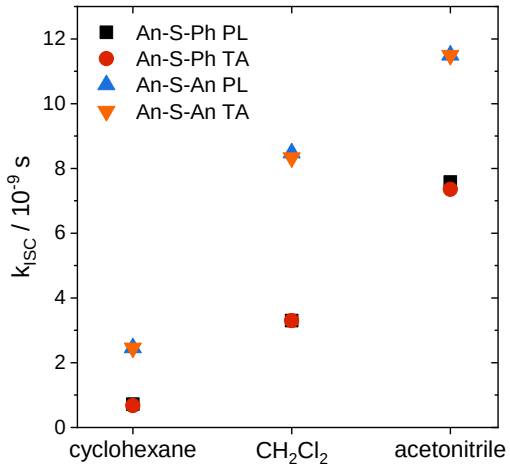

Figure 4.3.8. Intersystem crossing rates (k_{ISC}) as a function of solvent polarity (cyclohexane, ε = 2.02; CH_2Cl_2, ε = 8.93; acetonitrile, ε = 36.64)[61] for **An-S-Ph** calculated from the PL lifetimes (black squares) and TA lifetimes (red circles) compared with the rates for **An-S-An** calculated from the PL lifetimes (blue up triangles) and TA lifetimes (orange down triangles). Intersystem crossing is faster in more polar solvents and faster for **An-S-An** than for **An-S-Ph**.

*4.3.3 Excited state dynamics of **An-SO$_2$-Ph** and **An-SO$_2$-An**.*

The SO_2-bridged compounds (**An-SO$_2$-Ph** and **An-SO$_2$-An**) behave similarly to the S-bridged compounds in that their PL decays also depend on solvent polarity. The PL time traces of **An-SO$_2$-Ph** are mono-exponential with lifetimes of 3.6 ns in cyclohexane, 230 ps in CH_2Cl_2 and 130 ps in acetonitrile (Figure 4.3.9A). However, the PL time traces for **An-SO$_2$-An** are biexponential in all solvents, with a prompt decay component that cannot be resolved within the instrument response function of the streak camera. The long-lived tail of the decay has the same emission spectrum as the prompt component but with a lifetime on the order of 10 ns, accounting for roughly 50% of the total decay amplitude (Figure 4.3.9B).

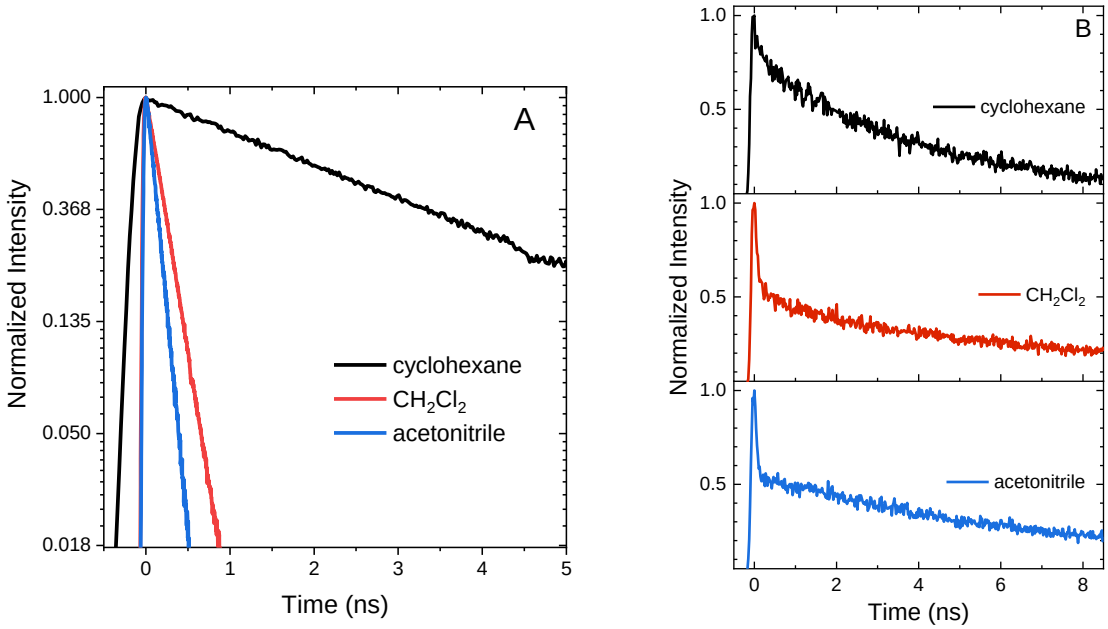

Figure 4.3.9. Normalized PL time traces integrated over all wavelengths for (A) **An-SO$_2$-Ph** shown on a natural log scale and (B) **An-SO$_2$-An** in cyclohexane, CH_2Cl_2, and acetonitrile.

The relaxation of the singlet state for the SO_2-bridged compounds is much faster than that observed for **An** or the S-bridged compounds, but ISC is not the culprit in this case. In the TA spectra of **An-SO$_2$-Ph**, only a short-lived $S_1 \rightarrow S_N$ feature is observed in each solvent (Figure 4.3.10). In polar solvents there is a slight blue shift of the $S_1 \rightarrow S_N$ feature, but it disappears on the same time scale as the PL lifetime. No signature $T_1 \rightarrow T_N$ features appear as the singlet disappears, which indicates that ISC does not play a major role. When probed at 400 nm, the recovery of the ground state absorption mirrors the PL decay, as the comparison in Figure 4.3.11 shows. This correlation suggests that internal conversion to the ground state must be the nonradiative pathway that quenches the PL. The rate of internal conversion becomes more rapid as the solvent polarity is increased. This type of solvent polarity enhanced internal conversion has been previously reported for carotenoid derivatives and was attributed to an excited singlet with some CT character.[62,63]

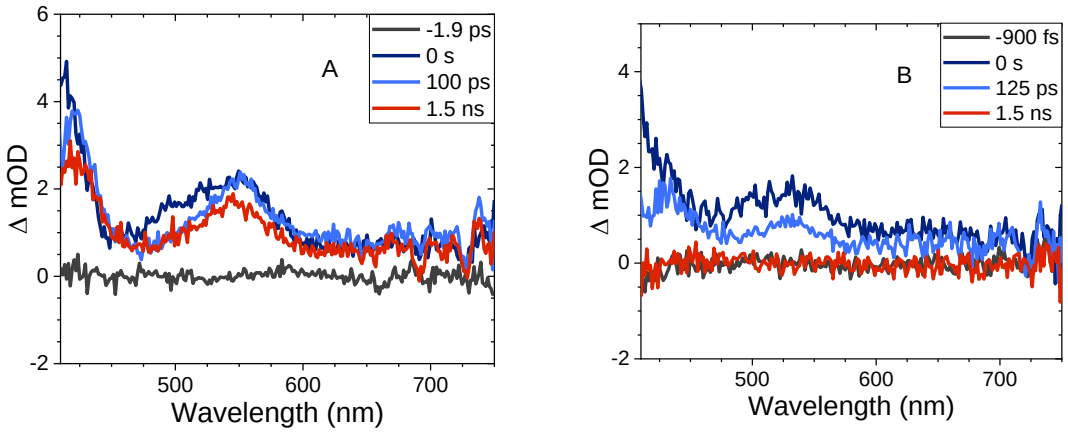

Figure 4.3.10. The transient absorption spectrum of **An-SO2-Ph** in cyclohexane (A) and CH_2Cl_2 (B).

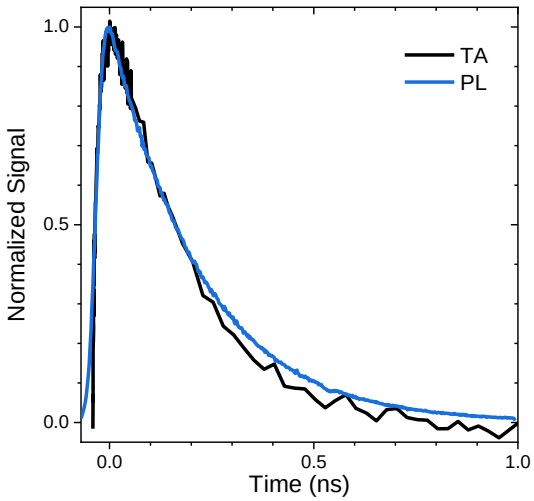

Figure 4.3.11. Comparison of the time traces from the transient absorption at 400 nm (TA, black) and photoluminescence (PL, blue) of **An-SO_2-Ph** in CH_2Cl_2. An exponential fit yields a lifetime of 225 ps for both the TA and PL time trace.

The behavior of the **An-SO_2-An** bichromophore is more complicated. The femtosecond TA spectrum for **An-SO_2-An** in CH_2Cl_2 is shown in Figure 4.3.12A. It is similar to that of **An-SO_2-Ph**, with broad $S_1 \rightarrow S_N$ features that are present at early times but disappear in less than 100 ps. Unlike **An-S-An** or **An-S-Ph**, the decay is slower in more polar solvents with the singlet absorption decaying within 3 ps in cyclohexane, 9 ps in CH_2Cl_2 and 15 ps in acetonitrile (Figure 4.3.12B). The rapid disappearance of the singlet absorption in the visible spectral range raises the question of where the population may be going. Again, the absence of a $T_1 \rightarrow T_N$ feature suggests that ISC is not a major factor. To see if the population is returning directly to the ground state as in **An-SO_2-Ph**, the bleach signal was monitored at 400 nm.

Kinetic traces of the 400 nm TA bleach features of **An-SO_2-An** show that there is a rapid (<100 ps) ground state recovery component in all three solvents, followed by a much

longer-lived component. The amplitude of the rapid component is much smaller for cyclohexane than for CH_2Cl_2 and acetonitrile (Figure 4.3.12C). The smaller magnitude of the picosecond bleach recovery in cyclohexane is consistent with the PL data in Figure 4.3.9B, where the fast decay component is smaller than in CH_2Cl_2 and acetonitrile. The rapid initial decay of the singlet state is limited by the instrument response in the PL measurements, but is clearly resolved in the visible and 400 nm fs-TA data. From the TA and PL data, **An-SO_2-An** appears to decay by two different pathways. One part of the population relaxes via rapid internal conversion directly to the ground state, similar to **An-SO_2-Ph**. But another portion ends up in an emissive state that survives for 10 ns or longer. Unfortunately, this long-lived state does not appear to have a strong absorption signature in the 400-700 nm range. But based on the broadened emission spectrum, it probably involves CT between the **An** moieties and is the likely precursor for the photocycloaddition reaction between neighboring anthracene rings.

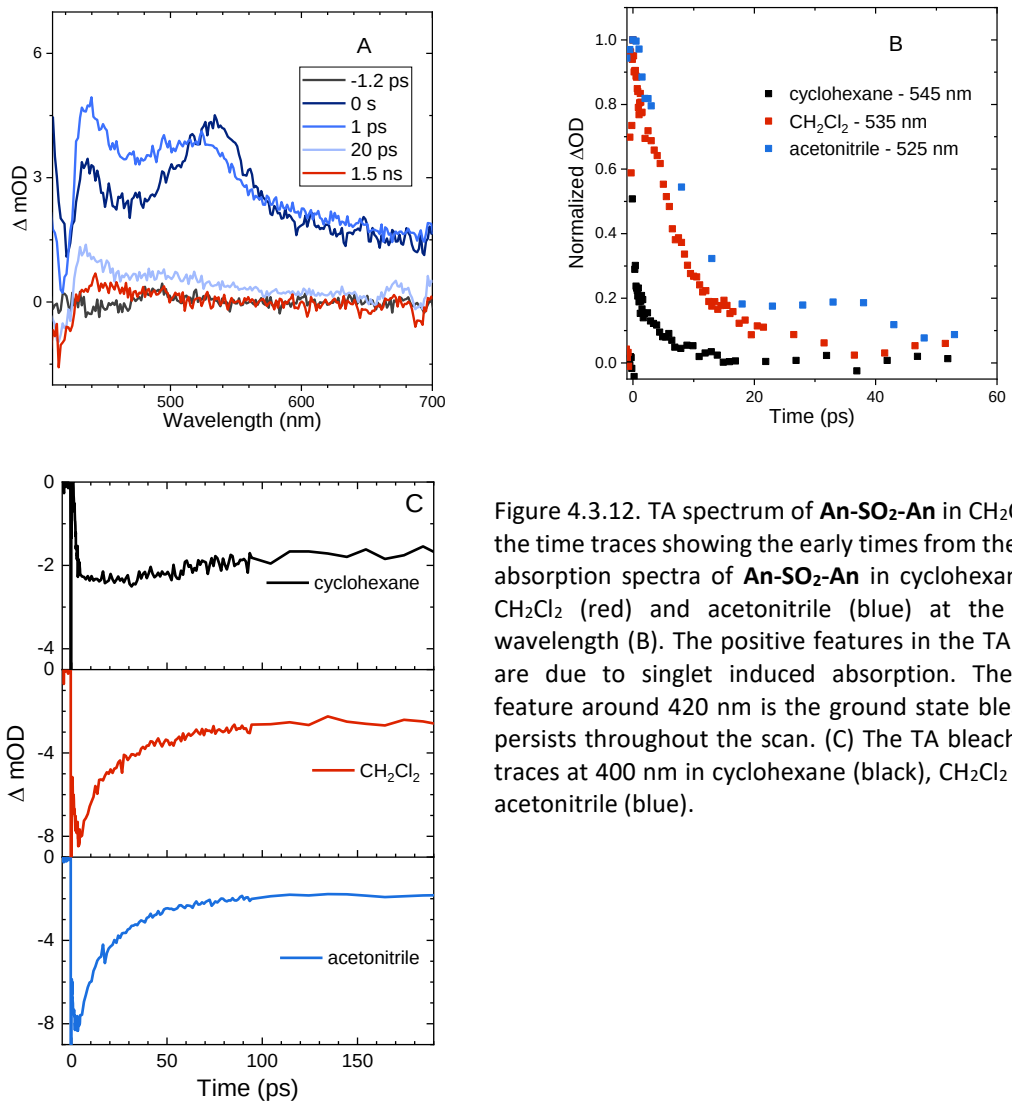

Figure 4.3.12. TA spectrum of **An-SO_2-An** in CH_2Cl_2 (A) and the time traces showing the early times from the transient absorption spectra of **An-SO_2-An** in cyclohexane (black), CH_2Cl_2 (red) and acetonitrile (blue) at the indicated wavelength (B). The positive features in the TA spectrum are due to singlet induced absorption. The negative feature around 420 nm is the ground state bleach which persists throughout the scan. (C) The TA bleach recovery traces at 400 nm in cyclohexane (black), CH_2Cl_2 (red), and acetonitrile (blue).

4.3.4 Time-dependent density functional theory analysis

The different behavior of the S- and SO_2-bridged compounds cannot be rationalized in terms of the simple screening model previously developed for the **T3** bichromophores.[64] For example, the **An-S-An** excited state appears to have significantly more CT character than **An-SO_2-An**, which is the opposite of what was observed for the **T3** compounds. In order to explain these discrepancies, we analyze the excited state

structure of the molecules using time-dependent density functional theory (TDDFT). All molecules rest in a "displaced" geometry, where the **An** and **Ph** moieties are rotated so that the π systems are offset from each other.

Computed excitation energies to the lowest excited state (Table 4.3.2) indicate very similar gaps for the two bridges, in good agreement with the absorption maxima in the steady-state spectra. The nature of the electronic transition can be assessed by means of the frontier molecular orbitals (MOs) (Figure 4.3.13). The highest occupied MO (HOMO) and lowest unoccupied MO (LUMO) of **An-S-An** and **An-SO_2-An** exhibit electron delocalization over the two anthracene moieties. While frontier MOs of SO_2-bridged dimers show virtually no involvement of the linker, there is a sizeable contribution of the S lone-pair electrons in the HOMO of **An-S-An**. Moreover, the oxidation state of the linker in **An-S-An** and **An-SO_2-An** tunes the relative stability of the in-phase and out-of-phase combination of the anthracene frontier MOs, resulting in swapped HOMO/HOMO-1 and LUMO/LUMO+1 character between **An-S-An** and **An-SO_2-An**. Conversely, the frontier MOs of **An-S-Ph** and **An-SO_2-Ph** are largely localized on the anthracene fragment. The most dramatic difference between the S- and SO_2-bridges are the much larger $\Delta\mu$ values for the S-bridged compounds, which implies these transitions have greater CT character. This is certainly consistent with the pronounced solvatochromism exhibited by **An-S-An** in particular (Figure 4.3.3).

	ΔE	strength	$\Delta\mu$	composition
An-S-An	3.46	0.42	-1.01	68 (H→L), 26 (H-1→L+1)
An-SO_2-An	3.48	0.29	-0.20	53 (H→L), 42 (H-1→L+1)
An-S-Ph	3.65	0.28	-0.70	93 (H→L)
An-SO_2-Ph	3.61	0.25	-0.29	94 (H→L)

Table 4.3.2. Computed excitation energies (in eV) to the lowest excited singlet state (S_1), oscillator strength, increase in the dipole moment (in Debye) upon excitation ($\Delta\mu = \mu(S_1) - \mu(S_0)$) and main molecular orbital contributions (in %). H = HOMO, L = LUMO.

From Table 4.3.2, the oscillator strengths for the transition to S_1 are very similar in all cases, except for **An-S-An**, which has a noticeably larger transition probability. Transition dipole moments (Figure 4.3.14) of both **Ph**-substituted dimers correspond to an **An** localized transition (L_a state) with the transition dipole along the **An** short molecular axis. In **An-SO_2-An**, the orientation of the total transition dipole moment is as expected for an H-type aggregate of two **An** molecules whose transition dipole moments are oriented side-by-side and add out-of-phase. On the other hand, the transition dipole moment to S_1 in **An-S-An** is oriented perpendicular to that of **An-SO_2-An** and corresponds to the in-phase combination of local dipoles, as expected for a J-type dimer. Again, this is consistent with the redshift and enhanced 0-0 vibronic peak in the **An-S-An** absorption spectrum (Figure 4.3.2).

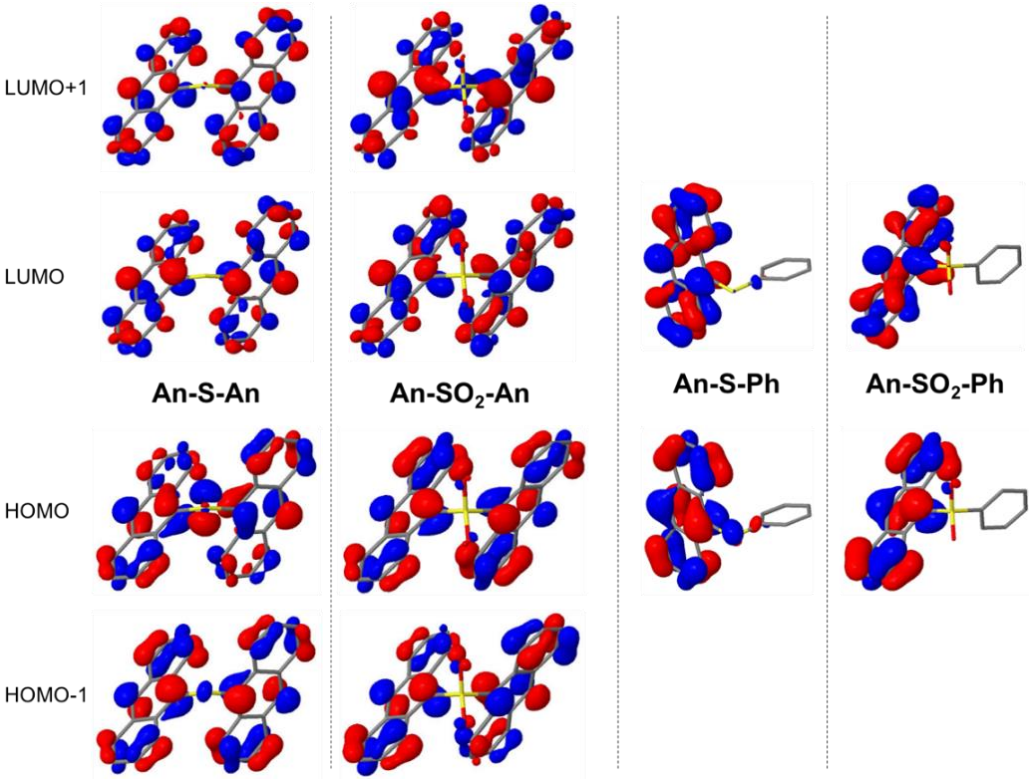

Figure 4.3.13. Frontier MOs contributing to the $S_0 \rightarrow S_1$ electronic transition.

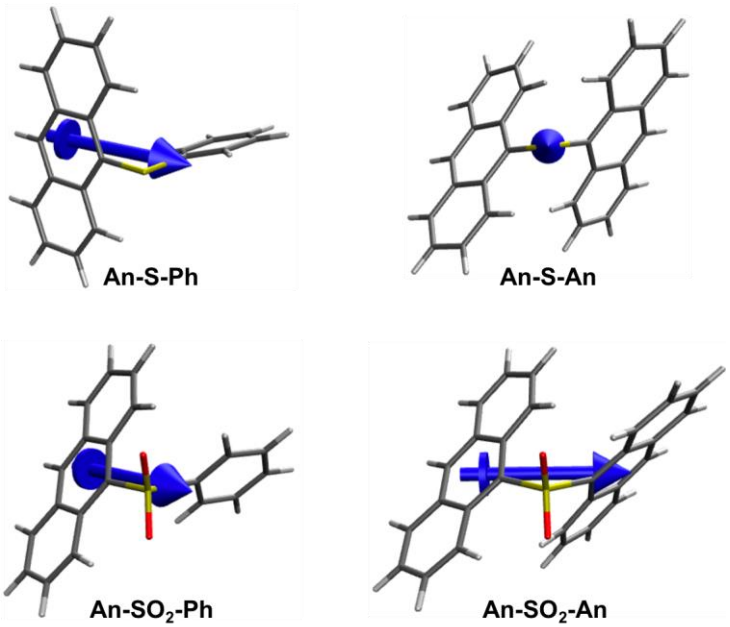

Figure 4.3.14. Representation of the transition dipole moments of the $S_0 \rightarrow S_1$ excitation.

Varying the oxidation state dramatically changes the degree of CT and the excitonic coupling between the **An** chromophores (Table 4.3.2 and Figure 4.3.14). Enhanced excitonic coupling increases the total oscillator strength of the **An-S-An** transition, which now reflects contributions from both **An** chromophores. To further characterize the nature of the S_1 state in **An-S-An** and **An-SO_2-An** and to understand the differences between S and SO_2 linkers, the transition to S_1 is decomposed in terms of diabatic contributions. The lowest state in **An-SO_2-An** is mainly obtained as the linear combination of local excitations (LE) of the two anthracenes. The excitation to S_1 in **An-SO_2-An** is almost purely of LE character, with a very small contribution of $\pi\rightarrow\pi^*$ charge transfer between anthracenes. The $\pi\rightarrow\pi^*$ CT contributions in **An-S-An** are estimated to account for 5% of the transition, slightly higher than in the SO_2-bridged dimer. But the S-bridged dimer also receives a sizeable contribution of electron transfer from the lone-pair electrons of the sulfide bridge to the anthracene units, i.e. $n(S)\rightarrow\pi^*$ (CT_B). The involvement of the lone-pair electrons in the transition to the lowest singlet has been observed in a computational study of a sulfur-bridged naphthalene dimer (**Naph-S-Naph**),[65] but not for the terthiophene counterpart (**T3ST3**).[64] In **T3ST3** the *n*(S) orbitals lie much lower in energy than the HOMOs of the two terthiophene moieties. As a result, there is no sizeable contribution from *n*(S) in the transition to lowest excited states of **T3ST3**, i.e. no relevant $n(S)\rightarrow\pi^*$ (CT_B) excitations within the computed lowest 10 excited singlet states.

Computational geometry relaxation on the S_1 potential energy surface of **An-SO$_n$-An** dimers results in two structural local minima. The first "displaced" conformation belongs to the C_2 symmetry point group and resembles the ground state minima with modified bond distances according to the $\pi \rightarrow \pi^*$ orbital promotions. It is this conformation that is likely reached after the initial relaxation in the S_1 state. The second set of minima corresponds to the C_{2v} symmetry group and involves an "eclipsed" geometry that shows a strong reduction of the C-S-C angle and shorter **An**-**An** interplane separation, with more coplanar anthracenes forming in the SO_2-bridged dimer. This geometry is expected to be more conducive to π-π interactions and photodimerization. In both dimers the S_1 eclipsed form is energetically lower than the displaced disposition, especially for the SO_2-bridged dimer. Stabilization of the eclipsed conformer is stronger in **An-SO$_2$-An** than in the **An-S-An** dimer, indicating stronger electronic coupling between the two **An** units in the former, in agreement with the lone-pair screening interaction model,[64] that is the weakening of the electronic CT interaction *via* screening by the S lone-pair electrons.

The character of the S_1 emission in the **Ph**-terminated compounds holds strong $\pi \rightarrow \pi^*$ character localized on the **An** with a CT_B contribution in the S-bridged case (similar to the $S_0 \rightarrow S_1$ transition at the Franck-Condon region), in agreement with the weak solvent dependence of emission peak maxima. The computed Stokes shifts are on the order of 0.6-0.7 eV, and transition strengths are close to the values computed at the ground state geometry. When the **Ph** group is replaced by **An**, calculations also predict strong Stokes

shifts for displaced forms (∼0.9 eV) that are even larger for the eclipsed minima (1.4 eV and 1.8 eV for **An-S-An** and **An-SO_2-An**, respectively). Furthermore, the eclipsed oscillator strengths are considerably lower with respect to the strengths at the absorbing Franck-Condon region. All the calculated Stokes shift values are much larger than the experimentally observed Stokes shifts in Figure 4.3.2, and it is likely that the TDDFT calculations overestimate the energy differences between the absorbing and relaxed geometries. The important point is that theory shows that there are two distinct excited state minima for the **An-SO_x-An** compounds, both with diminished oscillator strengths, in contrast to the single relaxed state in the **An-SO_x-Ph** compounds.

Both **An-SO_x-An** dimers can access two conformations, one of which may be a precursor to the photodimer, but the question is whether the initially excited states can survive long enough to populate the eclipsed conformation. For **An-S-An**, the experimental answer is no. Theoretically, the S lone pairs enable several distinct nonradiative relaxation pathways. The excited state singlet of the S-bridged dimers can decay by stabilizing the charge transfer contributions from the S lone-pairs to **An**, as recently discussed for S-bridged naphthalene dimers.[65] Structural rearrangement in this direction evolves towards an $n(S)\rightarrow\sigma^*$ state in which the angle between the two **An** moieties becomes linear (C-S-C angle of 180°), the S-C bonds elongate in order to stabilize the σ^* orbital, and the gap between ground state and excited state singlets shrinks considerably. The relaxation of the $n(S)\rightarrow\sigma^*$ state (elongated form) for the S-bridged molecules ultimately results in a small S_1/S_0 energy difference that can reach a state

crossing (conical intersection), thereby allowing the efficient funneling of the excited system to the ground state. Non-radiative decay through a conical intersection has been suggested as a viable channel in similar S-bonded molecules[65,66] and would only be available in the sulfide dimers, but not in the SO_2-bridged systems. However, internal conversion to S_0 does not appear to play a significant role in these S-bridged molecules, which mainly undergo ISC as shown in section 4.3.3.

To efficiently relax to the triplet state via ISC, two requirements need to be satisfied, that is: (1) a small energy gap between initial (singlet) and final (triplet) states, and (2) sizeable spin-orbit coupling (SOC). At the local excited state minimum the displaced conformer of **An-S-An** presents a large singlet-triplet gap (Table 4.3.3). The S_1-T_1 relative energy is also large for the **Ph**-substituted and the eclipsed form of **An-S-An**, while the energy difference with respect to T_2 is reduced, although for **An-S-Ph** the ISC process is energetically uphill. The computed SOCs to T_1 and T_2 for the S-bridged dimers are considerably larger than for anthracene and the SO_2-bridged compounds. Interestingly, the elongated conformer is calculated to have an extremely large SOC (159 and 178 cm^{-1} for **An-S-An** and **An-S-Ph** respectively), suggesting that it could also play a role in ISC. These results, which can be rationalized by means of El-Sayed's rule,[67] support the idea of faster ISC in S-bridged dimers. The S_1 and T_1 states have $n_{\perp}$(S)→σ* character, where the *n*(S) orbital involved is perpendicular to the **An**/**Ph** plane, i.e. the one which can interact with the π-system. On the other hand, the T_2 state has $n_{//}$(S)→σ* character. Therefore, the largest SOC matrix elements are those between states where the *n*(S)

orbital involved has different symmetry, i.e. S_1 with T_2. Moreover, the CT_B character of the $n(S)\rightarrow\pi^*$ and $n(S)\rightarrow\sigma^*$ orbitals agrees with the solvent polarity dependence of the ISC rate observed in Figure 4.3.8 for the S-bridged compounds.

		S_1/T_1		S_1/T_2	
		ΔE	SOC	ΔE	SOC
An		1.63	0.00	0.02	0.01
An-S-Ph	displaced	1.48	2.63	-0.23	1.75
	elongated	0.53	0.82	0.27	178.37
An-S-An	displaced	1.04	2.68	0.89	8.23
	eclipsed	0.98	0.02	0.27	4.10
	elongated	0.52	2.74	0.31	158.59
An-SO_2-Ph	displaced	1.48	0.15	-0.17	1.07
	eclipsed	1.46	0.06	-0.28	1.25
An-SO_2-An	displaced	1.07	0.30	0.92	1.15
	eclipsed	0.89	0.01	0.02	0.57

Table 4.3.3. Excited singlet-triplet energy gaps (in eV) and SOC (in cm^{-1}) between S_1 at the two lowest triplet states (T_1 and T_2) of S- and SO_2-bridge dimers at the excited state minima and at the crossing point. For the sake of completeness, the values of pristine anthracene (**An**) have been also included.

The absence of S lone pairs eliminates possible $n(S)\rightarrow\pi^*$ and $n(S)\rightarrow\sigma^*$ contributions to ISC and internal conversion for **An-SO_2-Ph** and **An-SO_2-An**. Thus, the formation of a stable, long-lived emissive species in **An-SO_2-An** is not surprising based on the calculations. The long-lived state probably corresponds to the displaced

conformation, judging by the similarity of the emission spectra at early (0-1 ns) and later (1-9 ns) times (Figure 4.3.15). On even longer timescales, we speculate that this state relaxes to the eclipsed form. In this conformation, the molecular geometry presents relatively short C···C distances (3.2 Å between the S-bonded carbons) and C···C bonding interactions in the excited state (Figure 4.3.16), suggesting that the eclipsed excimer can act as a precursor for the photocycloaddition reaction between **An** moieties.

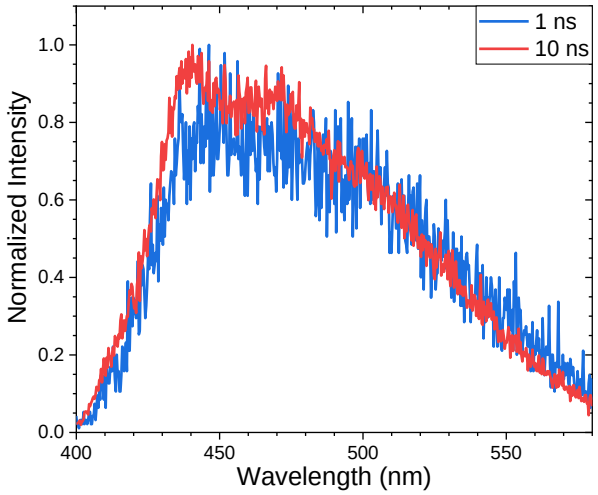

Figure 4.3.15. Time-resolved PL spectrum of **An-SO_2-An** in acetonitrile showing the signal integrated over 1 ns and 10 ns.

While the lack of ISC explains how **An-SO_2-An** can support a long-lived singlet state, the time-resolved measurements indicate that both SO_2-bridged compounds experience rapid internal conversion to the ground state as well. The origin of the fast internal conversion channel that dominates the **An-SO_2-Ph** relaxation and accounts for a substantial fraction of the **An-SO_2-An** relaxation is intriguing. Searches on the excited state potential energy surfaces of these two molecules uncovered no obvious signs of

conical intersections that would provide a path to the ground state. The solvent dependence shows that the partitioning of population to the ground state is enhanced in polar environments, suggesting an intermediate with CT character may be involved. The ability of the SO_2 group to induce rapid internal conversion, especially in **An-SO_2-Ph**, is unexpected since this highly oxidized group should be electronically inert.

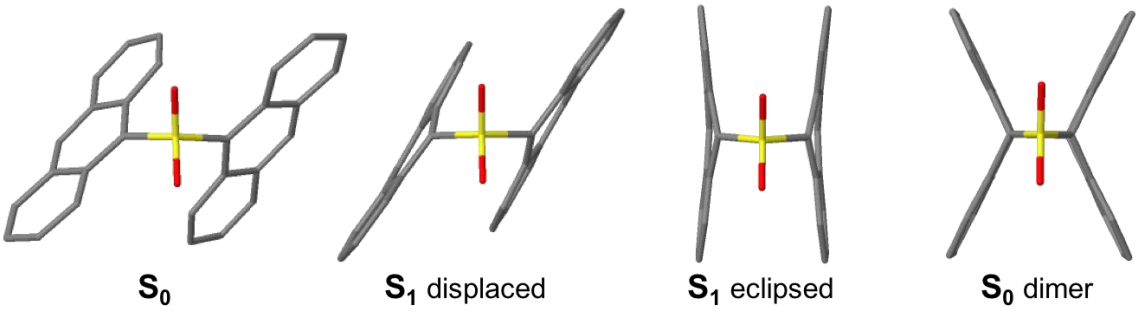

Figure 4.3.16. Optimized geometries of **An-SO_2-An**. From left to right: S_0, S_1 displaced, S_1 eclipsed and S_0 dimer.

4.3.5 Comparison of S- and SO_2-bridged relaxation dynamics

A simplified schematic of the photophysical behavior of the S- and SO_2-bridged bichromophores is given in Figure 4.3.17. The key difference between the two bridges is the participation of the sulfur atomic orbitals, which leads to a greater degree of CT in the **An-S-An** excited state and a rapid ISC rate that is sensitive to solvent polarity. The absence of the sulfur orbital contribution in **An-SO_2-An** allows this molecule to avoid ISC, but it is still subject to a solvent-dependent internal conversion channel of undetermined origin that competes with relaxation to a long-lived emissive state. This long-lived excited state is the likely precursor to formation of the eclipsed isomer which can undergo

photodimerization. The key finding is that by tuning the electronic structure of the linker atom, we can dramatically modulate the relaxation pathways of the dimer and enable photochemistry.

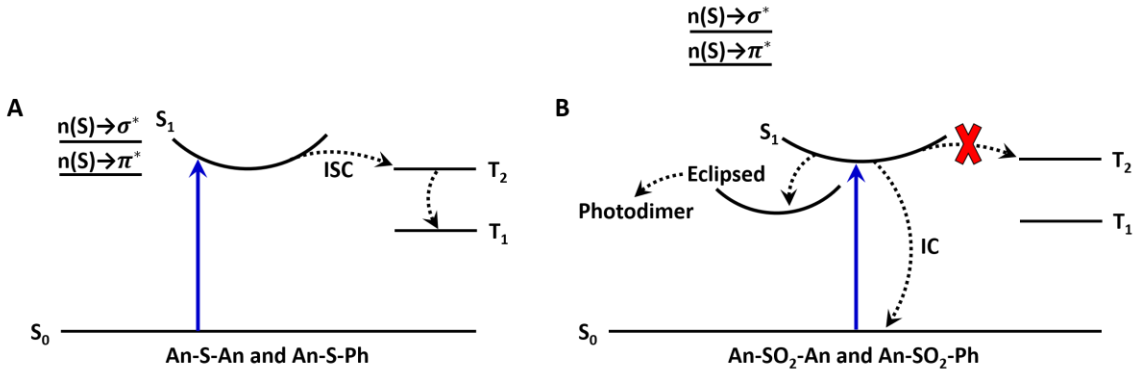

Figure 4.3.17. Jablonski diagram for the sulfide (A) and sulfone (B) bridges. The blue upward arrow represents photoexcitation. The dashed lines represent the nonradiative processes of intersystem crossing (ISC) and internal conversion (IC). Mixing of the n(S)→σ* and n(S)→π* linker orbitals enables ISC in the sulfide compounds; whereas, the lack of mixing in the sulfone compounds prevents ISC from occurring.

4.3.6 Tuning the bridge's electron density *via* the oxidation state imparts control over photophysics and photochemistry

The ability to tune the sulfur bridge oxidation state provides a way to investigate the role of the bridge electronic structure in modulating electronic interactions between chromophores. When the bridge and chromophore orbitals are closer in energy, as in the case of anthracene, orbital mixing can lead to unexpected effects, as seen for **An-S-An**, where this mixing leads to enhanced excited state CT character, a change from H-type to J-type excitonic coupling, and rapid ISC. When the bridge orbitals are shifted away by bridge oxidation, behavior is recovered that is more representative of two independent

chromophores that interact primarily via through-space Coulombic terms. In this case, the bridge affects the excitonic state primarily through geometrical factors and electronic screening, as demonstrated previously in the T3 dimers.[64] Here the linker has the ability to tune not only the photophysical but also the photochemical properties of the covalent assembly. In **An-SO_2-An**, tying up the lone pairs on the S prevents them from short-circuiting the photochemistry by ISC. The ability to engineer the photophysical and photochemical properties of molecular assemblies by tuning the linker electronic structure may prove useful for the design of functional organic optoelectronic materials.

4.4 References

(1) Christensen, P. R.; Nagle, J. K.; Bhatti, A.; Wolf, M. O. Enhanced Photoluminescence of Sulfur-Bridged Organic Chromophores. *J. Am. Chem. Soc.* **2013,** *135* (22), 8109.

(2) Heller, E.; Schmidt, G. M. J. Topochemistry. Part XXXIII. The Solid-State Photochemistry of Some Anthracene Derivatives. *Isr. J. Chem.* **1971,** *9* (4), 449.

(3) Wegner, G. Solid State Polymerization Mechanisms. *Pure Appl. Chem.* **1977,** *49* (4), 443.

(4) Ramamurthy, V.; Venkatesan, K. Photochemical reactions of organic crystals. *Chem Rev* **1987,** *87* (2), 433.

(5) Ihmels, H.; Leusser, D.; Pfeiffer, M.; Stalke, D. Solid-State Photolysis of Anthracene-Linked Ammonium Salts: The Search for Topochemical Anthracene Photodimerizations. *Tetrahedron* **2000,** *56* (36), 6867.

(6) Salzillo, T.; Venuti, E.; Della Valle, R. G.; Brillante, A. Solid-state photodimerization of 9-methyl-anthracene. *J Raman Spectrosc* **2017,** *48* (2), 271.

(7) Grebner, D.; Helbig, M.; Rentsch, S. Size-Dependent Properties of Oligothiophenes by Picosecond Time-Resolved Spectroscopy. *J. Phys. Chem.* **1995,** *99*, 16991.

(8) Yassar, A.; Horowitz, G.; Valat, P.; Wintgens, V.; Hmyene, M.; Deloffre, F.; Srivastava, P.; Lang, P.; Garnier, F. Exciton Coupling Effects in the Absorption and Photoluminescence of Sexithiophene Derivatives. *The Journal of Physical Chemistry* **1995,** *99* (22), 9155.

(9) Kasha, M. Energy Transfer Mechanisms and the Molecular Exciton Model for Molecular Aggregates. *Radiation Research* **1963,** *20* (1), 55.

(10) Kasha, M.; Rawls, H. R.; Ashraf El-Bayoumi, M. The Exciton Model in Molecular Spectroscopy. *Pure and Applied Chemistry* **1965,** *11* (3-4), 371.

(11) Spano, F. C. The Spectral Signatures of Frenkel Polarons in H- and J-Aggregates. *Acc. Chem. Res.* **2010,** *43* (3), 429.

(12) Van Bolhuis, F.; Wynberg, H.; Havinga, E. E.; Meijer, E. W.; Staring, E. G. J. The X-ray structure and MNDO calculations of α-terthienyl: A model for polythiophenes. *Synth. Met.* **1989,** *30* (3), 381.

(13) Kouki, F.; Spearman, P.; Valat, P.; Horowitz, G.; Garnier, F. Experimental determination of excitonic levels in α-oligothiophenes. *J. Chem. Phys.* **2000,** *113* (1), 385.

(14) Beenken, W. J. D.; Pullerits, T. Excitonic coupling in polythiophenes: Comparison of different calculation methods. *The Journal of Chemical Physics* **2004,** *120* (5), 2490.

(15) Krueger, B. P.; Scholes, G. D.; Fleming, G. R. Calculation of Couplings and Energy-Transfer Pathways between the Pigments of LH2 by the ab Initio Transition Density Cube Method. *The Journal of Physical Chemistry B* **1998,** *102* (27), 5378.

(16) Scholes, G. D. Long-range resonance energy transfer in molecular systems. *Annu Rev Phys Chem* **2003,** *54*, 57.

(17) Wong, K. F.; Bagchi, B.; Rossky, P. J. Distance and Orientation Dependence of Excitation Transfer Rates in Conjugated Systems: Beyond the Förster Theory. *The Journal of Physical Chemistry A* **2004,** *108* (27), 5752.

(18) Harcourt, R. D.; Ghiggino, K. P.; Scholes, G. D.; Speiser, S. On the origin of matrix elements for electronic excitation (energy) transfer. *The Journal of Chemical Physics* **1996,** *105* (5), 1897.

(19) Harcourt, R. D.; Scholes, G. D.; Ghiggino, K. P. Rate expressions for excitation transfer. II. Electronic considerations of direct and through–configuration exciton resonance interactions. *The Journal of Chemical Physics* **1994,** *101* (12), 10521.

(20) Scholes, G. D.; Harcourt, R. D.; Ghiggino, K. P. Rate expressions for excitation transfer. III. An ab initio study of electronic factors in excitation transfer and exciton resonance interactions. *The Journal of Chemical Physics* **1995,** *102* (24), 9574.

(21) Thompson, A. L.; Gaab, K. M.; Xu, J.; Bardeen, C. J.; Martinez, T. J. Variable Electronic Coupling in Phenylacetylene Dendrimers: The Role of Förster, Dexter, and Charge-Transfer Interactions. *J. Phys. Chem. A* **2004,** *108*, 671.

(22) Rossi, R.; Ciofalo, M.; Carpita, A.; Ponterini, G. Singlet-triplet intersystem crossing in 2,2':5',2''-terthiophene and some of its derivatives. *J. Photochem. Photobiol., A* **1993,** *70* (1), 59.

(23) Becker, R. S.; Seixas de Melo, J.; Maçanita, A. L.; Elisei, F. Comprehensive Evaluation of the Absorption, Photophysical, Energy Transfer, Structural, and Theoretical Properties of α-Oligothiophenes with One to Seven Rings. *The Journal of Physical Chemistry* **1996,** *100* (48), 18683.

(24) Bixon, M.; Jortner, J.; Verhoeven, J. W. Lifetimes for Radiative Charge Recombination in Donor-Acceptor Molecules. *Journal of the American Chemical Society* **1994,** *116* (16), 7349.

(25) Gould, I. R.; Young, R. H.; Mueller, L. J.; Albrecht, A. C.; Farid, S. Electronic Structures of Exciplexes and Excited Charge-Transfer Complexes. *Journal of the American Chemical Society* **1994,** *116* (18), 8188.

(26) Paa, W.; Yang, J. P.; Rentsch, S. Intersystem crossing in oligothiophenes studied by fs time-resolved spectroscopy. *Applied Physics B* **2000,** *71* (3), 443.

(27) Reyftmann, J. P.; Kagan, J.; Santus, R.; Morliere, P. EXCITED STATE PROPERTIES OF ∝aL-TERTHIENYL and RELATED MOLECULES. *Photochemistry and Photobiology* **1985,** *41* (1), 1.

(28) Beljonne, D.; Cornil, J.; Friend, R. H.; Janssen, R. A. J.; Bredas, J. L. Influence of Chain Length and Derivatization on the Lowest Singlet and Triplet States and Intersystem Crossing in Oligothiophenes. *J. Am. Chem. Soc.* **1996,** *118* (27), 6453.

(29) Martin, R. L. Natural transition orbitals. *The Journal of Chemical Physics* **2003,** *118* (11), 4775.

(30) Trinh, C.; Kirlikovali, K.; Das, S.; Ener, M. E.; Gray, H. B.; Djurovich, P.; Bradforth, S. E.; Thompson, M. E. Symmetry-Breaking Charge Transfer of Visible Light Absorbing Systems: Zinc Dipyrrins. *The Journal of Physical Chemistry C* **2014,** *118* (38), 21834.

(31) Piet, J. J.; Schuddeboom, W.; Wegewijs, B. R.; Grozema, F. C.; Warman, J. M. Symmetry Breaking in the Relaxed S1 Excited State of Bianthryl Derivatives in Weakly Polar Solvents. *Journal of the American Chemical Society* **2001,** *123* (22), 5337.

(32) Giaimo, J. M.; Gusev, A. V.; Wasielewski, M. R. Excited-state symmetry breaking in cofacial and linear dimers of a green perylenediimide chlorophyll analogue leading to ultrafast charge separation. *J. Am. Chem. Soc.* **2002,** *124*, 8530.

(33) Rentsch, S.; Yang, J. P.; Paa, W.; Birckner, E.; Schiedt, J.; Weinkauf, R. Size dependence of triplet and singlet states of α-oligothiophenes. *Phys. Chem. Chem. Phys.* **1999,** *1* (8), 1707.

(34) Fabiano, E.; Della Sala, F.; Cingolani, R.; Weimer, M.; Goerling, A. Theoretical Study of Singlet and Triplet Excitation Energies in Oligothiophenes. *J. Phys. Chem. A* **2005,** *109* (13), 3078.

(35) Weinhold, F., Landis, C. *Valency and Bonding: A Natural Bond Orbital Donor-Acceptor Perspective*; Cambridge: Cambridge University Press, 2005.

(36) Chesnut, D. B.; Quin, L. D. Nature of bonding in the sulfuryl group. *Journal of Computational Chemistry* **2004,** *25* (5), 734.

(37) Zhang, Q.; Silbey, R. Symmetry Breaking in a Simple Electron-Phonon Model with Electron Correlation. *J. Chem. Phys.* **1990,** *92*, 4899.

(38) Whited, M. T.; Patel, N. M.; Roberts, S. T.; Allen, K.; Djurovich, P. I.; Bradforth, S. E.; Thompson, M. E. Symmetry-breaking intramolecular charge transfer in the excited state of meso-linked BODIPY dyads. *Chemical Communications* **2012,** *48* (2), 284.

(39) Bartynski, A. N.; Gruber, M.; Das, S.; Rangan, S.; Mollinger, S.; Trinh, C.; Bradforth, S. E.; Vandewal, K.; Salleo, A.; Bartynski, R. A.et al. Symmetry-Breaking Charge Transfer in a Zinc Chlorodipyrrin Acceptor for High Open Circuit Voltage Organic Photovoltaics. *Journal of the American Chemical Society* **2015,** *137*, 5397.

(40) Terenziani, F.; Painelli, A.; Katan, C.; Charlot, M.; Blanchard-Desce, M. Charge Instability in Quadrapolar Chromophores: Symmetry Breaking and Solvatochromism. *J. Am. Chem. Soc.* **2006,** *128*, 15742.

(41) Lewis, F. D.; Daublain, P.; Zhang, L.; Cohen, B.; Vura-Weis, J.; Wasielewski, M. R.; Shafirovich, V.; Wang, Q.; Raytchev, M.; Fiebig, T. Reversible Bridge-Mediated Excited-State Symmetry Breaking in Stilbene-Linked DNA Dumbbells. *J. Am. Chem. Soc.* **2008,** *112*, 3838.

(42) Schütz, M.; Schmidt, R. Deactivation of 9,9'-Bianthryl in Solution Studied by Photoacoustic Calorimetry and Fluorescence. *The Journal of Physical Chemistry* **1996,** *100* (6), 2012.

(43) Grabner, G.; Rechthaler, K.; Köhler, G. Two-State Model for the Photophysics of 9,9'-Bianthryl. Fluorescence, Transient-Absorption, and Semiempirical Studies. *The Journal of Physical Chemistry A* **1998,** *102* (4), 689.

(44) Aldern, R. G.; Parson, W. W.; Chu, Z. T.; Warshel, A. Calculation of Electrostatic Energies in Photosynthetic Reaction Centers. *J. Am.Chem. Soc.* **1995,** *117*, 12284.

(45) Lunkenheimer, B.; Kohn, A. Solvent Effects on Electronically Excited States Using the Conductor-Like Screening Model and the Second-Order Correlated Method ADC(2). *J. Chem. Theor. Comp.* **2013,** *9*, 977.

(46) Lu, R.; Lin, J. A Interpretation of Stepwise Bond Dissociation Energies of CH_4. *Comp. Theor. Chem.* **2014,** *1037*, 10.

(47) Endo, A.; Sato, K.; Yoshimura, K.; Kai, T.; Kawada, A.; Miyazaki, H.; Adachi, C. Efficient up-conversion of triplet excitons into a singlet state and its application for organic light emitting diodes. *Applied Physics Letters* **2011,** *98* (8), 083302.

(48) Uoyama, H.; Goushi, K.; Shizu, K.; Nomura, H.; Adachi, C. Highly efficient organic light-emitting diodes from delayed fluorescence. *Nature* **2012,** *492* (7428), 234.

(49) Wei, S.; Xia, J.; Dell, E. J.; Jiang, Y.; Song, R.; Lee, H.; Rodenbough, P.; Briseno, A. L.; Campos, L. M. Bandgap Engineering through Controlled Oxidation of Polythiophenes. *Angew. Chem. Int. Ed.* **2014,** *53*, 1832.

(50) Spano, F. C.; Mukamel, S. Superradiance in Molecular Aggregates. *J. Chem. Phys.* **1989,** *91*, 683.

(51) Greyson, E. C.; Vura-Weis, J.; Michl, J.; Ratner, M. A. Maximizing singlet fission in organic dimers: theoretical investigations of triplet yield in the regime of localized excitation and fast coherent electron transfer. *J. Phys. Chem. B* **2010,** *114*, 14168.

(52) Smith, M. B.; Michl, J. Recent advances in singlet fission. *Ann. Rev. Phys. Chem.* **2013,** *64*, 361.

(53) Berkelbach, T. C.; Hybertsen, M. S.; Reichman, D. R. Microscopic theory of singlet exciton fission. I. General formulation. *J. Chem. Phys.* **2013,** *138*, 114102/1.

(54) Vallett, P. J.; Snyder, J. L.; Damrauer, N. H. Tunable Electronic Coupling and Driving Force in Structurally Well-Defined Tetracene Dimers for Molecular Singlet Fission: A Computational Exploration Using Density Functional Theory. *J. Phys. Chem. A* **2013,** *117*, 10824.

(55) Christensen, P. R.; Patrick, B. O.; Caron, E.; Wolf, M. O. Oxidation-State-Dependent Photochemistry of Sulfur-Bridged Anthracenes. *Angew. Chem. Int. Ed. Engl.* **2013,** *52* (49), 12946.

(56) Rettig, W.; Paeplow, B.; Herbst, H.; Müllen, K.; Desvergne, J.-P.; Bouas-Laurent, H. Intramolecular Excimer Formation in Short- and Long-Chainlength Di(9-anthryl) Bichromophoric Compounds and Relation to Ground State Properties. *New J. Chem.* **1999,** *23* (4), 453.

(57) Birks, J. B. *Photophysics of Aromatic Molecules*; Wiley - Interscience: New York, 1970.

(58) Bensasson, R.; Land, E. J. Triplet-Triplet Extinction Coefficients via Energy Transfer. *Trans. Faraday Soc.* **1971,** *67* (0), 1904.

(59) Meyer, Y. H.; Astier, R.; Leclercq, J. M. Triplet-Triplet Spectroscopy of Polyacenes. *J. Chem. Phys.* **1972,** *56* (2), 801.

(60) Compton, R. H.; Grattan, K. T. V.; Morrow, T. Extinction Coefficients and Quantum Yields for Triplet—Triplet Absorption Using Laser Flash Photolysis. *J. Photochem.* **1980,** *14* (1), 61.

(61) *CRC Handbook of Chemistry and Physics*; 99th ed.; CRC Press/Taylor & Francis: Boca Raton, FL, 2018.

(62) Bautista, J. A.; Connors, R. E.; Raju, B. B.; Hiller, R. G.; Sharples, F. P.; Gosztola, D.; Wasielewski, M. R.; Frank, H. A. Excited State Properties of Peridinin: Observation of a Solvent Dependence of the Lowest Excited Singlet State Lifetime and Spectral Behavior Unique among Carotenoids. *J. Phys. Chem. B* **1999,** *103* (41), 8751.

(63) Pang, Y.; Prantil, M. A.; Van Tassle, A. J.; Jones, G. A.; Fleming, G. R. Excited-State Dynamics of 8′-Apo-β-caroten-8′-al and 7′,7′-Dicyano-7′-apo-β-carotene Studied by Femtosecond Time-Resolved Infrared Spectroscopy. *J. Phys. Chem. B* **2009,** *113* (39), 13086.

(64) Cruz, C. D.; Christensen, P. R.; Chronister, E. L.; Casanova, D.; Wolf, M. O.; Bardeen, C. J. Sulfur-Bridged Terthiophene Dimers: How Sulfur Oxidation State Controls Interchromophore Electronic Coupling. *J. Am. Chem. Soc.* **2015,** *137* (39), 12552.

(65) Climent, C.; Barbatti, M.; Wolf, M. O.; Bardeen, C. J.; Casanova, D. The Photophysics of Naphthalene Dimers Controlled by Sulfur Bridge Oxidation. *Chemical Science* **2017,** *8* (7), 4941.

(66) Woo, K. C.; Kang, D. H.; Kim, S. K. Real-Time Observation of Nonadiabatic Bifurcation Dynamics at a Conical Intersection. *J. Am. Chem. Soc.* **2017,** *139* (47), 17152.

(67) El-Sayed, M. A. Spin—Orbit Coupling and the Radiationless Processes in Nitrogen Heterocyclics. *J. Chem. Phys.* **1963,** *38* (12), 2834.

Chapter 5: Intermolecular electronic states for unsensitized photon upconversion – interband assisted two-photon absorption in crystalline rubrene

5.1 The photophysical properties of RUB make it a popular photon conversion material

Photophysical phenomena in organic molecular materials can potentially form the basis of high-efficiency solar energy conversion technologies employed to surpass the Shockley−Queisser limit for single junction photovoltaic devices.[1-3] In a crystal composed of rubrene (RUB), the triplet pair state is approximately isoenergetic with the singlet state and both singlet fission and triplet fusion can be quite efficient enabling rubrene to function as a photon conversion material.[4-8] For organic triplet-triplet annihilation upconversion (TTA-UC), RUB is a commonly used emitter molecule due its long-lived triplet states and high PL quantum yield.[9-11] Most reported upconversion schemes are performed in solutions, since facile diffusion permits the triplet sensitization and subsequent fusion events to occur in different spatial regions. This prevents energy transfer from the emitter back to the sensitizer. UC in solid-state systems is more challenging due to decreased diffusion and typically has a lower overall efficiency.[12,13] A few recent results suggest that RUB could form the basis of a solid-state material that upconverts NIR photons. Of particular significance is the report by Liu et al. observing visible PL excited by a continuous wave (CW) 980 nm laser in crystalline powders of RUB in the absence of any sensitization.[14] The authors of that work attributed the "upconversion" to nonresonant two-photon absorption (2PA). Although they did not

attempt to extract a 2PA cross section, their data suggested it could be very high. Given the important role of RUB in solid-state NIR upconversion schemes, the origin of the upconversion in pristine crystals is examined here.

In agreement with Liu et al.,[14] it is found that crystalline RUB exhibits surprisingly intense NIR-visible upconversion using CW excitation at intensities as low as 20 W/cm^2. The PL generated by CW excitation is comparable to that generated by a femtosecond pulse train with the same average intensity but with peak intensities on the order of 10^5 times higher. The fact that the upconverted PL depends only on average intensity, not peak intensity, suggests that an intermediate electronic state is facilitating resonant two-photon absorption in pristine crystals of RUB. A large range of intensities for the PL power dependence are explored and a quartic regime is found at lower intensities. Moreover, there is a pronounced dependence of the per-pulse upconverted PL on the laser repetition rate. These observations lead to a model in which a long-lived ($\sim$1 μs) intermediate state facilitates two-photon absorption to the singlet state, after which it undergoes fission and fusion dynamics. Other polyacenes, tetracene (TET), diphenylhexatriene and perylene, do not exhibit similar behaviors, suggesting that the crystal packing in RUB plays a pivotal role in the observed photophysics. The observation of resonantly enhanced upconverted PL in a pristine molecular crystal suggests that intermolecular interactions in molecular crystals can give rise to interband states that enable photon upconversion even in the absence of triplet sensitizers.

5.2 The molecular 2PA properties of RUB

The 2PA properties of TET and RUB molecules were first studied in dilute solutions of dichloromethane. Surprisingly, only one prior report was found in the literature on the two-photon properties of RUB[15] and no previous reports were found for TET. The laser dye Coumarin 540A (C540A) was used as a standard for the 2PA at 800 nm, with a measured 2PA cross section δ = 47 x 10^{-50} cm^4/s.[16,17] All three molecules showed measurable PL only when excited using a femtosecond pulsed laser. When the same laser was used in CW mode, no fluorescence signal could be detected above the background. All three molecules also showed the quadratic dependence on intensity expected for nonresonant 2PA, and this dependence is shown in Figure 5.2.1. There is a slight saturation behavior for all three molecules at the highest intensities, as observed for other 2PA absorbers.[18] Using the equation[19,20]

$$\delta_{RUB} = \delta_{C540A}\left(\frac{f_{C540A}\cdot\phi_{C540A}\cdot S_{RUB}}{f_{RUB}\cdot\phi_{RUB}\cdot S_{C540A}}\right) \quad (5.2.1)$$

where f represents the fraction of the total PL spectrum within the range of the interference filter, φ is the PL quantum yield and S is the measured signal, the relative values of δ for RUB and TET can be determined by comparing their signals to that measured for C540A under the same conditions. The experimental parameters used are summarized in Table 5.2.1, along with the calculated δ values. At 800 nm excitation, RUB and TET have very similar 2PA cross-sections, which is not surprising considering that they have similar conjugated cores. Both δ values are about 30× smaller than that of C540A as

well as the previously reported value for RUB in a benzene solution (56 x 10^{-50} cm^4/s).[15] However, the open aperture Z-scan technique utilized in reference 30 can yield an effective 2PA cross section that is enhanced by excited state absorption[21] and their reported intensity dependence with a slope greater than 2 suggests that multiphoton processes other than 2PA are contributing to the cross section. Furthermore, the lower δ values for RUB and TET obtained in this work are consistent with experimentally determined values for other polycyclic aromatic hydrocarbons such as naphthalene, anthracene and perylene.[17,22,23]

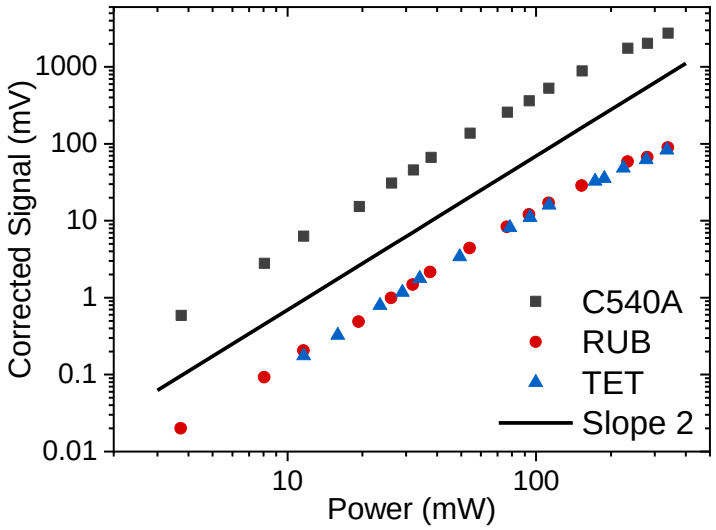

Figure 5.2.1. Log-log plots of the relative intensity of the integrated PL for samples of coumarin 540 A, rubrene and tetracene in dilute solutions of dichloromethane excited via Nonresonant 2PA.

Sample	QY	f_{coll}	δ $(\times 10^{-50} cm^4 * s * photons^{-1})$
C540A	0.53[24]	0.19	47[16,17]
RUB	0.98[25]	0.61	1.6
TET	0.17[25]	0.16	1.4

Table 5.2.1. The parameters used to determine the 2PA cross sections of the chromophores used. All dilute (300 uM) solutions in dichloromethane were degassed prior to the measurements. QY is the quantum yield of the chromophore and f_{coll} is the integrated area under the PL spectrum excited with a pulsed 800 nm laser over the range of the interference filter.

5.3 Upconverted PL in crystalline RUB

The crystal packing in RUB leads to a large separation of the conjugated cores due to the twisted phenyl rings, and Biaggio has suggested that the spectroscopic properties of this molecular crystal can be approximated by an oriented gas of RUB molecules, with only minor perturbations by Coulombic interactions.[26] TET, on the other hand, forms a close-packed herringbone crystal where strong Coulomb and charge-transfer interactions lead to a large Davydov splitting[27,28] and other excitonic effects such as superradiance.[29] With these packing differences in mind, crystalline RUB should behave similarly to the solution phase, while crystalline TET might show some significant deviations. Instead, it was crystalline RUB that exhibited qualitatively new behavior. The first surprising observation is illustrated in Figure 5.3.1. RUB microcrystalline powder displays bright yellow-orange emission (~600 nm) which is easily discerned by eye under both pulsed

(Figure 5.3.1A) and CW excitation (Figure 5.3.1B) at 800 nm. The PL spectrum is similar for all three wavelengths (Figure 5.3.1C), but the high energy side of the emission is suppressed for longer wavelength excitation, as can be expected because these wavelengths penetrate deeper into the crystal and the PL undergoes more self-absorption as it escapes. All other molecular crystals tested (TET, perylene, diphenylhexatriene) show a clear dependence on the peak power of the laser, with at least an order of magnitude more upconverted PL under pulsed excitation compared to CW excitation, whereas upconverted PL in RUB is approximately the same under pulsed and CW excitation.

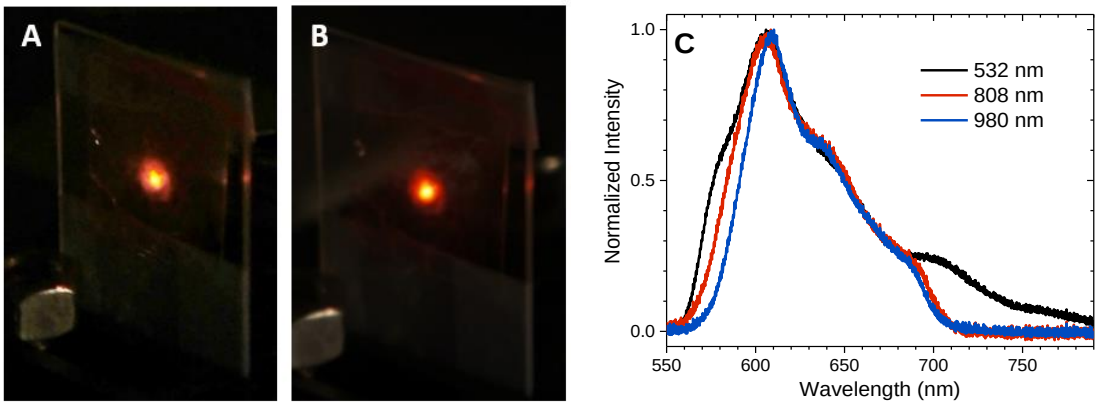

Figure 5.3.1. Images of the upconverted visible (~ 600 nm) emission observed from crystalline rubrene powder with femtosecond pulsed (A) and continuous wave (B) NIR excitation at 800 nm. An average intensity of 4 kW/cm^2 was used to excite the powder which corresponds to a peak intensity of 0.4 GW/cm^2 for the femtosecond pulse train. The PL intensity appears essentially unchanged using either continuous wave or pulsed excitation. (C) The steady-state PL obtained from pristine single crystals of RUB using CW excitation. For each wavelength the laser was incident upon the ***ab*** facet of the crystal and polarized parallel to the ***b*** axis.

The dependence of the upconverted PL on the incident laser intensity highlights another difference between crystalline RUB and TET (Figure 5.3.2). The power law with exponent 2 observed in TET is a hallmark of a two-photon process, which is proportional to the incident laser intensity squared. Perylene and diphenylhexatriene crystals also

showed the usual I^2 dependence over the whole range of intensities for both pulsed and CW excitation (Figure 5.3.3). For these crystals, the dependence on peak power and the power law of 2 both suggest nonresonant 2PA as the dominant mechanism leading to upconverted PL in TET and the other crystals. However, direct absorption to the triplet state followed by TTA, can also generate an I^2 dependence. This pathway has been previously observed in anthracene[30] as well as TET.[31] Even though the $S_0 \rightarrow T_1$ transition is formally forbidden, in many organic crystals its weak absorption is sufficient to generate enough triplet density to observe TTA if intense NIR sources are used.

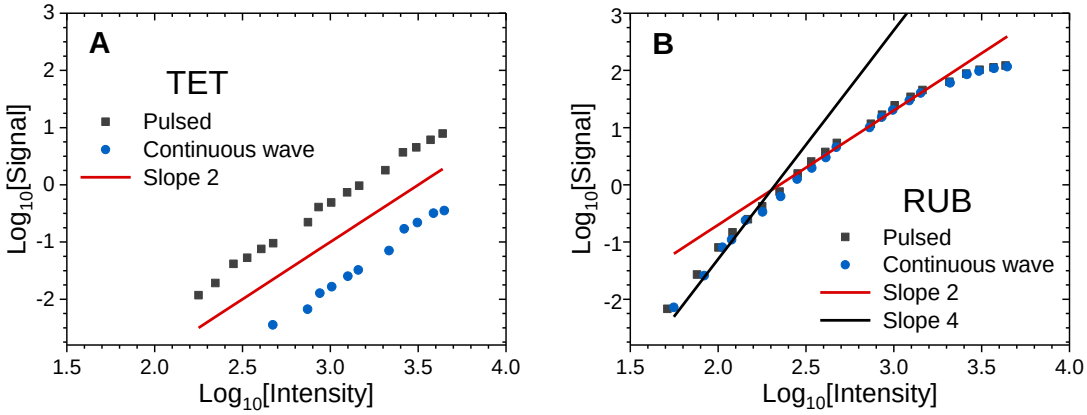

Figure 5.3.2. Comparison of the excitation intensity dependence (W/cm^2) of the integrated upconverted PL signal for pulsed and continuous wave laser excitation at 800 nm for TET (A) and RUB (B) crystals. Lines with a slope of 2 and 4 are included to guide the eye. Linear fits of the intensity dependence yield slopes of 2.03 ± 0.03 and 3.75 ± 0.16 for the middle and low range intensities, respectively.

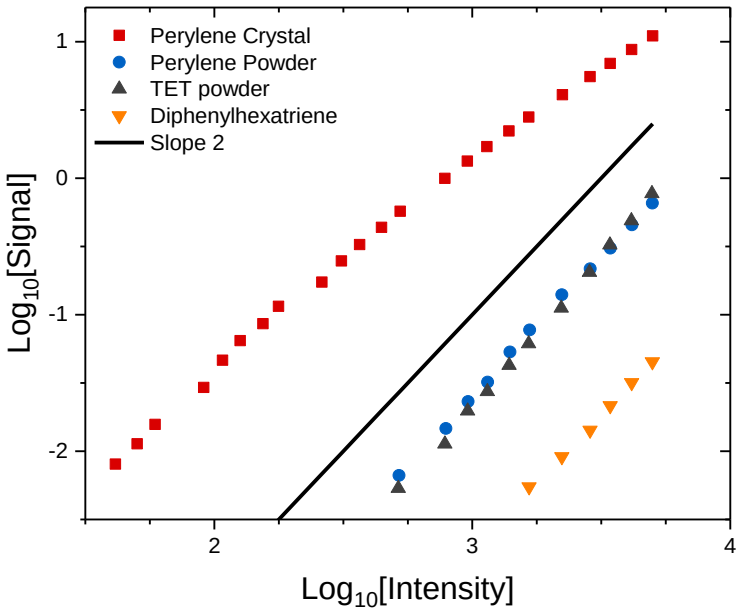

Figure 5.3.3. Log-log plot of the intensity (W/cm^2) dependent PL of other polyacene microcrystalline powders and crystals. Each sample was excited with a CW 808 nm diode laser. CW excitation produces some upconverted PL in these samples, but a quadratic dependence on the laser intensity is observed.

The upconverted PL observed in RUB, on the other hand, has a different intensity dependence, with a log-log plot exhibiting a slope of 4 at lower intensities that turns to a slope of 2 and eventually begins to flatten out at the highest intensities. Similar intensity dependences are observed in RUB for excitation wavelengths of 800 nm, 808 nm and 980 nm (Figure 5.3.4A). The results are quite robust amongst different samples of RUB. Pristine crystals, crystalline powder out of the supplier's bottle and RUB crystals which are more than 4 years old, all show the same behavior (Figure 5.3.4B).

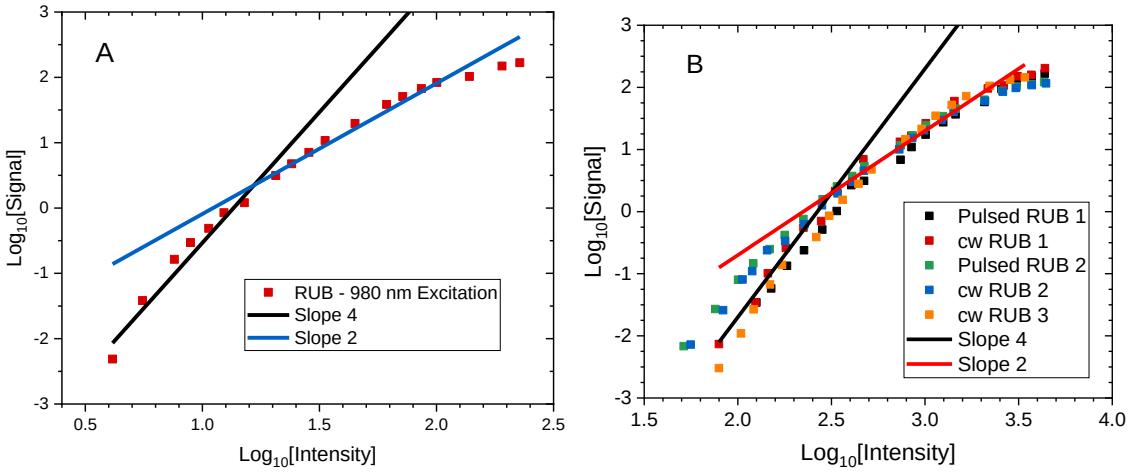

Figure 5.3.4. Log-log plot of the intensity (W/cm^2) dependent PL of a pristine rubrene crystal excited with a 980 nm laser diode (A) and for three separate pristine crystals of rubrene using the Vitesse 800 nm pulsed and CW output with polarization aligned parallel to the ***b*** axis of each crystal (B).

5.4 NIR absorbance and PL in crystalline RUB

These results raise two questions: (1) why does CW excitation lead to efficient 2PA in RUB? (2) Why does the upconverted PL have a quartic dependence upon the incident intensity? To answer question (1), the 2PA process is considered in more detail. The mechanism of nonresonant 2PA can be described in terms of a three-state system in which the final state is populated via a virtual intermediate state between the initial and final real states.[21,32,33] The virtual state cannot support a real population, and the two photons must arrive within a very short time interval ($\Delta t = 10^{-15} - 10^{-16}\ s$) to reach the excited singlet state. If the intermediate state is a real state that can support an excited state population, then the requirement of simultaneous arrival of two photons is lifted.[33] To access the excited singlet through the resonant intermediate, the second

photon must only arrive before the decay of this state. A resonantly enhanced intermediate state would explain the fact that the upconverted PL observed in RUB depends only on average intensity, rather than the peak intensity within the femtosecond pulse train.

If the 2PA in crystalline RUB proceeds through a real intermediate state, then this state should have some spectroscopic signature. The most logical candidate for a transition in the NIR would be the $S_0 \rightarrow T_1$ transition in molecular RUB. A concentrated (~ 2 mM) solution of RUB in dichloromethane was prepared and placed in a 10 cm cuvette for the NIR absorption measurement, however, no measurable absorption is observed beyond 650 nm (Figure 5.4.1A). Given that this measurement is sensitive to an absorbance of 0.005 or less, an upper limit of $\varepsilon \leq 0.005\ M^{-1}cm^{-1}$ can be placed on any NIR transition in the isolated molecule. Of course, the CW 2PA is only seen in crystalline samples, so the lack of any absorptive features in the solution spectrum is not surprising. The absorption of a single RUB crystal was directly measured out to 1700 nm using a microspectrometer with unpolarized light (Figure 5.4.1B). The oscillatory feature present over the NIR range is an etalon effect which allows us to estimate a crystal thickness of 5 μm.[34] There was no detectable NIR absorption above the level of 0.04 for a 5 μm thick crystal. This suggests that the crystal has an absorption coefficient of less than 40 cm^{-1}. To compare with solution studies, an effective concentration of 2.4 M is calculated for the crystal, which places an upper limit on the molar absorption coefficient $\varepsilon \leq 35\ M^{-1}cm^{-1}$. It should be noted that the absorption in a crystal is highly anisotropic, and it is possible

that correctly polarized light would be able to pick up a low amplitude absorption in this wavelength region. The light from the microspectrometer used in this study was unpolarized, and the absorption coefficients here should be regarded as a rough estimate. A full polarization study is necessary to accurately assess the absorption properties of the crystal in the NIR.

Even though the presence of a low-energy intermediate state could not be detected in the absorption, evidence for such states was found by looking at the NIR emission after CW 808 nm excitation. In Figure 5.4.2 the steady-state PL spectrum is shown for this excitation wavelength. The emission extends from 950 nm past 1200 nm,

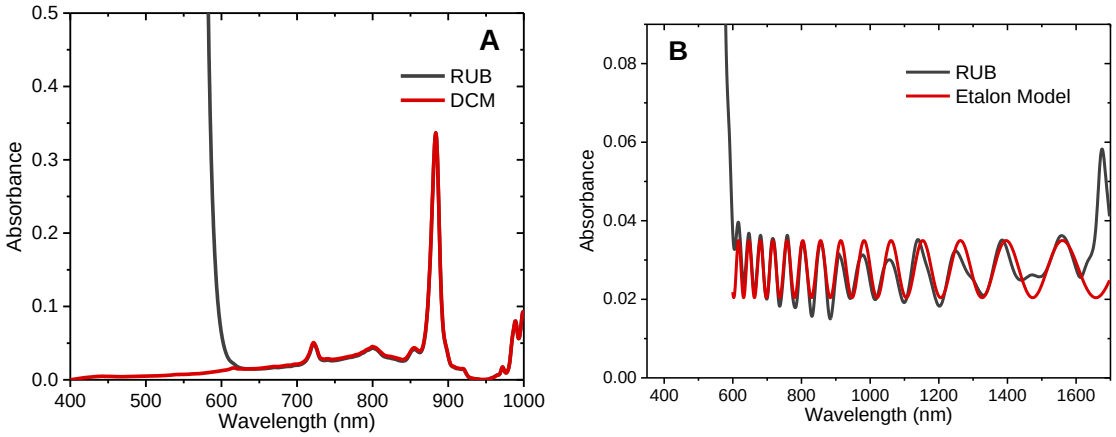

Figure 5.4.1. The NIR absorption of rubrene solution (black line) in a 10 cm cuvette compared to the baseline absorption of the solvent dichloromethane (red line) (A) and crystalline rubrene absorption spectrum (black line) overlaid with the calculated background (red line) using the method described in ref. 47 (B).

with two prominent peaks at 980 nm and 1060 nm. The peak at 1060 nm is likely a Raman peak with a separation of 3000 cm^{-1} from the excitation wavelength. The 980 nm peak of this PL is at a higher energy than that expected for RUB phosphorescence, which should be around 1070 nm based on a triplet energy of 1.15 eV. There were no experimental

phosphorescence spectra for RUB found in the literature. It is also not clear that this emitting state is solely responsible for the enhanced 2PA. Given that its emission peaks at 980 nm, it is unlikely to absorb strongly at this wavelength, so it may not be able to facilitate the experimentally observed 2PA at 980 nm. Nevertheless, the presence of PL in this wavelength range proves the existence of low-energy states in RUB with appreciable oscillator strength.

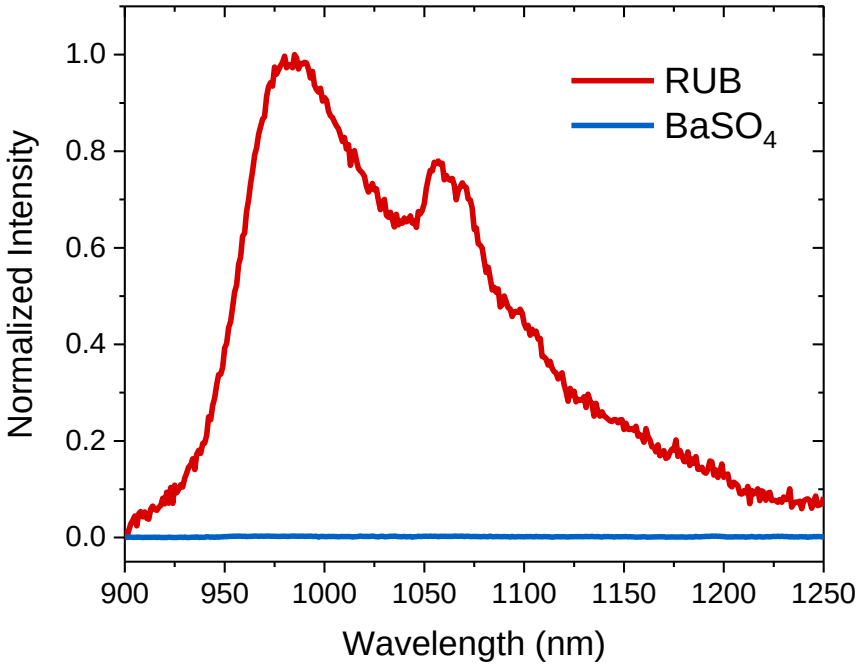

Figure 5.4.2. NIR PL of RUB crystal (red line) and $BaSO_4$ powder (blue line) to show background sensitivity. The PL is excited along the ***b*** axis of the RUB crystal with a vertically polarized 808 nm laser diode and collected through an 850 nm long wave pass filter. The peak at 1060 nm is likely a Raman peak with a separation of 3000 cm^{-1} from the excitation wavelength.

5.5 Photophysical properties of the interband state in RUB

Since the upconverted PL is the most easily detectable signature of the intermediate state, it is used to investigate the nature of this state in more detail. The upconverted PL in crystalline RUB depends upon the polarization of the incident photons (Figure 5.5.1). The vapor transport grown RUB crystals used for this study are orthorhombic in the D_{2h}^{18} point group and the crystallographic axes are defined in the space group *Acam* (*a* = 14.4 Å, *b* = 7.18 Å, *c* = 26.9 Å), consistent with previous studies.[26,35] A distinct anisotropy is observed in the PL intensity induced on the ***ab*** surface with the 980 nm diode laser when the excitation is polarized parallel to different crystallographic axes. Polarizing the excitation light along the ***b*** axis (0°) yields the brightest PL while polarizing along the ***a*** axis (90°) minimizes the PL. However, a similar anisotropy for single crystals was reported by Biaggio and coworkers using a pulsed 772 nm laser, with a factor of 4 enhancement in the upconverted PL when the polarization is aligned parallel to the ***b*** axis.[36] The anisotropy depicted in Figure 5.5.1 is more pronounced than what has been previously reported, with 3 orders of magnitude more intense upconverted PL from exciting with polarization parallel with the ***b*** axis relative to the ***a*** axis. The highly oriented nature of the two-photon transition at 980 nm suggests that it does not originate from a randomly oriented defect or impurity. In addition, exciting the crystal on the ***bc*** facet leads to a similar anisotropy with more intense signal along the ***b*** axis. The signal from the bc

facet was multiplied by a factor of 3 to better illustrate the anisotropy. The ***bc*** facet is only a few microns wide which makes it difficult to produce a symmetrical polar plot; whereas, the ***ab*** facet is typically 1 mm^2 making the polarization dependence much less susceptible to subtle variations in crystal thickness. It is interesting that both facets find the strongest interband mediated 2PA along the ***b*** axis despite the fact that the strongest molecular transition dipole moment corresponds to the ***c*** axis. Furthermore, the highest charge carrier mobilities and longest triplet diffusion lengths are found along the ***b*** axis of the crystal. This suggests that the same intermolecular interactions which lead to favorable transport properties along the ***b*** axis may also contribute to interband mediated 2PA.

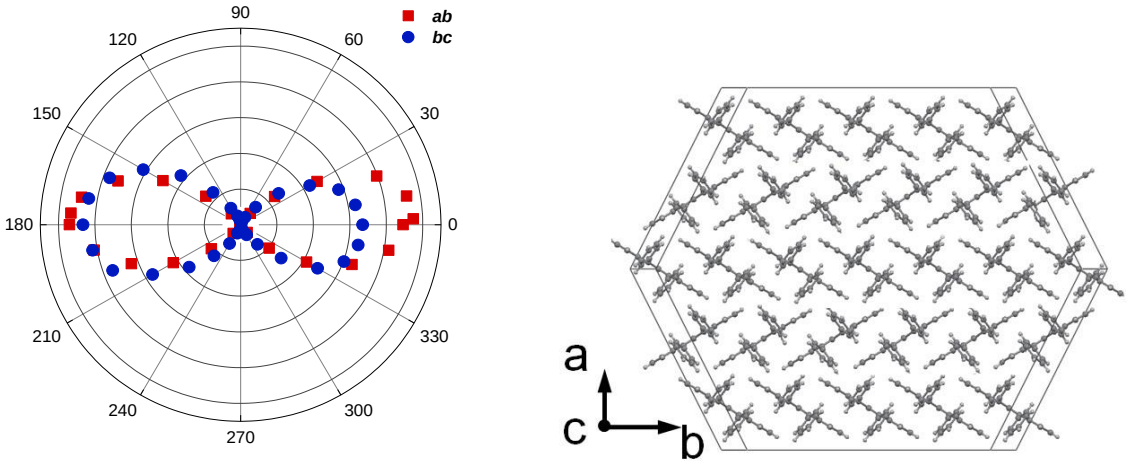

Figure 5.5.1. Polarization dependence of upconverted (visible) PL in crystalline rubrene excited along the ***ab*** (red squares) and ***bc*** (blue circles) facets using 980 nm NIR laser excitation. An angle of zero degrees corresponds to excitation linearly polarized along the ***b*** axis and an angle of 90 degrees corresponds to the crystallographic ***a*** axis (red squares) or the ***c*** axis (blue circles). Crystal packing on the ***ab*** facet of rubrene is shown for clarity.

Additional evidence for the role of a long-live intermediate state is obtained by measuring the upconverted PL intensity as a function of the laser repetition rate. In the

limit of negligible ground state depletion, the PL signal of a material which solely undergoes non-resonant 2PA should show no dependence on the repetition rate of the laser. Each pulse transfers an equal amount of population to the excited state, independent of how quickly the pulses follow each other. If a resonant intermediate state participates in the 2PA process, however, a dependence upon the pulse spacing of the laser will be observed when the lifetime of the intermediate state is comparable to or longer than the pulse spacing.[37,38] The initial pulse populates the excited singlet state through a resonant 2PA processes, but some population will be left in the intermediate state. Between pulses, the intermediate state population will partially decay back to the ground state, but if a pulse arrives before it fully decays, it can transfer population from both S_0 and the intermediate state, increasing the total PL signal. For a resonant 2PA mechanism, the PL signal per pulse should be greater for shorter pulse spacings and gradually decrease as the pulse spacing increases. Indeed, this is observed for single crystals of RUB (Figure 5.5.2). For comparison, the repetition rate dependent PL of TET powder and the laser dye Rhodamine B (Rhod B) in a PMMA matrix were also measured. Both samples show no dependence on the laser repetition rate to within the measurement error, confirming that nonresonant 2PA is the dominant mechanism leading to the PL.

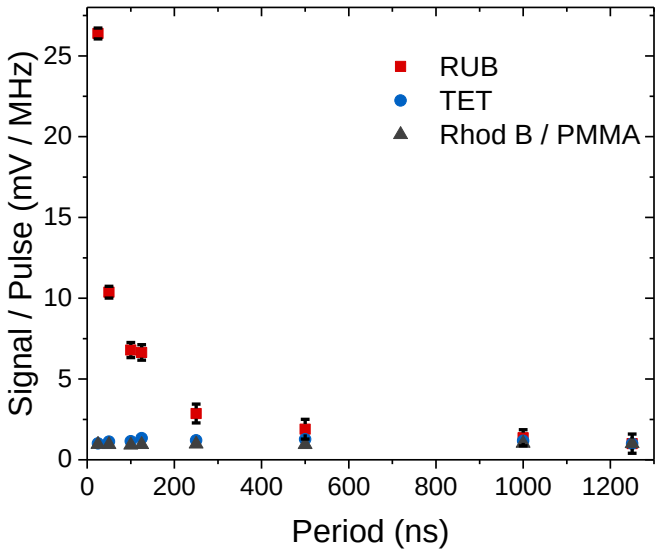

Figure 5.5.2. Dependence of the per-pulse upconverted (visible) PL intensity on the pulse spacing of the exciting NIR laser (800 nm). The error bars represent the standard deviation of 9 separate scans taken on five different spots of the same pristine RUB crystal which was ~100 µm thick (red squares). RUB was excited along the crystallographic ***b*** axis. For comparison, the same data for crystalline TET and the dye Rhodamine B in a polymer show no dependence on pulse period. All measurements were performed under vacuum.

5.6 Intensity-dependent kinetic modeling

In order to quantitatively model the dependence of the PL on laser intensity and repetition rate, a 4-state model outlined in Figure 5.6.1 is implemented. This model leads to the following system of kinetic equations:

$$\frac{dN_{S_0}}{dt} = -\sigma_{0i} I N_{S_0} + k_i N_i + \left(k_2 - k_{fiss}\right) N_{S_1} + k_{trip} N_{T_1} + \left(k_{TTQ} + k_{TTS}\right) {N_{T_1}}^2 \qquad (5.6.1)$$

$$\frac{dN_i}{dt} = \sigma_{0i} I N_{S_0} - \left(\sigma_{i2} I + k_i\right) N_i \qquad (5.6.2)$$

$$\frac{dN_{S_1}}{dt} = \sigma_{i2} I N_i - \left(k_2 + k_{fiss}\right) N_{S_1} + k_{TTS} {N_{T_1}}^2 \qquad (5.6.3)$$

$$\frac{dN_{T_1}}{dt} = -k_{trip} N_{T_1} + 2k_{fiss} N_{S_1} - \left(2k_{TTS} + k_{TTQ}\right) {N_{T_1}}^2 \qquad (5.6.4)$$

In Equations (5.6.1) - (5.6.4), I is the laser intensity (photons·s^{-1}·cm^{-2}), and the absorption cross sections for transitions from $S_0 \rightarrow i$ and $i \rightarrow S_1$ are given by σ_{0i} and σ_{i2}, respectively. The rate k_i describes nonradiative relaxation from $i \rightarrow S_0$, while k_2 represents the radiative relaxation rate from $S_1 \rightarrow S_0$. The rate of singlet fission is given by k_{fiss}, triplet fusion by k_{TTS} and nonradiative relaxation of the triplet by k_{trip}. A triplet quenching term is included, k_{TTQ} describing an interaction between triplets which returns one of them to the ground state, $T_1 + T_1 \rightarrow T_1 + S_0$. The radiative rate, $k_2 = 6.25 \times 10^7$ s^{-1}, is known from time-resolved PL measurements,[10] and k_{trip} is estimated to be 1.67×10^4 s^{-1} based on the decay of the delayed fluorescence signal (Figure 5.1.1) as well as previous measurements by Biaggio and coworkers.[39] Previous work which used pump-probe spectroscopy provides $k_{fiss} = 5 \times 10^{10}$ s^{-1} where the correlation between the decay of singlet induced absorption and the growth of the triplet induced absorption is assigned to singlet fission.[40-43] Exponential fits to the time traces of the singlet and triplet features yield two fission times, the longer time has been taken, which is reported to be approximately 20 ps, to represent k_{fiss} here. The triplet recombination rate, $k_{TTS} = 10^{-12}$ cm^3/s, is also determined from previous work where a lower limit (10^{-13} cm^3/s) was estimated from a fit to the PL decay[39] and a more precise value ($5.4 \pm 1.0 \times 10^{-12}$ cm^3/s) was found from a transient grating measurement.[44] It is assumed that $k_{TTQ} < k_{TTS}$. This leaves σ_{0i}, σ_{i2}, and k_i as the only completely unknown parameters.

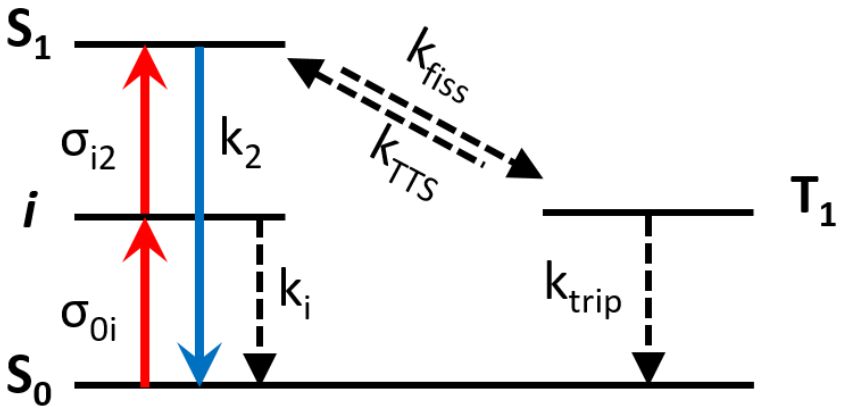

Figure 5.6.1. A Jablonski diagram showing the parameters used in the kinetic model (Equations 2-5). The parameters are described in the text. Fission and fusion produce or annihilate triplets on separate RUB molecules, respectively. Here, the T_1 state represents these separate, degenerate triplets for simplicity. The triplet quenching mechanism described by rate k_{TTQ} is omitted for clarity.

This kinetic model can be used to describe both the intensity dependence of the PL shown in Figure 5.3.4 and the repetition rate dependence shown in Figure 5.5.2. Both measurements depend nonlinearly on the model parameters, so the goal was to find a set of reasonable parameters that could consistently describe both sets of data. It cannot be ruled out that there may exist a different set of parameters that reproduce these data equally well. From numerical simulations, it is found that the detailed shape of the PL signal versus pulse period curve is sensitive to the σ_{0i} and σ_{i2} values as well as k_i. In the low S_0 depletion limit, when less than 1% of the population is excited by each pulse, the decrease of the per-pulse PL signal versus pulse period is not a simple exponential decay. By assuming the ratio $\sigma_{0i}/\sigma_{i2} = 0.01$, Equations (5.6.1) - (5.6.4) can be solved numerically for a train of δ-function pulses. The calculated signals are overlaid with the data in Figure 5.6.2A. A value for the intermediate lifetime $\tau_i = 1/k_i = 1.5$ µs yields a decent match to the

data. Representative curves for other values of τ_i deviated from the data points at long times. This lifetime is long compared to the S_1 state but much shorter than that of the T_1 state as detected via the delayed fluorescence decay (60 µs).

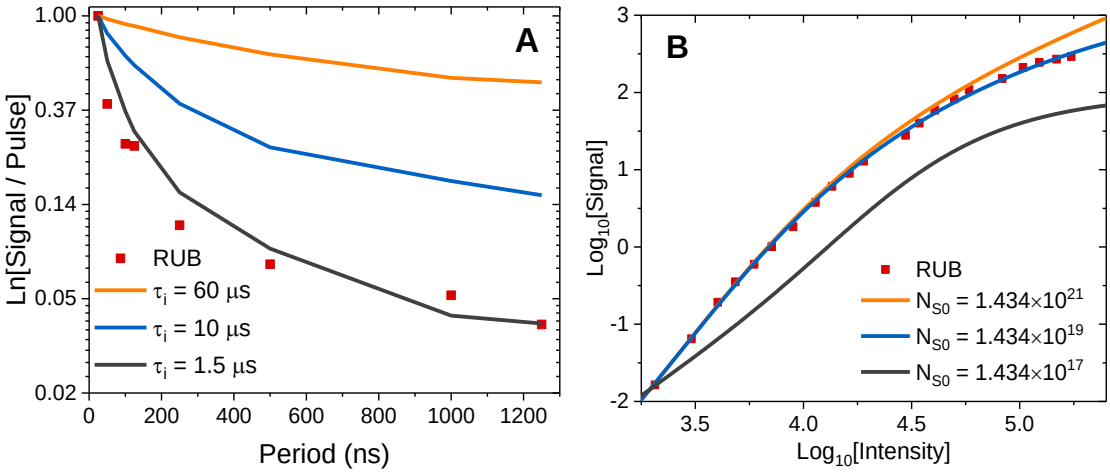

Figure 5.6.2. (A) Modelling of the dependence of the per pulse signal on the period of the laser pulses. The red squares are the data points. The solid lines are calculated with the δ pulse simulation described in the text assuming an intermediate state lifetime (τ_i) of 60 µs (orange), 10 µs (blue), 1.5 µs (black). (B) Modelling of the dependence of the upconverted PL observed in single crystals on average 800 nm laser intensity. The red squares are the data points. The solid lines represent a four-state model described by rate Equations 2-5 in a steady state ($dN_X/dt = 0$) for different interband state densities. $N_{S0}=1.434\times10^{21}$ cm^{-3} assumes that the density of interband states equals the density of RUB molecules in the crystal (orange line). Reducing the interband density by a factor of 10^2 (blue line) leads to a good overlap with the experimental points, while reducing it by a factor of 10^4 (black line) leads to poor overlap. The intensity units for this plot are (photons/ns*µm^2) for computational convenience and multiplying this number by 2.48×10^{-2} gives intensity in W/cm^2 at 800 nm.

The physical origin of the intensity dependence of the PL signal is now examined. At high intensities, the slope of 2 which turns to a slope of 1 can be understood as PL induced by 2PA which begins to saturate at high intensities and has been observed before in other materials.[45] At lower intensities, there is an asymptotic quartic (power exponent 4) dependence on laser intensity that is more surprising. This type of intensity dependence has been observed previously in anthracene, however.[46,47] It arises because

the PL due to TTA is proportional to the square of the triplet population, which in turn is proportional to the initial singlet population. Since the initial singlet population generated via 2PA is also proportional to the square of the incident intensity, the delayed PL is expected to have a quartic dependence on the laser intensity, as observed. It is important to emphasize that this quartic intensity dependence is a general phenomenon that should be observed any time a triplet population that undergoes TTA is created by 2PA.

To analyze the intensity dependence quantitatively, k_i = 0.67 μs^{-1} is fixed to be consistent with the repetition rate data. Assuming a CW laser excitation at 800 nm with constant steady-state densities of all the involved species, dN_x/dt is set to zero and Equations (5.6.1) - (5.6.4) are solved for the equilibrium populations at a fixed laser intensity *I*. First it is assumed that $N_{S0}(0) = 1.434 \times 10^{21}$ molecules/cm^3, the density of molecules in a pure RUB crystal. In this case, the best match to the data is obtained when $\sigma_{0i} = 2 \times 10^{-20}$ cm^2 and $\sigma_{i2} = 2 \times 10^{-16}$ cm^2, but these parameters could not reproduce the saturation behavior at the highest intensities (Figure 5.6.2). The calculated signal did not turn over as quickly as the experimental signal at the highest intensities. In view of the low absorbance of the samples in this wavelength range, increasing the σ_{0i} value did not seem reasonable. Instead, the $N_{S0}(0)$ value was lowered, and an improved fit to the data was found when $N_{S0}(0) = 1.44 \times 10^{19}$ molecules/cm^3 with $\sigma_{0i} = 2 \times 10^{-18}$ cm^2 and $\sigma_{i2} = 2 \times 10^{-16}$ cm^2. The lower $N_{S0}(0)$ value corresponds to a 1% concentration of sites with an enhanced $0 \rightarrow i$ absorption. The linear absorbance, proportional to $N_{S0}(0) \times \sigma_{0i}$, remains the same. But the nonlinear intensity curve is quite sensitive to the change: as the number of

participating ground state molecules is decreased, it becomes easier to saturate the system by putting all of them in an excited state. The PL curve now rolls over at lower intensities and more closely matches the data.

These calculations also confirm that the I^4 dependence of the PL arises from the combination of 2PA and TTA, both of which contribute a factor of I^2 to the emissive S_1 population. When k_{fiss} = 0 and no T_1 population is produced, we observe only an I^2 dependence over the whole intensity range (Figure 5.6.3). The existence of singlet fission in RUB serves to suppress the contribution of the initially excited S_1 population to the overall PL signal, making PL generated by TTA the dominant component, as surmised by previous workers.[4,48] The I^4 dependence for a 2PA process is to be expected for any system in which TTA is the dominant contributor to the PL. Finally, we emphasize that the parameters in Table 5.6.1 should be interpreted with caution. For example, in most cases changing the parameter by a factor of 2 did not generate a large deviation from the data. The graphs in Figure 5.6.3 illustrate the sensitivity of the calculated intensity dependence on different model parameters.

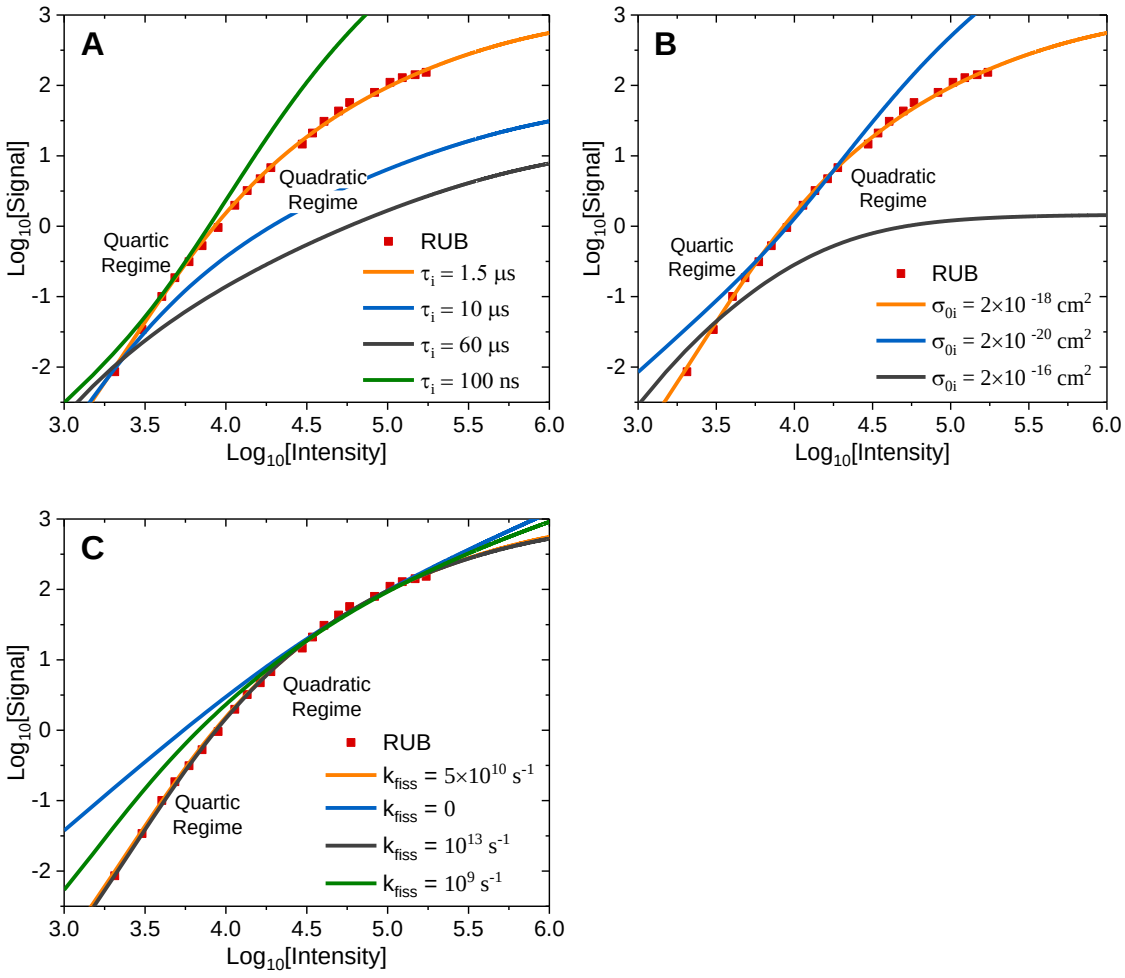

Figure 5.6.3. Log-log plots comparing the intensity dependence of the upconverted PL obtained with the model (solid lines) described in the main text and the experimental data (red squares). Here we explore the sensitivity of the model to changes in (A) the intermediate state lifetime (τ_i), (B) the cross section of the intermediate state (σ_{0i}), and (C) the rate of singlet fission (k_{fiss}). For each plot, only the indicated variable is changed while all other parameters are kept the same as reported in table 2 in the main text. In each plot the region associated with an I^4 dependence is identified as the quartic regime and the I^2 dependent region is identified as the quadratic regime. The intensity of the 800 nm radiation for each plot is given in photons/ns×μm^2 which can be converted to W/cm^2 by multiply the intensity by 2.48×10^{-2}. The model is quite sensitive to the lifetime of the intermediate state with longer lifetimes causing the intensity dependent curve to saturate too quickly without capturing either the quartic or quadratic regimes; whereas, a shorter lifetime leads to a curve with a steeper dependence on the intensity that does not saturate quickly enough. The model is also sensitive to the magnitude of the intermediate cross section showing fast saturation and poor agreement with the experimental data with the largest cross section. A smaller cross section is able to describe the experimental data over part of the quartic and quadratic regions, but does not capture the saturation. The model is least sensitive to the rate of singlet fission where fs and ps fission rates both show good agreement with the experimental data over the whole range of intensities. The ns fission time deviates from the data at low and high intensities; whereas, turning off fission altogether does not describe the data well and leads to a curve that exhibits a slope of 2 which saturates at high intensity.

k_i (s^{-1})	k_2 (s^{-1})	k_{fiss} (s^{-1})	k_{trip} (s^{-1})	k_{TTS} (cm^3 /s)	k_{TTQ} (cm^3 /s)	σ_{0i} (cm^2)	σ_{i2} (cm^2)
6.67×10^5	6.25×10^7	5×10^{10}	1.67×10^4	10^{-12}	10^{-14}	2×10^{-18}	2×10^{-16}

Table 5.6.1. The parameters used for the kinetic model described in the text that reproduce data in Figure 5.6.2. It must be emphasized that these parameters are not the result of a linear-least squares fit but are derived from literature sources and constraints described in the text.

5.7 What leads to an interband state in crystalline RUB?

The identity of the low energy interband state in RUB is the most interesting question raised by this work. One obvious candidate is the unperturbed molecular T_1 state. However, this state is unlikely for several reasons. First, the anisotropy in Figure 5.5.1 suggests that the $S_0 \rightarrow i$ transition is not oriented along the short axis of the molecule, which lies along the direction of light propagation, perpendicular to the ***ab*** crystal face. If we assume that the $S_0 \rightarrow T_1$ transition in RUB is similar to that of anthracene and lies along the short molecular axis,[49] it would not couple to the light incident perpendicular to the ***ab*** face and would not be expected to show a strong anisotropy. Second, the $S_0 \rightarrow T_1$ cross section for molecular RUB has not been measured, but it can safely be assumed to be less than 10^{-21} cm^2 based on measurements performed here, much smaller than the values of σ_{0i} needed to fit our data. Third, from the measurements of the delayed fluorescence lifetime, the bulk crystal T_1 lifetime is too long to be consistent with the $\underline{\tau_i}$ value obtained for the interband state. Finally, in dilute solution, molecular RUB acts as a normal chromophore that undergoes nonresonant 2PA. Furthermore, if there were significant

absorption directly to the T_1 state, TTA could only generate an I^2 dependence at low intensities, not the observed I^4 dependence.

Although the unperturbed $S_0 \rightarrow T_1$ transition has negligible oscillator strength at the molecular level, there is evidence that intermolecular interactions can enhance this oscillator strength. One example is the noncovalent association of O_2 to a conjugated molecule, which can enhance its $S_0 \rightarrow T_1$ transition via a charge-transfer interaction,[50,51] resulting in absorption coefficients on the order of 100 $M^{-1}cm^{-1}$ in pressurized solutions.[52] It is unlikely that O_2 plays a role in the current experiments, since exposing the crystals to a vacuum of 10^{-5} Torr for 48 hours did not reduce the upconverted PL signal. Furthermore, O_2 has a low energy singlet state at ~8000 cm^{-1} that is known to act as an energy acceptor for RUB triplet states, an O_2 defect would be expected to quench the TTA.[53] But O_2 is not the only molecule that can lead to this effect. Adding a small amount of 2-methylanthracene to an anthracene crystal has been shown to enhance its phosphorescence yield by an order of magnitude.[54] This result suggests that interactions between conjugated molecules can also affect the $S_0 \rightarrow T_1$ transition, although the mechanism has not been investigated in any detail.

Given that the upconversion effect is observed for samples of varying purity and under different atmospheres, it is unlikely that it results from an extrinsic impurity molecule. Instead, the most likely explanation is that the interband state arises from some defect that is present in RUB itself. One possibility is that intermolecular interactions involving only RUB molecules could be responsible for the enhanced 2PA. RUB can

crystallize in a variety of polymorphs[55] and its PL spectrum is highly sensitive to different preparation conditions.[26,56] These facts suggest that RUB single crystals can possess a variety of internal molecular packing configurations, and it is possible that one or more of these configurations leads to an enhanced $S_0 \rightarrow T_1$ transition. A second possibility is that chemically modified RUB molecules give rise to interband states. Recent theoretical work has shown that atomic defects generated by O or H-atom insertion into pentacene and RUB molecules can induce interband states, although the spin multiplicity of these states is not specified.[57,58] Irkhin et al. used H bombardment to introduce a high concentration of such defects into a RUB crystal and found that they lowered the triplet lifetime to ~1 μs, close to what we obtain for the intermediate state.[59] In the samples studied here, such defective molecules would be present in much lower concentrations and would not affect the bulk triplet lifetime. Chemical defects can also be introduced during an experiment. When organic crystals are exposed to high-vacuum gauges in vacuum chambers, certain defects (traps) can be created at the surface of the crystals.[60] However, these vacuum-induced surface traps are an unlikely origin of the interband absorption, since it is present in air, under vacuum, and also in inert gas atmospheres.

Finally, it is noted that these mechanisms are not mutually exclusive. For example, a chemically modified RUB molecule could also give rise to defective packing at specific sites within the crystal. Such sites would still have a well-defined orientation that leads to highly anisotropic absorption, as observed. A triplet on such a site would also be expected to have a different energy than that of the bulk triplet excitons. This site would act as a

2PA "hotspot," producing singlets that rapidly fission and produce at least one mobile triplet that can diffuse and undergo TTA to generate the delayed fluorescence signal. It is possible that the different molecular configuration at this site would also affect the rates of other photophysical processes. This would explain why the interband state lifetime, τ_i = 1.5 μs, is shorter than that measured for bulk triplets. Characterizing the structure of such defect sites will be a challenge for future investigations.

5.8 Conclusion

This work shows that crystalline RUB supports a NIR 2PA process that generates upconverted PL in the visible range even using low power CW laser excitation. The upconverted luminescence is readily observed by eye. The origin of this enhanced 2PA process is a resonant interband state with a lifetime of 1.5 μs. After absorption, a model that assumes the singlets undergo fission and then triplet-triplet annihilation can reproduce the intensity dependence of the PL signal specifically the $I^4 \rightarrow I^2$ which has been seen before in anthracene crystals. Our results suggest that the interband state that facilitates the 2PA arises from a low concentration species. The generality of this effect suggests that this species is not an extrinsic impurity molecule like O_2, but possibly a chemically modified RUB molecule or packing defect. It is hypothesized that this species can enhance oscillator strength to the $S_0 \rightarrow T_1$ optical transition. However, it should be stressed that the precise origin of this interband state and its oscillator strength has not

been conclusively determined, and further experiments, for example a careful measurement of the PL excitation spectrum, will be necessary to establish its exact nature. Such investigations are warranted, since the results in this paper suggest that it may be possible to design interband states in purely organic molecular solids with useful photophysical properties.

5.9 References

(1) Shockley, W.; Queisser, H. J. Detailed Balance Limit of Efficiency of p-n Junction Solar Cells. *J Appl Phys* **1961,** *32* (3), 510.

(2) Shpaisman, H.; Niitsoo, O.; Lubomirsky, I.; Cahen, D. Can up- and down-conversion and multi-exciton generation improve photovoltaics? *Sol. Energy Mater. Sol. Cells* **2008,** *92* (12), 1541.

(3) Congreve, D. N.; Lee, J.; Thompson, N. J.; Hontz, E.; Yost, S. R.; Reusswig, P. D.; Bahlke, M. E.; Reineke, S.; Van Voorhis, T.; Baldo, M. A. External Quantum Efficiency Above 100% in a Singlet-Exciton-Fission–Based Organic Photovoltaic Cell. *Science* **2013,** *340* (6130), 334.

(4) Biaggio, I.; Irkhin, P. Extremely efficient exciton fission and fusion and its dominant contribution to the photoluminescence yield in rubrene single crystals. *Applied Physics Letters* **2013,** *103* (26), 263301.

(5) Bera, K.; Douglas, C. J.; Frontiera, R. R. Femtosecond Raman Microscopy Reveals Structural Dynamics Leading to Triplet Separation in Rubrene Singlet Fission. *J. Phys. Chem. Lett.* **2017,** *8* (23), 5929.

(6) Sutton, C.; Tummala, N. R.; Beljonne, D.; Brédas, J.-L. Singlet Fission in Rubrene Derivatives: Impact of Molecular Packing. *Chem. Mater.* **2017,** *29* (7), 2777.

(7) Breen, I.; Tempelaar, R.; Bizimana, L. A.; Kloss, B.; Reichman, D. R.; Turner, D. B. Triplet Separation Drives Singlet Fission after Femtosecond Correlated Triplet Pair Production in Rubrene. *J. Am. Chem. Soc.* **2017,** *139* (34), 11745.

(8) Piland, G. B.; Burdett, J. J.; Kurunthu, D.; Bardeen, C. J. Magnetic Field Effects on Singlet Fission and Fluorescence Decay Dynamics in Amorphous Rubrene. *J. Phys. Chem. C* **2013,** *117* (3), 1224.

(9) Singh-Rachford, T. N.; Castellano, F. N. Photon upconversion based on sensitized triplet–triplet annihilation. *Coord. Chem. Rev.* **2010,** *254* (21–22), 2560.

(10) Huang, Z.; Li, X.; Mahboub, M.; Hanson, K. M.; Nichols, V. M.; Le, H.; Tang, M. L.; Bardeen, C. J. Hybrid Molecule–Nanocrystal Photon Upconversion Across the Visible and Near-Infrared. *Nano Letters* **2015,** *15* (8), 5552.

(11) Nienhaus, L.; Wu, M.; Geva, N.; Shepherd, J. J.; Wilson, M. W. B.; Bulović, V.; Van Voorhis, T.; Baldo, M. A.; Bawendi, M. G. Speed Limit for Triplet-Exciton Transfer in Solid-State PbS Nanocrystal-Sensitized Photon Upconversion. *ACS Nano* **2017,** *11* (8), 7848.

(12) Wu, T. C.; Congreve, D. N.; Baldo, M. A. Solid state photon upconversion utilizing thermally activated delayed fluorescence molecules as triplet sensitizer. *Applied Physics Letters* **2015,** *107* (3), 031103.

(13) Sripathy, K.; MacQueen, R. W.; Peterson, J. R.; Cheng, Y. Y.; Dvorak, M.; McCamey, D. R.; Treat, N. D.; Stingelin, N.; Schmidt, T. W. Highly efficient photochemical upconversion in a quasi-solid organogel. *Journal of Materials Chemistry C* **2015,** *3* (3), 616.

(14) Liu, H.; Yan, F.; Li, W.; Lee, C.-S.; Chu, B.; Chen, Y.; Li, X.; Han, L.; Su, Z.; Zhu, J.et al. Up-conversion luminescence of crystalline rubrene without any sensitizers. *Org. Electron.* **2010,** *11* (5), 946.

(15) Sailaja, R.; Bisht, P. B.; Singh, C. P.; Bindra, K. S.; Oak, S. M. Influence of multiphoton events in measurement of two-photon absorption cross-sections and optical nonlinear parameters under femtosecond pumping. *Opt Commun* **2007,** *277* (2), 433.

(16) Wolleschensky, R.; Feurer, T.; Sauerbrey, R.; Simon, U. Characterization and optimization of a laser-scanning microscope in the femtosecond regime. *Appl Phys B* **1998,** *67* (1), 87.

(17) Makarov, N. S.; Drobizhev, M.; Rebane, A. Two-photon absorption standards in the 550–1600 nm excitation wavelength range. *Opt Express* **2008,** *16* (6), 4029.

(18) Fischer, A.; Cremer, C.; Stelzer, E. H. K. Fluorescence of coumarins and xanthenes after two-photon absorption with a pulsed titanium–sapphire laser. *Appl. Opt.* **1995,** *34* (12), 1989.

(19) Xu, C.; Webb, W. W. Measurement of two-photon excitation cross sections of molecular fluorophores with data from 690 to 1050 nm. *Journal of the Optical Society of America B* **1996,** *13* (3), 481.

(20) Lee, S.; Thomas, K. R. J.; Thayumanavan, S.; Bardeen, C. J. Dependence of the Two-Photon Absorption Cross Section on the Conjugation of the Phenylacetylene Linker in Dipolar Donor−Bridge−Acceptor Chromophores. *J. Phys. Chem. A* **2005,** *109* (43), 9767.

(21) Rumi, M.; Perry, J. W. Two-photon absorption: an overview of measurements and principles. *Adv. Opt. Photon.* **2010,** *2* (4), 451.

(22) Webman, I.; Jortner, J. Energy Dependence of Two-Photon-Absorption Cross Sections in Anthracene. *J. Chem. Phys.* **1969,** *50* (6), 2706.

(23) Birks, J. B. *Photophysics of Aromatic Molecules*; Wiley - Interscience: New York, 1970.

(24) Grabolle, M.; Spieles, M.; Lesnyak, V.; Gaponik, N.; Eychmüller, A.; Resch-Genger, U. Determination of the Fluorescence Quantum Yield of Quantum Dots: Suitable Procedures and Achievable Uncertainties. *Anal. Chem.* **2009,** *81* (15), 6285.

(25) Murov, S. L. C., Ian; Hug, Gordon L. *Handbook of Photochemistry*; 2nd ed.; Marcel Dekker, Inc.: New York, 1993.

(26) Irkhin, P.; Ryasnyanskiy, A.; Koehler, M.; Biaggio, I. Absorption and photoluminescence spectroscopy of rubrene single crystals. *Phys. Rev. B* **2012,** *86* (8), 085143.

(27) Nakashima, T. T.; Offen, H. W. Crystal Spectra of Tetracene and Rubrene under Pressure. *J. Chem. Phys.* **1968,** *48* (11), 4817.

(28) Yamagata, H.; Norton, J.; Hontz, E.; Olivier, Y.; Beljonne, D.; Brédas, J. L.; Silbey, R. J.; Spano, F. C. The nature of singlet excitons in oligoacene molecular crystals. *J. Chem. Phys.* **2011,** *134* (20), 204703.

(29) Lim, S.-H.; Bjorklund, T. G.; Spano, F. C.; Bardeen, C. J. Exciton Delocalization and Superradiance in Tetracene Thin Films and Nanoaggregates. *Phys. Rev. Lett.* **2004,** *92* (10), 107402.

(30) Port, H.; Rund, D. Temperature dependent triplet absorption spectra of anthracene crystals. Photoexcitation spectroscopy with a dye-laser. *Chem Phys Lett* **1978,** *54* (3), 474.

(31) Vaubel, G.; Baessler, H. Delayed Fluorescence and Triplet Lifetime in Tetracene Crystals. *physica status solidi (b)* **1970,** *37* (1), K31.

(32) Peticolas, W. L. Multiphoton Spectroscopy. *Annu. Rev. Phys. Chem.* **1967,** *18* (1), 233.

(33) Wu, C. W., W. W. In *Top. Fluoresc. Spectrosc.*; Lakowicz, J. R., Ed.; Plenum Press: New York, 1997; Vol. 5: Nonlinear and Two-Photon-Induced Fluorescence.

(34) Manifacier, J. C.; Gasiot, J.; Fillard, J. P. A simple method for the determination of the optical constants n, k and the thickness of a weakly absorbing thin film. *Journal of Physics E: Scientific Instruments* **1976,** *9* (11), 1002.

(35) Podzorov, V.; Menard, E.; Borissov, A.; Kiryukhin, V.; Rogers, J. A.; Gershenson, M. E. Intrinsic Charge Transport on the Surface of Organic Semiconductors. *Phys. Rev. Lett.* **2004,** *93* (8), 086602.

(36) Irkhin, P.; Biaggio, I. Two-photon absorption spectroscopy of rubrene single crystals. *Phys. Rev. B* **2014,** *89* (20), 201202.

(37) Jiang, X.-F.; Pan, Y.; Jiang, C.; Zhao, T.; Yuan, P.; Venkatesan, T.; Xu, Q.-H. Excitation Nature of Two-Photon Photoluminescence of Gold Nanorods and Coupled Gold Nanoparticles Studied by Two-Pulse Emission Modulation Spectroscopy. *J. Phys. Chem. Lett.* **2013,** *4* (10), 1634.

(38) Ippen, E. P.; Shank, C. V.; Woerner, R. L. Picosecond dynamics of azulene. *Chem Phys Lett* **1977,** *46* (1), 20.

(39) Ryasnyanskiy, A.; Biaggio, I. Triplet exciton dynamics in rubrene single crystals. *Phys. Rev. B* **2011,** *84* (19), 193203.

(40) Ishibashi, Y.; Inoue, Y.; Asahi, T. The excitation intensity dependence of singlet fission dynamics of a rubrene microcrystal studied by femtosecond transient microspectroscopy. *Photochemical & Photobiological Sciences* **2016,** *15* (10), 1304.

(41) Ma, L.; Zhang, K.; Kloc, C.; Sun, H.; Michel-Beyerle, M. E.; Gurzadyan, G. G. Singlet fission in rubrene single crystal: direct observation by femtosecond pump-probe spectroscopy. *Phys. Chem. Chem. Phys.* **2012,** *14* (23), 8307.

(42) Miyata, K.; Kurashige, Y.; Watanabe, K.; Sugimoto, T.; Takahashi, S.; Tanaka, S.; Takeya, J.; Yanai, T.; Matsumoto, Y. Coherent singlet fission activated by symmetry breaking. *Nat. Chem.* **2017,** *9*, 983.

(43) Ma, L.; Galstyan, G.; Zhang, K.; Kloc, C.; Sun, H.; Soci, C.; Michel-Beyerle, M. E.; Gurzadyan, G. G. Two-photon-induced singlet fission in rubrene single crystal. *J. Chem. Phys.* **2013,** *138* (18), 184508/1.

(44) Ward, K. A.; Richman, B. R.; Biaggio, I. Nanosecond pump and probe observation of bimolecular exciton effects in rubrene single crystals. *Appl. Phys. Lett.* **2015,** *106* (22), 223302/1.

(45) Wang, C. H.; Tai, O. Y.-H.; Wang, Y.; Tsai, T.-H.; Chang, N.-C. Non-quadratic-intensity dependence of two-photon absorption induced fluorescence of organic chromophores in solution. *J. Chem. Phys.* **2005,** *122* (8), 084509.

(46) Singh, S.; Jones, W. J.; Siebrand, W.; Stoicheff, B. P.; Schneider, W. G. Laser Generation of Excitons and Fluorescence in Anthracene Crystals. *J. Chem. Phys.* **1965,** *42* (1), 330.

(47) Silver, M.; Zahlan, A. B. Intensity Dependence of Laser-Induced Delayed Fluorescence. *J. Chem. Phys.* **1964,** *40* (5), 1458.

(48) Ma, L.; Zhang, K.; Kloc, C.; Sun, H.; Soci, C.; Michel-Beyerle, M. E.; Gurzadyan, G. G. Fluorescence from rubrene single crystals: Interplay of singlet fission and energy trapping. *Phys. Rev. B* **2013,** *87* (20), 201203.

(49) Padhye, M. R.; McGlynn, S. P.; Kasha, M. Lowest Triplet State of Anthracene. *J. Chem. Phys.* **1956,** *24* (3), 588.

(50) Tsubomura, H.; Mulliken, R. S. Molecular Complexes and their Spectra. XII. Ultraviolet Absorption Spectra Caused by the Interaction of Oxygen with Organic Molecules1. *J. Am. Chem. Soc.* **1960,** *82* (23), 5966.

(51) Kristiansen, M.; Scurlock, R. D.; Iu, K. K.; Ogilby, P. R. Charge-transfer state and singlet oxygen (1.DELTA.g O2) production in photoexcited organic molecule-molecular oxygen complexes. *J. Phys. Chem.* **1991,** *95* (13), 5190.

(52) Evans, D. F. 257. Perturbation of singlet-triplet transitions of aromatic molecules by oxygen under pressure. *Journal of the Chemical Society (Resumed)* **1957**, DOI:10.1039/JR9570001351 10.1039/JR9570001351(0), 1351.

(53) Darmanyan, A. P. Laser photolysis study of the mechanism of rubrene quenching by molecular oxygen. *Chem Phys Lett* **1982,** *86* (4), 405.

(54) Brillante, A.; Craig, D. P.; Mau, A. W. H.; Rajikan, J. Impurity induced phosphorescence in anthracene crystal. *Chem Phys Lett* **1975,** *30* (1), 5.

(55) Jurchescu, O. D.; Meetsma, A.; Palstra, T. T. M. Low-temperature structure of rubrene single crystals grown by vapor transport. *Acta Crystallographica Section B* **2006,** *62* (2), 330.

(56) Chen, Y.; Lee, B.; Fu, D.; Podzorov, V. The Origin of a 650 nm Photoluminescence Band in Rubrene. *Adv. Mater. (Weinheim, Ger.)* **2011,** *23* (45), 5370.

(57) Northrup, J. E.; Chabinyc, M. L. Gap states in organic semiconductors: Hydrogen- and oxygen-induced states in pentacene. *Phys. Rev. B* **2003,** *68* (4), 041202.

(58) Tsetseris, L.; Pantelides, S. T. Large impurity effects in rubrene crystals: First-principles calculations. *Phys. Rev. B* **2008,** *78* (11), 115205.

(59) Irkhin, P.; Biaggio, I.; Zimmerling, T.; Dobeli, M.; Batlogg, B. Defect density dependent photoluminescence yield and triplet diffusion length in rubrene. *Appl. Phys. Lett.* **2016,** *108* (6), 063302/1.

(60) Podzorov, V.; Menard, E.; Pereversev, S.; Yakshinsky, B.; Madey, T.; Rogers, J. A.; Gershenson, M. E. Interaction of organic surfaces with active species in the high-vacuum environment. *Applied Physics Letters* **2005,** *87* (9), 093505.

Chapter 6: Singlet fission in tetracene single crystals – the effect of temperature on the dynamics of fission and the nature of the correlated triplet pair state

As mentioned in section 1.4, one central mechanistic detail of singlet fission which is still up for debate is the nature of the correlated triplet pair state, ^{1}(TT). While it is well accepted that fission must proceed through such a state, it is unclear how this state decays. Do the triplets diffuse through the sample as ^{1}(TT) and only separate after decoherence, or do the triplets diffuse independently while maintaining spin entanglement, ^{1}(T-----T)? Understanding how ^{1}(TT) decays into separate triplets, $T_1 + T_1$, has important implications for the applicability of multiexciton generation to solar energy technologies. In addition, if the triplets are able to diffuse independently while remaining spin entangled, then fission materials may also find use in emerging spintronic and quantum computing applications. Of the proposed pathways for ^{1}(TT) decay, separation into free triplets is believed to be the dominant pathway;[1-6] however recent reports also suggest that ^{1}(TT) can decay both radiatively[4,7,8] and nonradiatively[9] to the ground state. Identifying commonalities of ^{1}(TT) behavior in fission materials is a crucial goal for the field.

Recently, Sirringhaus and coworkers identified a general trend in polyacenes which undergo fission. Regardless of the polycrystalline material, they determined that the triplet pair state is bound with a binding energy of $\sim$ 30 meV relative to free triplets.[7] By monitoring the photoluminescence of thin film samples, they noticed that the 0-0

component of the spectra decreased with time leaving only a redshifted component. This redshifted emission became more prominent at lower temperatures, and the kinetics of this peak matched that of a transient absorption feature that was ascribed to ^{1}(TT) which was extracted with a spectral decomposition technique. Weak quantum beats were extracted from the photoluminescence decay and the envelope of the beating could be described by the kinetics of the ^{1}(TT) decay. Furthermore, the generation of free triplets from ^{1}(TT) showed a dependence on temperature. These results led them to conclude that the redshifted component of the photoluminescence spectra was the result of emission from ^{1}(TT) and that the temperature dependence required to form free triplets meant that ^{1}(TT) in polyacenes always lies lower in energy than the excited singlet and free triplets.

These sweeping conclusions are quite surprising considering that singlet fission in tetracene is endoergic.[10-14] Equally surprising is the claim that ^{1}(TT) can be clearly identified in time resolved photoluminescence spectra. Emission from a doubly excited state requires a simultaneous two-electron transfer to the ground state in order to yield a photon. While Sirringhaus and coworkers cite a Herzberg-Teller mechanism for the efficient photoluminescence, it is not clear how ^{1}(TT) would show such strong emission when it lies so close to S_1 energetically. Presumably any contribution to the emission from ^{1}(TT) would be overwhelmed by emission from S_1. Additionally, the prominence of this feature at low temperature suggests another more likely origin – defect emission. Fission in tetracene has shown an extreme dependence on sample morphology, in particular,

with fission times ranging between tens of picoseconds[15-19] to hundreds of picoseconds.[11,20-24] The faster fission times are typically reported in thin film samples whereas single crystals tend to have longer fission times. Such varied results with a seeming dependence on sample preparation suggests that at least two pathways of singlet fission may be operative in tetracene – an uphill pathway which is dominant in single crystals of tetracene and a defect-mediated pathway which dominates samples with ill-defined sample morphology. The subsequent sections will focus on recent efforts to understand the mechanism of singlet fission and the decay of ^{1}(TT) in single crystals of tetracene over a temperature range of 20 – 500 K.

6.1 Temperature dependence of the photoluminescence spectra

The room temperature photoluminescence (PL) spectrum for a thin crystalline sample of tetracene excited on the *ab* facet with 400 nm is shown in figure 6.1.1. The 0-0 peak at 535 nm is clearly visible while the 0-1 transition appears as a shoulder centered at 570 nm. This spectrum is reproducible in the solution grown tetracene crystals used in this work and is a good indicator that the crystals are ultrathin, since thicker crystal will lead to a diminished 0-0 peak due to self-absorption.

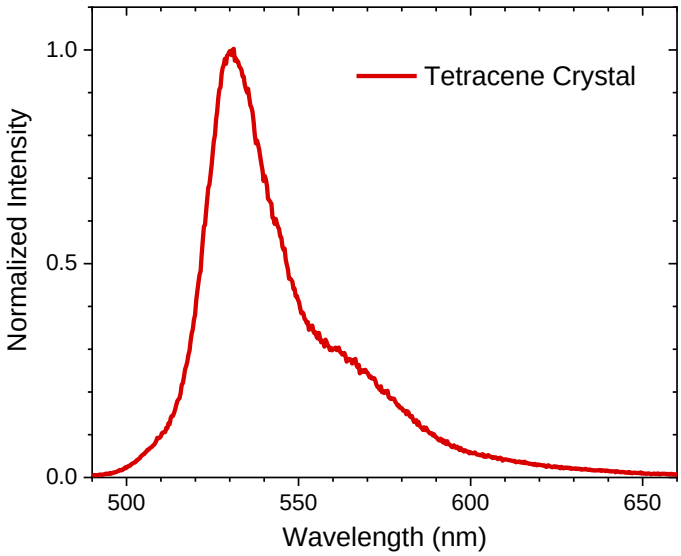

Figure 6.1.1. The room temperature PL spectrum of crystalline tetracene excited with 400 nm.

The high temperature PL spectra of crystalline tetracene is shown in figure 6.1.2A. The intensity of the 0-0 peak diminishes with increasing temperature, which is expected for a J-type aggregate like tetracene.[25,26] Because the crystal is sealed and covered in fomblin oil (See section 2.1.5), at temperatures of 450 K and above the crystal begins to dissolve and monomeric tetracene begins to contribute to the spectrum. At cryogenic temperatures more J-type aggregate behavior is observed in short time windows as evidenced by the strong enhancement of the 0-0 peak relative to the 0-1 (Figure 6.1.2B).[25,26] In longer time windows, more of the red feature is present as the temperature is decreased (Figure 6.1.3). Of interest is the interplay between these two features when the spectral slices are analyzed at different points of the decay. Beginning at 150 K a transient red feature appears centered around 615 nm. At this temperature the feature is broad and featureless and by 100 ns the original spectrum is all that is

detected. This changes at lower temperatures where the red feature has some structure and is centered closer to the 0-1 peak at 570 nm. The original spectrum is regenerated at times longer than 100 ns for 77 K, but below 77 K the original spectrum is never recovered although the 0-0 peak does show some resurgence at 50 and 20 K. The mechanism underpinning this behavior is not clear, but it likely is the result of lower energy defects within the crystal. This would explain why the red feature is more persistent at 50 and 20 K; whereas, the prompt spectrum is recovered for 150 and 77 K. The fact that transient red feature appears at temperatures near 150 K and below may also be the result of a phase change within the crystal, which has been previously reported to occur at 140 K.[27] Since the original spectrum is recovered at moderately cold temperatures (T >77 K), it seems unlikely that the redshifted emission is the result of ^{1}(TT) since it should not be able to thermally access the singlet state at these temperatures. To gather more information on the dynamics of ^{1}(TT) time resolved measurements are performed next.

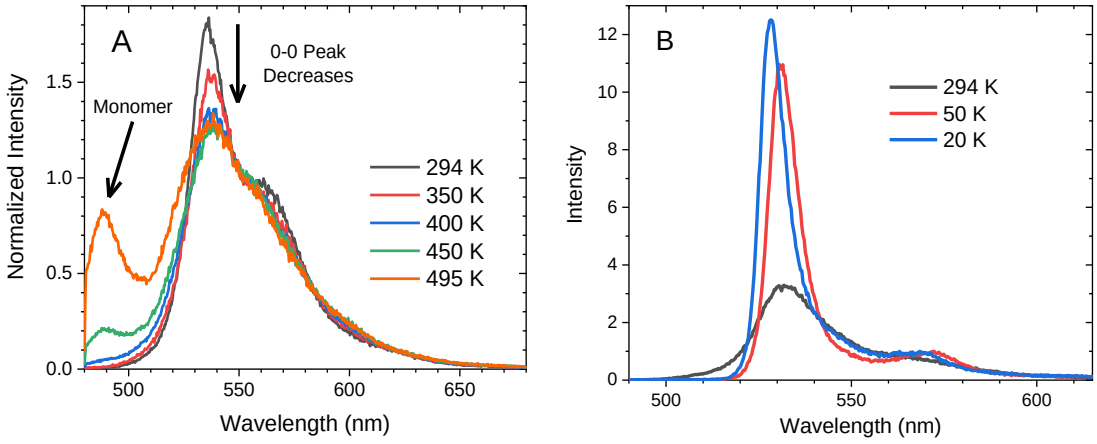

Figure 6.1.2. (A) The high temperature PL spectra compared to room temperature integrated over all time in a 10 ns window. (B) The low temperature PL spectra compared to room temperature integrated over all time in a 1 ns window.

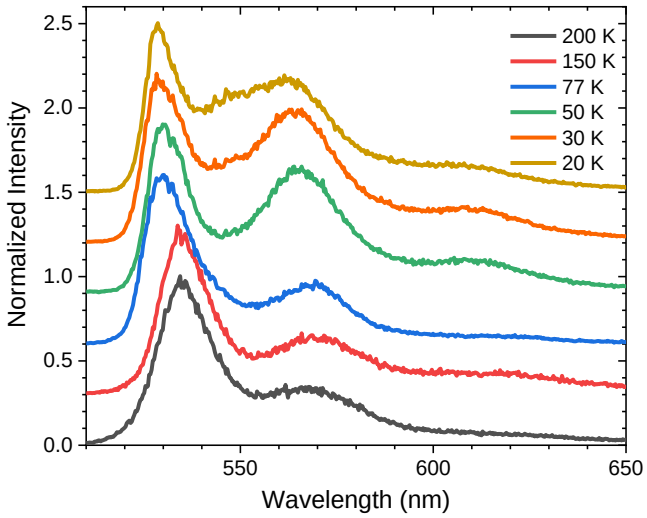

Figure 6.1.3. Offset PL spectra of crystalline tetracene integrated over all time in a 1 µs window.

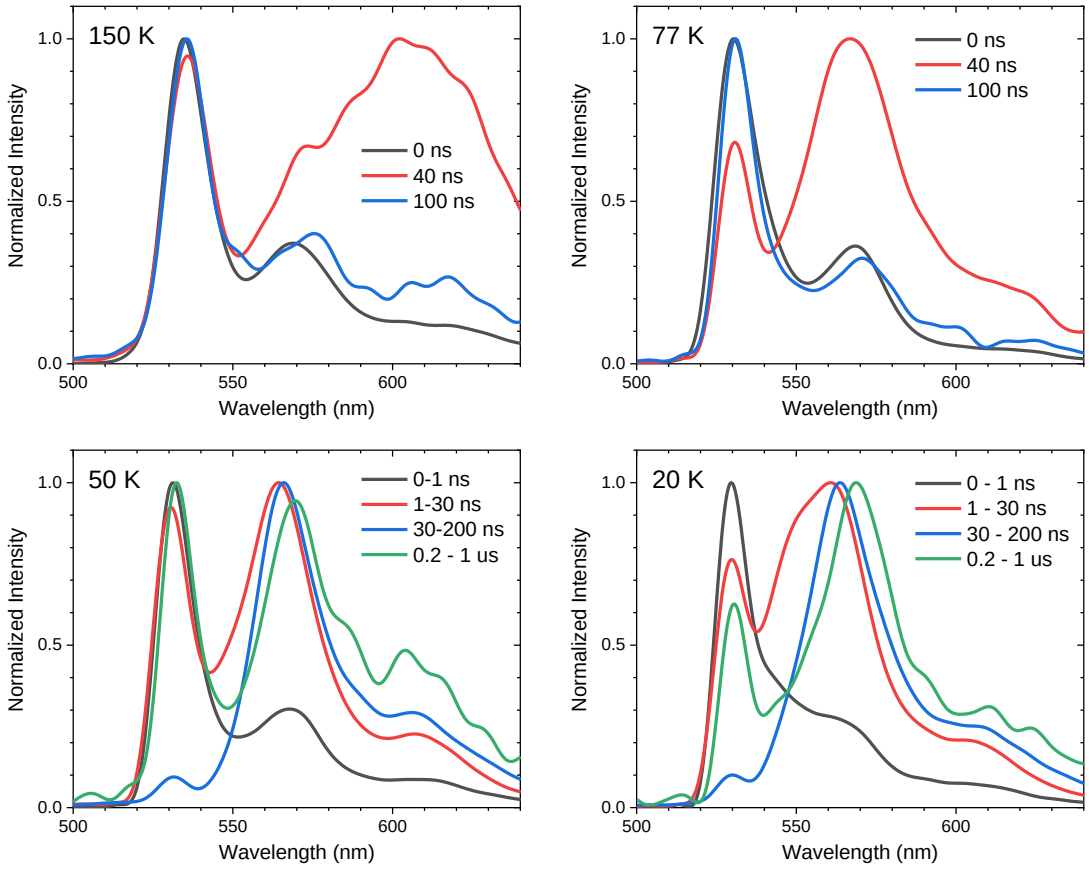

Figure 6.1.4. Smoothed PL spectra at cryogenic temperatures showing the spectral evolution.

6.2 Temperature dependence of the photodynamics and quantum beat damping

At elevated temperatures the rate of the prompt decay increases as can be seen in figure 6.2.1 where the prompt decay becomes shorter with increasing temperature. At the top end of the temperature range the decay is nonexponential which is the result of the temporal oscillations beginning earlier due to faster fission rates. By fitting the photoluminescence decays with an exponential function, the fission rate can be extracted and plotted versus inverse temperature to determine the activation energy for the process (Figure 6.2.2). Using this analysis an activation energy of 550 cm^{-1} is calculated, which is in good agreement with previous reports of singlet fission in tetracene at elevated temperatures.[10] These results support the idea that in single crystals of tetracene the dominant pathway of fission is activated.

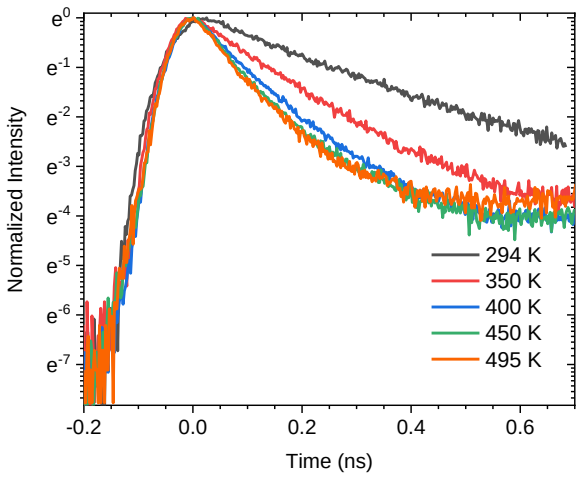

Figure 6.2.1. The PL decay of crystalline tetracene at elevated temperatures in a 1 ns window.

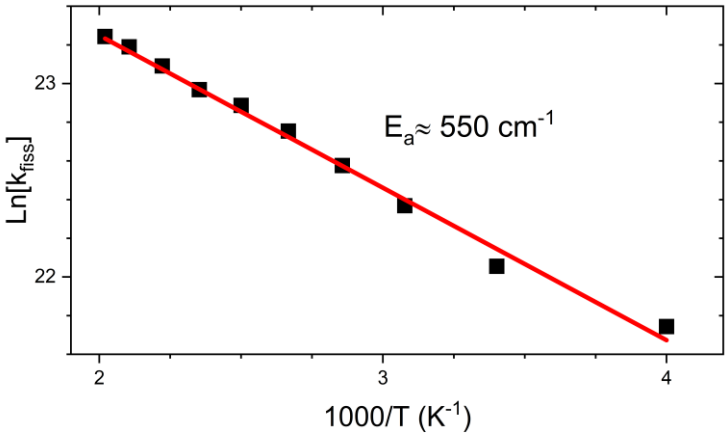

Figure 6.2.2. An Arrhenius plot of the extracted fission rates from the temperature dependent measurements of the prompt PL decays.

Because the temporal oscillations are an indirect means to monitor the correlated triplet pair, the temperature dependence of the quantum beats were examined. If the triplet pair state is truly bound with respect to free triplets, then a temperature dependence should emerge in the oscillations. The two cases being considered are shown in Figure 6.2.3. If the evolution of ^{1}(TT) into T_1 + T_1 is activated then at elevated temperatures the quantum beats, which are the evidence for ^{1}(TT), should be damped. If instead the oscillations do not show a dependence on the temperature, then ^{1}(TT) must evolve into ^{1}(T----T) without decoherence. If the damping coefficient is observed to have a dependence on temperature, then the binding energy can be calculated with an Arrhenius plot analogous to that used to determine the activation energy of fission. When the temporal oscillations are analyzed as a function of temperature, a clear increase in the amplitude of the oscillations with increased temperature is observed (Figure 6.2.4). This is not surprising as previous modeling has suggested that a faster fission rate would

increase the amplitude of the beats.[28] At 495 K, the crystal begins to melt and the decay deviates from the trend after a few ns. This is the result of contributions from monomeric tetracene overlapping with the crystalline spectrum. The monomeric background was not removed as there is not precedent for how tetracene should behave in PFPE at such an elevated temperature, and it is beyond the scope of the current project to determine that behavior. By fitting the decays with a multiexponential function, the temporal oscillations can be isolated and analyzed separately (Figure 6.2.5). Using equation 6.2.1, the extracted oscillations can be fit where A is the amplitude of the oscillations, t is the time, ν is the frequency, ϕ is the phase and α is the damping coefficient. The frequency of the oscillations are set to 1.08 GHz per previous results on quantum beats in crystalline tetracene.[28] The rest of the parameters are allowed to vary. This procedure is a somewhat crude approximation of the oscillations since multiple beat frequencies are present in the oscillations and their contributions may change with temperature.[28]

$$y(t) = A\cos(2\pi\nu t - \phi)\, e^{-\alpha t} \qquad (6.2.1)$$

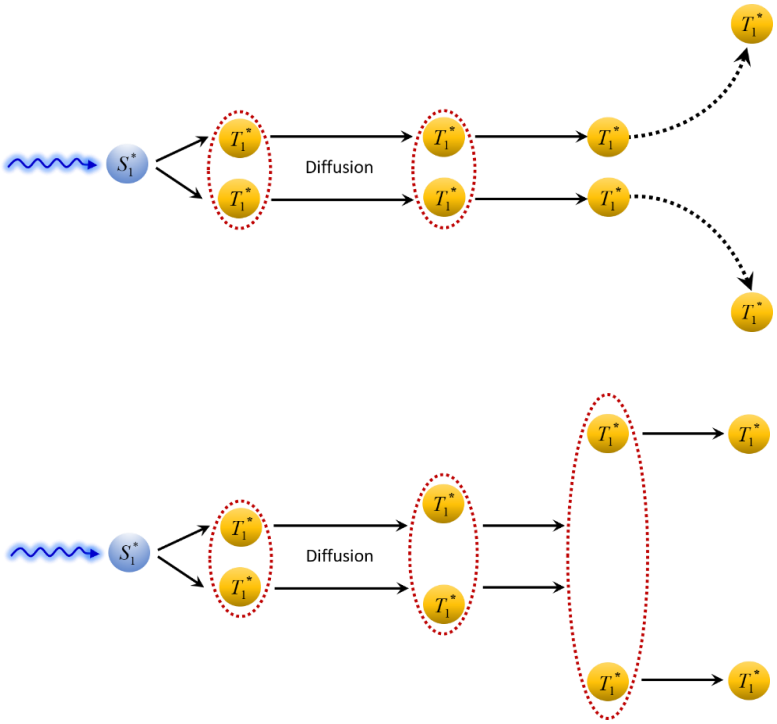

Figure 6.2.3. A cartoon showing triplets generated from singlet fission that remain bound during diffusion throughout the crystal (top) or are free to diffuse while still remaining spin entangled (bottom).

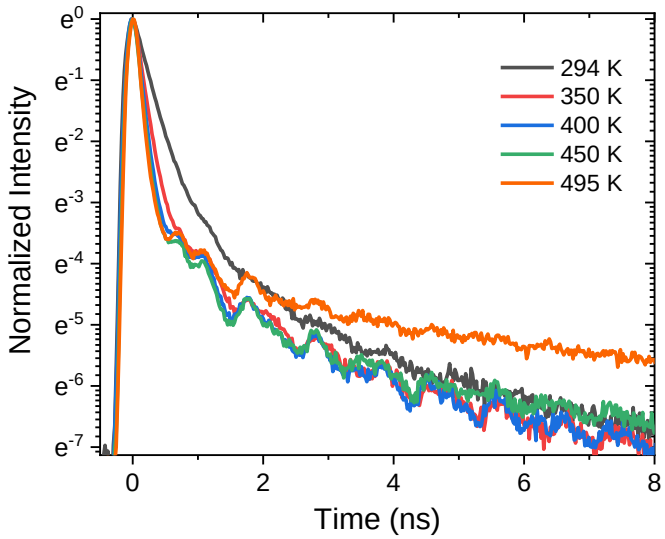

Figure 6.2.4. The raw PL decay of crystalline tetracene at elevated temperatures showing an enhancement of the quantum beat amplitude with increased temperature. At the highest temperature, the monomeric contribution to the decay causes the decay to appear longer and leads to lower amplitude oscillations.

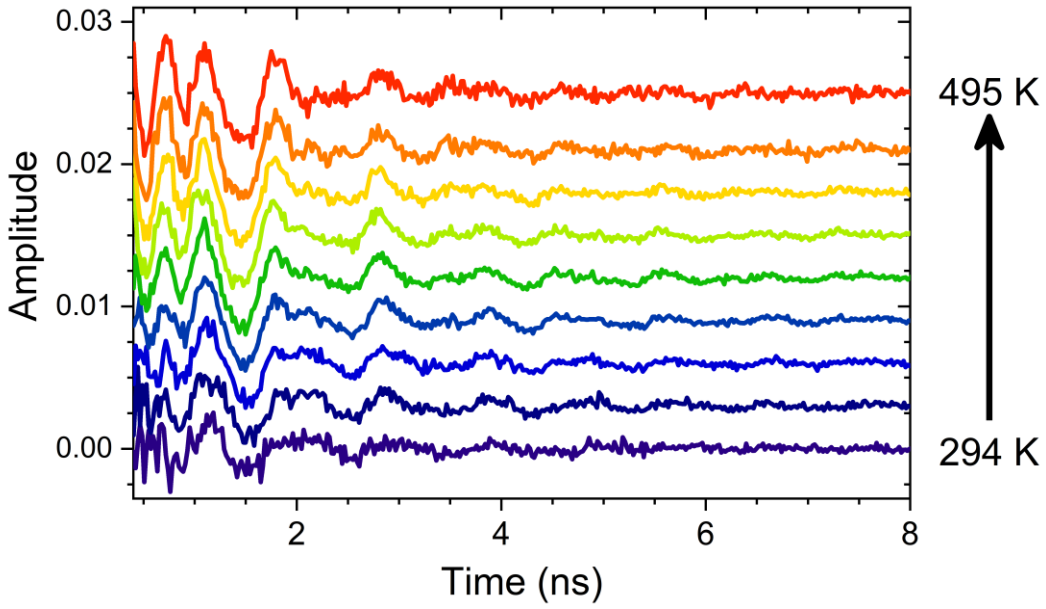

Figure 6.2.5. Extracted temporal oscillations in a 10 ns window showing the increased amplitude with increasing temperature. The damping of the oscillations appears mostly constant.

A trend does emerge in the value of the damping coefficient when fitting the quantum beats with equation 6.2.1. When the damping coefficient is plotted versus the inverted temperature a binding energy can be calculated (Figure 6.2.6). The binding energy is less than kT indicating that the triplets should be free to diffuse independently while remaining entangled at room temperature. As mentioned above, this is a crude fitting procedure and the value should be interpreted with caution. However, the value of 165 cm^{-1} is not too far off that determined by Sirringhaus and coworkers of ~240 cm^{-1} which inspires confidence in this simple analysis.[7] Obtaining a lower binding energy in a high quality single crystal also suggests that morphology is important to the decay of ^{1}(TT), which has been recently suggested by other workers.[9]

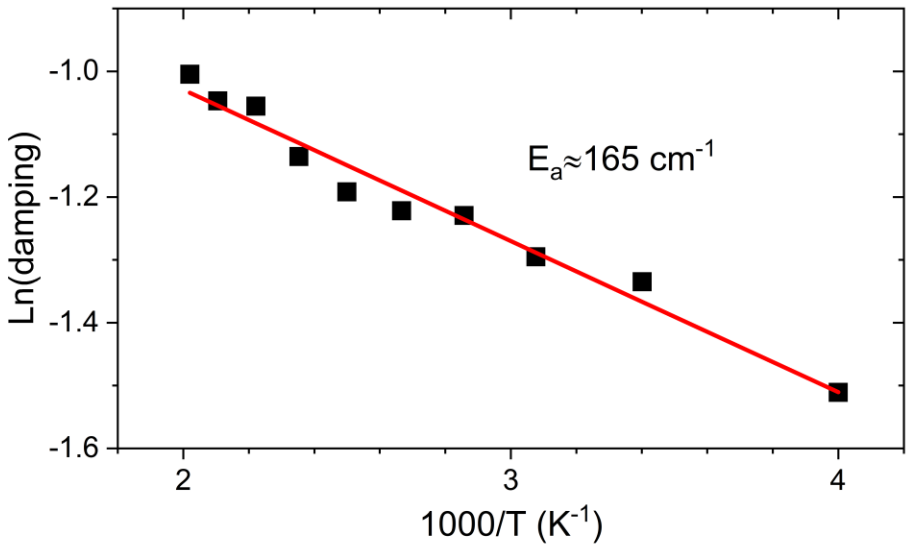

Figure 6.2.6. Arrhenius plot of the damping coefficient determined from fitting the temporal oscillations with equation 6.2.1.

6.3 Conclusions and Future Work

A few conclusions can be drawn from the limited data already obtained in this study though much work still needs to be done. Singlet fission in crystalline tetracene consistently and reproducibly generates ^{1}(TT) in ~ 200 ps and the process is endoergic with an activation energy of 550 cm^{-1}. At low temperature the decay is still fast, but the emergence of photoluminescence redshifted with respect to the 0-0 peak suggests that a defect state may mediate singlet fission at lower temperatures and could be the reason for so many conflicting reports regarding the temperature dependence of fission. It is unlikely that emission originates from ^{1}(TT) and spectral features attributed to it are more

likely low energy defects. While a binding energy between the correlated triplets can be extracted from the quantum beats, at room temperature the triplets are free to diffuse independently while maintaining spin coherence. This result is consistent with previous studies which concluded that the triplets must either diffuse or at least be greater than nearest neighbor distances apart.[28,29]

In the future, it would be informative to repeat the experiment at 4 K to see if the transiently redshifted photoluminescence overwhelms the emission at longer times. A kinetic model of the data should also be developed which looks at the possibility of two paths to generate the triplet pair state. An analysis like this could provide valuable insight on the origin of the activated pathway and whether it involves a state lower in energy than S_1. Further insight may also be gained by repeating these measurements in a magnetic field, which should only alter the triplets potentially allowing the conversion of ^{1}(TT) into $T_1 + T_1$ to be optically detected.

6.4 References

(1) Monahan, N. R.; Sun, D.; Tamura, H.; Williams, K. W.; Xu, B.; Zhong, Y.; Kumar, B.; Nuckolls, C.; Harutyunyan, A. R.; Chen, G.et al. Dynamics of the triplet-pair state reveals the likely coexistence of coherent and incoherent singlet fission in crystalline hexacene. *Nat. Chem.* **2016,** *9*, 341.

(2) Breen, I.; Tempelaar, R.; Bizimana, L. A.; Kloss, B.; Reichman, D. R.; Turner, D. B. Triplet Separation Drives Singlet Fission after Femtosecond Correlated Triplet Pair Production in Rubrene. *J. Am. Chem. Soc.* **2017,** *139* (34), 11745.

(3) Korovina, N. V.; Das, S.; Nett, Z.; Feng, X.; Joy, J.; Haiges, R.; Krylov, A. I.; Bradforth, S. E.; Thompson, M. E. Singlet Fission in a Covalently Linked Cofacial Alkynyltetracene Dimer. *J. Am. Chem. Soc.* **2016,** *138* (2), 617.

(4) Stern, H. L.; Cheminal, A.; Yost, S. R.; Broch, K.; Bayliss, S. L.; Chen, K.; Tabachnyk, M.; Thorley, K.; Greenham, N.; Hodgkiss, J. M.et al. Vibronically coherent ultrafast triplet-pair formation and subsequent thermally activated dissociation control efficient endothermic singlet fission. *Nat. Chem.* **2017,** *9*, 1205.

(5) Pensack, R. D.; Ostroumov, E. E.; Tilley, A. J.; Mazza, S.; Grieco, C.; Thorley, K. J.; Asbury, J. B.; Seferos, D. S.; Anthony, J. E.; Scholes, G. D. Observation of Two Triplet-Pair Intermediates in Singlet Exciton Fission. *J. Phys. Chem. Lett.* **2016,** *7* (13), 2370.

(6) Folie, B. D.; Haber, J. B.; Refaely-Abramson, S.; Neaton, J. B.; Ginsberg, N. S. Long-Lived Correlated Triplet Pairs in a π-Stacked Crystalline Pentacene Derivative. *J. Am. Chem. Soc.* **2018,** *140* (6), 2326.

(7) Yong, C. K.; Musser, A. J.; Bayliss, S. L.; Lukman, S.; Tamura, H.; Bubnova, O.; Hallani, R. K.; Meneau, A.; Resel, R.; Maruyama, M.et al. The entangled triplet pair state in acene and heteroacene materials. *Nature Communications* **2017,** *8*, 15953.

(8) Lukman, S.; Richter, J. M.; Yang, L.; Hu, P.; Wu, J.; Greenham, N. C.; Musser, A. J. Efficient Singlet Fission and Triplet-Pair Emission in a Family of Zethrene Diradicaloids. *J. Am. Chem. Soc.* **2017,** *139* (50), 18376.

(9) Musser, A. J.; Clark, J. Triplet-Pair States in Organic Semiconductors. *Annu. Rev. Phys. Chem.* **2019,** *70* (1), 323.

(10) Piland, G. B.; Bardeen, C. J. How Morphology Affects Singlet Fission in Crystalline Tetracene. *J. Phys. Chem. Lett.* **2015,** *6* (10), 1841.

(11) Arnold, S.; Whitten, W. B. Temperature dependence of the triplet exciton yield in fission and fusion in tetracene. *The Journal of Chemical Physics* **1981,** *75* (3), 1166.

(12) Geacintov, N.; Pope, M.; Vogel, F. Effect of Magnetic Field on the Fluorescence of Tetracene Crystals: Exciton Fission. *Phys. Rev. Lett.* **1969,** *22* (12), 593.

(13) Merrifield, R. E.; Avakian, P.; Groff, R. P. Fission of singlet excitons into pairs of triplet excitons in tetracene crystals. *Chem Phys Lett* **1969,** *3* (3), 155.

(14) Tomkiewicz, Y.; Groff, R. P.; Avakian, P. Spectroscopic Approach to Energetics of Exciton Fission and Fusion in Tetracene Crystals. *The Journal of Chemical Physics* **1971,** *54* (10), 4504.

(15) Wappelt, A.; Bergmann, A.; Napiwotzki, A.; Eichler, H. J.; Jüpner, H. J.; Kummrow, A.; Lau, A.; Woggon, S. Picosecond time-resolved luminescence of tetracene thin films. *J Appl Phys* **1995,** *78* (8), 5192.

(16) Lim, S.-H.; Bjorklund, T. G.; Spano, F. C.; Bardeen, C. J. Exciton Delocalization and Superradiance in Tetracene Thin Films and Nanoaggregates. *Phys. Rev. Lett.* **2004,** *92* (10), 107402.

(17) Voigt, M.; Langner, A.; Schouwink, P.; Lupton, J. M.; Mahrt, R. F.; Sokolowski, M. Picosecond time resolved photoluminescence spectroscopy of a tetracene film on highly oriented pyrolytic graphite: Dynamical relaxation, trap emission, and superradiance. *J. Chem. Phys.* **2007,** *127* (11), 114705.

(18) Grumstrup, E. M.; Johnson, J. C.; Damrauer, N. H. Enhanced Triplet Formation in Polycrystalline Tetracene Films by Femtosecond Optical-Pulse Shaping. *Phys. Rev. Lett.* **2010,** *105* (25), 257403.

(19) Wilson, M. W. B.; Rao, A.; Johnson, K.; Gelinas, S.; di Pietro, R.; Clark, J.; Friend, R. H. Temperature-Independent Singlet Exciton Fission in Tetracene. *J. Am. Chem. Soc.* **2013,** *135* (44), 16680.

(20) Smith, A. W.; Weiss, C. Fluorescence decay time measurements in tetracene crystals. *Chem Phys Lett* **1972,** *14* (4), 507.

(21) Alfano, R. R.; Shapiro, S. L.; Pope, M. Fission rate of singlet excitons in a tetracene crystal measured with picosecond laser pulses. *Opt Commun* **1973,** *9* (4), 388.

(22) López-Delgado, R.; Miehée, J. A.; Sipp, B. Fluorescence decay time measurements in tetracene crystals excited with synchrotron radiation. *Opt Commun* **1976,** *19* (1), 79.

(23) Fleming, G.; Millar, D.; Morris, G.; Morris, J.; Robinson, G. Exciton fission and annihilation in crystalline tetracene. *Aust. J. Chem.* **1977,** *30* (11), 2353.

(24) Klein, G. Kinematics of triplet pairs in anthracene and tetracene crystals. *Chem Phys Lett* **1978,** *57* (2), 202.

(25) Bardeen, C. J. Excitonic Processes in Molecular Crystalline Materials. *MRS Bulletin* **2013,** *38* (01), 65.

(26) Spano, F. C. The Spectral Signatures of Frenkel Polarons in H- and J-Aggregates. *Acc. Chem. Res.* **2010,** *43* (3), 429.

(27) Venuti, E. V., R. G. D.; Farina, L.; Brillante, A.; Masino, M.; Girlando, A;. Phonons and structures of tetracene polymorphs at low temperature and high pressure. *Phys. Rev. B: Condens. Matter Mater. Phys.* **2004,** *70*, 104106.

(28) Burdett, J. J.; Bardeen, C. J. Quantum Beats in Crystalline Tetracene Delayed Fluorescence Due to Triplet Pair Coherences Produced by Direct Singlet Fission. *J. Am. Chem. Soc.* **2012,** *134* (20), 8597.

(29) Wang, R.; Zhang, C.; Zhang, B.; Liu, Y.; Wang, X.; Xiao, M. Magnetic dipolar interaction between correlated triplets created by singlet fission in tetracene crystals. *Nature Communications* **2015,** *6*, 8602.

Chapter 7: Conclusions

"I am turned into a sort of machine for observing facts and grinding out conclusions."
– Charles Darwin

7.1 Perspective and future directions

Light not only can serve as a source of power but it can also serve as a probe for photochemical and photophysical processes important to developing the next generation of smart materials and optoelectronics. In chapter 3, molecular motifs which exhibit enhanced sensitivity toward hydrostatic pressure were investigated in photoisomers of anthracene.[1] While adjacent, strained, four-membered rings formed in Dewar 9-tert-butylanthracene make intuitive sense for increased mechanophoric ability, it was instead determined that large structural changes are better correlated with sensitivity toward mechanical stress. Still questions remain as to how chemical modification might further the response of molecules to pressure. Tethered anthracene derivatives which photodimerize could form the basis of further studies. One avenue for exploration involves the symmetry of the photodimer. While [4+4] photodimerization in anthracene involves bonding at the 9,10 positions, other derivatives such as 1,2-di(9-anthryl)ethanone can undergo [4+2] photodimerization forming bonds between the 9,10 carbons on one anthracene moiety to the 1,2 carbons on the second moiety, yielding much larger structural changes (Figure 7.1.1, left).[2] Another aspect worth exploring is

decorating the tethers with chemical groups that can protrude from the photodimer and potentially serve as handles which generate localized anisotropic strain upon the application of hydrostatic pressure thereby enhancing the pressure sensitivity. A good example of this type of molecule is the photodimer containing a three-membered episulfone ring formed by the sulfone-bridged anthracenes (Figure 7.1.1, right). Alkyl groups can be easily attached to each anthracene chromophore opposite the sulfone linker and the pressure sensitivity can be measured as a function of the decorator group.

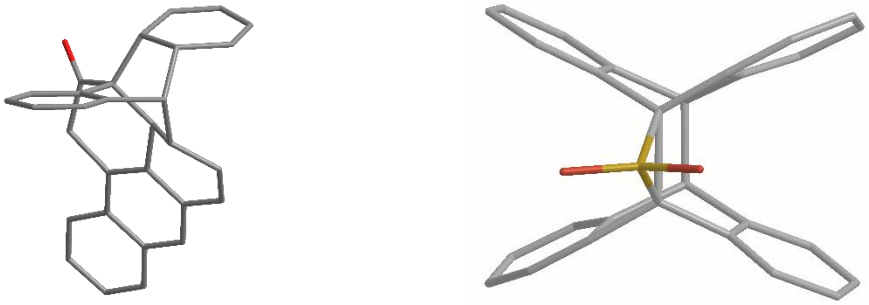

Figure 7.1.1. The [4+2] photodimer formed by 1,2-di(9-anthryl)ethanone (left) and the [4+4] photodimer formed from the sulfone bridged anthracenes discussed in chapter 4 (right).

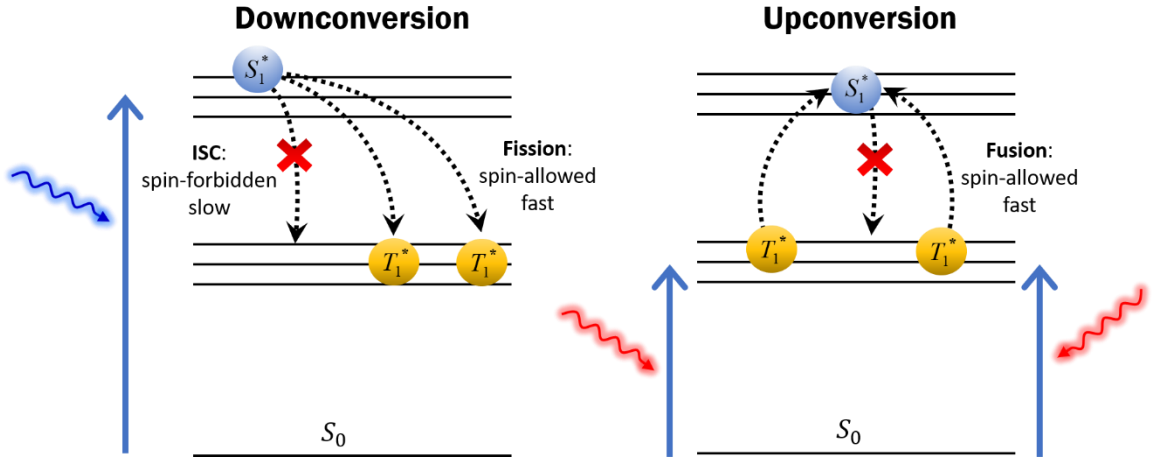

Figure 7.1.2. Cartoon illustrating downconversion where a high energy photon is absorbed generating an excited singlet state which rapidly converts to two triplet excitons at roughly half the energy of the singlet through a spin allowed process of singlet fission (left). Upconversion is the inverse process in which two low energy photons sensitize triplets which can pool their energy to form a higher energy singlet state (right).

Efficiently harnessing solar energy is a primary hurdle preventing such a promising renewable source from supplanting the current dominance of hydrocarbons as the preeminent fuel source. In this dissertation an emphasis was placed on the viability of multiexciton processes in organic materials to surpass the efficiency limits of current solar technologies. For instance, a high energy photon can be absorbed by an organic fission material that takes one photon and downconverts it into two lower energy charge carriers so that the excess energy of the photon is not wasted as heat (Figure 7.1.2). The inverse strategy of upconverting two low energy photons into one charge carrier enables more of the solar spectrum to be utilized. If both upconversion and downconversion could be implemented in conjunction with a silicon single junction cell, then power conversion efficiencies can theoretical reach 50% (Figure 7.1.3).[3]

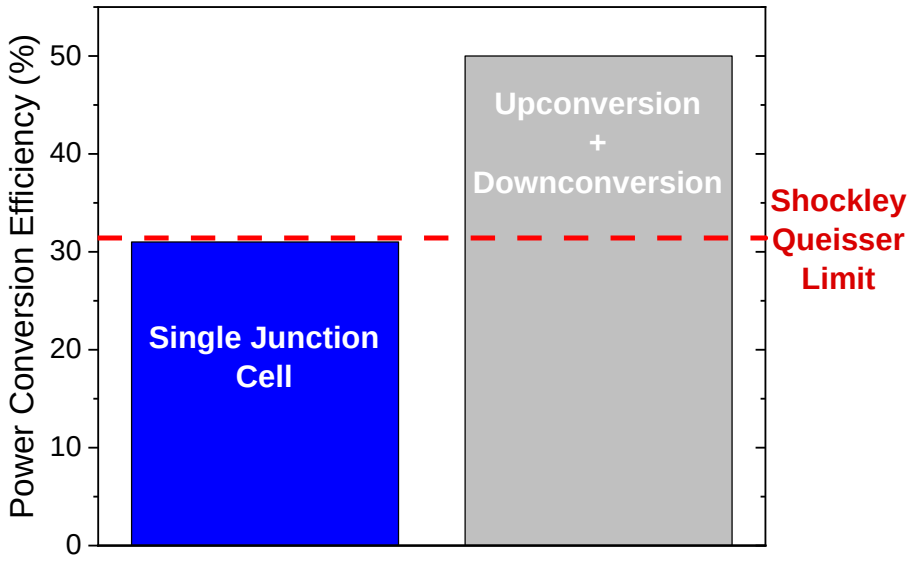

Figure 7.1.3. Diagram illustrating the theoretical limits of current single junction silicon cells (blue) and how that limit can be surpassed by more efficient solar harvesting strategies utilizing photon conversion.

An important aspect that dictates the efficiency of these multiexciton processes is the degree of charge transfer (CT) in the excited state as was discussed in chapter 1. The CT state can be envisioned as the pathway linking the singlet state and the doubly excited triplet pair state. By increasing the CT character of the excited state more efficient interconversion between singlet states and multiexciton states can be achieved (Figure 7.1.4).

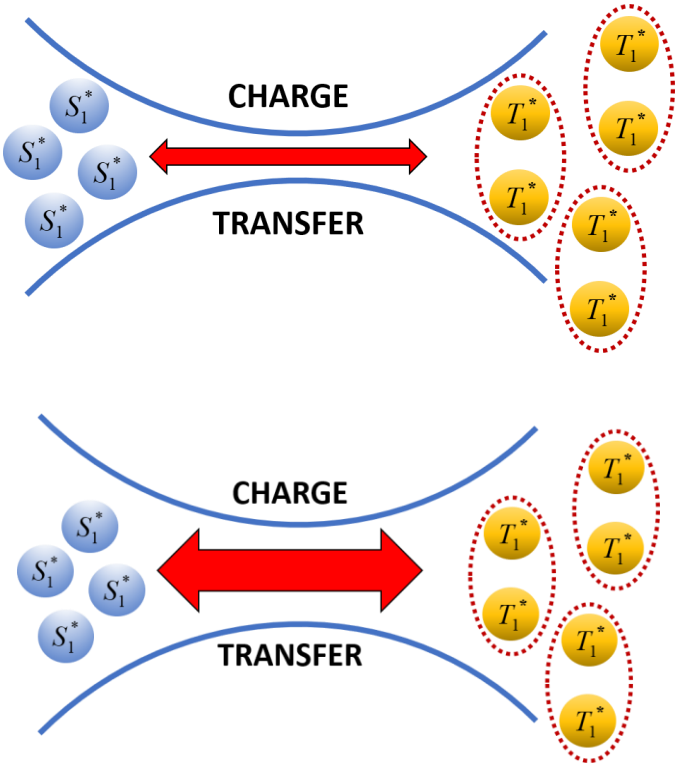

Figure 7.1.4. Cartoon illustrating that the degree of charge transfer is the bottleneck between the singly excited singlet state, S_1, and the doubly excited state, ^{1}(TT). By increasing the charge transfer character of the excited state the bottleneck can be opened facilitating more efficient interconversion.

The focus of chapter 4 was to find ways to increase excited state CT character in covalently tethered dimers.[4] These dimers provide a structurally well-defined unit to gain

fundamental insights on controlling interchromophore interactions that could lead to facile formation of CT states. Using a sulfur atom as the linker between chromophores provides a unique intramolecular handle for tuning the photophysics simply by oxidizing the bridge. Moreover, oxidation of the bridge does not alter the geometry between chromophores so that electronic effects are able to be isolated in these simple systems. It was found that for both terthiophene and anthracene chromophores that the fully oxidized sulfone bridge led to increased CT character of the excited state. In both cases, the SO_2 bridge turned off intersystem crossing. For the terthiophene chromophores this resulted in enhanced photoluminescence; whereas, in anthracene it enabled photodimerization. An electron screening model was developed to describe the effect of the bridge oxidation state on the dimers. A cartoon illustrating this effect is shown in figure 7.1.5. In the unoxidized S bridge, lone pairs on the bridge screen the interaction between chromophores. By oxidizing the bridge, the electron density can be tied up in polarized S=O bonds which enables the chromophores to "see" each other and stabilize the CT contributions that mix with the neutral states.

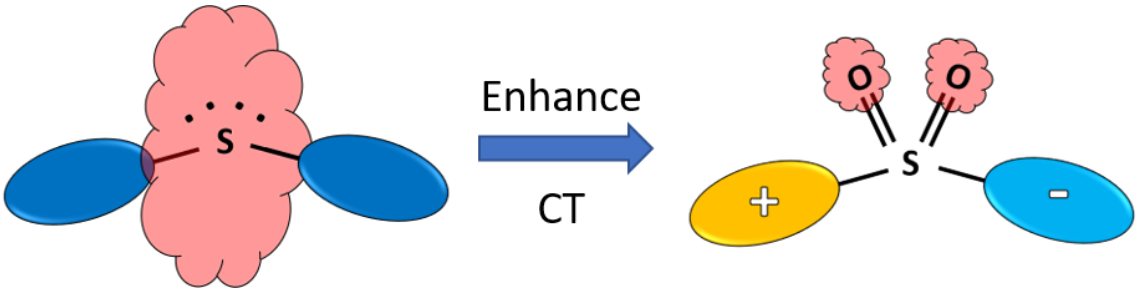

Figure 7.1.5. Cartoon illustrating the electrostatic screening model. In the unoxidized sulfur bridge the increased electron density of the lone pair electrons screens the interaction between chromophores (blue). By oxidizing the sulfur atom, the electron density is pulled away from the bridge allowing the chromophores to interact and form CT states.

A brief survey of the literature illustrates the utility of the sulfone bridge in optoelectronic applications where this motif is commonly used, but the origin of the effect had not been previously determined. Because of our studies on sulfur-bridged dimers, these results can now be understood on a fundamental level. In an organic photovoltaic, oxidation of thiophene lead to improved device performance through enhanced charge separation which, in light of our results, must be the product of increased CT character from using SO_2.[5] Oxidation of sulfur has also been shown to modulate the band gap in polythiophenes which can be explained by the formation of extend CT states.[6] Adachi and coworkers used a diphenylsulfone bridged molecule which undergoes thermally activated delayed fluorescence (TADF) to fabricate an efficient blue organic light emitting diode (OLED).[7] Such TADF molecules take advantage of intramolecular CT states to achieve spatial separation between the singlet and triplet states which allows the energy of these states to be tuned such that the dark triplet can thermally access the bright singlet state. The ability of SO_2 to facilitate CT states explains why SO_2 is often found in OLEDs that take advantage of TADF. Finally, the most impressive example is from a recent report looking at intramolecular singlet fission and the role of the CT intermediate state in singlet fission.[8] Intramolecular fission in polymers with an oxidized thiophene is reported, but an easily overlooked detail is that they briefly mention that singlet fission does not occur with the unoxidized thiophene! This is an astounding result which is readily explained by our studies on enhancing CT in simple dimer systems.[4] The unoxidized thiophene screens the interactions between the donor and acceptor of

the system which prevents CT states from forming. Once the thiophene is oxidized the CT state is stabilized and singlet fission, which requires appreciable CT character of the excited state, can occur. Furthermore, these results show that using SO_2 in fission materials is a promising avenue for further research. Future studies should explore sulfur-bridged chromophores which undergo fission such as tetracene or pentacene. Such studies could better correlate both the role of the bridge in tuning the CT character of the excited state and the role of CT intermediates in facilitating the formation of multiexciton states.

In chapter 5, the uncanny ability of crystalline rubrene to perform NIR-to-visible upconversion without extrinsic sensitizers was found to be the result of an interband state that was present in every crystalline sample.[9] Rubrene is an often used component of photon upconversion schemes in both solution and the solid state, and these results call into question reported solid state upconversion schemes since sensitizers are apparently not required. The lifetime of the interband state was determined to be 1.5 μs by monitoring the upconverted photoluminescence as a function of the pulse spacing and fitting that data with a four-state kinetic model. The triplet state of rubrene could be ruled out as the interband state since the lifetime of the triplet is much longer (100 μs) and the intensity dependence was quartic and not quadratic. That this effect was polarized along the high mobility axis of rubrene precludes an extrinsic defect as the origin of the interband state and seems more than coincidental.

While this work was not able to conclusively identify the origin of the interband state, we can speculate about a possible culprit – free charges in rubrene. By measuring the electron paramagnetic resonance (EPR) spectrum of rubrene microcrystals, it can be determined whether any unpaired electrons are present in the sample. A weak signal is obtained for rubrene, pointing toward the possibility of free charges present in rubrene even in the absence of an excitation source (Figure 7.1.6). Since charge mobility in rubrene is highly favored along the *b* axis and the upconversion is most efficient along this same axis it seems reasonable that polarons could lead to some weakly absorbing interband state that enables NIR upconversion in rubrene (Figure 7.1.7). To test this, more experiments are required. Particularly, charge modulation spectroscopy seems the most promising technique to test the idea of polaron absorption in crystalline rubrene. Another interesting experiment would be to illuminate rubrene with NIR light and then take an EPR spectrum. It is possible that it takes very little for these charges to be built up and perhaps photoexcitation leads to an irreversible increase in background polarons.

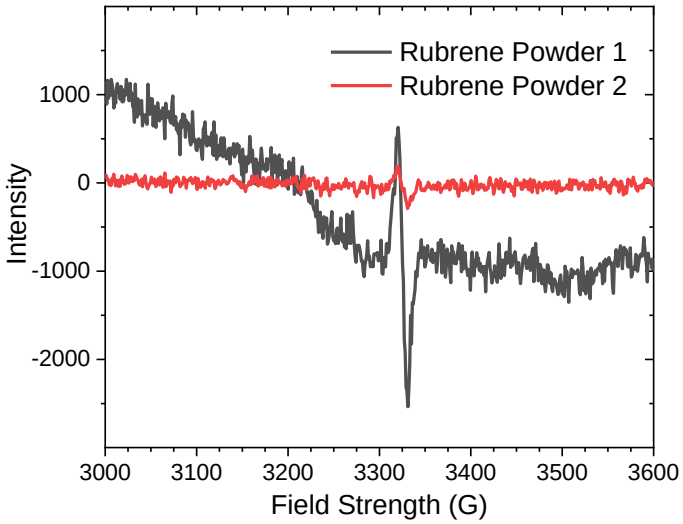

Figure 7.1.6. EPR spectra of two microcrystalline samples of rubrene showing a paramagnetic response in the absence of photoexcitation.

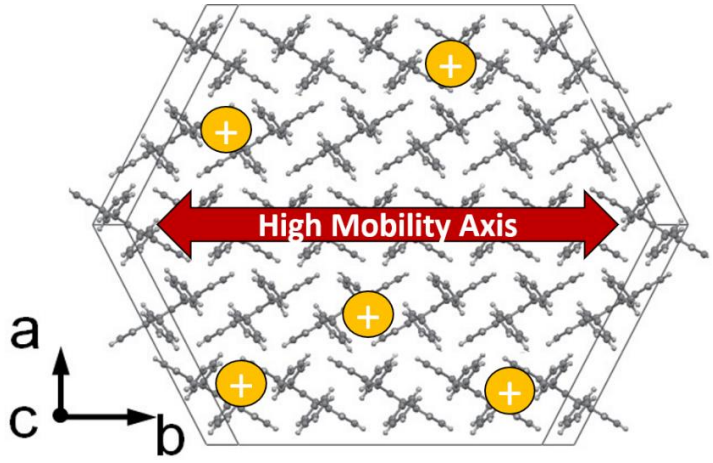

Figure 7.1.7. Crystal packing structure of rubrene highlighting the high mobility b axis. A low concentration of free charges (polarons) could be the origin of the interband state.

Finally, in chapter 6, the mechanism of singlet fission was explored over the temperature range of 20 – 500 K in high quality single crystals of tetracene (Figure 7.1.8). It was demonstrated that the predominant pathway of fission in single crystals of tetracene is activated, with an activation energy of 550 cm^{-1}. The spin entangled triplet pair state, ^{1}(TT), is evidence in the photoluminescence decay as temporal oscillations

known as quantum beats. The damping of the quantum beats has a small dependence on temperature with an extracted binding energy of 165 cm^{-1}. This small binding energy suggests that ^{1}(TT) rapidly evolves into ^{1}(T----T) where the triplets independently diffuse while maintaining spin coherence. Red shifted photoluminescence is observed at lower temperatures, but the resurgence of the original spectrum at later times for temperatures above 77 K suggests that this emission originates from a crystal defect rather than ^{1}(TT).

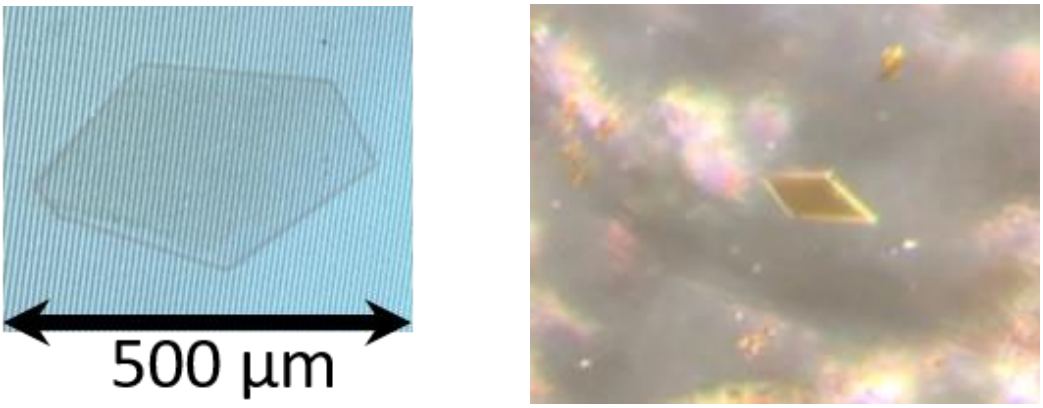

Figure 7.1.8. Images of high quality, solution grown tetracene crystals used in the singlet fission study. Quantum beats are predominant in crystals which form stretched hexagons as shown.

While these results solidify certain mechanistic parts of fission in crystalline tetracene, the strong sensitivity toward sample morphology leaves many questions unanswered. Are there two routes of singlet fission available in crystalline tetracene – the endoergic pathway and a defect-mediated pathway? The existence of two routes could rectify the discrepancies between the faster fission times reported in polycrystalline samples versus single crystals. Furthermore, does morphology influence the decay of ^{1}(TT)? The fact that quantum beats are readily observed in single crystals for ~10 ns

supports the idea that ^{1}(TT) decay could be different than what is observed in the more commonly measured polycrystalline films where quantum beats require some work to extract. If triplet hopping is the dominant diffusion mechanism for migration after fission,[10] then it seems that disorder could strongly influence the behavior of the multiexciton state in endoergic fission materials unlike what has been observed in exoergic fission materials.[11] Perhaps the most significant challenge for the field is identifying the individual steps of fission particularly with regard to the decay of the multiexciton state. For example, does ^{1}(TT) have an optical signature that is distinctly different from ^{1}(T----T), and can the moment that free triplets are generated be distinguished from the separated triplet pair state? Currently, optical measurements cannot distinguish from ^{1}(TT) and ^{1}(T----T), while features associated with free triplets are often identified through sensitization experiments. One possible direction for future exploration along these lines, is to look for a magnetic field dependence in the fluorescence decay as an indicator for when the overall singlet spin state of the triplet pair become free triplets, since a magnetic field will have no effect on the singlet states but should perturb the triplets. Another aspect of the triplet pair states that is rarely considered is the role ^{1}(TT) plays in upconversion schemes. Presumably triplet fusion into a singlet state proceeds through a correlated triplet pair state, but it remains to be seen whether they can be identified with the same techniques developed for fission. Spin entangled states in organic semiconductors remains an active area of research and with time hopefully the nature of ^{1}(TT) can be pinned down.

In this dissertation, photophysics and photochemistry of organic chromophores were studied using a variety of steady-state and ultrafast spectroscopies with the goal of establishing fundamental design principals and insights for controlling the response of molecules to force and light. Molecules that undergo large structural changes can serve as better mechanophores compared to molecules only incorporating ring strain. Tethered dimers served as a testbed for interchromophore interactions where it was demonstrated that CT character can be tuned intramolecularly by changing the oxidation state of the linker. Photon upconversion in crystalline rubrene was demonstrated to occur without sensitization. The interband state which is the likely the result of some CT or polaron state can potentially serve as a basis for all organic upconversion schemes. Finally, the correlated triplet pair state produced via fission was identified using quantum beats and found to have a small binding energy suggesting that triplets can diffuse independently while remaining spin entangled. The fundamental insights provided in this dissertation will inform future research seeking to apply mechanophores and exciton manipulation to smart materials and third generation photovoltaic technologies.

7.2 References

(1) Tong, F.; Cruz, C.; Jezowski, S.; Zhou, X.; Zhu, L.; Al-Kaysi, R. O.; Chronister, E. L.; Bardeen, C. J. Pressure Dependence of the Forward and Backward Rates of 9-tert-Butylanthracene Dewar Isomerization. *J. Phys. Chem. A* **2014,** *118* (27), 5122.

(2) Becker, H. D. Unimolecular Photochemistry of Anthracenes. *Chem. Rev.* **1993,** *93* (1), 145.

(3) Shpaisman, H.; Niitsoo, O.; Lubomirsky, I.; Cahen, D. Can up- and down-conversion and multi-exciton generation improve photovoltaics? *Sol. Energy Mater. Sol. Cells* **2008,** *92* (12), 1541.

(4) Cruz, C. D.; Christensen, P. R.; Chronister, E. L.; Casanova, D.; Wolf, M. O.; Bardeen, C. J. Sulfur-Bridged Terthiophene Dimers: How Sulfur Oxidation State Controls Interchromophore Electronic Coupling. *J. Am. Chem. Soc.* **2015,** *137* (39), 12552.

(5) Camaioni, N.; Ridolfi, G.; Fattori, V.; Favaretto, L.; Barbarella, G. Oligothiophene-S,S-dioxides as a class of electron-acceptor materials for organic photovoltaics. *Applied Physics Letters* **2004,** *84* (11), 1901.

(6) Wei, S.; Xia, J.; Dell, E. J.; Jiang, Y.; Song, R.; Lee, H.; Rodenbough, P.; Briseno, A. L.; Campos, L. M. Bandgap Engineering through Controlled Oxidation of Polythiophenes. *Angew. Chem. Int. Ed.* **2014,** *53*, 1832.

(7) Zhang, Q.; Li, B.; Huang, S.; Nomura, H.; Tanaka, H.; Adachi, C. Efficient Blue Organic Light-Emitting Diodes Employing Thermally Activated Delayed Fluorescence. *Nat. Photon.* **2014,** *8*, 326.

(8) Busby, E.; Xia, J.; Wu, Q.; Low, J. Z.; Song, R.; Miller, J. R.; Zhu, X. Y.; Campos, Luis M.; Sfeir, M. Y. A design strategy for intramolecular singlet fission mediated by charge-transfer states in donor–acceptor organic materials. *Nature Materials* **2015,** *14*, 426.

(9) Cruz, C. D.; Choi, H. H.; Podzorov, V.; Chronister, E. L.; Bardeen, C. J. Photon Upconversion in Crystalline Rubrene: Resonant Enhancement by an Interband State. *J. Phys. Chem. C* **2018,** *122* (31), 17632.

(10) Korovina, N. V.; Das, S.; Nett, Z.; Feng, X.; Joy, J.; Haiges, R.; Krylov, A. I.; Bradforth, S. E.; Thompson, M. E. Singlet Fission in a Covalently Linked Cofacial Alkynyltetracene Dimer. *J. Am. Chem. Soc.* **2016,** *138* (2), 617.

(11) Broch, K.; Dieterle, J.; Branchi, F.; Hestand, N. J.; Olivier, Y.; Tamura, H.; Cruz, C.; Nichols, V. M.; Hinderhofer, A.; Beljonne, D.et al. Robust singlet fission in pentacene thin films with tuned charge transfer interactions. *Nature Communications* **2018,** *9* (1), 954.